MECHANISMS OF METAL DEPOSITION ON GOLD NANOPARTICLE SUBSTRATES

By

Patrick Joseph Straney

B.S., University of Delaware, 2010

M.S., University of Pittsburgh, 2013

Submitted to the Graduate Faculty of

The Kenneth P. Dietrich School of Arts and Sciences in partial fulfillment

of the requirements for the degree of

Doctor of Philosophy

University of Pittsburgh

2017

UNIVERSITY OF PITTSBURGH

DIETRICH SCHOOL OF ARTS AND SCIENCES

This dissertation was presented

by

Patrick J. Straney

It was defended on

December 14th, 2016

and approved by

Dr. Geoffrey Hutchison, Associate Professor, Department of Chemistry

Dr. Nathaniel Rosi, Professor, Department of Chemistry

Dr. Goetz Veser, Professor, Department of Chemical and Petroleum Engineering

Dissertation Advisor: Dr. Jill E. Millstone, Associate Professor, Department of Chemistry

Prof. Jill E. Millstone

MECHANISMS OF SECONDARY METAL DEPOSITION ON GOLD NANOPARTICLE SUBSTRATES

Patrick J. Straney, PhD

University of Pittsburgh, 2017

Understanding the chemical mechanisms underlying multimetallic nanoparticle nucleation and growth is crucial for translating the unique properties that emerge on the nanoscale. However, limited knowledge of nanoscale nucleation and growth processes challenges our ability to synthesize and characterize these materials in a robust and reproducible fashion. This dissertation identifies and describes synthetic mechanisms that direct metal on metal growth processes for gold nanoparticle substrates with unprecedented chemical detail.

In Chapter 1, the dissertation is introduced with a background on the processes that influence multimetallic nanoparticle formation in relation to classic thin film growth modes. Specifically, the chapter focuses on metal-on-metal nucleation and growth mechanisms and highlights current advances in the synthesis of multimetallic nanoparticles through island-type deposition pathways. Chapter 2 demonstrates homogeneous nucleation as a robust, scalable, and sustainable method to synthesize anisotropic Au nanorods and nanoprisms relative to traditional seed mediated strategies. With effective methods to synthesize anisotropic Au nanoparticles, Chapter 3 builds on these results and uses Au nanoparticles as substrates for secondary metal deposition and multimetallic nanoparticle formation. Specifically, Chapter 3 describes pathways of Pt island deposition and identifies chemical mechanisms impacting surface chemistry vs. redox mediated growth pathways.

Building on these results, Chapter 4 identifies the use of metal-ligand surface chemistry to promote edge, facet, or vertex selective nucleation of Pd, Pt, and Au nanoparticles on anisotropic Au nanoparticle substrates. Finally, Chapter 5 describes the deposition of Cu on Au nanoprisms and the challenges of incorporating 3d transitions metals into traditional noble metal syntheses. Together, these chapters demonstrate metal-ligand surface chemistry as a robust and efficient means of influencing the morphology, composition, and properties of multimetallic transition metal nanostructures.

TABLE OF CONTENTS

LIST OF TABLES

LIST OF FIGURES

ACKNOWLEDGEMENTS

I would like to first start by thanking my research mentor, Dr. Jill Millstone. Her passion for science and her motivation inspires me to become both a better scientist and person. I would also like to thank my research group, specifically Dr. Christopher Andolina, for their time and making my experience through graduate school so meaningful. Lastly, I would like to thank my parents and family for their never-ending support and guidance over the course of my education.

1.0 NANOISLAND DEPOSITION ON COLLOIDAL NANOPARTICLE SUBSTRATES

1.1 INTRODUCTION

Multimetallic nanoparticles are an emerging class of materials able to synergistically combine properties from each component in order to enhance overall optoelectronic,[1-2] magnetic,[3-4] and/or catalytic[5-7] performance in the combined materials. For a given combination of metals, the chemical and physical properties depend on the size, shape, and surface chemistry of the nanoparticle, as well as the distribution of elements within the given morphology. Given the strong relationship between particle architecture and particle properties, these multimetallic nanomaterials exhibit exceptionally tunable chemical and physical behaviors.[8-14] Multimetallic nanomaterials may be classified into three broad categories: core@shell, Janus-type, or alloyed morphologies (Figure 1). Traditional multimetallic nanomaterials such as core@shell and alloyed nanoparticles have been reviewed extensively.[13,15-16] For a subset of core@shell materials, the shell is comprised of individual metal islands instead of a continuous shell, and these islands are typically randomly distributed across the surface of the core particle. Multimetallic nanoparticles that exhibit "discontinuous" or island type interfaces are emerging as an independent class of materials which may exhibit properties distinct from their

"continuous" core@shell counterparts. Here, the island type growth pathways can be differentiated from other types of multimetallic nanomaterials and multimetallic nanomaterial growth pathways by the fact that the metal-metal interface remains discontinuous even after more than one monolayer of the new metal is introduced.

Nanostructures exhibiting nanoisland surfaces are attractive due to their high surface area compared to traditional core@shell or alloyed nanostructures.[17-18] Surfaces comprised of both types of metals may also impart multifunctionality to the nanostructure for applications in plasmon-enhanced catalysis[19-20] or as handles for the construction of more complex nanoparticle constructs.[21] Yet, the factors driving nanoisland growth (as opposed to layer-by-layer deposition) are often metal- and synthesis-specific which presents challenges to large scale synthesis and implementation of these materials.

Here, we review the synthesis and mechanisms of metal nanoisland formation on noble metal surfaces. We begin by reviewing nanoisland formation mechanisms, which have been used to describe growth on both thin-film and nanoparticle substrates. After discussing factors influencing nanoisland formation, we highlight recent reports concerning the synthesis and characterization of nanoparticles with nanoisland-structured surfaces. Specifically, we focus on the growth of nanoislands on colloidal metal nanoparticle substrates and detail how differences in substrate crystallinity, morphology, and composition impact nanoisland formation and growth.

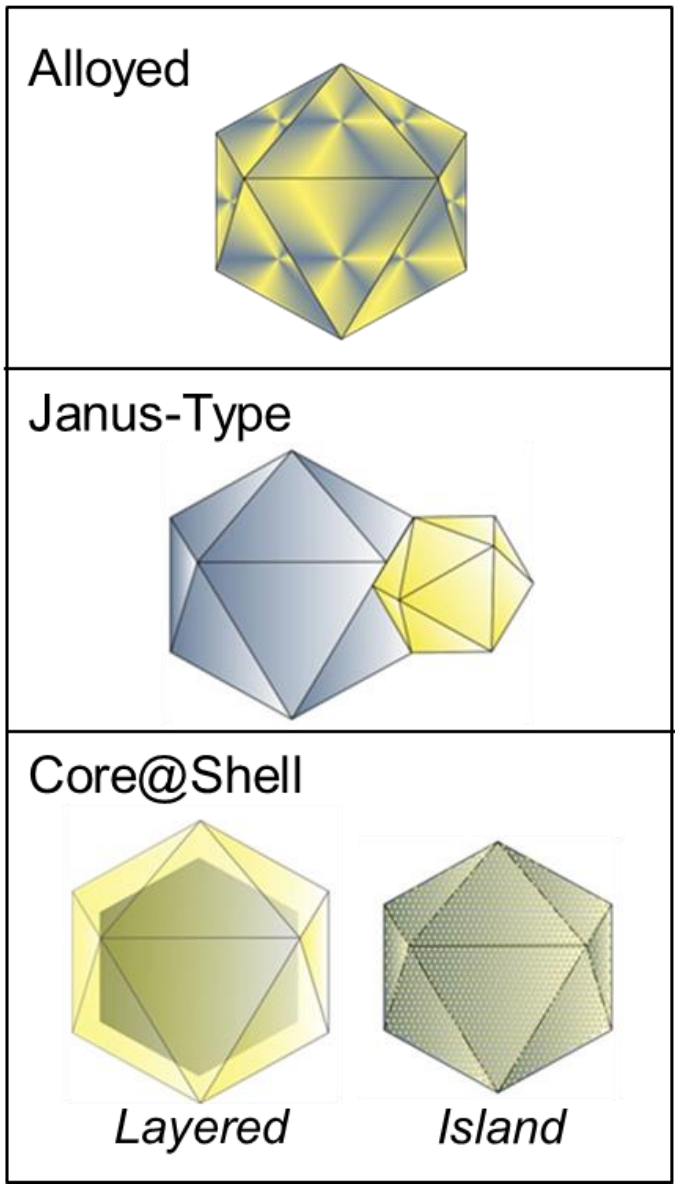

Figure 1. Cartoons depicting possible morphologies of multimetallic nanoparticles into the broad categories of alloyed, Janus-type, and core@shell architectures.

1.2 NANOISLAND FORMATION MECHANISMS

1.2.1 Classic Descriptions of Thin-Film Growth Processes

Experimentally, epitaxial metal-on-metal deposition may be classified into three categories depending on the surface structure of the secondary metal and the extent of deposition: layered, island, and layer+island (Figure 2). Layered growth, also referred to as Frank van der Merwe (FM) deposition, proceeds by the progressive formation of continuous monolayers. Here, a complete monolayer is deposited prior to the formation of additional atomic layers. For nanoparticle substrates, this type of growth pathway typically leads to core@shell nanoparticle products. For island growth modes, a portion of the underlying substrate will always remain exposed after growth and hence the metal-metal interface will remain discontinuous (provided the absence of any post-synthetic fusion or ripening processes). This growth mode, also called Volmer-Weber (VW) growth, leads to nanoisland formation even at surface coverages greater than one monolayer. A combination of layer+island growth may also be observed and is called Stranski-Krastanov (SK) growth. In SK growth modes, layered growth transitions to an island growth pathway after some critical surface coverage threshold (*vide infra*).[22] Since the pathway of deposition influences the resulting composition, morphology, and properties of the final film product, understanding conditions that promote a specific deposition pathway is critical for designing and synthesizing these multimetallic materials.

In determining whether a particular metal addition will exhibit layered or island growth, several chemical and physical parameters are taken into consideration. For example, enthalpic interactions between the metal substrate atoms and the incoming adatom will depend upon the specific crystallographic orientation of the substrate and the surface chemistry at each unique surface site.[23] Typically, these interactions are quantified in terms of the bond energy between a single atom of the substrate metal and the nanoisland metal, or by approximating the rates of adsorption/desorption (K_d), among other parameters. In the next section, we describe properties of the substrate, depositing metal, as well as interactions between the two that ultimately influence the growth modes observed.

1.2.2 First Monolayer Growth Factors

1.2.2.1 Trends in Bond Enthalpy and Lattice Mismatch

It has been shown that the active pathway of metal deposition can be predicted from the bond enthalpies between the adatom and a surface atom within the substrate. If there is a large thermodynamic driving force for adatom-substrate bond formation, the adatom will completely wet the substrate surface resulting in layered growth. Conversely, if adatom-adatom bond formation is favored, island growth will be observed. For a given combination of metals, the pathway of metal deposition can be more accurately predicted when the bond energetics are compared to the degree of lattice mismatch. For instance, Lorenz and Staikov investigated the change in deposition pathway depending on the adatom-substrate vertical interaction energy for a given degree of lattice mismatch using scanning tunneling microscopy (STM).[24] In the case of Ag on Au(100), the relatively small lattice mismatch (d_{Ag} = 0.289 nm, d_{Au} = 0.235 nm), and high bond dissociation

energy (221.3 kJ/mol) produced layer-by-layer growth up to 40 monolayers. For Pb on Ag(111), however, the significant degree of lattice mismatch (d_{Ag} = 0.289 nm, d_{Pb} = 0.350 nm) prevented formation of a uniform Pb monolayer[24] despite Pb-Ag bonds having a higher bond strength than Pb-Pb bonds.[25] Generally, a combination of metals exhibiting a lattice mismatch of approximately 5% or greater will exhibit VW deposition.[26]

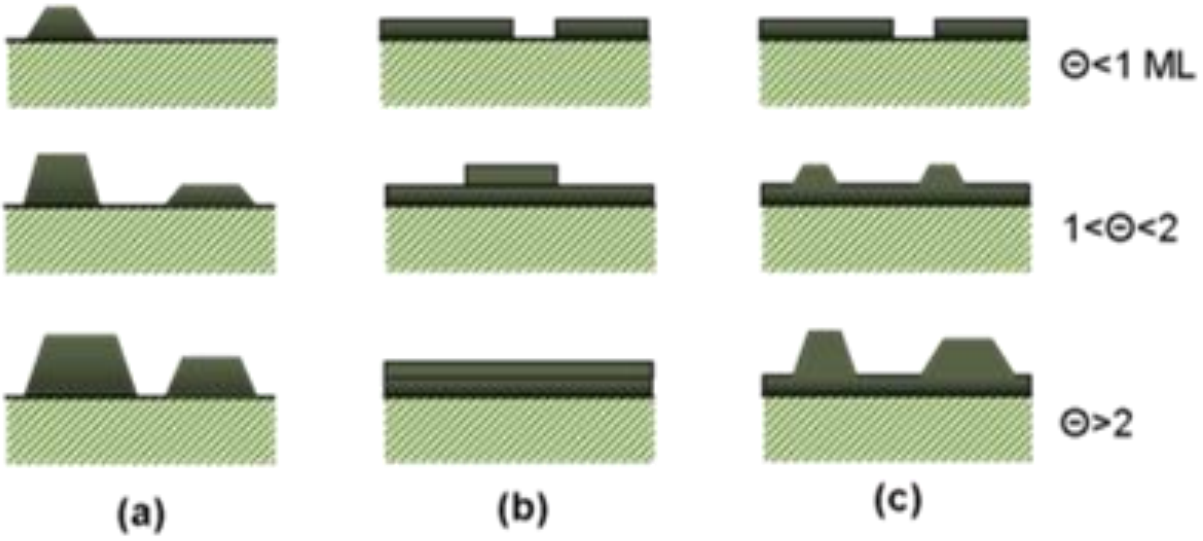

Figure 2. Cross-sectional views of the three, possible metal-on-metal deposition pathways for a given extent of monolayer surface coverage (θ). (A) Volmer-Weber nanoisland growth, where the metal-metal interface remains discontinuous after multiple monolayers of surface coverage. (B) Frank-van der Merwe layer-by-layer growth, where a continuous monolayer is formed before subsequent formation of another layer. (C) Stranski-Krastanov layer+island growth, where continuous monolayer growth is initially observed followed by island growth at higher extents of surface coverage. Reproduced from Wikipedia Commons, 2016.

1.2.2.2 Mechanical Considerations in Monolayer Formation

In addition to the energetics of metal-metal interactions at the surface, mechanical factors associated with the formation of the metal-metal interface may also impact the observed mode of growth. Typically, as the extent of metal deposition increases, and multiple layers of the secondary metal are formed, the generation of stress and crystallite strain can induce a transition from the initial deposition mode. In terms of stress quantification, the overall strain generated at the multimetallic interface is a balance between compressive and tensile stress at the surface layer, which result from island deposition and monolayer formation, respectively.[27-28] Island nucleation exerts a compressive stress on the substrate, the magnitude of which is largely dependent upon the difference in lattice constants or surface energies of the nanoisland and substrate components or the presence of surface defects.[29] However, nucleation of a 2D island (for conditions where the extent of secondary metal deposition is less than one monolayer) will create step sites which may drive the coalescence of individual islands into a uniform monolayer. Upon formation of a monolayer, however, tensile stress is always introduced to the system, the magnitude of which is dependent upon the number of crystalline defects and/or presence of grain boundaries between merging islands. If the magnitude of tensile stress is less than the compressive stress (which is dependent upon the location and rate of adatom diffusivity at grain boundaries) the islands will coalesce to form a discrete monolayer.[28,30]

The propensity for 2D island coalescence (here, by a mechanism of "filling in" void substrate between metal island sites by additional adatom flux) depends on the flux and chemical potential of incident adatoms to either pre-existing 2D island sites or grain boundaries at their interface with the substrate (Figure 3). Yu and Thompson recently

proposed a model of island coalescence where the active mode of growth is a balance between the average grain size (*d*, as measured by TEM) and separation distance between the islands.[30] For monometallic systems, classic nucleation theory predicts the average spacing between nanoislands (*L*) will be dependent upon the metal lattice spacing (λ), rate of deposition (*R*), and diffusivity constant (D_0) as described in the following equation:

$$L_{island} = \lambda n^{-1/2} \left[\left(\frac{D_0}{R\lambda} \right) e^{-E_s/k_B T} \right] \quad \text{(Eq. 1)}$$

where n is a dimensionless prefactor and E_s is the activation energy for surface diffusion.[30-31] Here, adatoms incorporated at grain boundary sites relative to island sites exert a greater extent of compressive stress on the substrate,[32] leading to an increased rate of adatom desorption (Figure 3). Given the theoretical prefactor maximum of 0.25, the island spacing distance of Ni islands on Ni(111) was approximately 10 nm, larger than the average grain size as measured by TEM.[33] Under conditions $d < L_{island}$, which are typically achieved by using low deposition rates or high temperatures, the compressive stress is independent of average grain size, and island growth is predominantly observed. However, for systems where $d > L_{island}$, a tensile stress component is introduced which may promote or hinder monolayer depending on the relative magnitudes of tensile and compressive stress at the surface layer.

1.2.2.3 Impact of Substrate Crystallinity on Monolayer Formation

As a direct consequence of these atomistic and mechanical impacts on metal growth modes, substrate crystallinity, surface roughness, and the presence of surface reconstructions also influence the observed deposition pathway. Here, the Terrace-Ledge(Step)-Kink model, pioneered by Kossel and Stranski, is a useful tool for

demonstrating how substrate topology can influence transitions between FM and VW deposition. Theoretically, at the initial stages of deposition, slow rates of adatom incorporation (but high flux rates of incoming adatoms from the surrounding medium) promotes adatom diffusion to sites of high coordination number, acting as a single nucleation site for the layer, and leads to the formation of a single monolayer before subsequent growth of a second layer. Specifically, adatom incorporation on a terrace site generates higher energy steps which then drives growth in the lateral direction (parallel to the substrate surface) until monolayer formation is complete.[34] However, with increased adatom flux, the rate of adatom incorporation increases relative to the rate of adatom diffusion, causing incorporation at non-equilibrium positions (i.e. terrace sites on island nuclei instead of at the edge sites). In turn, these adatoms at non-equilibrium sites exhibit higher chemical potentials relative to adatoms positioned at sites of higher coordination (i.e. edge or kink), and drive growth in all directions to form rough surfaces consistent with island mechanisms of deposition.[35]

Apart from the crystallographic orientation of the substrate, the presence of crystalline defects and surface reconstructions may also impact metal nucleation and growth processes. For example, Au(111) substrates with Pt layers 1-10 nm in thickness can exhibit both layer and layer+island modes of deposition depending on the roughness of the Au(111) substrate.[36] On monoatomically flat Au(111) substrates, electron beam deposition of Pt has been shown to proceed in a layered growth mode.[36] However, upon oxidation of the Au(111) using nitric acid, the increased surface roughness induced a transition to layer+island growth of Pt (Figure 4).[36] This transition was correlated to the diffusional barrier of a Pt atom to diffuse from an island onto a lower terrace site. On flat

surfaces, there is a low barrier for adatom diffusion (diffusion barrier of Cu adatom diffusion on flat Cu(111) is 0.029 eV, compared to a diffusion barrier of 0.5 eV for step sites)[37] to a lower energy terrace site, often facilitating layered growth.[34] On rough surfaces, however, a significant step-edge barrier, or the energetic barrier for an adatom to descend over a step edge, hinders adatom diffusion to lower terraces. Consequently, nuclei on the top of islands are stabilized and island growth persists.[36]

Besides chemical oxidation of the substrate, the presence of naturally occurring surface reconstructions due to lattice strain or molecular adsorbates may also impact the observed growth pathway. STM of Ru electrodeposition on herringbone reconstructed Au(111) surfaces observed Ru incorporation exclusively at the *hcp* regions of Au. At higher extents of Ru coverage, layered growth was observed, yet the Ru lattices exhibited significant defects due to the presence of the substrate surface reconstruction.[38] The herringbone reconstruction often facilitates the organization of VW nucleation sites, hence allowing for the deposition of nanoisland arrays exhibiting long-range order. For instance, Ni nanoisland nucleation was observed to occur preferentially at the edges of the herringbone reconstruction, forming a striped array of Ni islands across the Au surface.[39] Similar results were obtained for the deposition of Cu nanoislands on Au(111)-(22x$\sqrt{3}$) reconstructed surfaces (Figure 5).[40] Here, STM shows the formation of Cu nanoislands with triangular morphologies in ordered arrays selectively at the *hcp* regions of the Au substrate herringbone surface reconstruction. Further, the Cu nanoislands exhibited an identical surface reconstruction, indicating epitaxial translation of both island crystallinity and surface geometry from the underlying substrate. [40]

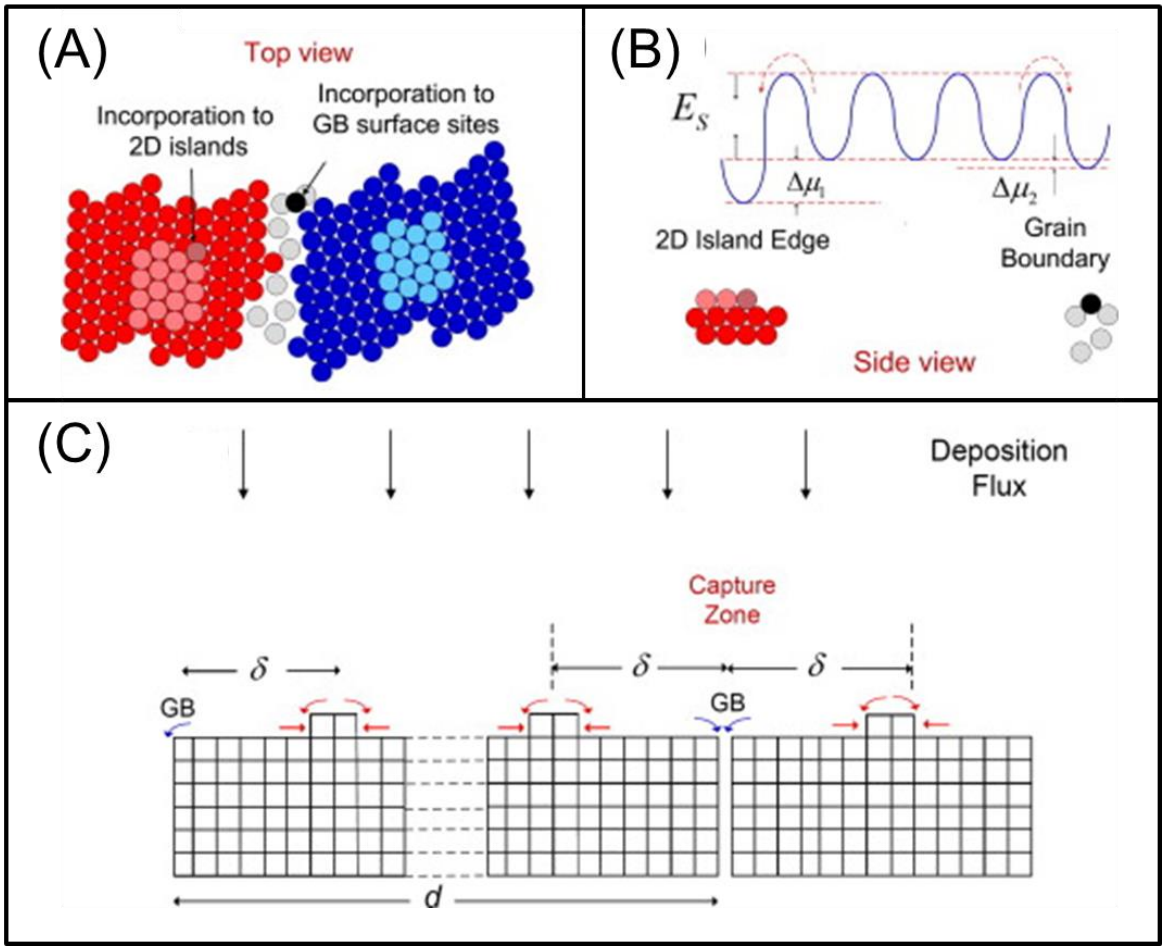

Figure 3. Model depicting compressive component of stress at multimetallic interface. (A) Disruption of packing geometry at grain boundaries (GB) relative to island sides. (B). Activation energy (E_s) and chemical potential (μ) difference between island and GB. (C) for addition at either island or grain boundary. (C) Adatoms outside of the capture zone (*width* = 2δ for grain size of d) will be incorporated to islands before reaching the GB sites. Adapted with permission from reference 30. Copyright 2014 Elsevier.

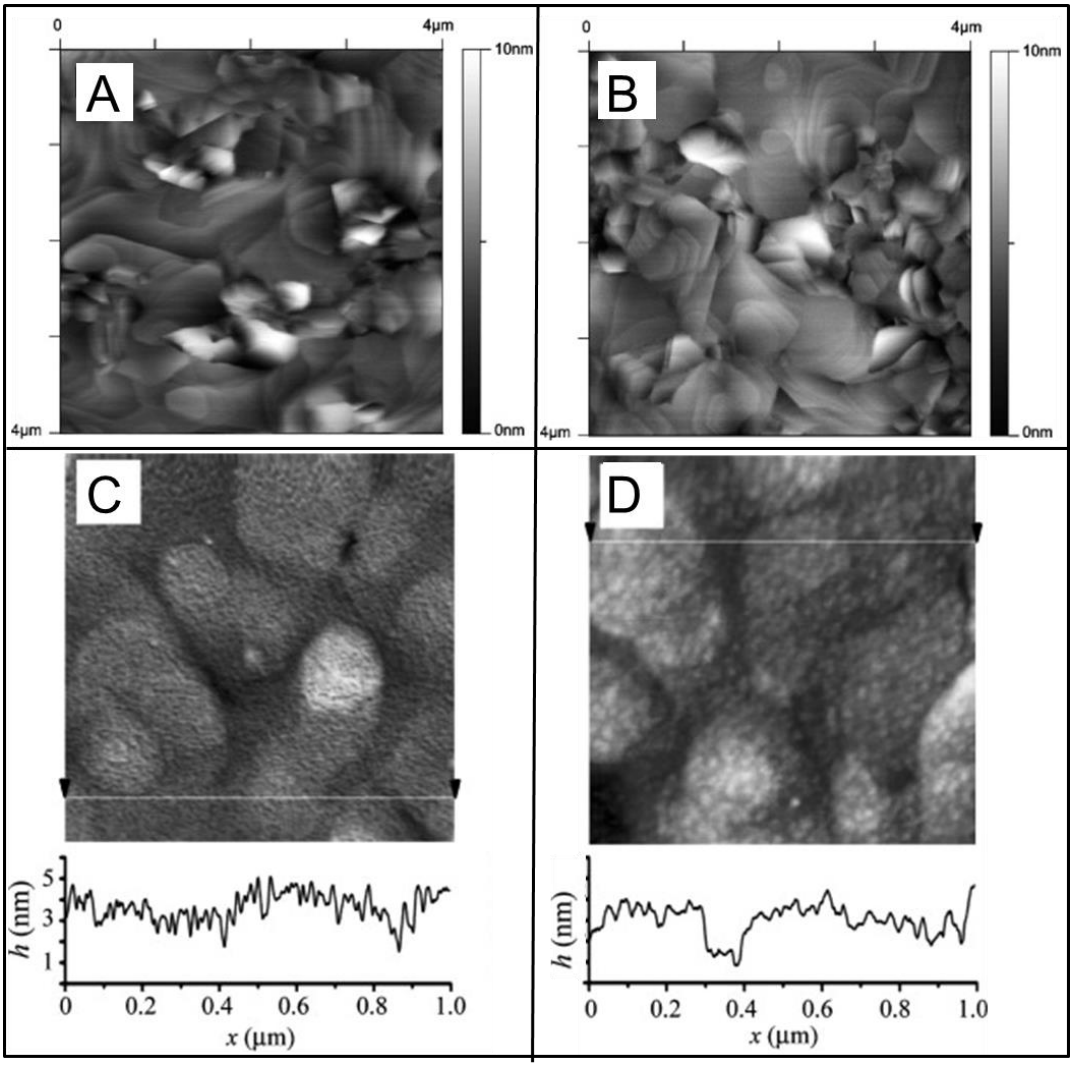

Figure 4. Pt deposited on Au(111) before (A, B) and after (C, D) surface roughening with nitric acid for 2 nm (A, C) and 4 nm (B, D) Pt film thicknesses indicating a transition from layer to layer+island growth with increasing surface roughness. Adapted with permission from reference 36. Copyright 2008 Elsevier.

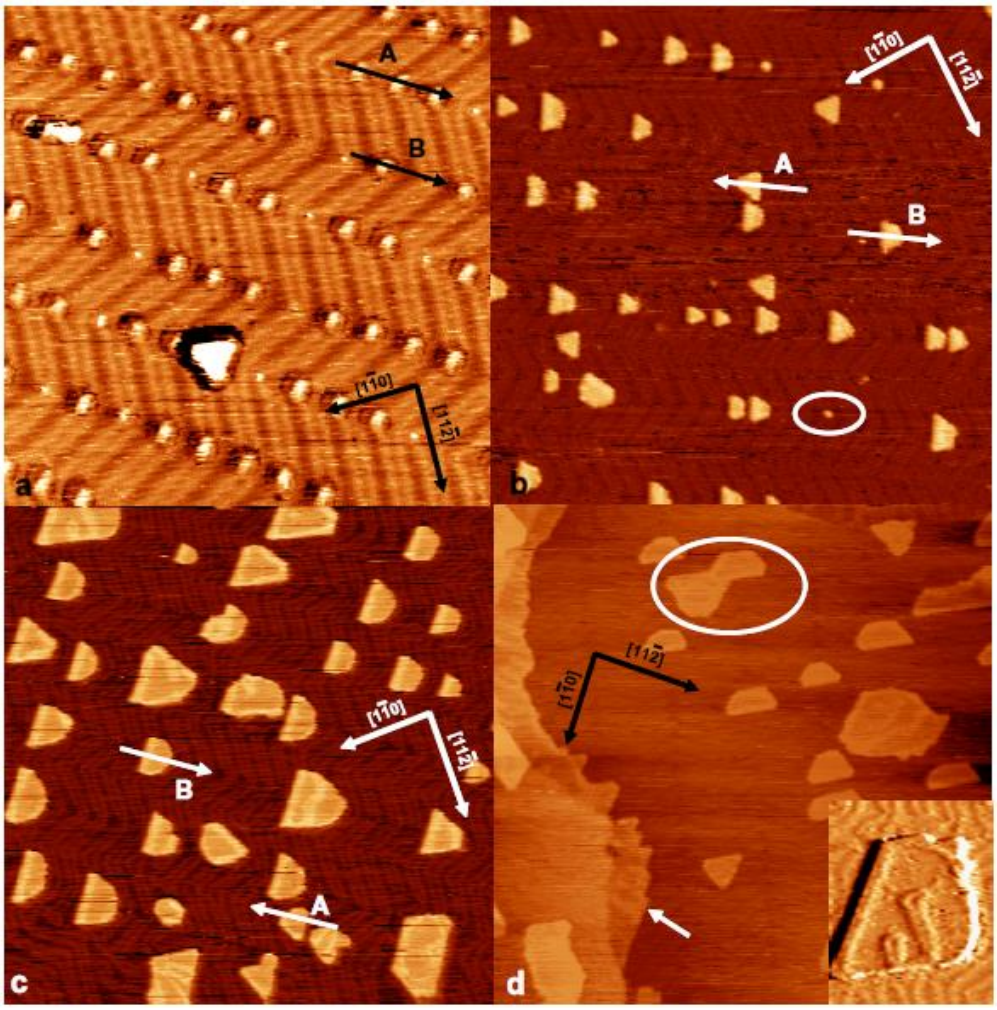

Figure 5. STM images showing the evolution of the Cu overlayer with increased surface coverage: (A) 0.025 ML depicting the (22×√3) reconstruction, (B) at 0.062 ML the islands evolve into a triangular morphology, (C) 0.18 ML and continued island growth, (D) at 0.36 ML, islands begin to fuse into an incomplete monolayer. Adapted with permission from reference 40. Copyright 2011 Institute of Physics.

1.2.3 Factors Impacting Deposition of Subsequent Monolayers

After an initial monolayer has been deposited, competition between tensile stress and compressive stress can lead to a change in the active pathway of deposition. As a general rule, adatom substrate systems with low extents of tensile stress (e.g. Ag on Au) will grow in a layered pattern, while systems with high tensile stress (e.g. Pt on Au) will deposit as discrete islands. However, for systems which exhibit layered growth, the introduction of surface defects and/or deformities often lead to surface roughening after deposition of only a few atomic layers and a transition to layer+island growth.[41] Here, the build-up of tensile stress leads to surface defects which hinder subsequent epitaxial deposition. These surface defects act as high energy nucleation sites and prevent adatom diffusion and monolayer formation. Overall, this transition allows the system to alleviate tensile stress at the cost of increasing compressive stress through island formation. As mentioned in the previous section, such transitions are observed for metal combinations with negligible lattice mismatch (e.g. Ag on Au(111),[42] however a wide range of elemental combinations exhibit layer+island modes of deposition (e.g. Si(001)/Ge,[43] Au on Mo(110),[44] Fe_3O_4 on Au(111)),[45] including the majority of noble metal combinations. For example, STM of Ag deposited on Au(111) electrodes indicates surface roughening after only two monolayers of Ag. Interestingly, redox mediated pathways of layered growth are a promising means of improving the extent of layered deposition through underpotential deposition (UPD) of a template monolayer. Here, UPD is the reduction of a metal cation at a potential less negative than the equilibrium potential on a foreign metal substrate, spontaneously depositing up to two monolayers of the reduced metal cation.[46] For example, UPD of Pb or Cu atoms templates layered Ag deposition on Au(111) for over 200 monolayers. [47-48] Pb or Cu adatom UPD promotes a subsequent Galvanic replacement

reaction (GRR), where the template adatoms are oxidized to reduce and deposit Ag^+ in a highly uniform Ag monolayer across the Au(111) surface.

For many metal combinations, however, the pathway of deposition is dynamic and changes with the extent of deposition. As the number of deposited layers increases, the generation of tensile stress can induce a fragmentation of the surface and a transition from layered to island growth. For example, STM of Pd deposition on Au(111) indicates that Pd initially deposits in a layered growth mode. However, after several layers of deposition, the generation of surface defects and tensile strain induced a transition to layer+island growth. After this transition, Pd adatoms selectively incorporated at pre-existing Pd islands, resulting in the formation of dendritic Pd nanostructures.[49] Similar layer+island growth mechanisms are observed for Pt(111)/Ag,[50] Pt(111)/Pd,[51] and Au(111)/Rh.[52] As this transition can occur after only a single monolayer, it can be difficult to experimentally differentiate island from layer+island growth, especially for small (typical diameter of 5-200 nm) and highly faceted nanoparticle substrates.

1.3 NANOISLAND DEPOSITION ON COLLOIDAL NANOPARTICLE SUBSTRATES

1.3.1 Nanoparticle Substrates: Synthesis, Composition, and Morphology

In the previous section, we outlined important parameters that determine mechanisms of metal-on-metal deposition. Yet, even for the same metal combinations, changes in deposition pathways on nanoparticle substrates are observed depending on the specific experimental conditions used. Here, we build on knowledge obtained from metal deposition on thin film substrates to describe and understand mechanisms of nanoisland deposition on colloidal nanoparticle substrates.

Multimetallic nanoparticles decorated with nanoislands are emerging as a unique class of materials which exhibit distinct properties from their core@shell counterparts of similar composition.[13] Typically, these materials are synthesized using seed mediated strategies, where nucleation of the nanoparticle substrate "seed" and deposition of surface islands occur at separate times and in separate chemical environments.[53] Nanoparticle substrates are generally monometallic noble metals (e.g. Ag,[54] Au,[55] and Pd,[56]) and can be synthesized in a wide array of morphologies. Specifically, Ag and Au nanoparticle substrates are polyhedral,[57-58] rod-like,[59-61] or plate-like,[62-63] while Pd nanoparticle substrates are polyhedral in morphology.[64-65] As will be demonstrated in this section, the islands can be comprised of a variety of metals to create a suite of multimetallic nanoparticles with surface island architectures.

1.3.2 Challenges Associated with Colloidal Nanoparticle Substrates Compared to Thin Films

Generally, a given combination of metals will exhibit similar growth pathways regardless of length scale (i.e. 0D vs 1D vs 2D), however colloidal nanoparticle systems introduce new synthetic parameters and challenges which can induce deviations from a predicted pathway. At the nanoscale, one factor that may have an exaggerated influence on final particle morphologies is the metal-metal redox interactions between the NP substrate and deposited metal. The difference in redox potentials between the nanoisland and substrate components must be considered in order to encourage or prevent process such as UPD or GRR, which are well known to influence nanoparticle nucleation and growth processes.[66-67] The reduction potential of the nanoisland metal precursor also influences the kinetics of island deposition, as do the strength of the chemical reducing agent, and synthetic conditions like temperature or solvent necessary all of which may also impact nanoisland growth. Generally, stronger reducing agents enable faster rates of deposition, encouraging adatom incorporation at island sites as opposed to grain boundaries.[30]

In addition to redox chemistry, mechanical forces such as tensile and compressive stress[68] described previously also continue to impact the thermodynamics of adatom incorporation, although these factors may be more difficult to determine for nanoparticle substrates and are not often reported.

1.3.3 Mechanisms of Nanoisland Deposition on Colloidal Nanoparticle Substrates

1.3.3.1 Enthalpic Driving Forces of Nanoisland Growth

As was observed in thin film deposition, the bond dissociation energy and degree of lattice mismatch are two important parameters which determine the mode of growth. However, nanoisland deposition on nanoparticle substrates appears to depend more on the bond enthalpy than the degree of strain caused by lattice mismatch. For instance, Au and Pd exhibit a 4.77% lattice mismatch, but the higher Au-Pd bond dissociation energy often encourages layer or layer+island deposition motifs (Table 1).[69] In an early observation of Pd nanoisland growth on Au nanorods, Yang overgrew electrochemically prepared Au nanorod substrates with Ag, Au, and Pd. Consistent with previous thin-film investigations, Ag and Au deposited in a layered fashion while Pd formed 2-4 nm nanoislands on the surface due to the larger mismatch between the Au and Pd lattices. As the concentration of Pd increased, however, the Pd nanoislands were observed to fuse into a polycrystalline shell, likely due to the thermodynamic favorability of Au-Pd bond formation (Table 1). This transition from island to layer growth is commonly observed in the Au-Pd system, leading to a majority of core@shell AuPd nanoparticle products.[70]

Similar enthalpic driving forces are observed even in cases where there are smaller lattice mismatches. For instance, Xia et al. deposited Pt on the surface of truncated octahedral Pd nanoparticles and observed Pd dendrite deposition with branch diameters of ~3 nm. As Pd and Pt exhibit a negligible lattice mismatch of 0.77%, the high Pt-Pt bond dissociation energy drives the homogenous nucleation of Pt nanoparticles which are subsequently incorporated at the Pd surface by oriented attachment process.[71] Enthalpic driving forces for VW deposition are perhaps most notable in the Au-Pt system. Here,

Tian and coworkers investigated the impact of atomic radii, bond dissociation energy, and electronegativity on the growth mode of Ag, Pd, and Pt on colloidal Au nanocubes (Figure 6).[26] Consistent with previous results, only Pt exhibited VW deposition due to the enthalpic driving force for Pt-Pt bond formation. Indeed, Pt deposition on Au nanoparticle substrates has become one of the most frequently investigated systems of nanoisland growth. In a recent analysis of Pt nanoislands on Au nanoprism surfaces, a tilt series of HAADF-STEM images were obtained and used to study the 3D structure of the Pt nanoislands via tomographic reconstruction (Figure 7).[72] Similar to Pt deposition on films of Au(100) and Au(111),[73] the Pt nanoislands were found to exhibit irregular "tree like" morphologies, where islands branch outward as they grow longer in length consistent with a dendritic type of growth pathway often observed for larger Pt nanoparticles. Interestingly, electron energy loss spectroscopy (EELS) indicated that the LSPR of the underlying Au nanoparticle retained similar modes and extended into the Pt nanoislands, suggesting possible LSPR coupling and charge transfer between Au and Pt components, as supported by recent investigations.[74]

Table 1. Bond Dissociation Energies and Lattice Mismatch Percentages for Au, Pd, and Pt.[69]

Metal Combination	**Bond Dissociation Energy (kJ/mol)**	**Lattice Mismatch (%)**
Au-Au	226.2	0.0
Au-Pd	142.7	4.7
Au-Pt[75]	234.5	4.0
Pd-Pd	143.0	0.0
Pd-Pt	191.0	0.76
Pt-Pt	306.7	0.0

core@shell	atomic radius r_{core} vs r_{shell}	bond dissociation energies $E_{core-core}$ vs $E_{shell-shell}$	electronegativity (Paulings) X_{core} vs X_{shell}	experimental observation of epitaxial growth
Pt@Au	small	high	low	no
Pt@Ag	small	high	high	no report
Pt@Pd	large	high	high	yes
Au@Pd	large	high	high	yes
Au@Ag	equal	high	high	yes
Au@Pt	large	low	high	no
Ag@Pd	large	high	low	no
Ag@Au	equal	low	low	no
Ag@Pt	large	low	low	no
Pd@Au	small	low	low	no
Pd@Ag	small	low	high	no report
Pd@Pt	small	low	low	no report

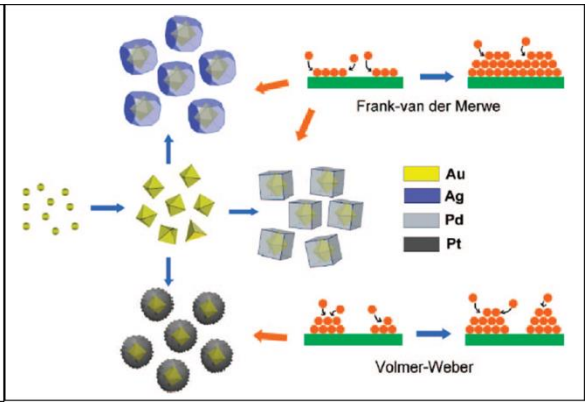

Figure 6. Table comparing atomic radius, bond dissociation energy, and electronegativity of Ag, Au, Pd, and Pt (left) and a cartoon depicting the experimentally observed deposition pathway of Ag, Pd, and Pt on Au nanoparticle seeds (right). Here, Ag and Pd were found to deposit in a layered growth mode, while Pt deposited in an island morphology. Adapted with permission from reference 26. Copyright 2008 American Chemical Society.

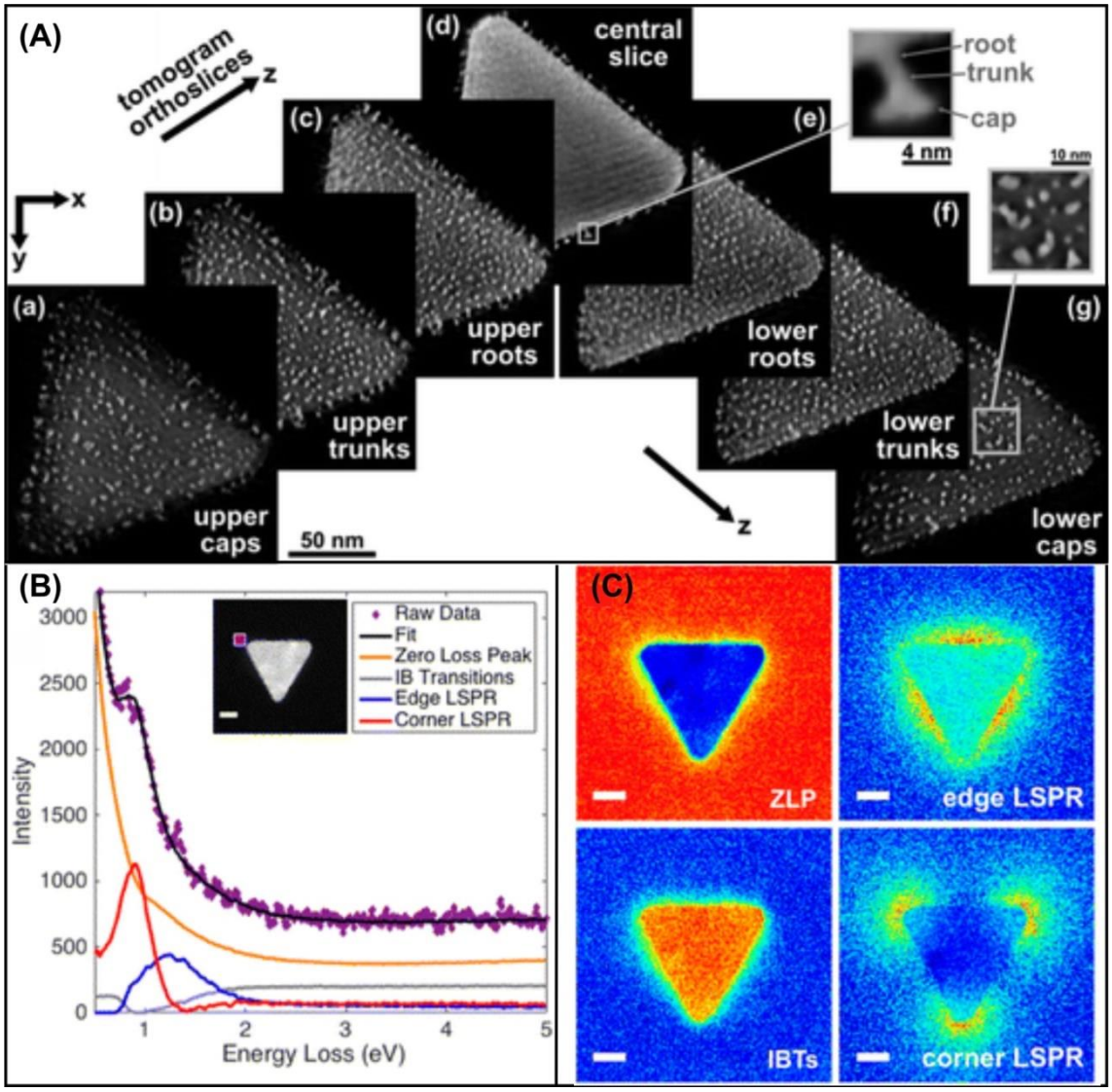

Figure 7. (A) Tomographic sequential orthoslices of Pt nanoislands in epitaxial contact with the Au nanoprism surface indicating the root, trunk, and cap island morphologies. (B) Electron energy loss (EELS) spectrum imaging. (C) EELS mapping of LSPR. Reproduced with permission from reference 72. Copyright 2016 American Chemical Society.

1.3.3.2 Impact of Substrate Crystallinity and Surface Adsorbates

In addition to the impact of metal-metal bond energies and lattice interactions, nanoparticle substrate properties such as crystal facet populations also impact the growth mode of depositing metal. Further, since colloidal nanoparticle surfaces are bound by ligand adsorbates, the surface reactivity of a given crystal facet is also dependent upon the specific facet-ligand interactions. For example, a ligand may exhibit differences in packing geometry, density, or binding kinetics (as measured by the ligand dissociation constant, K_D) for a given crystallographic facet.[76] Further, these ligands are often present in near molar concentrations and introduce counterions and trace impurities which may also adsorb to the surface of the nanoparticle substrate or otherwise interact with the incoming secondary metal.

As all colloidal nanoparticles have surface adsorbates, it can be difficult to decouple the impact between surface crystallinity and surface chemistry for a specific pathway of metal deposition. In 2010, Han et al. investigated the impact of substrate crystallinity on the observed mode of nanoisland deposition.[77] Here, Au nanoparticles bound by low index facets (e.g. Au(100), Au(110), Au(111)) were used as substrates for Pt nanoisland deposition. Epitaxial deposition of Pt nanoislands was observed on all facets, suggesting no crystallographic preference for Pt nanoisland nucleation and growth. However, when there is a large difference in crystal facet reactivity, due to either the surface energy or facet-ligand interactions, facet-selective nanoisland deposition is observed. For example, Xie and coworkers observed a difference in selectivity between the end and side facets of the Au nanorod substrate depending on the ratio of Pt precursor to gold nanorod seeds.[78] At the lowest Pt:Au ratios, Pt was found to only deposit selectively on the edges of the nanorod (100) and (110) side facets at sites of highest curvature. Here, a higher

concentration of defects in the CTAB bilayer would likely occur at areas of high substrate curvature, leading to Pt island formation at the ends of the rods. Furthermore, the higher surface energy of the (250) facet discourages ligand dissociation, effectively passivating the (250) facets from Pt island deposition. However, as the amount of Pt precursor was increased relative to the number of gold nanorod seeds, deposition was observed on the high index (250) facets,[79] and uniform Pt nanoisland deposition was observed on the entire nanorod surface.

Even for nanoparticle substrates of identical crystallinity, the mode of nanoisland deposition can differ depending on the identity of the NP substrate capping ligand. For instance, Pt was found to exhibit a preference for deposition on Au(100) facets in the presence of and on Au(111) facets in the presence of poly(vinylpyrrolidone) (PVP). Here, Lee and coworkers deposited Pt nanoislands on a variety of PVP-functionalized Au nanoparticle substrates, including cubes, octahedral, and pseudo-spherical nanoparticles.[80] For the pseudo-spherical particles, uniform Pt nanoisland deposition was observed across the entirety of the Au nanoparticle surface, indicative of the highly faceted and irregular surfaces of pseudospherical particles. For the cubic nanoparticle substrates, deposition was found to proceed first on the flat, square planar (100) surfaces, rather than the (111) faceted corners. Surprisingly, no deposition was observed on the Au octahedral nanocrystals unless the reaction temperature was elevated to 50 °C. Under these conditions, Pt nanoislands formed first on the corners of the octahedron, again showing a preference for nanoisland formation on only Au(111) facets. As PVP is postulated to have similar interactions with the {111} and {100} surfaces, the difference in facet

selectivity was initially unexpected and is likely driven by the presence of additional nanoparticle shape directing reagents, such as 1,5-pentanediol or $AgNO_3$.

Even the presence of additional halides in solution can cause significant deviations in nanoisland growth, either by altering the redox potential of the nanoisland metal precursor or by adsorbing to the surface of the nanoparticle substrate and participating in either face-blocking or even participating in the deposition chemistry. For example, Rh nanoisland deposition on Au and Pd nanoparticle substrates only proceeded in the presence of iodide anions. HRTEM and SAED analysis indicated that ~3 nm Rh nanoislands grew in an epitaxial fashion directly from the surface of the Pd or Au nanoparticle substrates and exhibited a truncated pyramidal morphology (Figure 8).[81] Here, iodide was postulated to lower the reduction potential of the Rh ions or to oxidatively activate the surface of the nanoparticle substrate to encourage Rh nanoisland deposition Similarly, halide adsorption to the nanoparticle surface can also impact the surface chemistry and reactivity, leading to facet-selective pathways of nanoisland growth. For instance, in an investigation of Rh nanoisland deposition on Pd nanoparticle substrates, facet-selective deposition of Br^- on Pd(100) confined Rh nanoisland nucleation to only Pd(111) surfaces.

As highlighted in the previous examples, the presence of organic and halide surface adsorbates can impact the observed mode of Pt nanoisland deposition. Interestingly, even the presence of gaseous surface adsorbates can drive facet-selective Pt nanoisland nucleation and growth. For example, facet selectivity was observed when Pt was reduced Au nanorod substrates when water was saturated with either Ar or CO gas.[82] In the presence of Ar gas, Pt nanoislands selectively deposited at the ends of the rod. However,

adsorption of CO to the ends of the nanorods slowed Pt nanoisland nucleation and growth, encouraging even deposition across the Au nanorod surface.

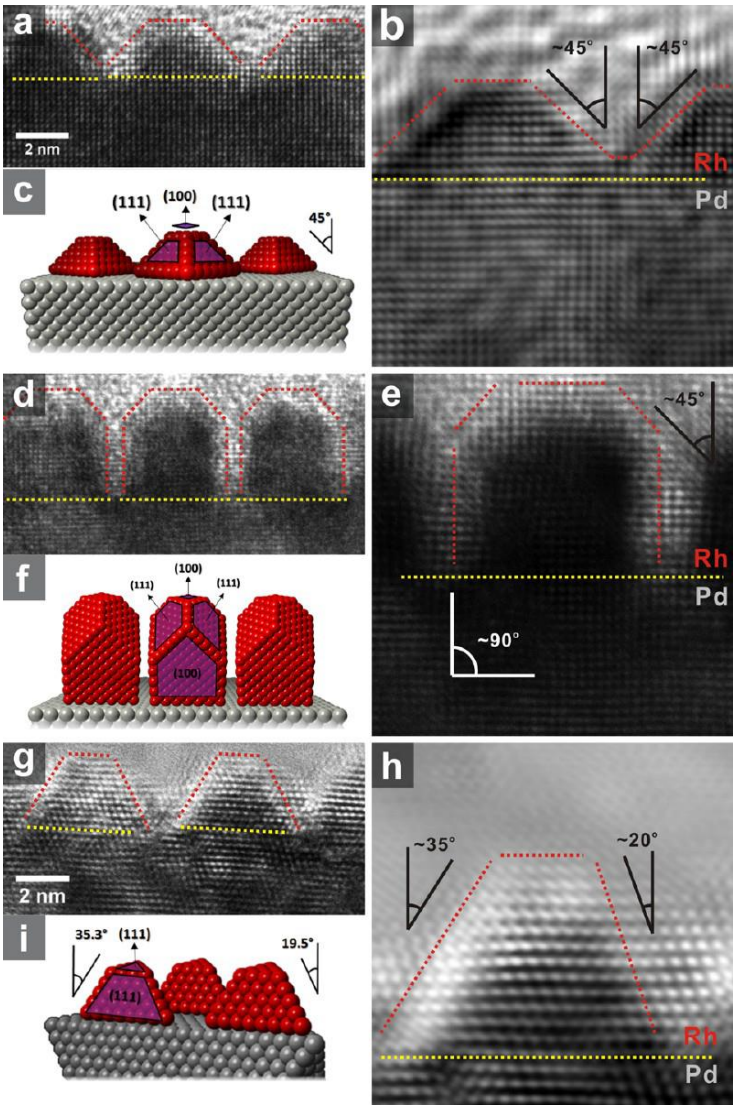

Figure 8. Surface structures of the Rh overgrowth. (a,d,g) HRTEM images, (b,e,h) FFT-enhanced images, (c,f,i) crystal models for (a−c) island overgrowth on Pd nanocubes, (d−f) column growth on Pd nanocubes, and (g−i) island growth on nanooctahedra. Reproduced with permission from reference 81. Copyright 2012 American Chemical Society.

1.3.3.3 Redox Mechanisms Impacting Nanoisland Formation on Nanoparticle Substrates.

Redox processes such as UPD and subsequent GRR can also strongly influence the mode of nanoisland deposition on nanoparticle substrates. Typically, spectator metals can deposit on the surface of the nanoparticle core (e.g. Ag^+ on Au(111)) by a UPD process. UPD changes the redox potential of metal atoms at the surface of the nanoparticle substrate and can often induce GRR with the nanoisland metal precursor. For example, Ag UPD has been used to drive FM deposition of Pt on Au nanorod substrates. Here, oxidation the Ag UPD monolayer atoms by Pt(IV) was found to replace the Ag monolayer with a Pt monolayer, promoting uniform deposition and core@shell Au@Pt growth.[83]

Redox processes like UPD and GRR have also been proposed to alter the crystal facet surface reactivity of the nanoparticle substrate leading to changes in the observed metal deposition pathway. Liz-Marzan and coworkers investigated the role of Ag^+ UPD on mechanisms of Pt island formation on Au nanorods in the presence and absence of Ag (Figure 9).[84] Here, defects in the ligand bilayer at the ends of the rods accelerated the rate of Ag^+ UPD, leading to end-selective Pt nanoisland deposition by GRR.[84] Similar trends in Ag^+ UPD and Pt nanoisland facet-selectivity were also observed for Au nanodiscs.[85]

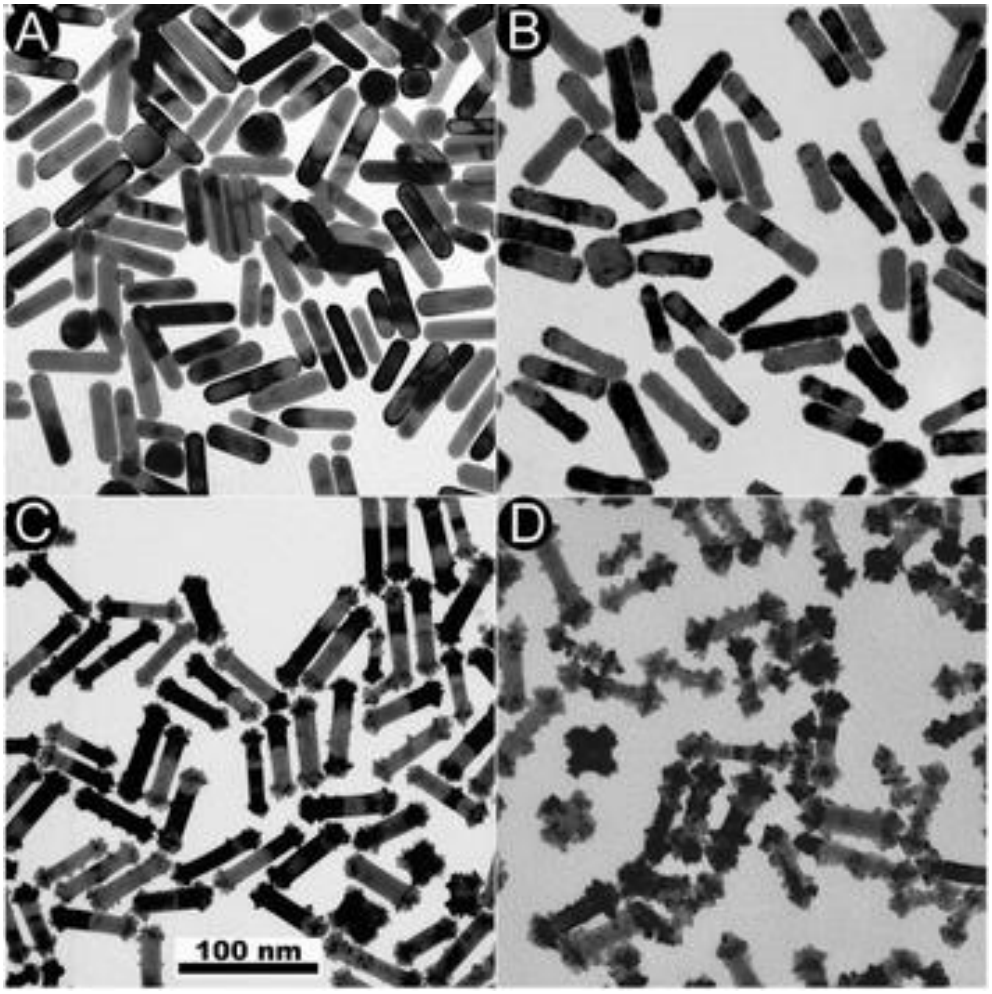

Figure 9. Representative TEM images of the initial Au nanorods (A) and Au@Pt obtained in the absence (B) or in the presence of Ag, for a 1:5 and 1:1 molar ratio of Pt:Au. Reproduced with permission from reference 84. Copyright 2006 Royal Society of Chemistry.

1.4 OUTLOOK

Taken together, the work highlighted in the previous sections suggests that the active pathway of metal deposition on NP substrates is driven by a balance between chemical and physical forces as observed in thin film studies, yet is highly dependent on experimental conditions, such as crystallinity, capping ligand, and redox potential for a given combination of metals. The mechanisms which impact the pathway of metal deposition are often difficult to identify and quantify, which ultimately constrains the design, production, and application of these materials. The following chapters will present progress towards developing a robust and rational framework that establishes critical insights into the chemical mechanisms underlying the synthesis of noble metal nanoparticles with nanoisland surface architectures.

2.0 SEEDLESS INITIATION AS AN EFFICIENT, SUSTAINABLE ROUTE TO ANISOTROPIC GOLD NANOPARTICLES

(Portions of this work were published previously and are reprinted with permission from Straney, P. J.; Andolina, C. M.; Millstone, J. E. Langmuir, **2013**, *29*, 4396-4403. Copyright 2013 American Chemical Society).

2.1 INTRODUCTION

Over the last decade, it has become clear that noble metal nanoparticles exhibit an exciting and potentially useful range of previously unobserved physical properties.[20,86-87] Anisotropic gold nanoparticles have received particular attention,[88-89] and have shown promise in applications ranging from gene delivery[90-91] to photovoltaics.[92] However, there remains a gap between the promise of these materials and their implementation into society-shaping technologies. In part, this gap stems from difficulties in developing efficient nanoparticle syntheses that minimize the use of constituent reagents while maximizing the tunability of the resulting products. Therefore, mechanistic investigations go hand in hand with studies that address synthetic efficiency, sustainability and cost.[93-94] Here, we use the principles of green chemistry to develop and characterize the seedless initiation of anisotropic gold nanoparticle growth.

Green chemistry principles begin with three fundamental tenets: prevention of waste, atom economy, and the reduction of hazardous materials.[95] Prevention of waste leads to the elimination of unnecessary reagents from a given synthetic pathway and, from a nanochemistry perspective, also presents the opportunity to eliminate mechanistic "red-herrings." Here, improving atom economy is interpreted for nanochemistry as a more efficient use of reagents in order to maximize product atoms out for reagent atoms in. This efficiency can be particularly challenging for reagents such as surfactants which have concentration dependent supramolecular architectures that may or may not impact final nanoparticle outcomes.[96-101] Finally, a more efficient synthesis in terms of steps, reagent use, and reaction conditions (e. g. temperature and pressure) simultaneously addresses issues of synthetic hazards both up and downstream of the synthetic process.

A broadly used strategy for preparing anisotropic gold nanoparticles is a seed-mediated approach.[88-89] A key aspect of these syntheses is the separation of nanoparticle nucleation, in both time and chemical environment, from subsequent nanoparticle growth. The separation of these two stages is achieved by first generating seeds using a strong reducing agent and subsequently adding these particles to a separate reaction environment that typically contains metal ion precursors, a weak reducing agent, capping ligands, and additional shape directing agents, together termed a "growth solution." This approach has produced a wide range of particle shapes,[89] yet has remained limited in reproducibility and rational tunability often due to ambiguity in the role of each reagent in the particle growth process.

Here, we use a homogeneous nucleation strategy to synthesize two well-studied anisotropic gold nanoparticles, nanorods and nanoprisms. This synthetic approach is then used to eliminate several chemical reagents and reaction steps from typical particle preparations while still

achieving similar nanoparticle products and product yields. Our results shed new light on factors that influence the evolution of gold nanoparticle shape, and present a dramatically more efficient route to obtaining these architectures. In particular, these improvements have reduced the total amount of reagent used by as much as 90% by weight, and to the best of our knowledge, have yielded the first report of gold nanoplates synthesized using a seedless method.

2.2 EXPERIMENTAL

2.2.1 Materials and Methods

Cetyltrimethylammonium bromide (CTAB, 99%), hydrogen tetrachloroaurate trihydrate ($HAuCl_4 \bullet 3H_2O$, 99.99%), L-ascorbic acid (99%), silver nitrate ($AgNO_3$, 99.9999%), sodium borohydride ($NaBH_4$, 99.99%), sodium hydroxide (99.99%), sodium iodide (NaI, 99.999%), and trisodium citrate (99%) were obtained from Sigma Aldrich and used as received. All solutions were prepared using NANOpure™ (Thermo Scientific, 18.2 MΩ · cm) water and were made fresh prior to use. All water used during synthesis and work-up is NANOpure™. All reagents were used in air at room temperature unless otherwise noted. All solutions were prepared in water unless otherwise noted.

2.2.2 Glassware Cleaning Procedure

For the following procedures, all glassware was washed with aqua regia (3:1 hydrochloric acid to nitric acid by volume) and rinsed copiously with water. *Caution: aqua regia is toxic and corrosive and must be handled in a fume hood with proper personal protection equipment.*

2.2.3 CTAB Solution Preparation

CTAB solutions (at various concentrations) were prepared by heating the sealed mixture in a water bath (37 ºC) until it became clear. The solution was then sonicated for 30 seconds and allowed to cool to room temperature before use. If recrystallization of CTAB occurred either during storage or during use, the solution was treated as described above before continuing with the following reactions.

2.2.4 Synthesis of Seed-mediated Nanoprisms

Au nanorods were prepared according to literature protocols.[99] In order to prepare the nanorod seeds, 5.0 mL of a 0.5 mM solution of $HAuCl_4$ was mixed with 5.0 mL of a 0.2 M solution of CTAB and was vortexed for 5 seconds. A 0.01 M solution of $NaBH_4$ was freshly prepared, and 0.6 mL was added to the $HAuCl_4$-CTAB mixture while vortexing. This "seed" solution was allowed to rest for two hours undisturbed at room temperature to allow for degradation of excess BH_4^- . After the aging period, the nanorod growth solution was prepared. Briefly, 5.0 mL of a 1.0 mM solution of $HAuCl_4$ was added to a 20.0 mL scintillation vial. Next, 50-300 μL of 4 mM $AgNO_3$ was added, where larger volumes of $AgNO_3$ promoted the formation of Au nanorods

with increased aspect ratios. Next, 5.0 mL of 2.0 M CTAB was added, followed by the addition of 50 μL of 0.1 M ascorbic acid. The solutions were vortexed for 5 seconds, upon which the solution turned transparent. The seed solution was placed in a water bath at 37 °C to dissolve any crystallized CTAB for approximately 5 minutes, and 12 μL of the seed solution were added to the growth solution to initiate nanorod formation. The nanorods were allowed to grow, undisturbed at room temperature, for 24 hours.

2.2.5 Synthesis of Seed-mediated Nanoprisms

Au nanoprisms were prepared according to literature protocols (vide infra, **3.2.2**).[63,97]

2.2.6 Synthesis of Seedless Nanorods

In a typical synthesis, 5 mL of aqueous 200 mM CTAB solution was prepared and added to a 20 mL scintillation vial. To this, 100 μL of 4 mM $AgNO_3$ was added and the solution was mixed gently by shaking. Next, 5 mL of 1 mM $HAuCl_4 \bullet 3H_2O$ was added and the solution was mixed briefly by shaking. Upon addition of 50 μL of 100 mM L-ascorbic acid, the orange solution was stirred until turning colorless. Growth was initiated by injecting 10 μL of freshly prepared 2.25 mM $NaBH_4$ while stirring on a benchtop vortex mixer (Analog Vortex Mixer, 120V, 50/60Hz, Fisher Scientific). Mixing was continued for 10 seconds, after which the solution was left undisturbed for 30 minutes.

2.2.7 Synthesis of Seedless Nanoprisms

In a typical synthesis, 10 μL of 50 mM NaI was added to 10 mL of 50 mM CTAB. Following preparation of the surfactant-salt mixture, 275 μL of 10 mM $HAuCl_4 \bullet 3H_2O$ was added to the solution, followed by the addition of 55 μL of 100 mM L-ascorbic acid, after which the solution turned from orange to clear. To initiate nanoprism growth, a solution of 25 μM $NaBH_4$ was prepared, and 8 μL was added to the growth solution while slowly mixing on a vortex mixer. Mixing was continued for 10 seconds, and the solution was left undisturbed for 30 minutes. Purification of the reaction mixture was carried out by dividing the solution into 1.5 mL centrifuge tubes, and allowing the nanoplates to separate via sedimentation. Nanoprisms were separated from reaction impurities by removal of the supernatant and were stored in 50 mM CTAB.

2.2.8 CTAB Efficient Syntheses

Concentrated solutions of seedless nanorods and nanoprisms were prepared as described above, except that all stock solutions were increased in concentration while the concentration of CTAB remained unchanged. For example, in a synthesis denoted as a **5x** synthesis, the stock solution concentrations of $HAuCl_4$, $AgNO_3$, ascorbic acid, and $NaBH_4$ were increased by a factor of 5 (to 5 mM, 20 mM, 500 mM, 11.25 mM, respectively) while the concentration of the CTAB solution remained at 200 mM.

2.2.9 UV-vis-NIR Spectroscopy

Colloids were measured by ultraviolet-visible-near infrared spectroscopy (UV-vis-NIR) using a Cary 5000 spectrophotometer (Agilent, Inc.). Spectra were baselined to the spectrum of water, except in the case of nanoprisms, where D_2O (Cambridge Isotope Laboratories, D +99.9%) was used for all measurements. In CTAB-efficient syntheses, particle concentrations were too high to obtain extinction values and were instead volumetrically diluted with 50 mM aqueous CTAB to standard concentrations (*vide infra* and Supporting Information) before analysis. For example, to measure a **5x** reaction, samples were diluted to 20% of the as-synthesized concentration.

2.2.10 pH Growth Solution Measurements

After addition of ascorbic acid, the pH of the growth solutions for seeded and seedless protocols was measured with a 8172BNWP ROSS Sure-Flow Combination electrode (Thermo Scientific), and Orion 3 Star pH benchtop meter, calibrated with buffered solutions at pH 4, 7, and 10 (Fischer Scientific).

2.2.11 Transmission Electron Microscopy Analysis

A 1 mL aliquot of particles, as synthesized, was centrifuged at 8,000 RPM (Eppendorf Centrifuge 5424, rotor FA-45-24-11; 5424/5424R) for 5 minutes. After removal of the supernatant via syringe, particles were resuspended in 1 mL of water. This procedure was performed two additional times, after which particles were again collected by centrifugation and resuspended in 50 μL of water. A 10 μL aliquot of concentrated particles was drop cast onto a Formvar-backed copper TEM grid (Ted Pella, Formvar on 400 mesh Cu) and was slowly dried in

a humid environment. Samples were imaged on a FEI Morgagni 268 at 80 kV. TEM images were analyzed using ImageJ (open access software, http://rsbweb.nih.gov/ij/), using the particle analysis feature. Over 100 nanoparticles were measured to obtain reported values. All reported errors are the standard deviation in these measurements.

2.2.12 Scanning Electron Microscopy Analysis

Silicon wafer substrates (Ted Pella, p-doped (boron), 200 nm thermal oxide (silicon dioxide)) were first cleaned by sonicating in ethanol for five minutes. The substrate was then successively rinsed with ethanol and acetone, and dried under a stream of N_2 (*g*). Samples were prepared using the same procedure described for TEM analysis. Here, 10 μL of the resulting solution was drop cast onto the wafer and allowed to dry before imaging on a Raith Dual Beam EBL-SEM at various accelerating voltages.

2.3 RESULTS AND DISCUSSION

It has been proposed that seeds act as heterogeneous nucleation sites for subsequent NP growth.[89] Once formed, seeds are introduced into reaction solutions that have been tailored to promote seed particle growth while limiting concomitant homogeneous nucleation events. This method has facilitated the identification of reaction conditions that promote a variety of anisotropic nanoparticle growth pathways.[97,102-108] However, some reports suggest that seeding may be unnecessary to achieve anisotropic nanoparticle products.[109-110] Further, the structure of a seed is dynamic in solution.[111] After formation, seeds may undergo processes such as Ostwald ripening and coalescence which change the size, shape, and/or crystallinity of seeds over time.[112]

As a result, seeds exhibit limited "active" lifetimes after which they may introduce time-dependent heterogeneities in resulting nanoparticle size and shape (e. g., see Figure 10).

To avoid seed-induced heterogeneity in nanoparticle products and ultimately generate more efficient syntheses, we consider homogeneous nucleation as an attractive alternative to the seed-mediated routes commonly used to afford anisotropic gold nanoparticle growth. It is already known that the rate of gold precursor reduction (or possibly the concentration of available metal monomer) in the presence of existing nuclei can influence final nanoparticle shape.[110,113] We reasoned that homogeneous routes to anisotropic morphologies may be possible if the concentration of metal monomer was increased only briefly over the critical supersaturation concentration needed for homogeneous nucleation. Sodium borohydride was selected as the reducing agent because it degrades quickly into benign byproducts upon oxidation ($t_{1/2}$ = 0.0607 minutes at pH = 7),[114]and rapidly reduces $HAuCl_4$ to generate a short burst of nucleation (<100 ms), where this burst may then prevent subsequent homogeneous nucleation events at later stages of synthesis due to complete reaction of reducing agent and gold precursor.[115]

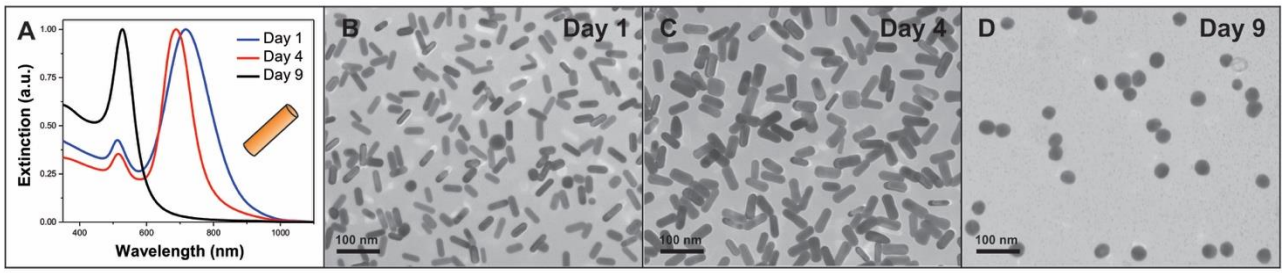

Figure 10. UV-vis-NIR extinction spectra (A) and transmission electron microscopy images (B-D) of nanoparticles produced using seeds of varying age. In all cases, the same batch of nanoparticle seeds was used to initiate particle growth. Seeds were stored at room temperature in a sealed glass vial and protected from light. After one day of aging, seeds produced rods in high yield (B). After four days of aging, a blue-shift is observed in the longitudinal LSPR (A,C). After nine days of aging, the seeds no longer produce anisotropic products (D). Average aspect ratios of particles for days 1, 4, and 9 were 2.6 ± 0.5, 2.2 ± 0.7, and 1.1 ± 0.2, respectively.

In a typical experiment, formation of gold nanoparticles (either nanorods or nanoprisms) was initiated by the addition of aqueous $NaBH_4$ to a solution containing $HAuCl_4$, CTAB and ascorbic acid. A key step in achieving anisotropic nanoparticle growth was modulating the ratio of $NaBH_4$ to $HAuCl_4$ in order to limit the amount of gold consumed during nucleation and thereby influence the concentration remaining for growth. Tuning this ratio in the presence of either silver nitrate or sodium iodide allowed for the formation of gold nanorods and nanoprisms, respectively (Figure 11). Using a seedless approach, nanorods were produced in greater than 90% yield and prisms in approximately 60% yield, comparable to as-synthesized yields reported using seed-mediated protocols.[97,116] Purified nanorods and nanoprisms synthesized via homogeneous nucleation were also comparable in size, shape and monodispersity to products obtained using seed-mediated approaches. UV-vis-NIR extinction spectra of nanorods (length = 40 ± 5 nm, diameter = 16 ± 4 nm) produced using homogeneous nucleation exhibited a characteristic longitudinal localized surface plasmon resonance (LSPR) at 790 nm and a transverse LSPR at 512 nm.[86] Nanoprisms (edge length = 186 ± 16 nm, thickness = 9 ± 1 nm) exhibited an in-plane dipole band at ~1400 nm and a quadrupole band at ~850 nm, consistent with previous literature reports.[116-117]

The crystallinity of products generated using seedless methods also matches their seed-mediated counterparts (Figure 12). Fast Fourier transform (FFT) analysis of high resolution transmission electron microscopy (HRTEM) images of nanorods aligned along the [011] zone axis is consistent with previous literature reports.[118] Nanoprisms produced using seeded and seedless methods also demonstrate similar architectures. Together, we conclude that the crystallinity of the resulting nanoparticles does not depend on the method used to generate the nanoparticle nuclei. Instead, the similarity of particle products formed using the two routes

suggests that anisotropic growth of colloidal gold nanoparticles may be most strongly influenced by the presence of shape directing additives (e.g. metal salts or halides) rather than the nucleation pathway.

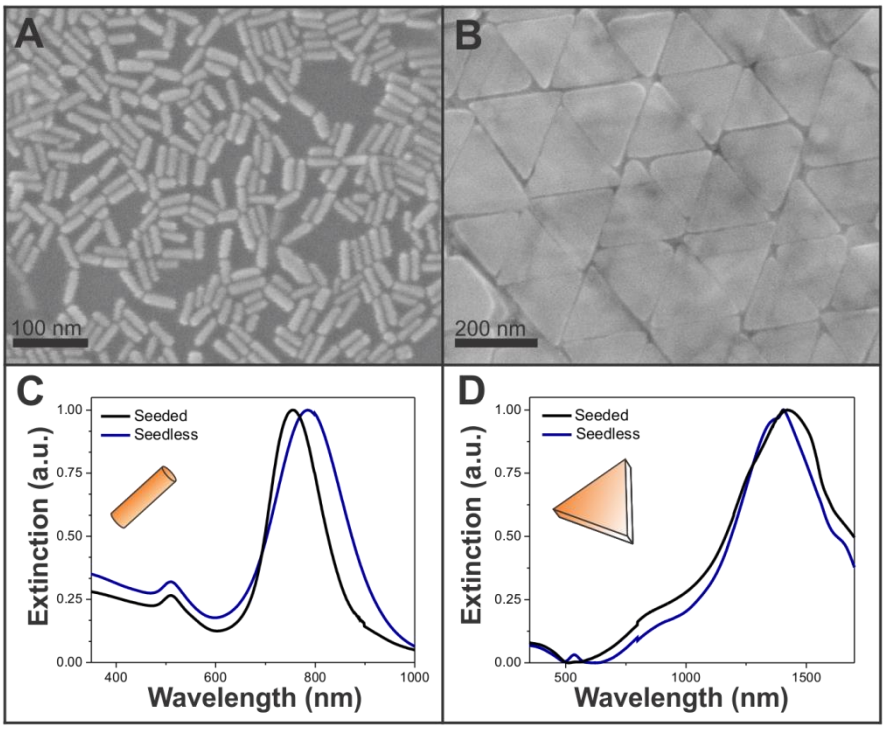

Figure 11. SEM images of nanorods (A) and nanoprisms (B) synthesized via homogeneous nucleation, and corresponding UV-vis-NIR spectra (C, D) showing characteristic optical features.

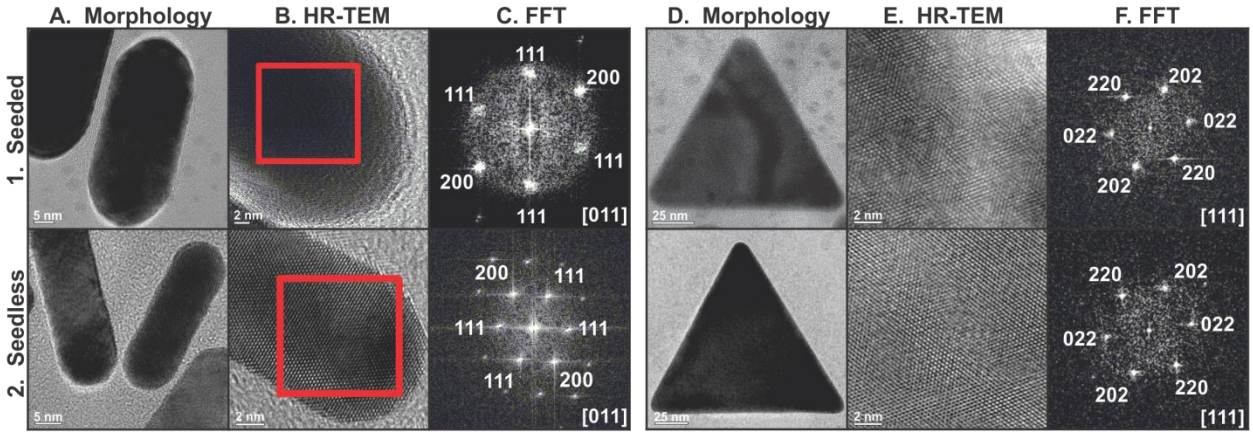

Figure 12. Seeded (1) and seedless (2) HRTEM analysis of particle morphology (A,D), lattice planes (B,E) and FFT analysis (C,F) of the lattice plane spacing for nanoprisms and nanorods, respectively.

In previous reports of nanorods synthesized using homogeneous nucleation, a major limitation has been the concomitant formation of pseudo-spherical impurities (d ~ 25 nm), which do not form using the seed-initiated method.[110] To suppress the formation of these particles, El-Sayed and coworkers introduce nitric acid to the reaction solution, lowering the pH to approximately 1.[110] A more acidic solution mitigates the reduction potential of $NaBH_4$ and results in the formation of fewer nuclei. We reasoned that a similar effect could be achieved by varying the ratio of reducing agent to metal precursor without the need for additional pH adjustment. Varying the ratio of $NaBH_4$:$HAuCl_4$ from 0.00045 to 0.045 produces particles of the desired shape, with nanorod aspect ratios ranging from 2.3 to 3.3 (Figure 13). At reducing agent to metal precursor ratios equal to and greater than 0.045, we began to observe a significant population of small pseudo-spherical AuNPs (d < 10 nm) (Figure 14). This observation is consistent with the recently proposed stochastic formation mechanism, where nuclei remain dormant until an activation event, and then proceed to grow rapidly after activation.[119] If the available gold precursor is exhausted prior to this activation event, pseudo-spherical impurities will subsist. Therefore, we investigated lower ratios of reducing agent to gold precursor in order to prolong the "growth-only" phase of nanorod formation. At ratios from 0.0045 to 0.00045, the average nanorod length increases slightly from 47 ± 5 nm to 51 ± 4 nm and the longitudinal LSPR shifts from 735 to 765 nm. This slight increase in rod length may be attributed to the availability of gold precursor per growing particle, where an increase in this ratio leads to larger rods.[113] At ratios below 0.00045, no further changes were observed in product morphology, indicating that excess metal precursor is not incorporated into the nanorod architectures.

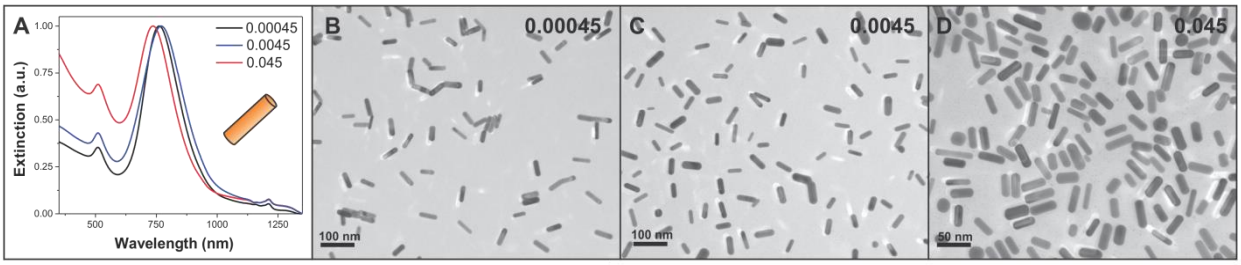

Figure 13. UV-vis-NIR spectra (A) and corresponding TEM images of nanorods produced over a range of $NaBH_4$:$HAuCl_4$ concentration ratios (B-D). At low reducing agent to metal precursor ratios (0.00045) (B), nanorods exhibit average lengths of 51 ± 4 nm with a corresponding LSPR at 770 nm. As the ratio of $NaBH_4$:$HAuCl_4$ is increased, nanorod length decreases (47 ± 5 nm, 35 ± 5 nm) and λ_{max} blueshifts (762 nm, 735 nm) at ratios of 0.0045 (C) and 0.045 (D), respectively.

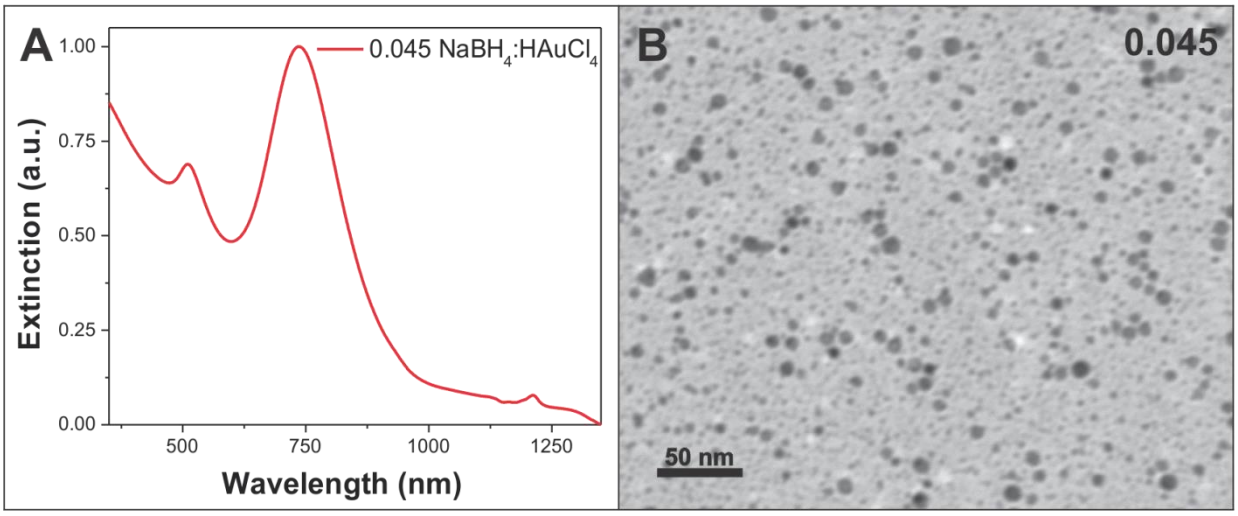

Figure 14. UV-vis-NIR spectrum (A) and selected TEM image (B) of nanoparticles produced in nanorod syntheses using higher reducing agent to metal precursor ratios (e. g. 0.045, $NaBH_4$:$HAuCl_4$) examined for the nanorod synthesis. The increase in pseudo-spherical NPs (B) may be attributed to an "excess" of nucleation sites in solution produced by the high concentration of reducing agent. With more gold consumed during nucleation, the subsequent phase of particle growth by diffusion is effectively shorter and the concentration of free gold is depleted before rod-like architectures emerge in high yield.

In the case of nanoprisms, similar trends in product morphology and spectral features were observed, where ratios of 0.0225 to 0.1 produced the desired shape in comparable yield to the analogous seed-mediated procedures (Figure 15). However, the range of $NaBH_4$:$HAuCl_4$ ratios that resulted in plate-like growth was found to be more narrow than for the seedless nanorod synthesis, and changes in product morphology were more pronounced. At a $NaBH_4$:$HAuCl_4$ ratio of 0.1, the major product was triangular nanoprisms (yield ~60%). At the lowest concentration of $NaBH_4$ found to promote plate-like growth (0.025), the nanoplates became hexagonal in shape with an average vertex-to-vertex length of 720 ± 70 nm. Although the particle shape recovers symmetry, the dipole LSPR shifts from 1420 to over 1600 nm and there is a marked broadening of the peak, likely due to particle scattering.[117] Again, these differences in product morphology may be rationalized by changes in the ratio of reducing agent to metal precursor using a La Mer model of nucleation and growth. At lower reducing agent to gold precursor ratios, fewer nucleation sites are present when the gold monomer concentration reaches a growth-only regime, and therefore the resulting particles exhibit larger dimensions. To the best of our knowledge, these experiments represent the first report of spectroscopically-discernible, colloidal gold nanoprisms using a seedless approach.

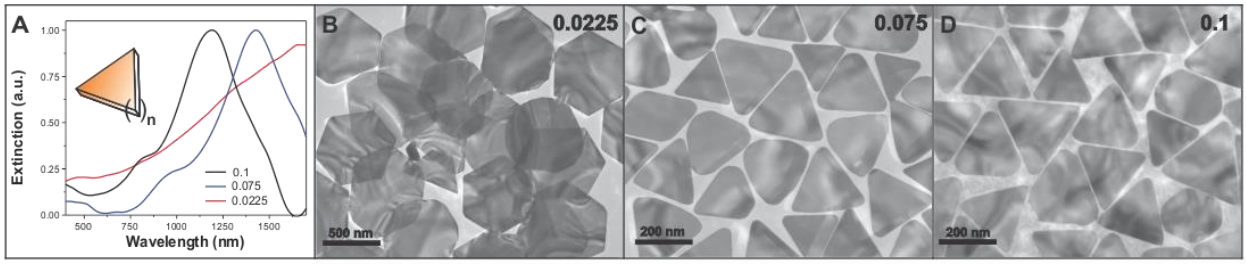

Figure 15. UV-vis-NIR spectra (A) and corresponding TEM images of nanoprisms produced over a range of $NaBH_4$:$HAuCl_4$ concentration ratios (B-D). At the lowest concentration of reducing agent relative to gold precursor (0.0225) (B), prisms exhibit hexagonal morphologies with an average vertex-to-vertex distance of 720 ± 20 nm and a corresponding in-plane dipole LSPR at 1674 nm. As the ratio of reducing agent to metal precursor increases, nanoprisms become triangular in shape with decreasing edge lengths (153 ± 21 nm, 120 ± 18 nm) and blue-shifted λ_{max} (1420 nm, 1180 nm) at ratios of 0.075 (C) and 0.1 (D), respectively.

After successful removal of the seed template, we were able to identify several additional reagents of limited mechanistic importance. First, nanorods and nanoprisms could be formed without further pH adjustment, and therefore reagents such as nitric acid and sodium hydroxide were removed. As previously mentioned, manipulation of the $NaBH_4$:$HAuCl_4$ ratio allowed for high shape yield of nanorods at a pH of 2 (as high as 95%), thereby eliminating the need to further acidify the solution using nitric acid. Nanoprisms, typically synthesized via seed-mediated methods at pH 8, are synthesized here at pH 3.2 without observable changes in product architecture. Sodium borohydride, a reducing agent in both methods, was required in comparable amounts for seedless initiation of nanorods, but could be reduced in quantity by over four orders of magnitude for the seedless synthesis of nanoprisms (*vide infra*). Last, the stabilizing ligand for seeds in the nanoprism synthesis, trisodium citrate, was found to have no effect on reaction outcome and was removed from the synthesis.

Eliminating the nanoparticle seed and removing extraneous reagents affords significant gains in synthetic efficiency. However, a key reagent well-known to be resistant to modifications of any type (e. g. concentration, chain length, counter ion) was the surfactant, CTAB (Figure 16).[113] One possible explanation for this sensitivity is the supramolecular architecture of the surfactant, which may play multiple roles in the synthesis of anisotropic nanoparticles including soft-templating and reagent sequestration. Therefore, instead of adjusting CTAB concentration (and thereby influencing surfactant micelle architecture)[100] we attempt to increase the efficiency of surfactant use. Here, reagent concentrations were increased between 3 and 15 times the concentrations used in our original seedless synthesis, while the concentration of CTAB was held constant at 200 mM and 50 mM for nanorods and nanoprisms, respectively. For example, in a nanorod synthesis denoted as **5x**, the concentrations of $HAuCl_4$, $AgNO_3$, ascorbic acid, and

$NaBH_4$ were increased to 5 mM, 20 mM, 500 mM, and 11.25 mM, respectively, while the concentration of CTAB remained at 200 mM. The resulting particle products were produced at approximately five times the concentration, as indicated by extinction measurements (extinction at 750 nm increased 4.65 times compared to spectra taken of as-synthesized solutions produced in the standard synthesis). Figure 17 shows TEM images of **5x** nanorods which are similar in both size and yield to those synthesized under standard conditions. Increasing concentrations to **10x** leads to a population of cuboidal impurities, evident in the extinction spectra by increased absorbance at 535 nm.[102] At concentrations exceeding **10x**, nanorods decrease in aspect ratios as well as yield, as indicated by the decreasing intensity and blue-shift of the longitudinal LSPR to 612 nm. At **15x** conditions, both the aspect ratio and the yield of nanorods relative to pseudospherical impurities was significantly decreased (Figure 18).

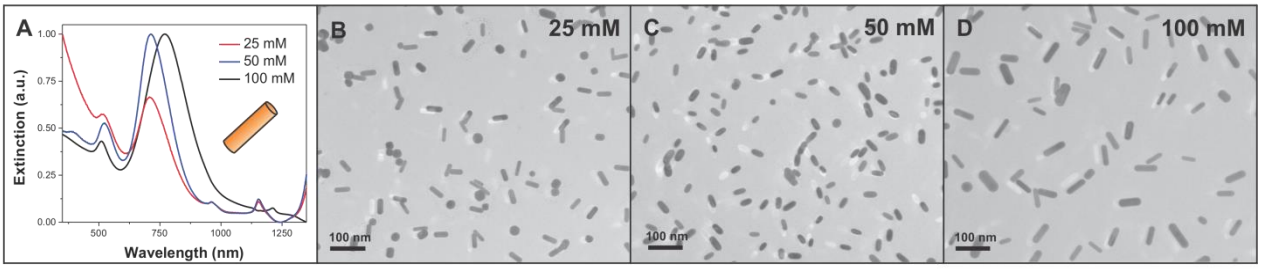

Figure 16. UV-vis-NIR extinction spectra (A) and transmission electron microscopy images (B-D) of nanoparticles produced using different CTAB concentrations. In a typical nanorod synthesis, as the concentration of CTAB increases, the yield of nanorods increases. At standard reaction concentrations, 100 mM (concentration in the final reaction mixture) (D), rods are produced in greater than 90% yield. After decreasing the concentration of CTAB by 50%, (to 50 mM), average rod length decreased from 47 ± 5 to 39 ± 4 nm (C). Using 25 mM CTAB, nanorod products were of similar length, however, the yield of nanorods compared to pseudo-spherical products was reduced (from 95 to 71%).

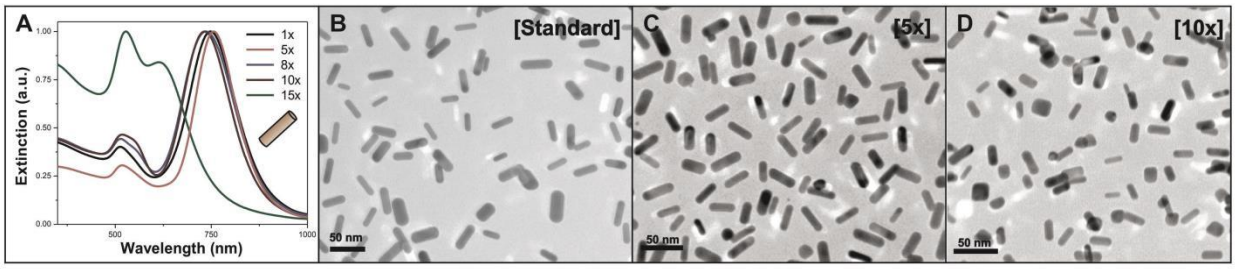

Figure 17. UV-vis-NIR spectra (A) and corresponding TEM images of nanorods produced using a CTAB-efficient, seedless approach (B-D). Upon increasing the reagent concentration with respect to CTAB concentration used in standard seedless conditions (B), no observable changes in product yield, monodispersity, or morphology were observed even at a five-fold increase, **5x** (C). At concentrations greater than **5x**, the formation of pseudo-spherical and cuboidal particles begins to become competitive with rod growth (D).

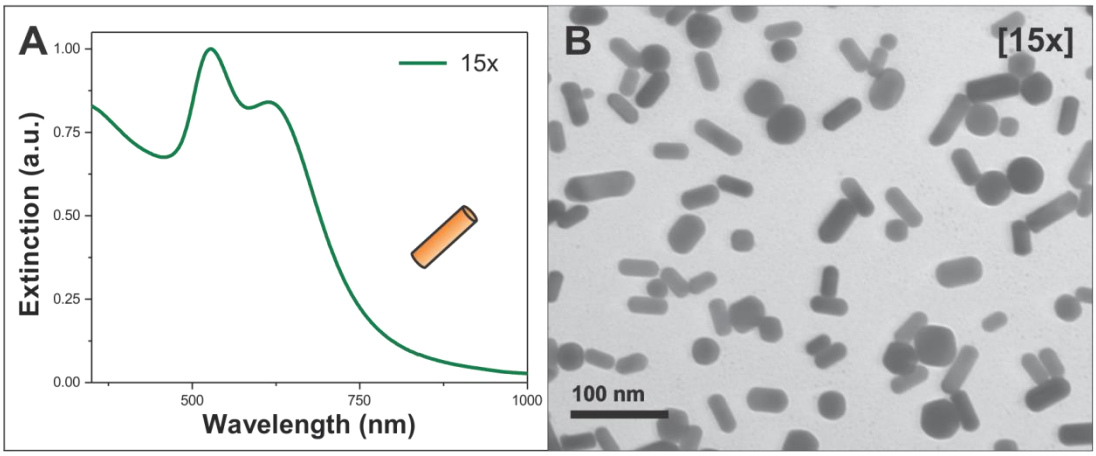

Figure 18. Extinction spectrum (A) and TEM image (B) of nanoparticles generated using 15x reaction conditions. For CTAB-efficient nanorod syntheses, as the concentration of reagents is increased relative to CTAB above 10x, pseudo-spherical and cuboidal particle yields increase. For 15x, growth is still predominantly anisotropic, however the yield of nanorods has significantly decreased relative to the standard 1x synthesis (from 92% to 59%).

Interestingly, conditions for plate-like growth were found to be more sensitive than nanorod growth to changes in reagent concentrations relative to CTAB concentration (Figure 19). In experiments where the concentrations of all reagents were increased by a factor of five (except for CTAB), 5x, the triangular prism shape was maintained, however edge lengths increased from 186 ± 16 nm to 217 ± 18 nm and thickness increased from 9 ± 1 nm to 25 ± 2 nm. When the reagent concentration was increased to 8x, plate-like growth was still observed in similar yield (~60%), however, prism thickness again increased slightly (28 ± 3 nm) and particles adopted hexagonal geometries. Further, vertex-to-vertex distance decreased from 217 ± 18 nm to 125 ± 18 nm. Combined these morphology changes led to a marked blue-shift of the dipole LSPR band (>250 nm), which can be attributed to both "snipping" of the prism edges[120] as well as an increase in particle thickness.[121] Previous work using gold nanoprisms as seeds demonstrated the modulation of nanoprism edge length with little change in prism thickness, but using much lower concentrations of metal precursor (50 μM).[122] On the other hand, preparation of bimetallic particles using gold nanoprism seeds has been shown to form bifrustum structures via Ag overgrowth.[123] Using a homogeneous nucleation strategy to initiate plate-like growth at relatively high precursor concentrations, we observe increases in both dimensions, as well as a shape change from triangular to hexagonal. The data are consistent with previously proposed growth mechanisms based upon the Terrace-Step-Kink (TSK) model. In these descriptions, it is postulated that Au atoms are incorporated into all facets of a growing particle, but incorporation rate is mediated by surface architecture (e.g. faster at low-coordination, step or kink sites relative to terrace sites). In nanoprisms, the side crystal facets have classically been described as preferable for atom addition due to a twin plane defect that results in a type of kink site,[98] whereas adsorption of Au atoms onto the top crystal facet is slow. At high concentrations of

metal monomer it is possible that either deposition on the broad, triangular sites competes effectively with the side facets or that the growth phase is sufficiently extended to permit observable growth in both particle dimensions.

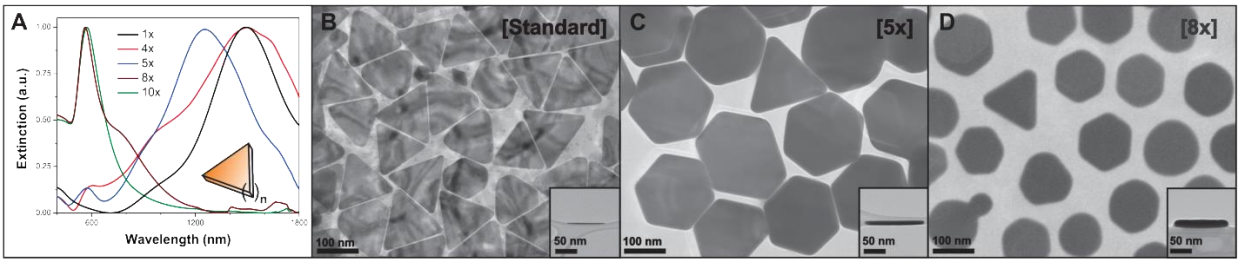

Figure 19. UV-vis-NIR spectra (A) and corresponding TEM images of nanoprisms produced using a CTAB-efficient, seedless approach (B-D). Using standard seedless conditions, nanoprisms exhibit characteristic optical features (in-plane dipole LSPR = 1510 nm) with average edge lengths of 143 ± 16 nm and average thickness of 9 ± 1 nm (B and inset). Prisms synthesized at **5x** displayed hexagonal morphologies with slightly longer vertex-to-vertex distances (217 ± 18 nm) and thickness of 25 ± 2 nm as well as a blue-shifted λ_{max} (1245 nm) (C and inset). At **8x** reagent concentrations, plate-like growth is still observed, but particles are smaller (vertex-to-vertex = 125 ± 18 nm) and thicker (28 ± 3 nm, D and inset).

Optimized conditions for nanorods and nanoprisms were found at 5x and 3x reagent concentrations, respectively (Figure 20). Extinction spectra taken of dilute nanoparticle products indicate that these particles exhibit characteristic spectral features. Efficient use of CTAB is crucial for the sustainability of nanoparticle syntheses, both in terms of atom economy and waste prevention. Since free CTAB has been shown to be both cytotoxic[124] and difficult to purify,[125] reducing the concentration required per particle synthesized should be helpful in expediting their translation into applications. Because CTAB is present in near-molar concentrations, it also dominates the synthetic cost of anisotropic gold nanoparticles – more than 4-6 times the cost of the constituent gold. Therefore, we present an analysis of sustainable reagent use in the seeded and seedless syntheses for both nanorods and nanoprisms. *N.B.* These calculations are based on estimates of concentration using the optical density of nanoparticle solutions at $\lambda_{max.}$ Because every nanoparticle has a unique extinction coefficient based on its size, shape, and composition, the relationship between solution optical density and particle concentration is challenging to present quantitatively due to particle size and shape distributions which can vary from synthesis to synthesis. Instead, comparisons of concentration made here are relative rather than quantitative and are not converted to molarity.

The total amount of reagents used in each synthesis is reported as the amount of reagents (in milligrams) to synthesize 1 mL of nanoparticles at the concentration produced in a standard seed-mediated synthesis as determined by optical density at λ_{max}. We refer to this value as the amount of reagents per standard mL of nanoparticles. For example, in a standard, seeded synthesis of nanorods[97] a total of 72.1 mg of reagents are used to produce 10.16 mL of nanorods. Therefore, 7.097 mg of reagents produce 1 mL of as-synthesized nanorods in this seed-mediated synthesis. Using our seedless method, 36.13 mg of reagents is used to produce 10.16 mL of nanorods at **1x**.

Therefore 3.556 mg of reagents produce 1 mL of nanorods using a seedless approach (Table 3). Here, optical density at the longitudinal LSPR is used to assess concentration. In both the seeded and seedless cases, the as-synthesized nanoparticle mixtures have similar optical density at the longitudinal LSPR peak maximum (OD = 0.62 at 706 nm, OD = 0.72 at 745 nm for seeded and seedless nanorods, respectively).

Figure 21 and Figure 22 summarize the series of calculations used to determine the final amount of reagent per standard mL of nanoparticles for nanorods and nanoprisms, respectively. Using the standard seeded and seedless values listed in Table 2, the amounts of each reagent required for the seed-mediated and seedless syntheses were plotted (top left). Next, these values were divided by the total reaction volume (1) to reach the concentration of reagents needed in the seed-mediated and seedless synthesis (in mg/mL). The seedless synthesis values were adjusted to reflect the amounts used in the CTAB efficient syntheses. For example, in the **5x** seedless nanorod synthesis, the concentrations of $HAuCl_4$, ascorbic acid, $NaBH_4$, and $AgNO_3$ were increased by a factor of 5 (2). Lastly, all values for the seedless syntheses were adjusted to reflect the total concentration of reagents needed to produce 1 mL of nanoparticles at concentrations produced in a standard seed-mediated synthesis and these are the values used to construct Figure 23 and Figure 24 (*vide infra*). Here, for instance, the reagent concentration values for the seedless 5x nanorods synthesis were divided by five to account for the increased nanorod yield per unit volume relative to the seed-mediated synthesis

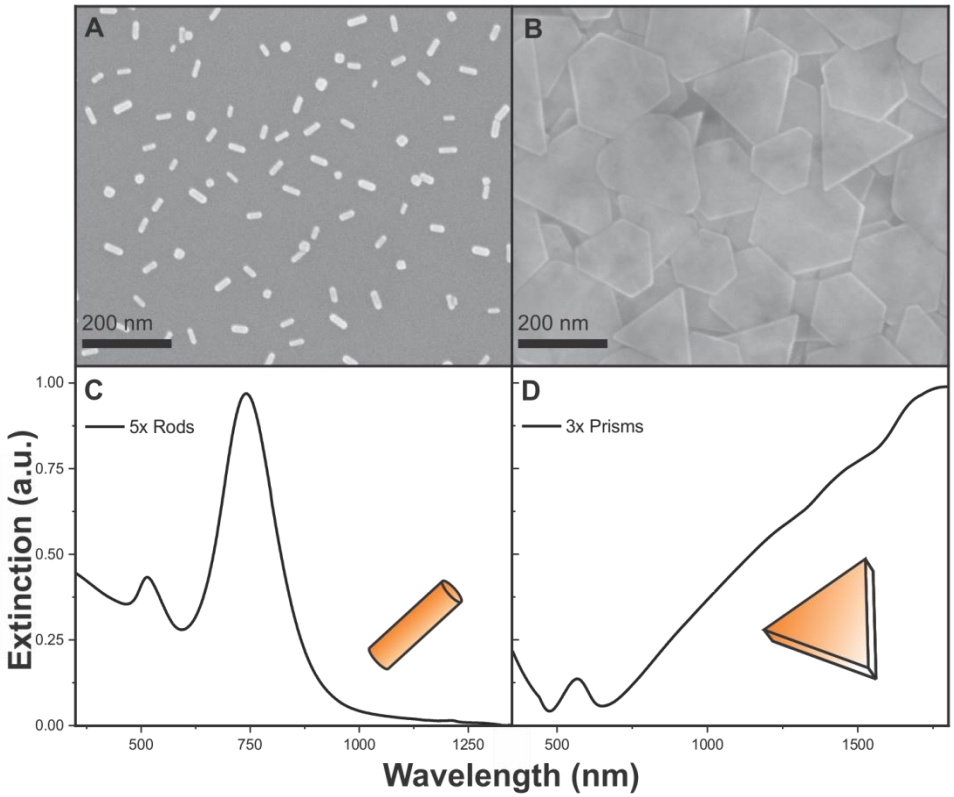

Figure 20. SEM images (A, B) and extinction spectra (C,D) of nanorods and nanoprisms, synthesized at 5x and 3x, respectively. Nanorods were 39 ± 6 nm in length, and nanoprisms had an average edge length of 183 ± 20 nm and average thickness of 21 ± 4 nm. These data demonstrate that characteristic morphologies and optical properties are observed from both shapes using CTAB-efficient, homogeneous nucleation reaction conditions.

Table 2. Total weight of reagents in seeded[97,126] and seedless syntheses for nanorods and nanoprisms.

Synthesis	$HAuCl_4$ (mg)	CTAB (mg)	Ascorbic Acid (mg)	$NaBH_4$ (mg)	$AgNO_3$ (mg)	NaI (mg)	Trisodium Citrate (mg)
Nanorods (seeded)	2.55	729	0.872	0.227	0.0679	--	--
Nanorods (seedless)	1.70	364	0.872	0.0009	0.0679	--	--
Nanorods (seedless, **5x**)	8.49	364	4.36	0.00428	0.340	--	--
Nanoprisms (seeded)	4.25	164	0.881	3.78	--	0.0675	2.94
Nanoprisms (seedless)	0.941	182	0.977	0.117	--	0.0749	--
Nanoprisms (seedless, **3x**)	2.82	182	2.99	0.351	--	0.203	--

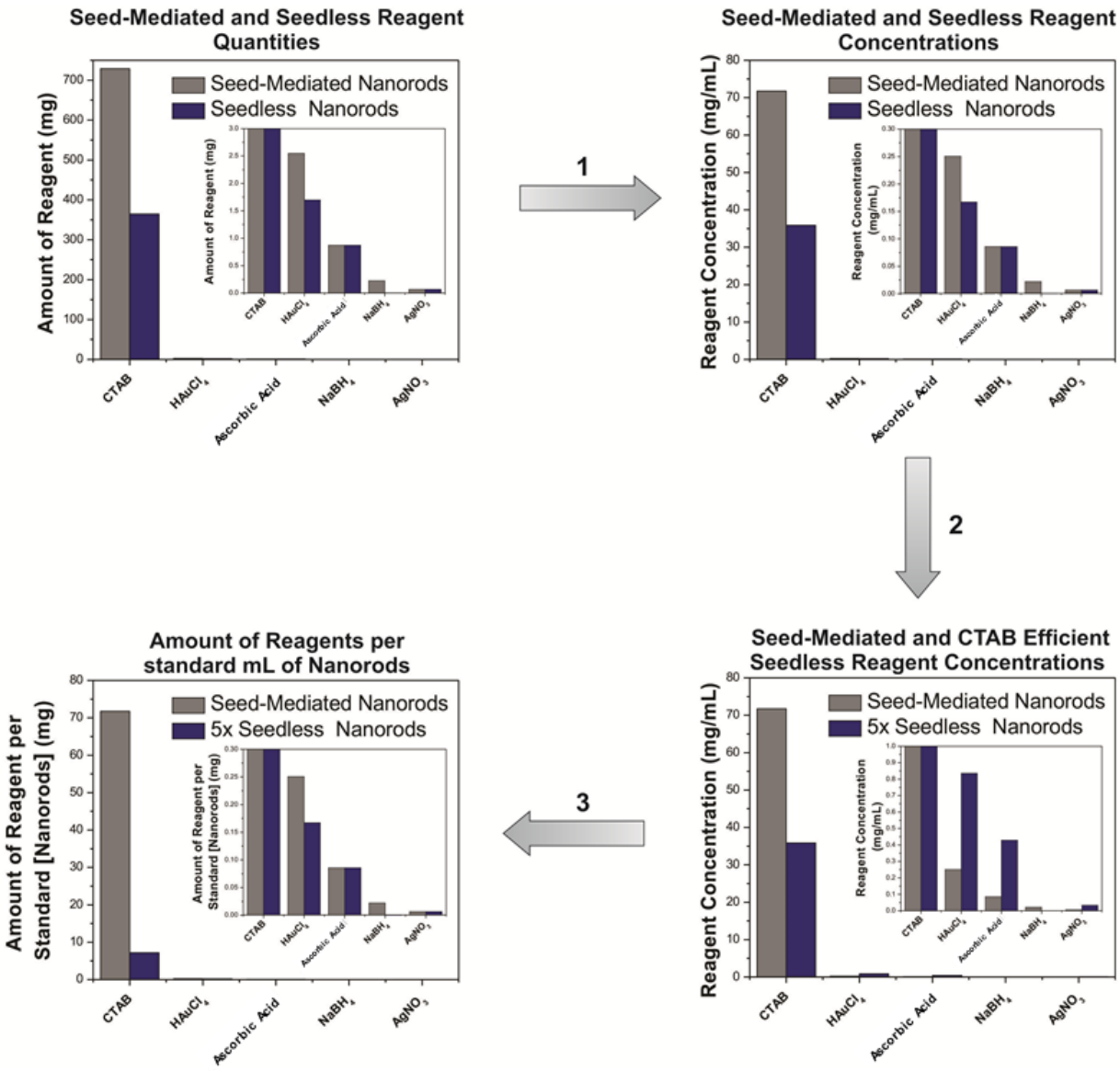

Figure 21. Flow-chart depicting the process used to determine the amount of reagents consumed in preparing a standard mL of nanorods using seed-mediated and seedless methods. Graph insets are a zoom-in of reagents that are used in much lower quantities than CTAB.

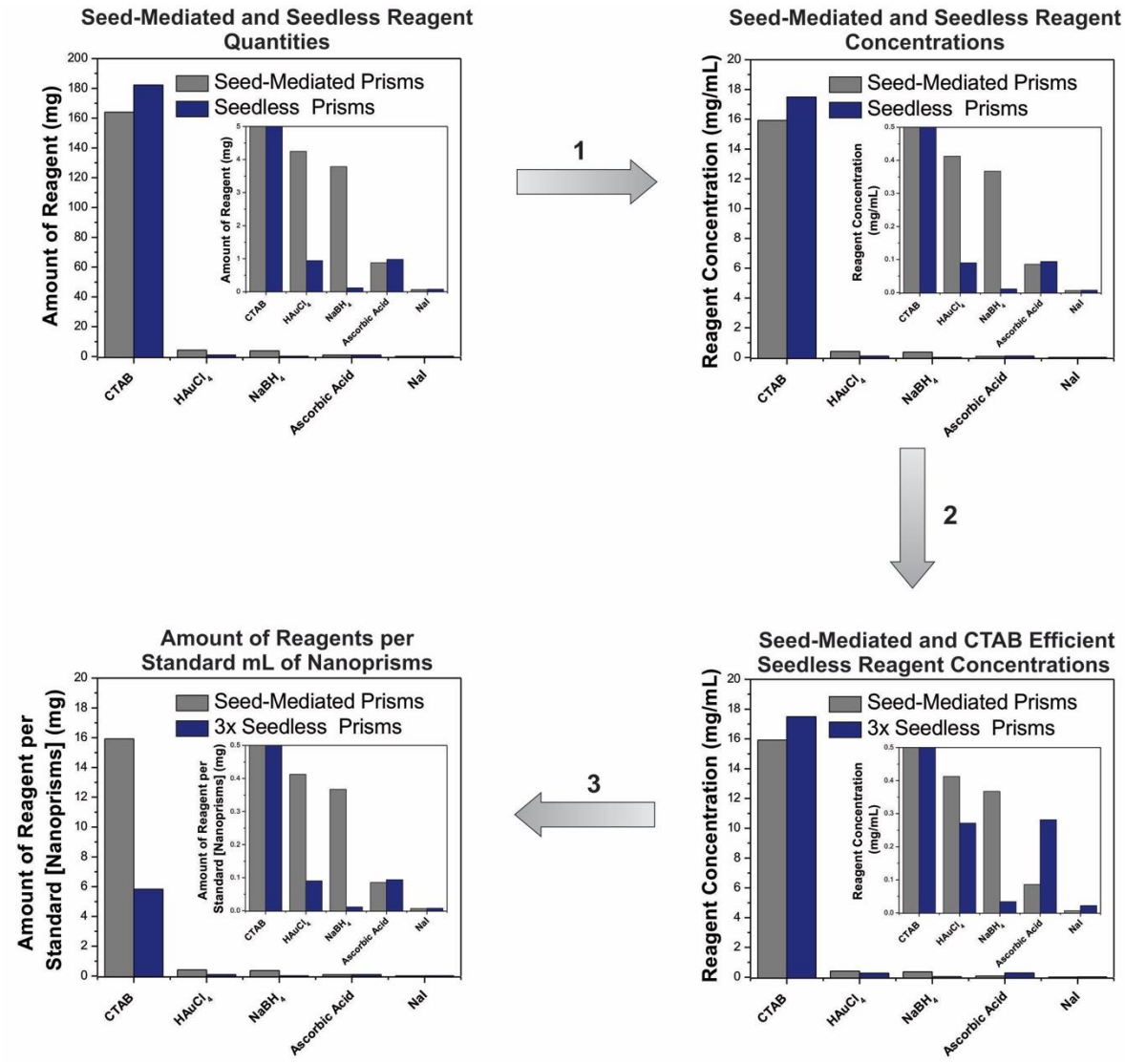

Figure 22. Flow-chart depicting the process used to determine the amount of reagents consumed in preparing a standard mL of nanoprisms using seed-mediated and seedless methods. Graph insets are a zoom-in of reagents that are used in much lower quantities than CTAB.

Table 3. Total amount of reagents per standard mL of nanoparticles in seeded[97,126] and seedless syntheses for nanorods and nanoprisms.

Synthesis	$HAuCl_4$ (mg)	CTAB (mg)	Ascorbic Acid (mg)	$NaBH_4$ (mg)	$AgNO_3$ (mg)	NaI (mg)	Trisodium Citrate (mg)
Nanorods (seeded)	0.251	71.8	0.0858	0.0223	0.00669	--	--
Nanorods (seedless)	0.167	35.9	0.0858	0.0000187	0.00669	--	--
Nanorods (seedless, 5x)	0.167	7.17	0.0858	0.0000187	0.00669	--	--
Nanoprisms (seeded)	0.412	15.9	0.0855	0.367	--	0.00655	0.286
Nanoprisms (seedless)	0.0903	17.5	0.0940	0.0112	--	0.00719	--
Nanoprisms (seedless, 3x)	0.0903	5.83	0.0940	0.0112	--	0.00719	--

Optimization of homogeneous nucleation conditions afforded reductions in the amount and total cost of CTAB by 80% and 66% for nanorods and nanoprisms, respectively (Table 4 and Table 5). These improvements, coupled with the elimination of seeds and extraneous reagents, allowed for a 91% and 88% decrease in the amount of reagents (by weight) necessary for the production of nanorods and nanoprisms, respectively (Table 6 and Figure 23). To standardize differences between reagent quantity and reagent price, the amounts of reagents per standard mL of nanoparticles for nanorods and nanoprisms were converted to cost per milligram using prices obtained from commercial suppliers. This conversion allows a rough estimate of the cost per standard mL of nanoparticles in order to compare the total synthetic efficiency of seed-mediated and seedless protocols. Overall, this translates to a reduction in the total amount of reagent cost per standard mL of nanoparticles by 81% and 72% in comparison to the seeded methods for seedless nanorods and prisms, respectively (Figure 24).

Table 4. Reagent Cost per Gram.

Reagent	Product Code (Sigma Aldrich)	Cost ($/g)
$HAuCl_4$	254169	196.60
$NaBH_4$	480886	3.97
$AgNO_3$	209139	3.88
CTAB	H9151	3.84
Ascorbic Acid	A7506	1.32
NaOH	306576	1.20
Trisodium Citrate	S4641	0.90
NaI	383112	0.68

Table 5. Cost of reagents per standard mL of nanoparticles in seeded and seedless syntheses for nanorods and nanoprisms.

Synthesis	$HAuCl_4$ ($)	CTAB ($)	Ascorbic Acid ($)	$NaBH_4$ ($)	$AgNO_3$ ($)	NaI ($)	Trisodium Citrate ($)
Nanorods (seeded)	0.0493	0.276	0.000114	0.0000887	0.0000259	--	--
Nanorods (seedless)	0.0329	0.137	0.000114	0.0000003	0.0000259	--	--
Nanorods (seedless, 5x)	0.0329	0.0276	0.000114	0.0000003	0.0000259	--	--
Nanoprisms (seeded)	0.0811	0.0611	0.000113	0.00146	--	0.00000445	0.000257
Nanoprisms (seedless)	0.0178	0.0672	0.000124	0.0000446	--	0.00000489	--
Nanoprisms (seedless, 3x)	0.0178	0.0403	0.000124	0.0000446	--	0.00000489	--

Table 6. Comparison of the total cost of reagents per standard mL of nanoparticle relative to the seed-mediated synthesis.

Synthesis	Total Cost ($)	Cost per Standard mL ($/mL)	Decrease from Seed-Mediated Synthesis (%)
Nanorods (seeded)	3.303	0.3250	--
Nanorods (seedless)	1.733	0.1708	47.46
Nanorods (seedless, 5x)	3.074	0.06057	81.37
Nanoprisms (seeded)	1.484	0.1440	--
Nanoprisms (seedless)	0.886	0.08511	40.92
Nanoprisms (seedless, 3x)	1.634	0.04033	72.00

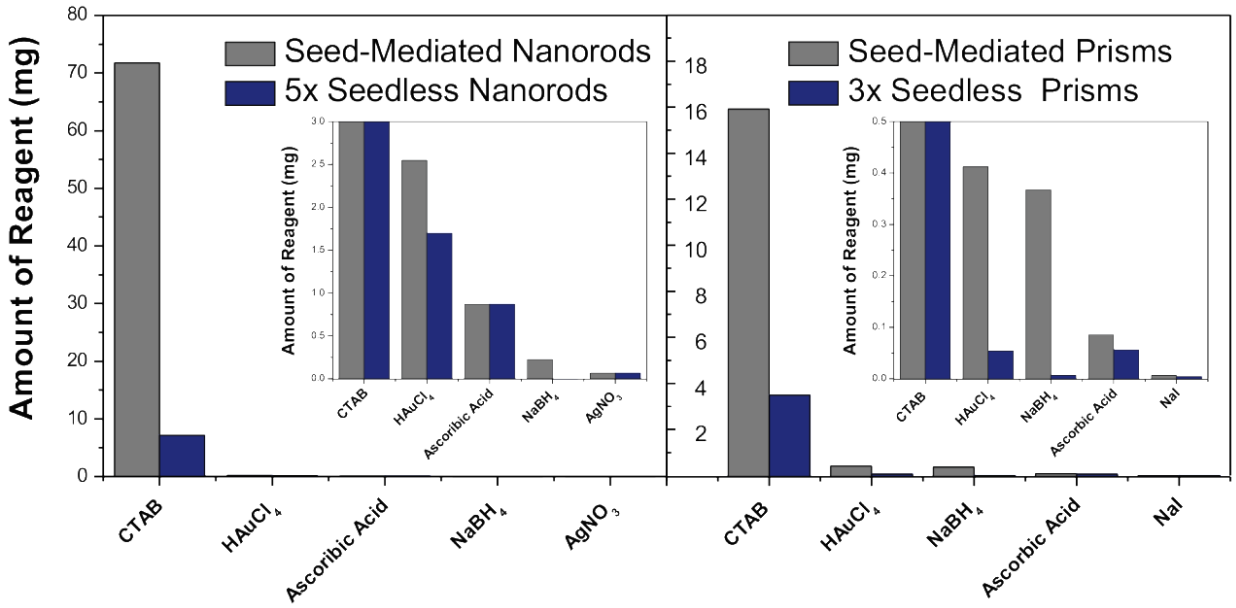

Figure 23. Comparison between the amount of reagents required for seed-mediated vs. seedless syntheses of gold nanorods (left) and gold nanoprisms (right). The total amount of reagent used is dominated by CTAB (as is the total cost, see SI). In total, the weight of reagents was reduced by 91% and 88% in the seedless CTAB-efficient synthesis of nanorods and nanoprisms, respectively, relative to the seed-mediated protocols. (Inset is a zoom-in of each bar graph to allow visualization of other reagents).

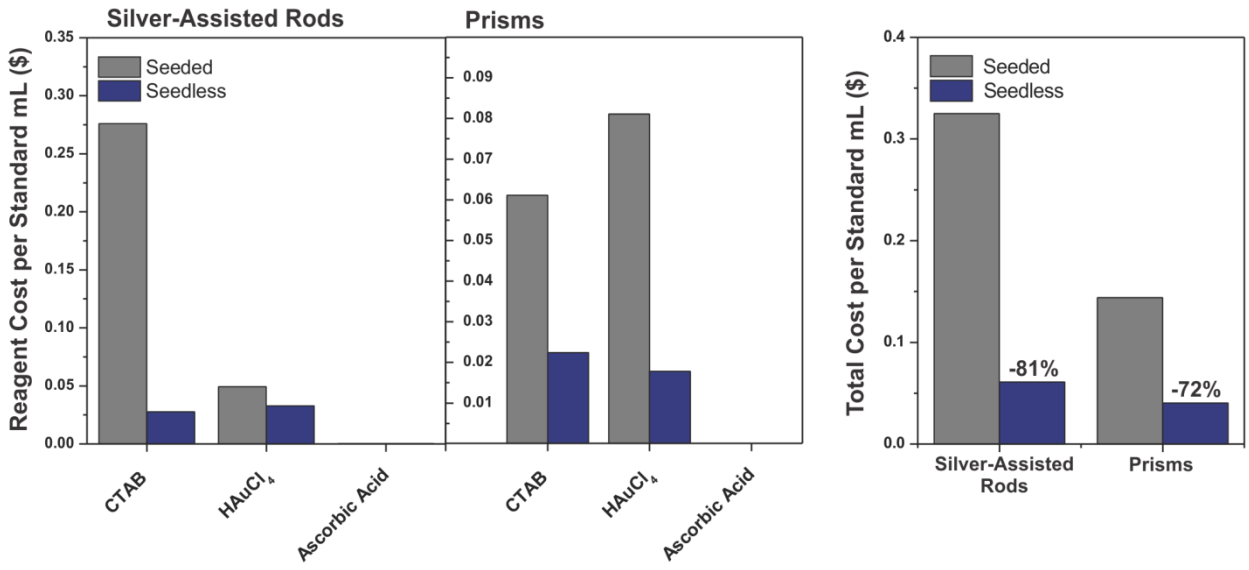

Figure 24. Total cost comparison between seed-mediated and seedless methods.

2.4 CONCLUSIONS

We have demonstrated the seedless synthesis of two canonical anisotropic gold nanoparticles: nanorods and nanoprisms. By eliminating the use of nanoparticle seeds and several other extraneous reagents, we distinguish between shape-directing and spectator reagents in these preparations. It is observed that seedless syntheses of gold nanorods and nanoprisms produce particles with almost identical optical and crystallographic properties using up to 90% (by weight) less reagent materials, and to the best of our knowledge, have yielded the first report of spectroscopically-discernible colloidal gold nanoplates using a seedless method. These results shed new light on the fundamental mechanisms leading to anisotropic gold nanoparticle growth, and should accelerate the discovery and commercialization of applications based on anisotropic noble metal nanoparticles.

3.0 DECOUPLING MECHANISMS OF PLATINUM DEPOSITION ON GOLD NANOPARTICLE SUBSTRATES

(Portions of this work were published previously and are reprinted with permission from: Straney, P. J.; Marbella, L. E.; Andolina, C. M.; Nuhfer, N. T.; Millstone, J. E., *J. Am. Chem. Soc.*, **2014**, *136*, 7873-7876. Copyright 2014 American Chemical Society).

3.1 INTRODUCTION

Multimetallic nanostructures are an exciting class of materials because they may exhibit new or enhanced properties when compared to their monometallic counterparts.[13,127-128] A myriad of multimetallic materials have been reported and are synthetically accessible in various sizes, shapes, and compositions.[13,129] Of the many different target compositions, platinum is a frequent component because of its broad utility in heterogeneous catalysis.[128,130] Forming multimetallic systems that include Pt can both enhance catalytic activity[131-133] as well as offer routes to reduce catalyst cost.[134-135]

One widely studied strategy for preparing Pt-containing nanoparticles (NPs) uses seed-mediated techniques.[136] In these syntheses, a monometallic NP substrate is used as a template for the addition of a second metal. When a second metal is introduced, it may deposit onto,[137-138]

alloy with,[139-140] and/or oxidize the existing particle substrate. However, the same metal combination may exhibit one or all of these reaction pathways – even within a single synthesis. The use of Pt in these syntheses is particularly challenging (both in seed-mediated and other wet chemical preparation strategies), because of the rapid hydrolysis of common precursors (e.g. $[PtCl_6]^{2-}$), and the sensitivity of these reactions to time, temperature, light, concentration, and pH.[141-143] For example, the efficiency of wet impregnation methods of γ-alumina exhibit heterogeneity in Pt particle content due to this speciation.[143] In Pt-containing multimetallic NP syntheses, this speciation may result in similar reaction conditions giving rise to markedly different morphologies. For example, Galvanic replacement reactions (GRRs) and core-shell products are both observed, sometimes in the same synthesis.[144-147]

3.2 EXPERIMENTAL

3.2.1 General Materials and Methods

Hexadecyltrimethylammonium bromide (CTAB, 99%), chloroplatinic acid (H_2PtCl_6, 8 wt. % in H_2O) hydrogen tetrachloroaurate trihydrate ($HAuCl_4 \cdot 3H_2O$, 99.999%), L-ascorbic acid (99%), sodium borohydride ($NaBH_4$, 99.99%), sodium hydroxide (99.99%), sodium iodide (NaI, 99.999%), and trisodium citrate (99%) were obtained from Sigma Aldrich and used as received. Poly(ethylene glycol) methyl ether thiol (PEGSH, average M_n by gel filtration chromatography (GFC) = 900 Da; 92% substitution by NMR) was purchased from Laysan Bio, Inc. (Arab, AL) and used as received. 11-amino-1-undecanethiol hydrochloride (AUT, 99.2%) was purchased from Dojindo (Rockville, MD) and used as received. NANOpure™ water (Thermo Scientific, >

18.2 MΩ•cm) was used for all washing, synthesis, and purification protocols as well as in the preparation of all solutions. All stock solutions were aqueous and prepared fresh before each reaction, unless otherwise noted. All glassware was washed with aqua regia (3:1 ratio of concentrated HCl and HNO_3 by volume) and rinsed thoroughly with water. *Caution: Aqua regia is highly toxic and corrosive and requires personal protective equipment. Aqua regia should be handled in a fume hood only.*

3.2.2 Synthesis of Au Nanoprisms

Au nanoprisms were synthesized according to a modified literature protocol.[63] Briefly, Au seeds were prepared by adding 0.25 mL of 0.1 M $NaBH_4$ to a rapidly stirring solution containing 9.0 mL of H_2O, 0.25 mL of 0.01 M $HAuCl_4$, and 0.25 mL of 0.01 M trisodium citrate. The solution was stirred for 30 seconds, and then allowed to rest undisturbed at room temperature for two hours to allow degradation of remaining $NaBH_4$. After the aging period, three growth solutions were prepared (referred to as **A**, **B**, and **C**). Here, **A** was prepared by adding 2.5 mL of 0.01 M $HAuCl_4$, 0.5 mL of 0.1 M NaOH, and 0.5 mL of 0.1 M ascorbic acid to 90.0 mL of 0.05 M CTAB solution that was also 50 μM in NaI. The solution was mixed by hand after the addition of each reagent and was optically transparent after all reagents were added. Solutions **B** and **C** were prepared in an identical manner, except that the volume of all reagents was decreased ten-fold (for example, the volume of 0.05 M CTAB/0.05 mM NaI solution was decreased from 90.0 mL to 9.0 mL). Au nanoprisms were synthesized using an iterative seed addition protocol, where growth was initiated by adding 1.0 mL of the seed solution to **A**. Immediately after seed addition, **A** was mixed by hand for two seconds (as measured by standard lab timer) and a 1.0 mL aliquot was quickly removed and added to **B**. After mixing **B** for two seconds, the entire

4contents of **B** was added to **C**, which was then mixed by hand for 10 seconds and allowed to react for ~ 2 h until nanoprism growth was complete.

3.2.3 Purification of Au Nanoprisms

Two hours after addition of the seed solution to the growth solution, the reaction mixture was heated in a water bath to 37 °C for one minute to dissolve any CTAB that may have recrystallized during the growth period which can interfere with purification by centrifugation. In order to purify the prisms from pseudospherical impurities and excess reagents, 90 mL of the reaction mixture was divided into 15 mL conical tubes and centrifuged at a gentle 120 rcf (Eppendorf centrifuge 5804 with swing bucket rotor A-4-44). After centrifugation, the nanoprisms deposit as a thin film on the walls of the conical tube, so both the supernatant and pellet were removed. The nanoprism film was resuspended in 1.0 mL of water, and this solution was then vortexed (Analogue Vortex Mixer, 120 V, 50/60 Hz, Fisher Scientific) to yield a slightly green, translucent colloid (Figure 25). The mixture was subsequently transferred to a 1.5 mL centrifuge tube and purified one additional time by centrifugation (5 minutes at 2200 rcf using a Spectrum mini-centrifuge (SC1006-R)). After removal of the supernatant, the nanoprism pellets were resuspended in 1.0 mL of water and recombined in a 15 mL centrifuge tube. The concentration of nanoprisms in the purified stock solution was determined by UV-vis-NIR spectroscopy, where concentration was measured as the optical density (O.D., a.u.) at λ_{max} (~1260 nm, see below for details pertaining to UV-vis-NIR measurements) of the in-plane dipole localized surface plasmon resonance (LSPR). The solution of purified nanoprisms was then diluted with water to an O.D. of 1.0 a.u. and used the same day.

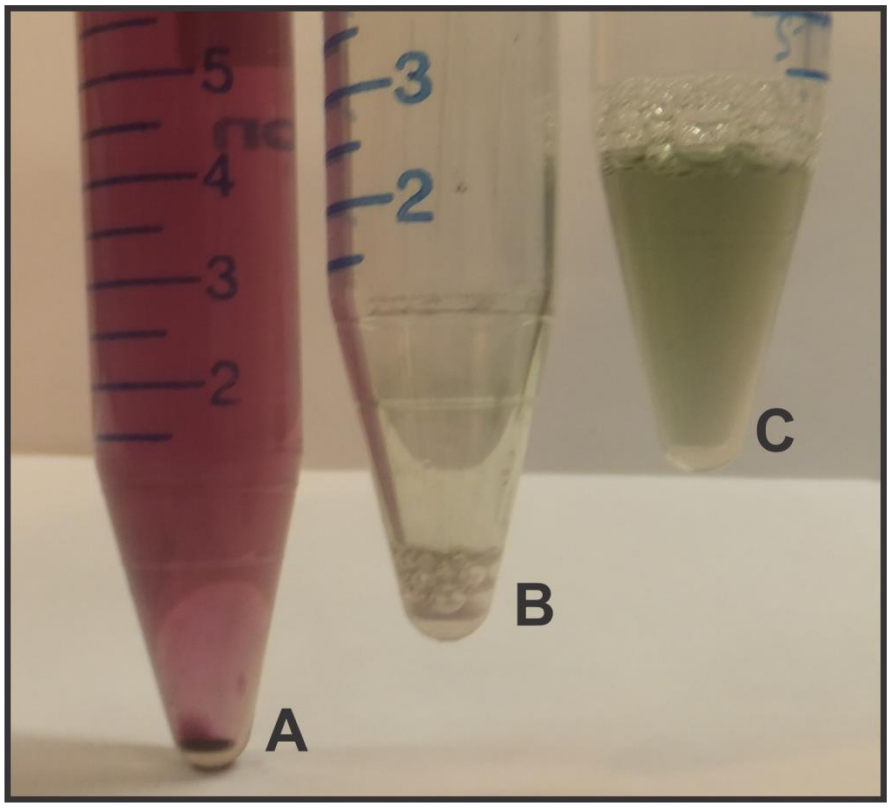

Figure 25. Photograph of Au nanoprism solutions before (A), during (B), and after (C) purification. Following centrifugation of the as-synthesized reaction mixture (A), both the supernatant and pellet are removed. The Au nanoprisms deposit on the sides of the conical tube as a thin film (B, green tinted tube), which is readily resuspended upon addition of H_2O (C).

3.2.4 Pseudo-Stellated Nanoprism Synthesis

0.5 mL of the prism stock solution ($O.D._{\lambda max}$ = 1.0 a.u.) was added to a 1.5 mL centrifuge tube and diluted with 0.5 mL of water. To this mixture, 1-20 µL of 20 mM ascorbic acid was added (for final H_2PtCl_6:ascorbic acid molar ratios ranging from 1:0.5 – 1:10), and the solution was briefly mixed by vortexing. Then, 4 µL of 10 mM H_2PtCl_6 was added, and the solution was mixed by vortexing again. After allowing one hour for completion of nanoparticle growth, the reaction mixture was purified from excess reagents by centrifugation (5 minutes at 2200 rcf using a Spectrum mini-centrifuge (SC1006-R)). After removal of the supernatant, the particles were resuspended in 1.0 mL of H_2O by brief sonication (~10 s).

3.2.5 UV-vis-NIR Spectroscopy

Colloids were measured by ultraviolet-visible-near infrared (UV-vis-NIR) spectroscopy using a Cary 5000 spectrophotometer (Agilent, Inc.). Spectra were baseline corrected with respect to the spectrum of water for optical density measurements or D_2O (Cambridge Isotope Laboratories, D +99.9%) for extinction spectra ranging from 200-1700 nm. In order to transfer nanoparticle products from water to D_2O, particles were resuspended in a 10 mM solution of CTAB in D_2O instead of water during purification.

3.2.6 Transmission Electron Microscopy

After Pt deposition, the resulting nanoparticle products were allowed to sediment out of solution as described above. The supernatant was removed, and the particles were resuspended in 50 µL of water by sonication. A 10 µL aliquot of the concentrated, purified particles was drop cast onto a Formvar-backed (Ted Pella, Formvar on 400 mesh Cu) or ultra-thin carbon (Ted Pella, Carbon Type A on 300 mesh Cu) TEM grids. One of the following microscopes was used for sample characterization: FEI Moriganai 268 at 80 kV (Microscopy and Imaging Facility, Department of Biology, University of Pittsburgh), JEOL JEM 2100 equipped with a Gatan Imaging Filter (GIF) Tridiem camera and Oxford Inca EDS detector at 200 kV (Nanoscale Fabrication and Characterization Facility, Peterson Institute of Nanoscience and Engineering, University of Pittsburgh), FEI Titan G2 80-300 TEM/STEM at 300 kV equipped with a GIF Tridiem camera and with third order spectrometer aberration correctors (Electron Microscopy Facility, Department of Materials Science and Engineering, Carnegie Mellon University). Scanning transmission electron microscopy characterization was performed using the JEOL JEM-2100F, or the FEI Titan G2 80-300.

3.2.7 Selected Area Electron Diffraction (SAED) Measurements

SAED images were obtained using the FEI Titan G2 80-300 TEM/STEM and analyzed using Digital Micrograph v2.10.1282.0 (Gatan, Inc.) and/or ImageJ v 1.47d (National Institutes of Health, USA) software. The angles between spots and the distances from the spots to the center point were measured to determine the orientation of the crystal lattice. Standard face-centered cubic (FCC) diffraction patterns were used to index the spots.

3.2.8 Scanning Electron Microscopy

Silicon wafer substrates (University Wafer, p-doped), 200 nm thermal oxide (SiO_2) were first cleaned by sonication in ethanol for 5 minutes. The substrate was then rinsed with ethanol and dried under air. Nanoparticle products were concentrated and purified as described for TEM analysis. A 10 µL aliquot of the resulting solution was then drop cast onto the silicon wafer substrate and allowed to dry. Samples were imaged using a Raith Dual Beam Electron Beam Lithography-SEM at 20 kV (Nanoscale Fabrication and Characterization Facility, Peterson Institute of Nanoscience and Engineering, University of Pittsburgh).

3.2.9 Measuring pH of H_2PtCl_6 Hydrolysis

To study H_2PtCl_6 hydrolysis, 125 µL of 0.2 M H_2PtCl_6 was mixed with 20 - 500 µL of 0.1 M NaOH. After the resulting solution was diluted to a total volume of 2.5 mL, the pH of the solution was measured using a 8172BNWP Ross Sure-Flow Combination electrode (Thermo Scientific), and Orion 3 Star pH Benchtop meter, calibrated with buffered solutions at pH 4, 7, and 10 (Fischer Scientific).

3.2.10 ^{195}Pt NMR Chemical Shift Referencing

In order to assign ^{195}Pt NMR chemical shifts, the resonances must be referenced first to a species of known chemical shift using an external reference ($[PtCl_6]^{2-}$). Chemical shift referencing is performed by setting a species with a well-established Larmor frequency to its corresponding chemical shift on the ppm scale. This procedure can be done with an internal or external

reference. In traditional ^{1}H NMR in organic solvent, chemical shifts are referenced to an internal standard of tetramethylsilane (TMS). This is done by adding a small amount of TMS to the sample solution itself, measuring the NMR spectrum, and setting the chemical shift of TMS to 0 ppm. On the other hand, external chemical shift referencing is often performed in solid state NMR techniques, where additional chemical species cannot be added directly to a sample, or in cases of solution state NMR where the standard reference solution is not chemically inert and/or the chemical shift interferes with chemical shifts of the species of interest. When using external referencing, the NMR spectrum of the chemical shift standard is measured and set to the correct frequency on the ppm scale. The sample is then removed from the magnet and the NMR spectrum of the sample of interest is measured, taking care to maintain temperature and alter the shimming parameters as little as possible.

Here we use the $[PtCl_6]^{2-}$ resonance of 0.10 M H_2PtCl_6 set to 0 ppm as an external standard chemical shift reference for all ^{195}Pt NMR experiments. Pt speciation in aqueous solution is known to be dependent upon time, temperature, light exposure, pH, and Pt ion concentration. For these reasons, an external referencing procedure was used because even if a coaxial NMR tube is used (with one tube containing the chemical shift reference, and one containing the sample of interest, physically separating the two chemicals and eliminating the influence of Pt concentration on speciation) it is the H_2PtCl_6 speciation itself that we are interested in and overlapping chemical shifts of the reference solution would obscure the quantification of each species in solution. Therefore, a reference spectrum of 0.1 M H_2PtCl_6 was acquired immediately before analysis of the hydrolyzed products at 10 mM concentration and various pH.

Due to slight deviations in magnetic field, shimming parameters, and/or slight fluctuations in temperature over the duration of the experiments, the chemical shift of $[PtCl_6]^{2-}$ in the samples at

various pH ranged from 0.04 to 0.57 ppm compared to the external chemical shift reference of 0.1 M H_2PtCl_6 at 0 ppm. These deviations are reasonable, and likely not indicative of a new or different chemical species when one considers that ^{195}Pt NMR chemical shifts are extremely sensitive to changes in electronic environment (*e.g.* changing from cis to trans arrangement of identical ligands on a Pt center typically results in chemical shift changes of 20 ppm or more), with a total chemical shift range of ~13,000 ppm.

3.2.11 Pt Speciation Identification by ^{195}Pt NMR spectroscopy

High resolution solution phase ^{195}Pt NMR spectra of 10 mM H_2PtCl_6 titrated with various amounts of NaOH were acquired on a Bruker 600 Ultrashield™ magnet (14.1 T) with AVANCE III 600 Console equipped with a BVT3000 temperature control unit. Single pulse spectra were recorded on a 5 mm broadband observe probe tuned to the Larmor frequency of ^{195}Pt (~129 MHz) with a deuterium lock (samples were measured in 90% H_2O, 10% D_2O). ^{195}Pt NMR chemical shifts were referenced with respect to 0.1 M H_2PtCl_6 in 10% D_2O at 0 ppm. Temperature was held at 298 K throughout the experiment and no ^{1}H decoupling was applied to minimize temperature-induced chemical shift changes. Typical 90° pulse lengths for ^{195}Pt were ~10 µs. A sweep width of 200 000 Hz was used, due to the large chemical shift range of ^{195}Pt. At least 20480 transients were acquired with 16384 data points and a recycle delay of 0.5 s. Fourier-transformation was performed with a line broadening factor of 2 Hz for chemical shift assignment.

3.2.12 $[PtCl_5L]^{n-}$ and $[PtCl_4L_2]^{n-}$ Complex Assignment (L = H_2O or OH^-, and n = 0, 1, or 2)

For the mono-substituted complexes $[PtCl_5(H_2O)]^-$ and $[PtCl_5(OH)]^{2-}$, only one signal is observed in the ^{195}Pt NMR spectra due to fast chemical exchange on the NMR time scale. Here, the signal position in ppm reflects the population-weighted average of $[PtCl_5(H_2O)]^-$ and $[PtCl_5(OH)]^{2-}$ chemical shifts (δ), according to the following equation:

$$\delta_{observed} = x\delta_{[PtCl_5(H_2O)]^-} + (1-x)\delta_{[PtCl_5(OH)]^{2-}}$$

Where $\delta_{observed}$ is the observed chemical shift of the mono-substituted species, x is the molar ratio of $[PtCl_5(H_2O)]^-$ in solution, $\delta[PtCl_5(H_2O)]^-$ is the chemical shift for $[PtCl_5(H_2O)]^-$ (at 10 mM, $\delta[PtCl_5(H_2O)]^-$ = 501 ppm), and $\delta[PtCl_5(OH)]^{2-}$ is the chemical shift for $[PtCl_5(OH)]^{2-}$ (at 10 mM, $\delta[PtCl_5(OH)]^{2-}$ = 660 ppm). A similar trend is observed for the di-substituted complexes $[PtCl_4(H_2O)_2]$ and $[PtCl_4(H_2O)(OH)]^-$, except at intermediate pH ranges (pH ~3 in this study), where separate signals are resolved presumably due to a slower rate of exchange on the NMR time scale. As reported by Didillion *et al.*,[148] at a pH range from approximately 3 to 7, hydrogen bonding between OH^- and H_2O ligands in the *cis*-$[PtCl_4(H_2O)(OH)]^-$ isomer slows the rate of proton exchange leading to two chemically distinguished signals for the di-substituted complexes. The relative population of each species in solution was calculated from the ^{195}Pt NMR signal integration and is reported in Table S1. Interestingly, at pH = 5.2 and above, no di-substituted complexes ($[PtCl_4L_2]^{n-}$) were observed. The lack of di-substituted complexes at high pH may be because 1) di-substituted species are not present in solution, 2) the di-substituted complexes are present at low concentrations that are below the detection limit in the time course of the NMR experiment, or 3) the di-substituted species (like the mono-substituted species) are also in the fast exchange regime and experience line-broadening, and subsequent lower signal-to-

noise, due to this exchange rendering the peaks unobservable in the time of the NMR experiment (although this third option seems unlikely given the hydrogen bonding descriptions above).

3.2.13 AUT and PEGSH Functionalized Nanoprism Substrates

To functionalize the CTAB-coated Au nanoprisms with PEGSH, 0.5 µL of 1 mM PEGSH was added to 1.0 mL of the purified Au nanoprism stock solution (O.D. = 1.0 a.u. at λ_{max} (approx. 1260 nm), see above) in a 1.5 mL centrifuge tube and mixed at 800 RPM (Eppendorf, Thermomixer® R mixer-incubator with 1.5 mL block) for 12 hours at room temperature. After functionalization with PEGSH, the Au nanoprisms were purified three times by centrifugation (5 minutes at 2200 rcf) and resuspended in 1.0 mL of H_2O. AUT-functionalized prisms were prepared using the same protocol, except here 2.0 µL of 2 mM AUT was added in place of the 0.5 µL of 1.0 mM PEGSH. Deposition of Pt was performed as described in the above section for deposition on CTAB-functionalized substrates.

3.2.14 Prism Ligand Characterization by ^{1}H NMR Spectroscopy

AUT, PEGSH, and CTAB functionalized prisms were purified from excess ligand by centrifugation using three successive rounds of centrifugation for 5 minutes at 2200 rcf and resuspended in water (to a concentration of OD = 1.0 a.u. at λ_{max} (approx. 1260 nm)). 6.0 mL of the purified prisms were concentrated by centrifugation (5 minutes at 2200 rcf using a Spectrum mini-centrifuge (SC1006-R)) and were resuspended to a final volume of 1.0 mL. The concentrated prisms were then dissolved by addition of 50 µL of concentrated aqua regia by heating at 37°C for 24 hours. Full dissolution of the prisms was monitored by UV-vis-NIR

spectroscopy. After dissolution, the prisms (with the small amount of aqua regia) were resuspended in 1.0 mL of D_2O, and analyzed by ^1H NMR spectroscopy. ^1H NMR spectra were collected on a Bruker 600 Ultrashield™ magnet (14.1 T) with AVANCE III 600 Console, using a WATERGATE W5 water suppression pulse train.[149] At least 2048 scans were recorded per sample, with a recycle delay of 5 s.

3.2.15 X-ray Photoelectron Spectroscopy

Silicon wafer substrates were prepared (*vide supra*), and 10 µL of purified Au nanoprisms functionalized with CTAB, AUT, or PEGSH in isopropanol were dropcast onto a 1x1 cm silicon wafer and allowed to dry. XPS spectra were obtained using an ESCALAB 250XI XPS with a monochromated, micro-focused Al Kα X-ray source (spot size = 200 µm; pass energy = 50 eV. Spectra were charge referenced to adventitious carbon (284.8 eV).[150]

3.3 RESULTS AND DISCUSSION

We use a combination of ^{195}Pt NMR and electron microscopy techniques to study the deposition of Pt on substrates. These studies demonstrate the critical role of initial Pt(IV) speciation in final NP outcomes. We then use insights gained from these studies to induce a controllable transition from surface chemistry to redox-mediated growth pathways which yields a suite of alloyed and multicomponent Au-Pt NPs. In a typical reaction, Au nanoprism substrates (edge length = 150 ± 25 nm, thickness = 8 ± 2 nm) were synthesized using literature protocols.[151] Nanoprisms were purified from excess reagents and NP impurities via centrifugation (see Supporting Information

(SI) for full synthesis details). Reduction of aqueous H_2PtCl_6 (CPA) with ascorbic acid (AA) in the presence of purified Au nanoprisms (but in the absence of added surfactants or other reagents) led to heterogeneous nucleation of nanoparticle islands arranged linearly across the Au prism surface (diameter, $d = 3.5 \pm 0.4$ nm; Figure 26).

The morphology, crystal structure and composition of the resulting particles were analyzed using electron microscopy techniques. High-resolution transmission electron microscopy (HRTEM) and selected area electron diffraction (SAED) images indicate that the islands are in epitaxial contact with the underlying prism substrate. This observation is important to understanding the deposition mechanism. Epitaxial growth indicates that the islands form from the particle substrate via a heterogeneous nucleation process as opposed to homogeneous nucleation and subsequent deposition onto the NP. These observations are also consistent with our time-dependent observations of the island growth pathway (*vide infra*, Figure 27 and Figure 28). At 2 minutes of growth, deposition is primarily confined to the edges of the Au nanoprism. While there is a low density of growth on the broad faces of the Au nanoprism, Pt nanoparticles present on these surfaces already exhibit a seemingly linear arrangement. As the reaction time increases, the density of growth on the broad faces of the Au nanoprism increases, and the linear arrangement becomes more apparent. By UV-vis-NIR spectroscopy, growth appears to be largely complete after 8 minutes of reaction time, however Pt island growth continues for an additional 30 minutes to 1h, corresponding to full prism surface coverage by Pt islands as shown in Figure 26.

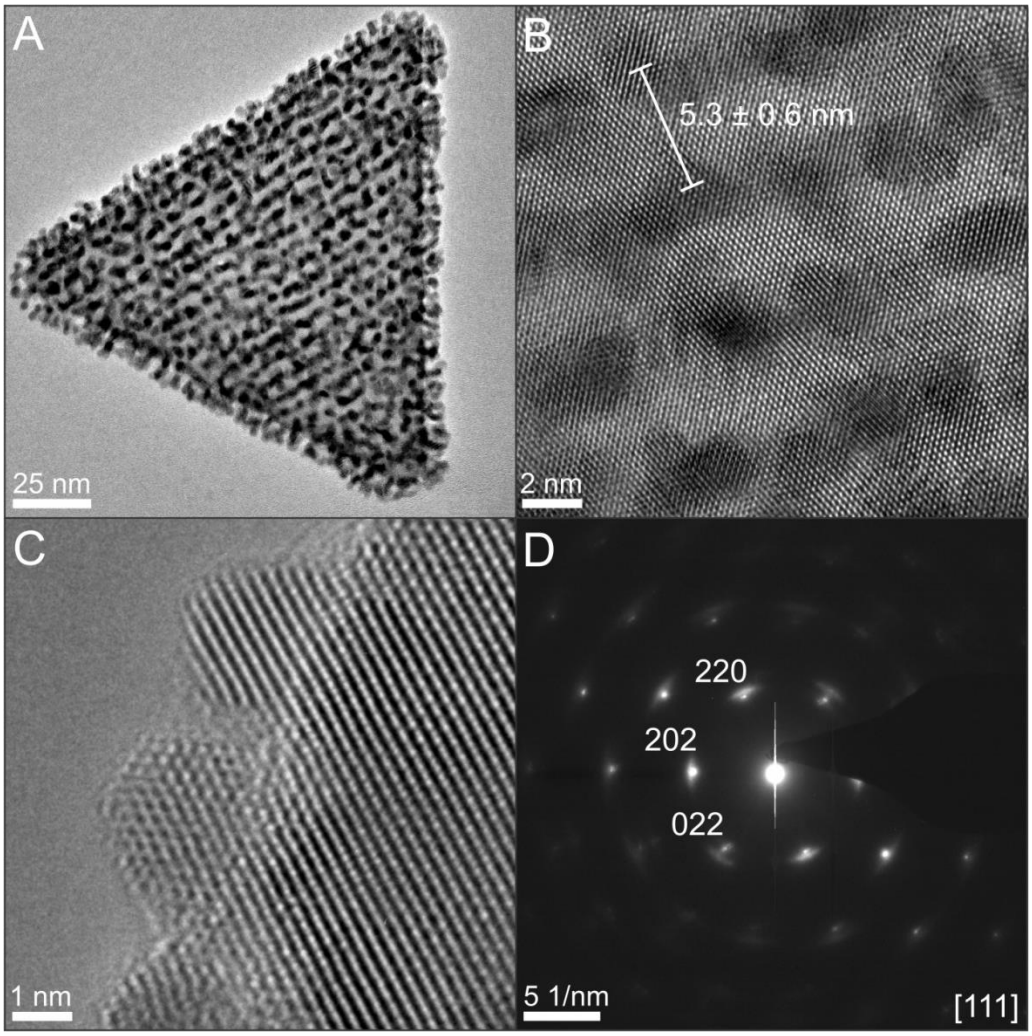

Figure 26. HRTEM images of Pt island-functionalized Au nanoprism (A), regular spacing between Pt island rows (B), and pendant Pt NPs (C). SAED pattern (D) indicates epitaxial alignment between Pt and Au components.

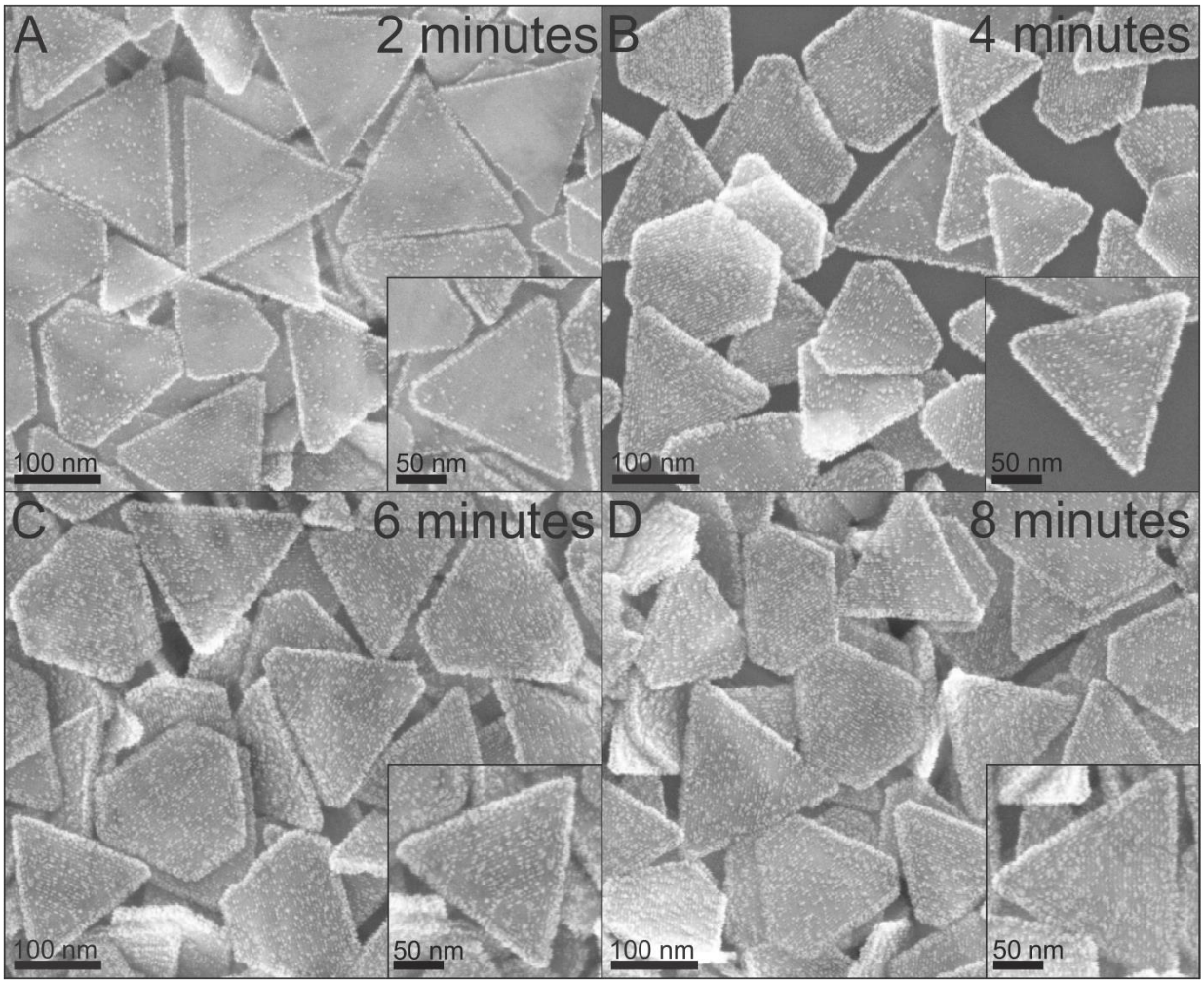

Figure 27. SEM images of pseudo-stellated nanoprisms indicating the extent of secondary metal deposition at 2 minutes (A), 4 minutes (B), 6 minutes (C), and 8 minutes (D) after addition of H_2PtCl_6 to the reaction solution, with higher magnification image inserts (lower right of each panel).

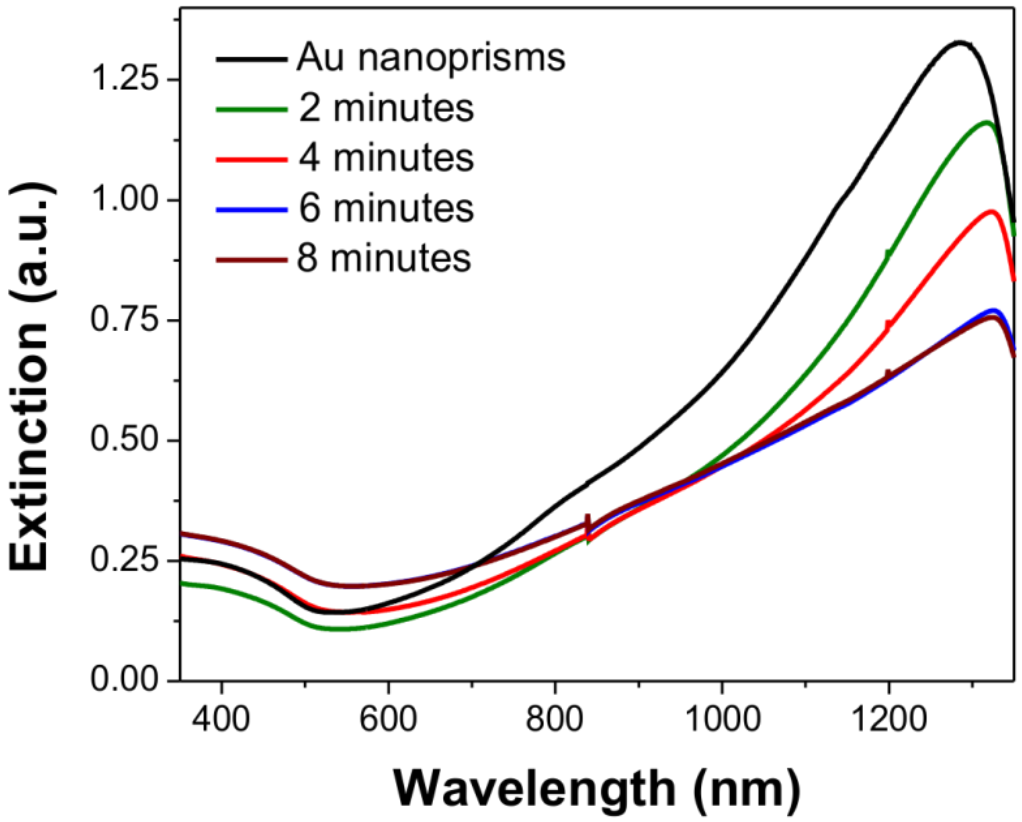

Figure 28. UV-vis-NIR spectra corresponding to the SEM images in Figure 27. As the extent of secondary metal deposition increases, the optical properties of the Au nanoprism become increasingly damped (as indicated by the broadening and decrease in intensity of the in-plane dipole LSPR). UV-Vis-NIR spectra were recorded every two minutes after addition of H_2PtCl_6 to the reaction mixture (N. B. cut off at 1350 nm is due to the interfering absorption of water).

The optical features of the resulting particle products were analyzed by UV-vis-NIR absorption spectroscopy and compared with the optical properties of pure Au nanoprisms. After Pt deposition, the localized surface plasmon resonance (LSPR) of the nanoprisms (in-plane dipole, λ_{max} ≈1260 nm) broadens and exhibits a hypsochromic shift that ranges from 10 to 150 nm, depending on the amount of Pt deposited (Figure 29). These optical features are consistent with damping of the Au LSPR.[152] Extent of LSPR damping is found to correlate with the density of islands on the nanoprism surface where increased density leads to decreased LSPR intensity and increased spectral breadth. Island density was controlled using classic NP synthesis strategies where keeping the metal ion to reducing agent ratio constant, we increase the total amount of metal ion and reducing agent used in the synthesis, leading to a larger quantity of similarly sized particles (this result can also be achieved by keeping the total amount of metal ion and reducing agent constant, and decreasing the amount of nanoprism seeds). Island growth was found to occur relatively rapidly, beginning with formation on the nanoprism side facets, and reaching complete coverage of the broad triangular faces approximately 1 hour after synthesis (Figure 27 and Figure 28).

The composition of the resulting particles was analyzed by scanning transmission electron microscopy-energy dispersive X-ray spectroscopy (STEM-EDS). Here, composition is reported as the intensity of the M edges of Au and Pt from a line scan obtained along the altitude of the triangle (Figure 30). The average distance between element peaks in the line scan correlates well with the analysis of island spacing from both SEM and bright field TEM images (5.4 ± 1.8 nm and 5.6 ± 1.8 nm for the Au-M and Pt-M edges, respectively). Interestingly, the Au and Pt signals rise coincidently, as opposed to a constant Au signal, expected from the flat top facet of the nanoprism substrate.[153-154] This modulation in both Au and Pt intensity is consistent with the

formation of island structures, where changes in thickness of the material interacting with the beam path combined with the similar edge energies of Au and Pt create a co-incidence in signal intensity and obscure quantitative comparison. Using additional STEM-EDS analysis of Pt islands pendant on the nanoprism side facets (Figure 31) we find that the islands are composed primarily of Pt, indicating little to no metal mixing between the Au substrate and the attached Pt NPs. Both the formation of these Pt islands (as opposed to the observation of oxidation or core-shell products) as well as a low degree of metal mixing are both consistent with observations in bulk and thin film Au-Pt systems.[36,155] Interestingly, many studies of Pt deposition on Au substrates show this VW type (i.e. island) growth, and Pt deposition on NP substrates has been observed to form related "dendritic" structures.[71,152]

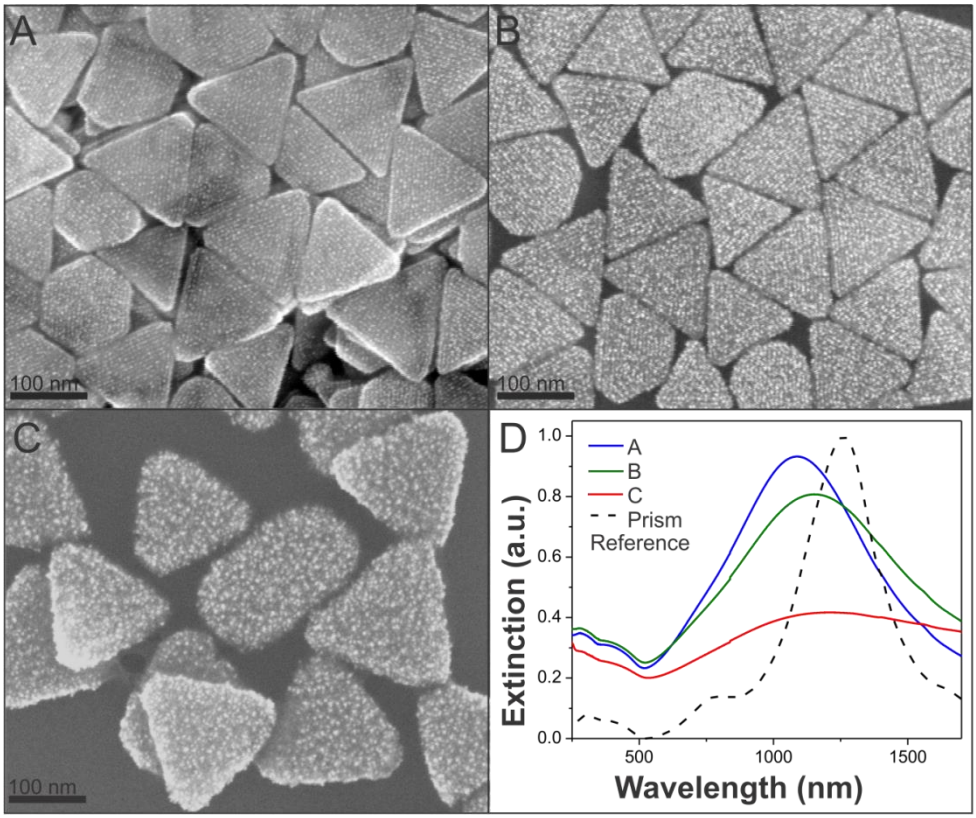

Figure 29. SEM of pseudo-stellated nanoprisms synthesized with 2 (A), 4 (B) and 6 µL (C) of 10 mM H_2PtCl_6 at an H_2PtCl_6:ascorbic acid molar ratio of 1:10. For conditions promoting an extended duration of island nucleation and growth, the island density increases, and increased damping of the nanoprism substrate LSPR is observed. Average nanoparticle radius was found to stay relatively constant (3.5 ± 0.4 nm) for all observed densities of island growth. As measured by UV-Vis-NIR spectroscopy (D), platinum deposition can dampen the optical features of the gold nanoprism substrate by ~5-60% for the lowest (A) and highest island densities (C), respectively.

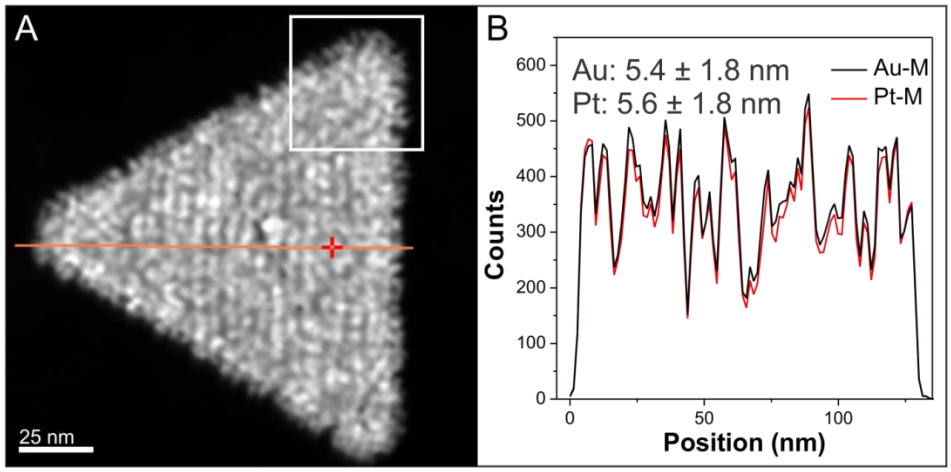

Figure 30. High angle annular dark field (HAADF)-STEM (A) and STEM-EDS line scan (B) of Au and Pt M edge intensity as a function of position (corresponds to orange line in (A)).

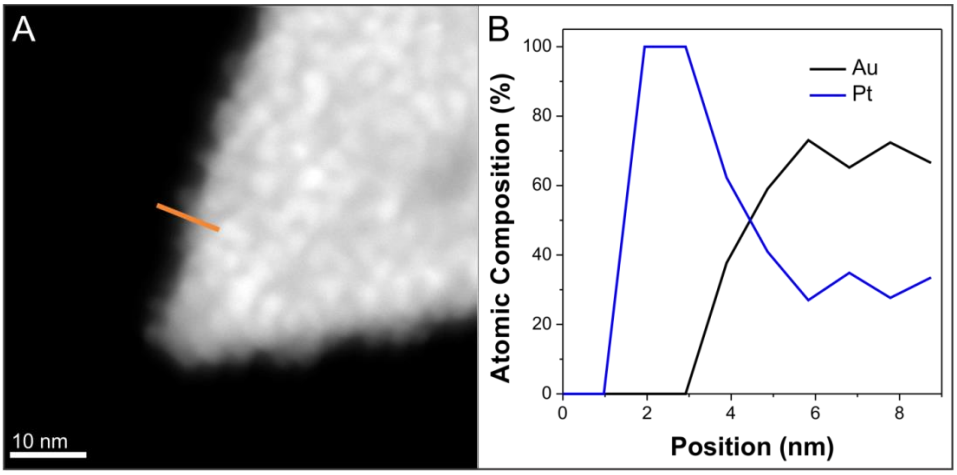

Figure 31. STEM-HAADF image (A) and corresponding EDS data (B) demonstrating the elemental composition of islands extending from side facets of the Au nanoprism. The atomic composition is measured across the position indicated by the orange line and suggests that the islands are comprised of primarily Pt.

With initial particle characterization in hand, we investigate two key aspects of the resulting particle morphology, (1) the observation of Pt deposition onto the nanoprism substrate and (2) the linear arrangement of the resulting islands. The first point is important because it may help to distinguish synthetic factors influencing Pt reduction pathways that are known to result in both deposition onto Au NP substrates (either in dendritic or core-shell modes) as well as to form frame-like architectures via GRR mechanisms. The second point indicates a route to creating entirely bottom-up metal NP assemblies on colloidal substrates – potentially offering remarkable synthetic control of both substrate and pendant NP features.

First, to elucidate factors influencing the reduction pathway of Pt(IV), we analyzed two synthetic parameters: Pt speciation and the ratio of Pt precursor to reducing agent. Because hydroxo substitution has been shown to increase the reduction potential of $[PtCl_6]^{2-}$ complexes,[156] differences in Pt speciation likely impact the reduction pathways of the metal ion precursor in NP syntheses (*i.e.* Pt(IV) reduction by an added reducing agent or by oxidation of the metal seed particle). In addition, as mentioned previously, the aqueous substitution of chloride ligands in CPA is well-known to be sensitive to time, temperature, light, complex concentration, and pH.[141] In order to study the influence of this speciation on NP formation, we induced Pt hydrolysis by addition of NaOH to the metal precursor solution (10 mM CPA, 4000 ppm). We used and analyzed all solutions within 2 h of preparation, and all solutions were protected from light (speciation was approximately constant over the timescale of our experimental procedures; Figure 32 and Figure 33). In aqueous solution at room temperature, the following reactions are representative of the speciation process at 10 mM CPA:

$$[PtCl_6]^{2-} + H_2O \rightleftharpoons [PtCl_5(H_2O)]^- + Cl^-$$
$$[PtCl_5(H_2O)]^- + H_2O \rightleftharpoons [PtCl_4(H_2O)_2] + Cl^-$$
$$[PtCl_5(H_2O)]^- \rightleftharpoons [PtCl_5(OH)]^{2-} + H^+$$
$$[PtCl_4(H_2O)_2] \rightleftharpoons [PtCl_4(OH)(H_2O)]^- + H^+$$

Keeping the age and concentration of the solution constant, we monitor the pH-dependent ligand substitution using ^{195}Pt NMR spectroscopy in order to use well-defined Pt precursors in subsequent synthesis steps. Pt(IV) complex populations in the absence of NaOH (solution pH = 1.8) consist of approximately 64% $[PtCl_4(H_2O)_2]$, 30% $[PtCl_6]^{2-}$, and 6% $[PtCl_5H_2O]^-$ (Figure 34 and Table 7). At pH 3.2, the relative concentration of $[PtCl_6]^{2-}$ increases from 30% to 37%. There is also a downfield shift and broadening of the peak corresponding to a mono- substituted Pt(IV) species. This peak shift indicates a mixed population of OH^- and H_2O mono-substituted species in the fast exchange regime on the NMR time scale. In the case of fast exchange (on the order of 10^{-5} s or faster), the chemical shift of the mono-substituted complex is a weighted average of the OH^- and H_2O substituted species.[143,157] Assuming that the observed chemical shift is due to this exchange process, approximately 7% of the mono-substituted species is due to OH^- coordination (using a weighted average analysis from known chemical shift values in this concentration regime of $[PtCl_5(H_2O)]^-$ = 501 ppm, $[PtCl_5(OH)]^{2-}$ = 660 ppm). Following the same analysis, at pH = 5.2, approximately 20% of the Pt species are coordinated to OH^- and the concentration of $[PtCl_6]^{2-}$ nearly doubles (37% to 70%). At pH = 8.6, populations of the Pt complexes were measured as a 1:2 ratio of $[PtCl_5(OH)]^{2-}$:$[PtCl_6]^{2-}$ (33% and 67%, respectively). Interestingly, at pH = 5.2 and above, no di-substituted complexes ($[PtCl_4L_2]$; where L = either OH^- or H_2O) were observed, and the majority of mono-substituted complexes contained a OH^- ligand, consistent with what may be expected from rising concentrations of OH^- and also in agreement with literature precedent.[141,143]

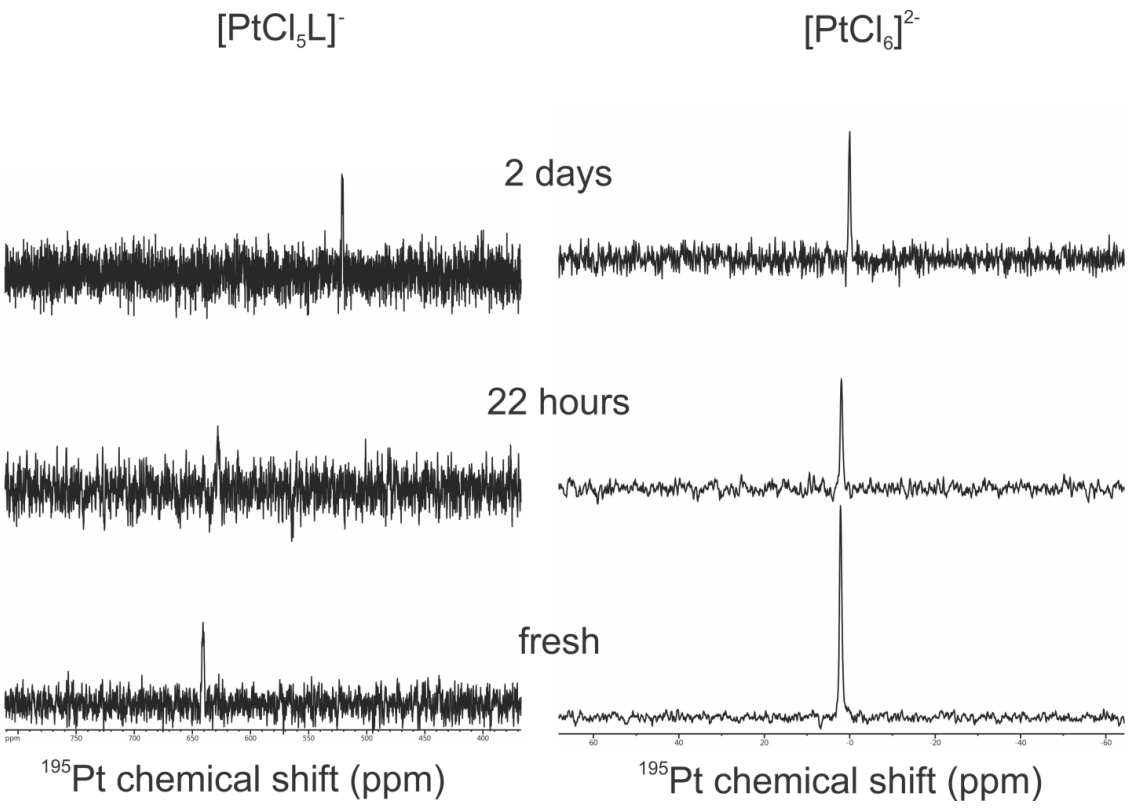

Figure 32. ^{195}Pt NMR spectra depicting the change in speciation of an aqueous solution of 10 mM H_2PtCl_6 (initial pH 8.6) aged over the course of 48 hours. For the mono-substituted complex $[PtCl_5L]^{n-}$ (left, here observed as a concentration weighted average of the $[PtCl_5(H_2O)]^-$ and $[PtCl_5(OH)]^{2-}$, *vide supra*), no significant changes in speciation were observed after 22 hours of aging (Figure 33). After two days of aging, a large shift (~100 ppm) towards lower ppm values was observed, indicating decreased hydroxo substitution and formation of $[PtCl_5(H_2O)]^-$. This time-dependent change in speciation was found to be consistent with previous literature results.[158]

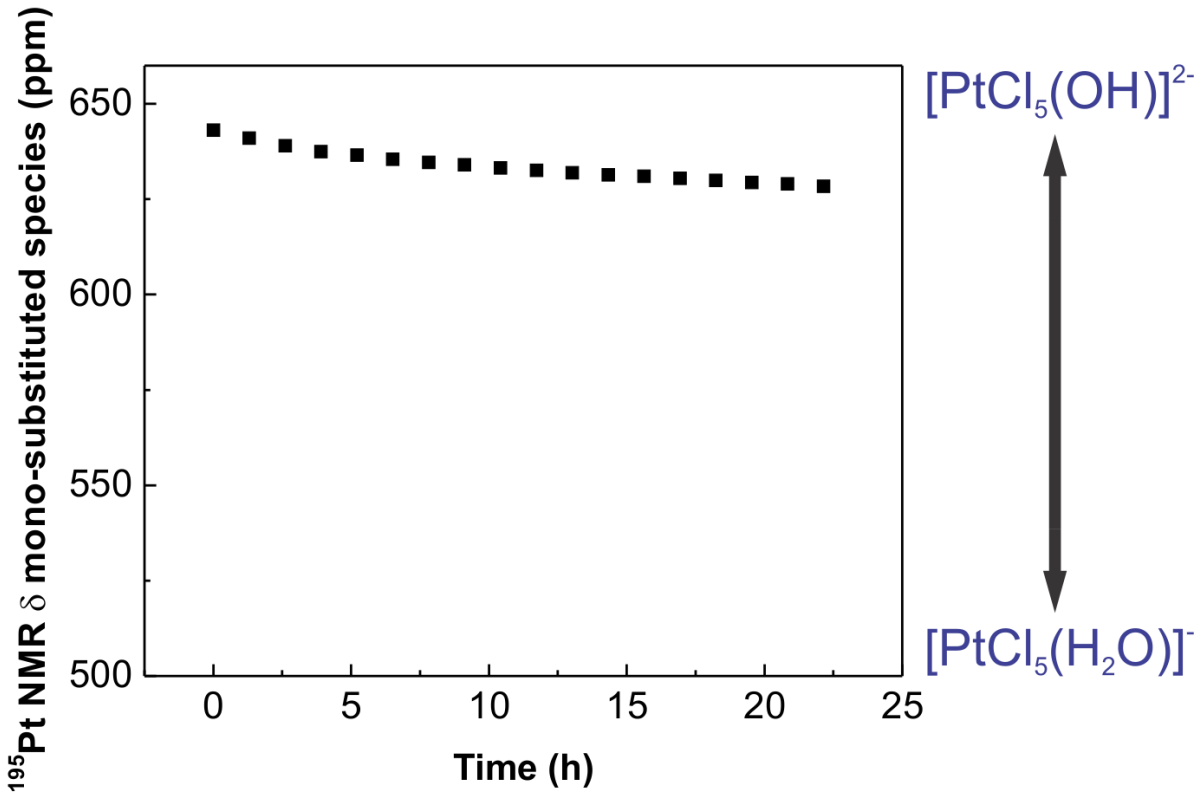

Figure 33. Change in the chemical shift (δ, ppm) of the mono-substituted $[PtCl_5L]^{n-}$ complex as a function of time, featuring a more in-depth analysis of the initial changes in $[PtCl_5L]^{n-}$ speciation over the duration of 22 hours (Figure 32). After the aging period, only a slight shift (~15 ppm) was observed in the peak position of the mono-substituted species (for comparison, a 18 ppm shift is observed for the *cis*- and *trans*- isomers of $[PtCl_4(OH)_2]^{2-}$).[158]

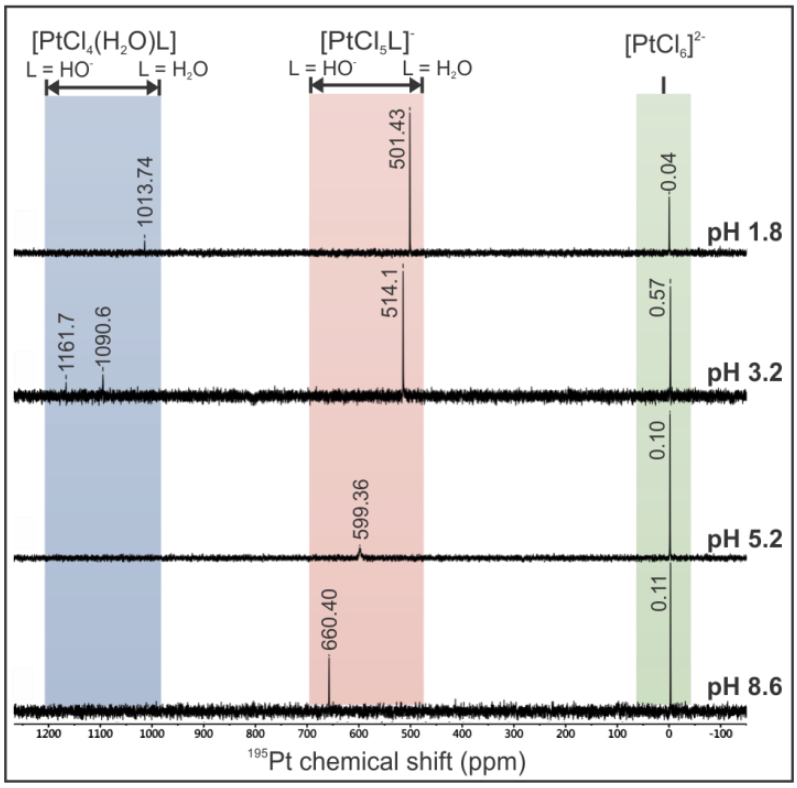

Figure 34. ^{195}Pt NMR analysis of CPA speciation as a function of pH. The mono-substituted (pink) and di-substituted complexes (blue) peak position reflects the weighted average of H_2O and OH^- substituted species.

Table 7. Relative population (%) of Pt species for a given pH.

Species	% Population pH 1.8	% Population pH 3.2	% Population pH 5.2	% Population pH 8.6
$[PtCl_6]^{2-}$	30	37	70	67
$[PtCl_5(H_2O)]^-$	64	44	11	0
$[PtCl_5(OH)]^{2-}$	0	4	19	33
$[PtCl_4(H_2O)_2]$	6	12	0	0
$[PtCl_4(H_2O)(OH)]^-$	0	3	0	0

Using these data, the pH of Pt precursor solutions can be correlated with Pt(IV) speciation and ultimately correlated to different NP outcomes (Figure 35). When the pH of Pt(IV) precursor solution is low, reduction of the metal cation occurs primarily via AA oxidation, as evidenced by lack of oxidation in the nanoprism substrate. As pH increases, the concentration of $[PtCl_5(OH)]^{2-}$ also increases and oxidation of the Au particle begins to appear. These results are consistent with previous electrochemical studies of $[PtCl_6]^{2-}$ in water, which show that OH^- substituted complexes are more readily reduced. Our results are consistent with these findings, where GRR-like products are only observed at increased populations of $[PtCl_5(OH)]^{2-}$ (e.g. pH = 5.2 and 8.6) indicating that $[PtCl_5(OH)]^{2-}$ is a more aggressive oxidant.

We can further examine the impact of this Pt speciation, by modulating the molar ratio of Pt(IV):AA (a traditional means of controlling the extent of NP growth). When the Pt precursor pH is held constant, the particle products follow well-known NP synthesis trends. For example, as the molar ratio of metal ion to reducing agent is increased, we observe a decrease in metal deposition onto the prism substrate (i.e. moving down a column in Figure 35). Conversely, when we hold the ratio of Pt(IV):AA constant and increase only the pH of the Pt precursor solution, the impact of Pt speciation is consistent with a progression toward GRR-mediated Pt reduction (moving across a row, Figure 35). The two competing Pt reduction pathways can be most clearly observed at pH = 8.6 (also the highest observed concentration of $[PtCl_5(OH)]^{2-}$). At this pH, Pt(IV) reduction by oxidation of the nanoprism substrate competes effectively with reduction by AA at a scale that is observable across all ratios of Pt(IV):AA tested. At low ratios of Pt(IV):AA, this oxidation results in the formation of "pores" in the prism surface in addition to linear Pt island formation. At higher Pt(IV):AA ratios, mixed-metal nanoframes are formed exclusively (Figure 35, bottom right and Figure 41, STEM-EDS).

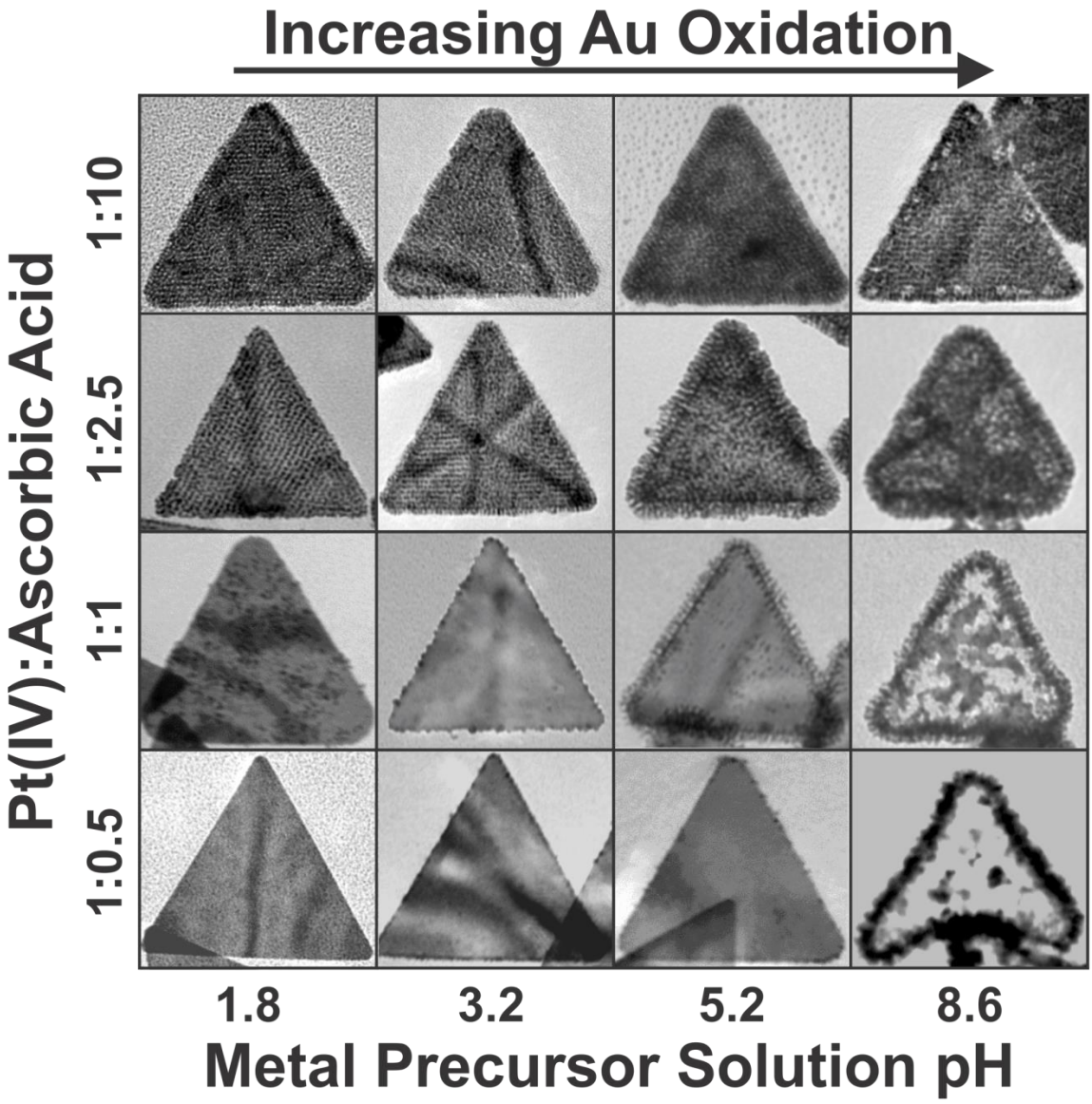

Figure 35. Comparison of nanoparticle morphologies as a function of Pt(IV):AA concentrations and metal ion precursor solution pH. See Figures 36-41 for supplementary TEM, UV-vis-NIR spectra, and STEM-EDS analysis of the nanoparticles pictured

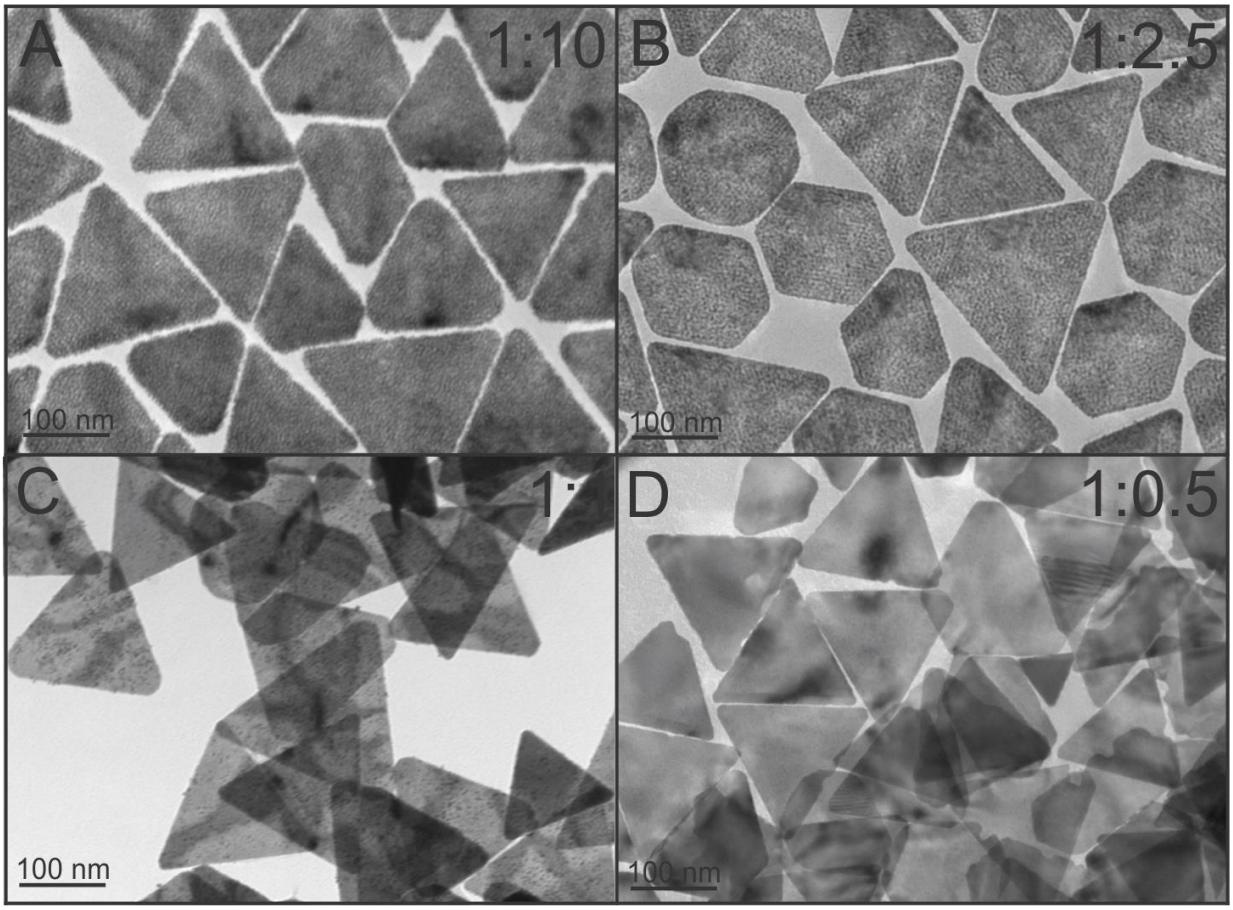

Figure 36. TEM images of pseudo-stellated prisms synthesized with H_2PtCl_6 (pH = 1.8) at H_2PtCl_6:ascorbic acid ratios of 1:10 (A), 1:2.5 (B), 1:1 (C), and 1:0.5 (D), and corresponding to column one of Figure 35. As the ratio of reducing agent to metal precursor was reduced, the extent of Pt deposition and the resulting island density decreased until Pt deposition was largely absent (D).

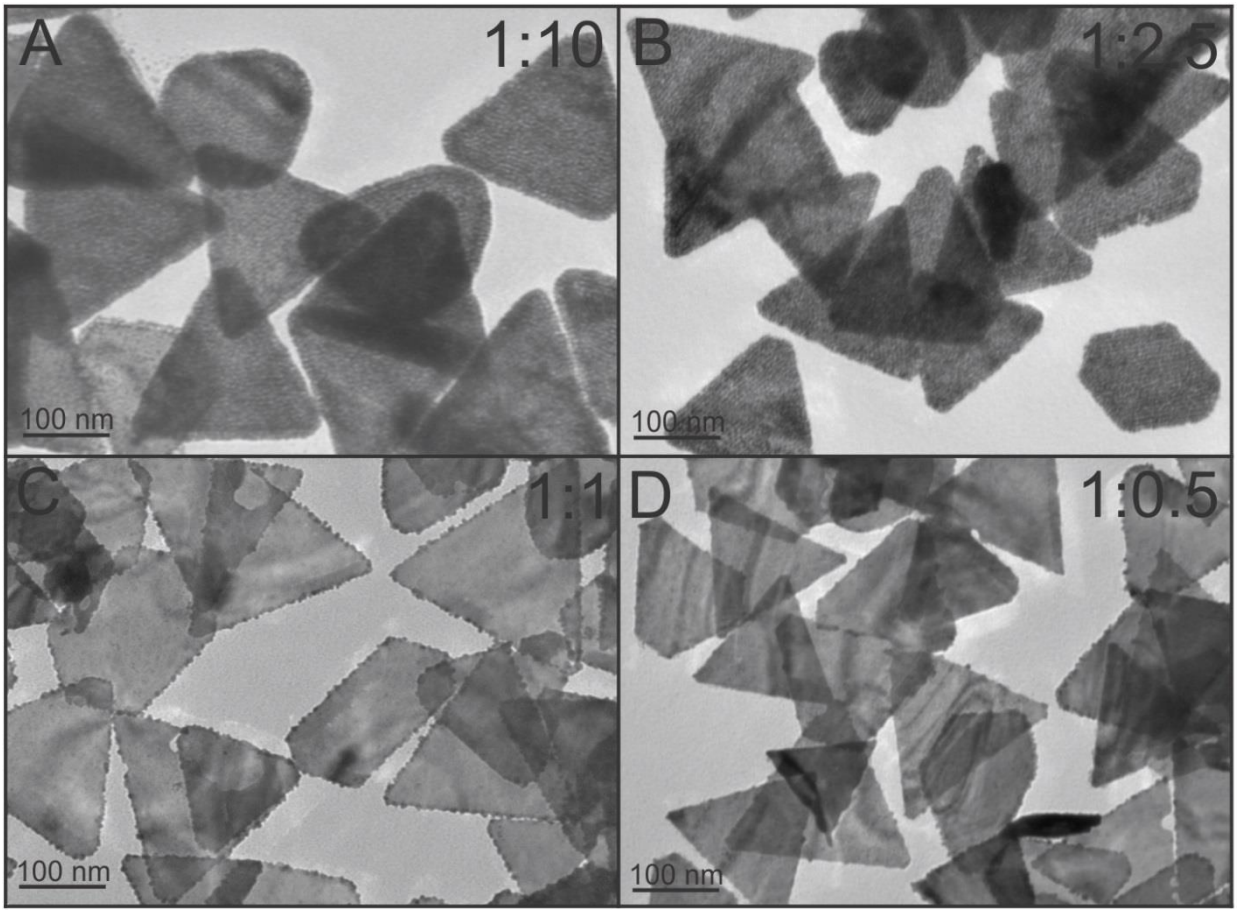

Figure 37. TEM images of pseudo-stellated prisms synthesized with H_2PtCl_6 (pH =3.2) at H_2PtCl_6:ascorbic acid ratios of 1:10 (A), 1:2.5 (B), 1:1 (C), and 1:0.5 (D), and corresponding to column 2 of Figure 35. As the ratio of reducing agent to metal precursor was reduced, a preference for deposition on the side of the prisms was observed, leading to the formation of gold nanoprisms substrates with Pt confined mostly to the Au side facets.

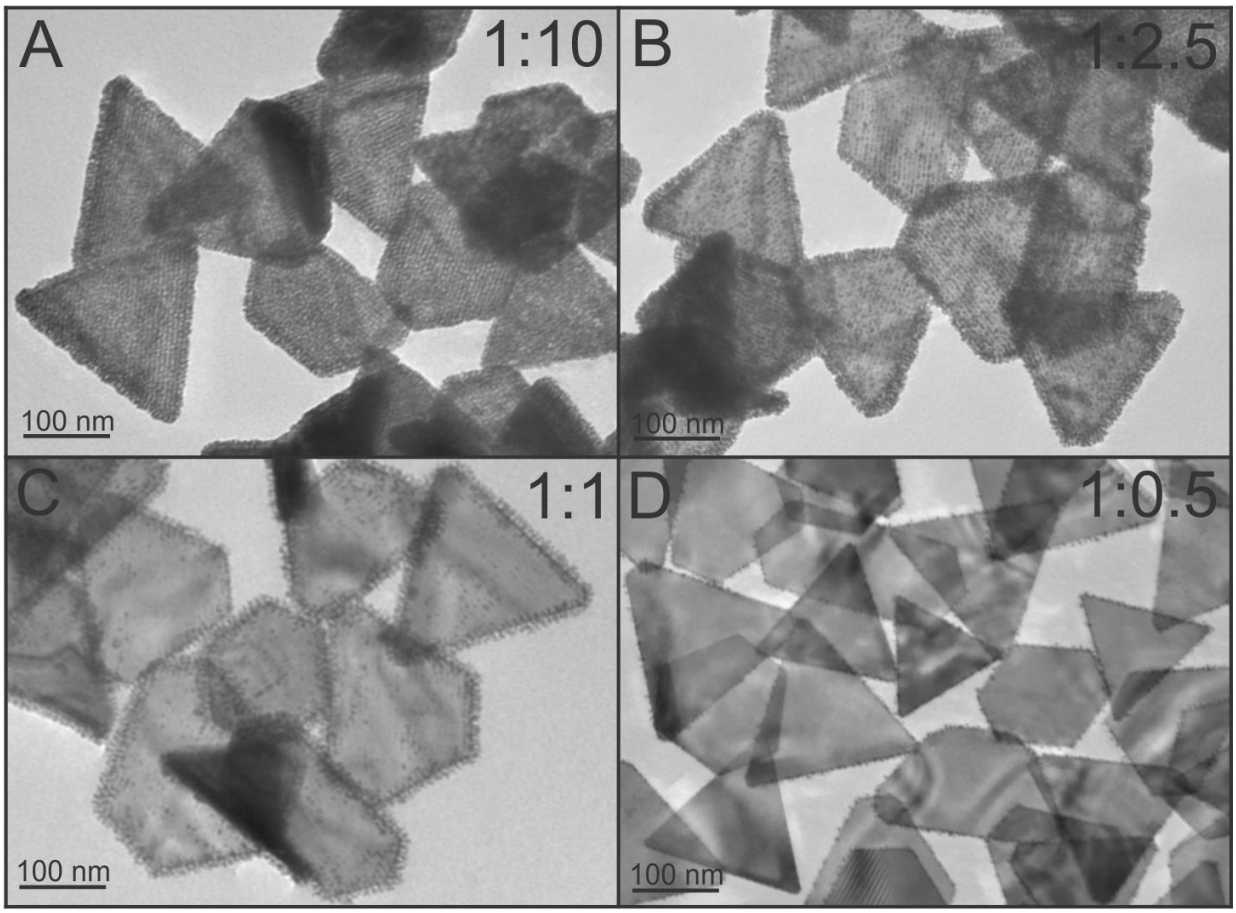

Figure 38. TEM images of pseudo-stellated prisms synthesized with H_2PtCl_6 (pH = 5.2) at H_2PtCl_6:ascorbic acid ratios of 1:10 (A), 1:2.5 (B), 1:1 (C), and 1:0.5 (D), and corresponding to column 3 of Figure 35. As the ratio of reducing agent to metal precursor was reduced, a transition from pseudo-stellated growth to side-mostly growth was observed, similar to the pH 3.2 case.

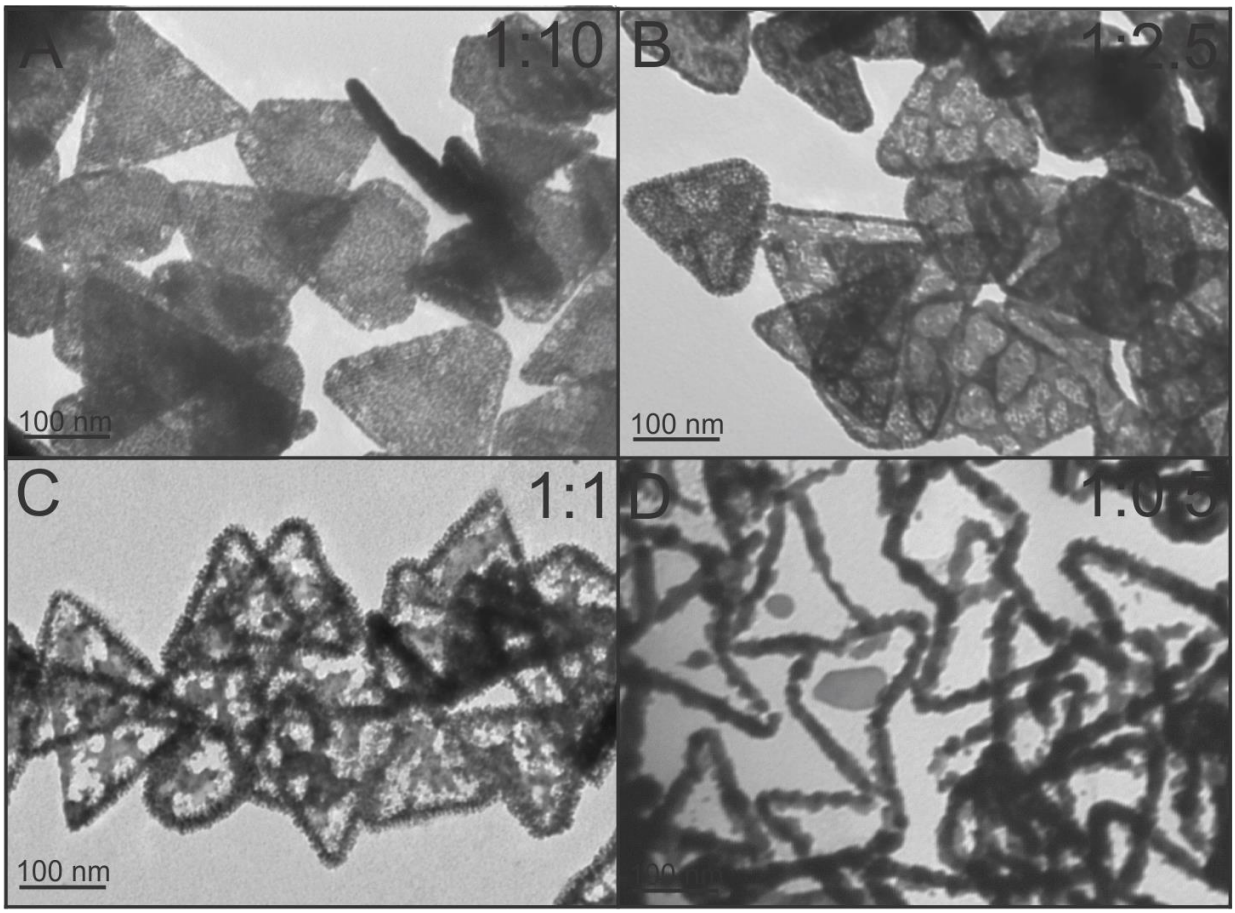

Figure 39. TEM images of pseudo-stellated prisms synthesized with H_2PtCl_6 (pH = 8.6) at H_2PtCl_6:ascorbic acid ratios of 1:10 (A), 1:2.5 (B), 1:1 (C), and 1:0.5 (D), and corresponding to column 4 of Figure 35. As the ratio of reducing agent to metal precursor was decreased, the extent of nanoprism oxidation increases, and proceeds from pore-formation in the nanoprisms substrate (but still a large extent of Pt island deposition observed) to the formation of alloyed nanoframes.

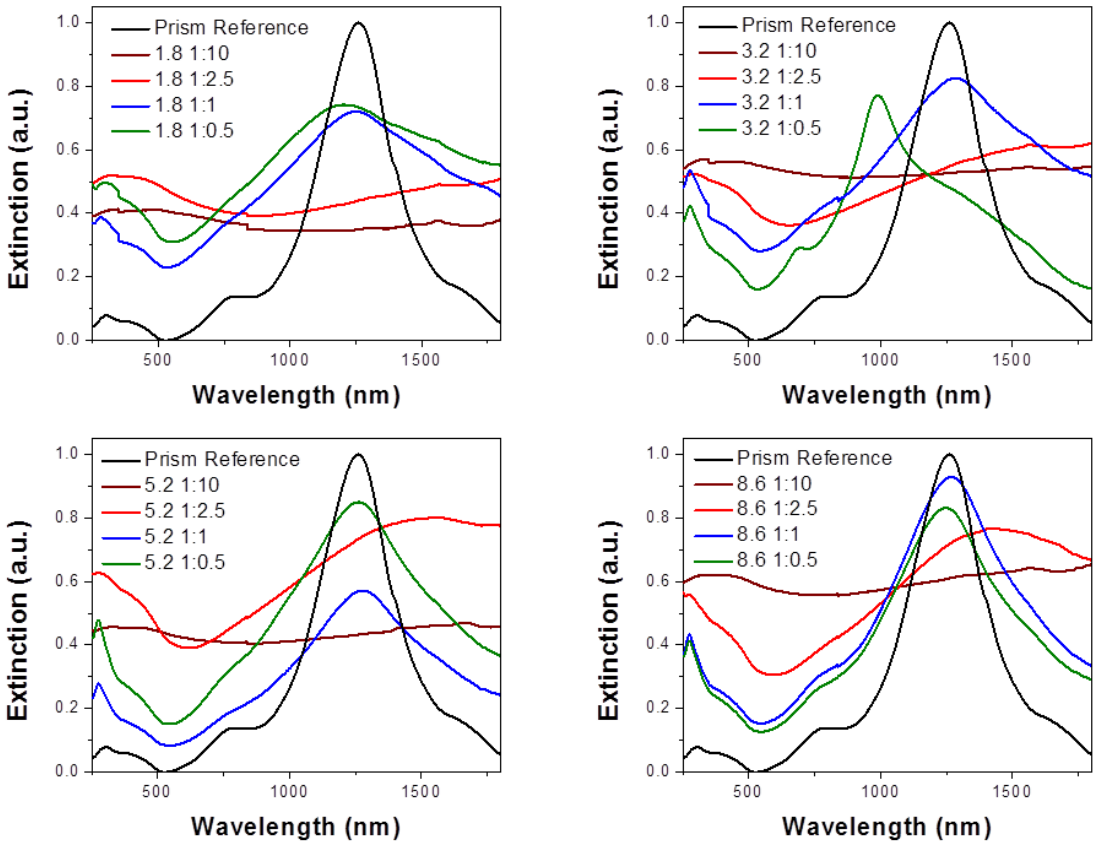

Figure 40. UV-vis-NIR spectra corresponding to prisms synthesized with H_2PtCl_6:ascorbic acid ratios of 1:10 to 1:0.5 for a given pH shown as Figure 35. As the extent of the nanoparticle growth is increased (corresponding to an increased amount of ascorbic acid), the Au nanoprism LSPR damping increases. Oxidation appears to have little effect on the optical properties of the Au nanoprism substrate (although slight changes in the position of λ_{max} were observed before/after deposition), as the nanoframes appear to retain characteristic LSPR features of the original Au nanoprism.

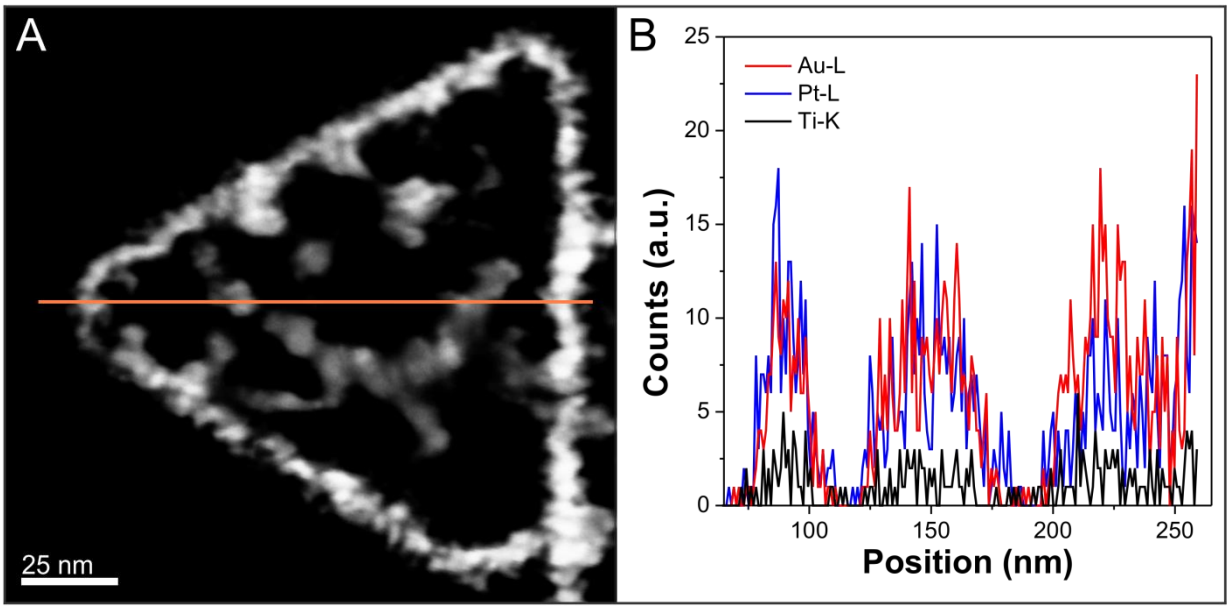

Figure 41. STEM-EDS linescan of nanoframes (A) and plot of measured edge intensity as a function of position (B). Here, the intensities of the Pt and Au L edges as compared to the measured background intensity (Ti-K edge) indicate that the nanoframes are comprised of both gold and platinum.

Insight into the role of Pt precursor speciation on Pt reduction pathways facilitated the study of a second key aspect of the syntheses: the formation of Pt islands in regular linear arrays. Conducting time-dependent formation studies, it was found that Pt islands form in linear paths during their initial growth, where new islands appear to "fill-in" lines across the prism surface (Figure 27). For these "pseudo-stellated" nanoprisms, Pt island rows are arranged with respect to either a single base of the triangular prism (~70% of NPs) or organized with respect to all three bases of the nanoprisms (~30% of NPs, Figure 42). In these "three-base" cases, each row appears to move inward towards the center of the prism, forming a pattern of concentric triangles of decreasing size. In all cases, row separation distances are 5.4 ± 0.7 nm, which is too large to result from the underlying crystal structure of the nanoprism (a_{Au} = 4.079 Å). Further, the broad faces of the nanoprism approach atomically flat, and so this growth pattern is also unlikely to be associated with surface step-edges or other defects.[153-154] Therefore, we hypothesized that the linear arrangement of Pt NP islands results from a supramolecular architecture formed by the organic ligand adsorbates (here, cetyltrimethylammonium bromide, CTAB) on the nanoprism surface, which may act as a "template" for the observed linear growth pattern.[159,33]

We tested this hypothesis by changing the ligands adsorbed to the Au nanoprism surface prior to Pt deposition. For the synthesis of pseudo-stellated nanoprisms, nanoprism seeds are purified from excess CTAB and other reagents via extensive washing using centrifugation. The final nanoprisms are then suspended in pure water and used in subsequent Pt addition reactions. Here, we exchanged this CTAB coating for two different ligands: 11-amino-1-undecanethiol (AUT) which is a small molecule that should form a relatively dense ligand layer and poly(ethylene glycol) methyl ether thiol (PEGSH, M_n = 900 Da) which forms a random coil in solution and should produce a less dense ligand shell. After purification from excess thiolated

ligands, exchange was confirmed by ^{1}H NMR and X-ray photoelectron spectroscopy (XPS) measurements (Figure 43-Figure **45**). Both AUT and PEGSH-coated Au nanoprisms exhibited markedly different secondary metal deposition patterns than those observed for the CTAB-functionalized nanoprisms. For both AUT and PEGSH functionalized nanoprisms, Pt deposition was primarily observed on the sides of the particles (where one may expect some defects in molecular ligand coatings) and with no regular deposition morphologies (Figure 46). It is important to note that there is no added CTAB in the deposition step for any of the Pt deposition experiments, so the influence of the ligands (whether CTAB or others) is likely mediating a heterogeneous nucleation step.

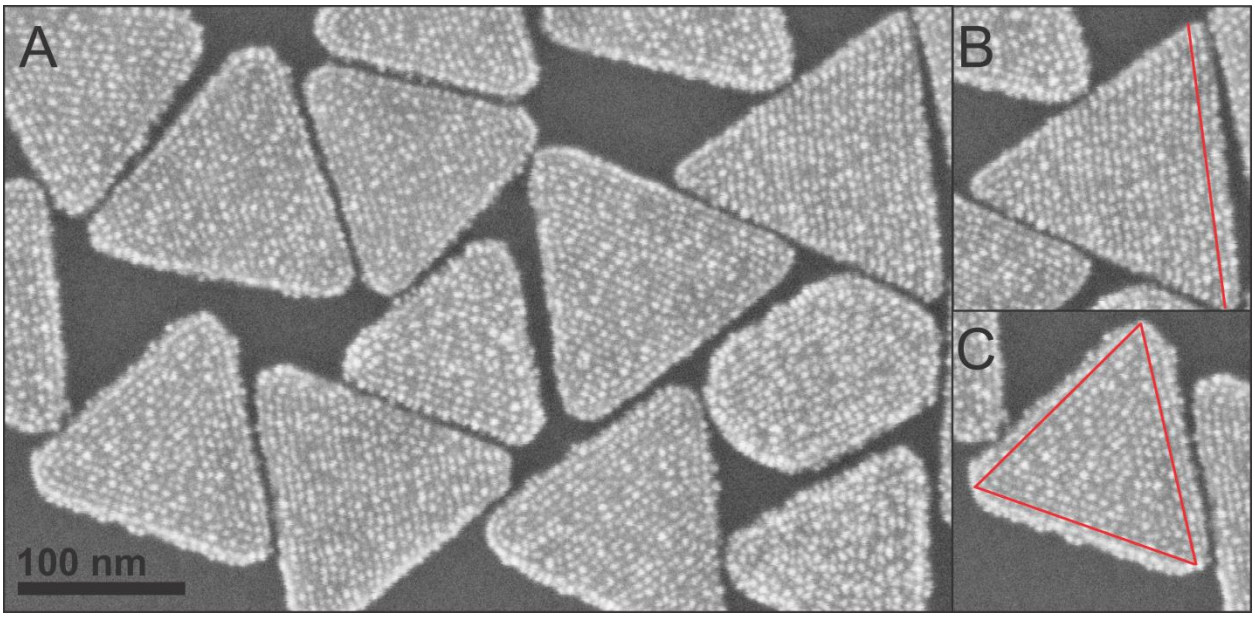

Figure 42. SEM image (A) of pseudo-stellated nanoprisms depicting the slight variation in the observed pattern of Pt nanoisland linear alignment. In a typical synthesis, approximately 70% of the rows are aligned with respect to a single base of the triangular nanoprism substrate (B), while the remaining 30% exhibit a three-base pattern of alignment (C).

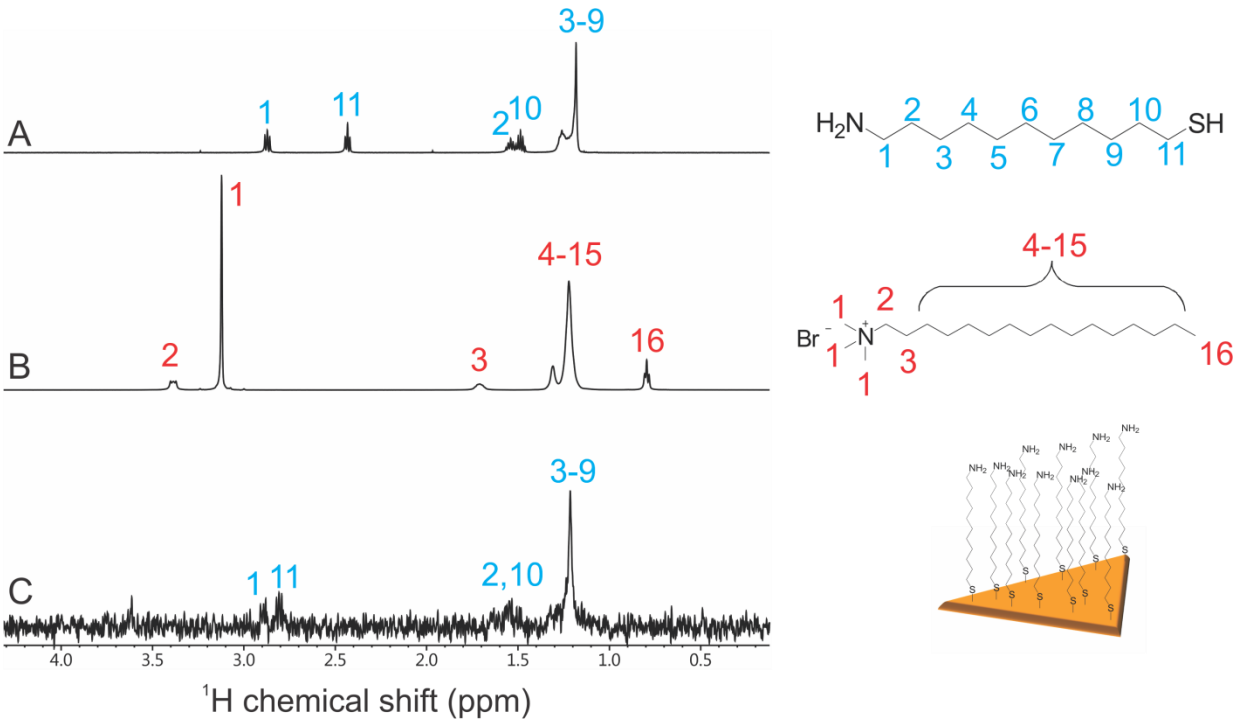

Figure 43. ^{1}H NMR spectra depicting CTAB displacement by AUT for experiments concerning Pt deposition on AUT functionalized nanoprism substrates (Figure 46A). Solutions of AUT, CTAB, and AUT-exchanged nanoprisms (after treatment with aqua regia, see above) were characterized using ^{1}H NMR spectroscopy. As indicated by the ^{1}H NMR spectra of pure AUT (A) and CTAB (B), the nanoprisms (C) are functionalized primarily with AUT. The triplet corresponding to the protons at Position 11 are shifted upfield in (C) due to disulfide formation.

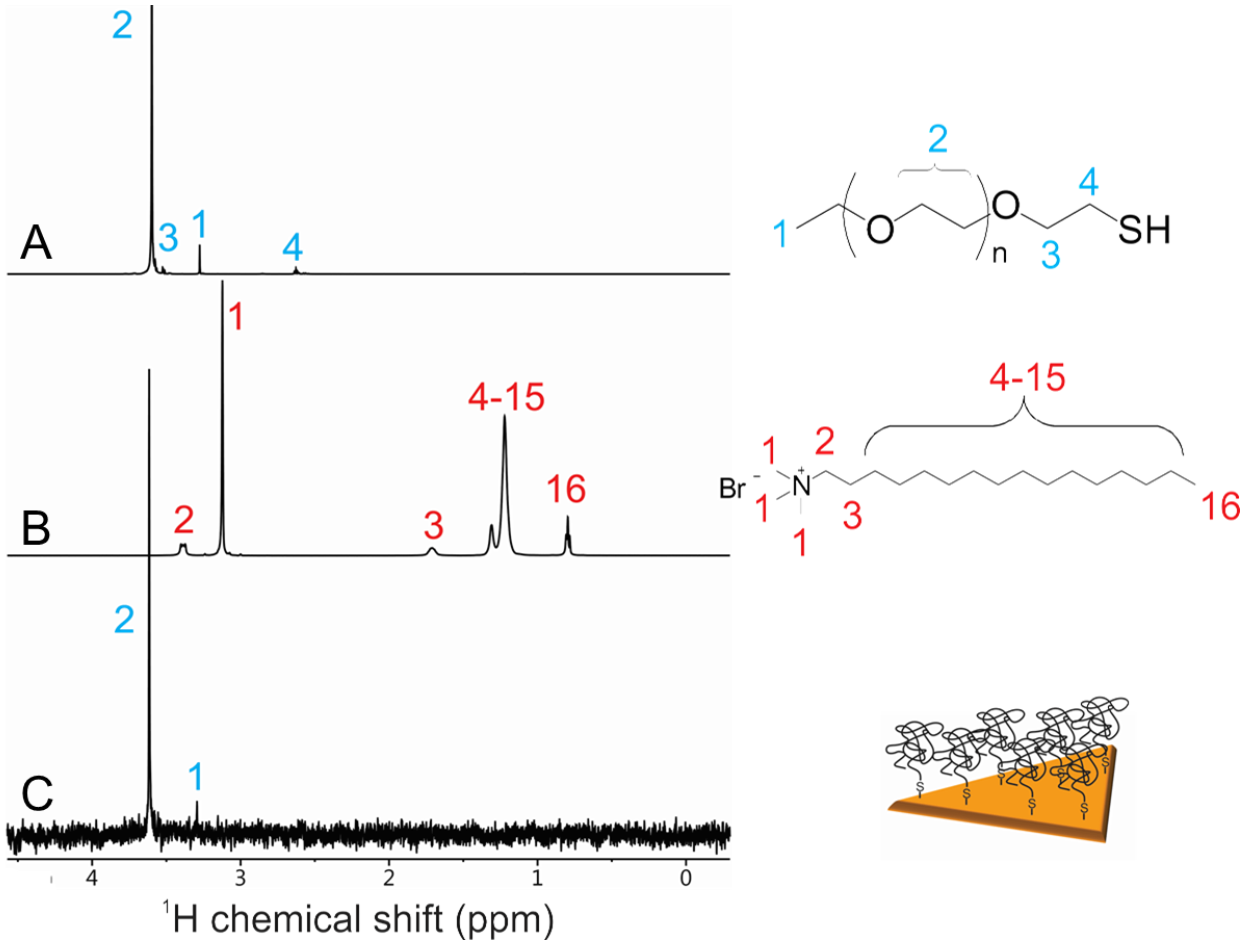

Figure 44. ^{1}H NMR spectra depicting CTAB displacement by PEGSH for experiments concerning Pt deposition on PEGSH functionalized nanoprism substrates **(**Figure 46B**)**. Solutions of PEGSH, CTAB, and PEGSH-functionalized nanoprisms (after treatment with aqua regia, see above) were characterized using ^{1}H NMR spectroscopy. As indicated by the ^{1}H NMR spectra of pure PEGSH (A) and CTAB (B), the nanoprisms (C) are functionalized primarily with PEGSH.

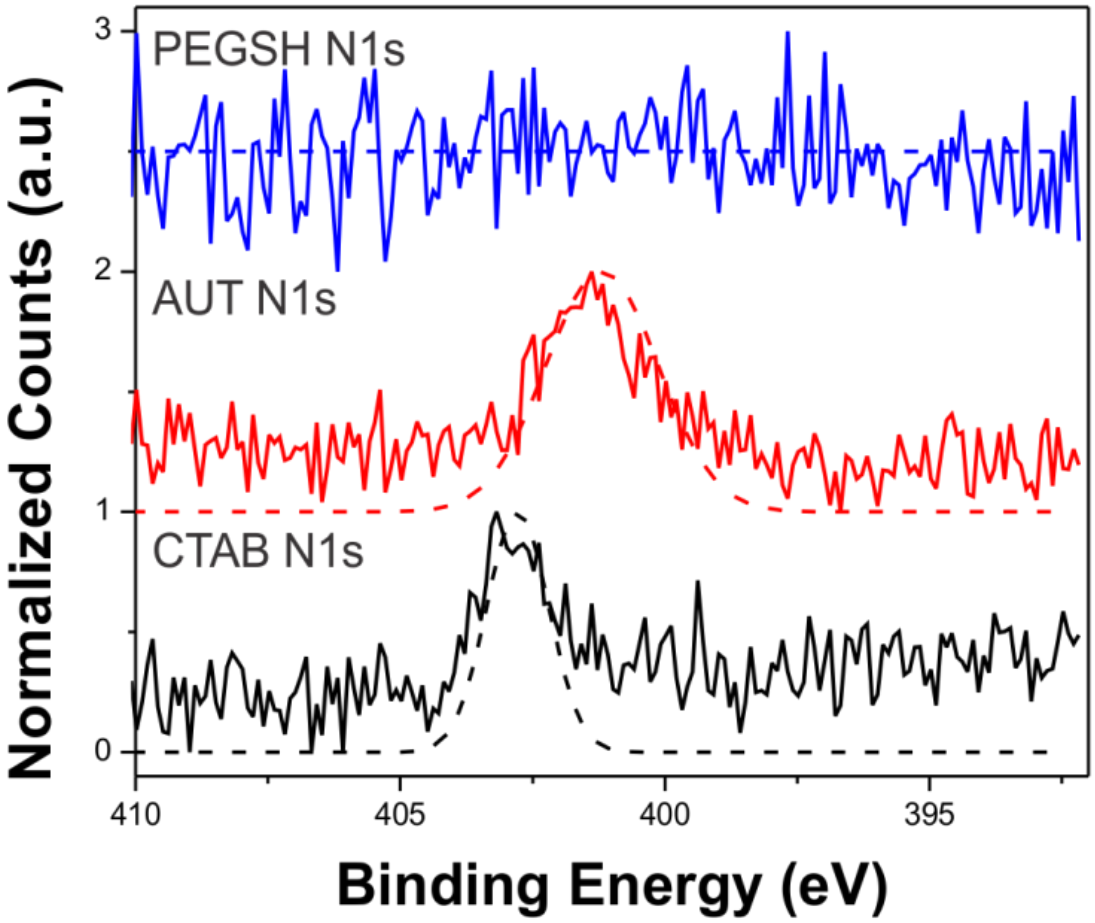

Figure 45. High-resolution N1s XPS spectra (solid lines) and approximate fits (dashed lines, added for visual clarity) of Au nanoprisms functionalized with CTAB, AUT, and PEGSH. Ligand exchange of CTAB by AUT was confirmed by the disappearance of the NMe_4^+ N1s signal (402.8 eV) and appearance of the amino ($-NH_2$) N1s signal (401.1 eV). Ligand exchange of CTAB by PEGSH was confirmed by the disappearance the NMe_4^+ N1s signal (402.8 eV).

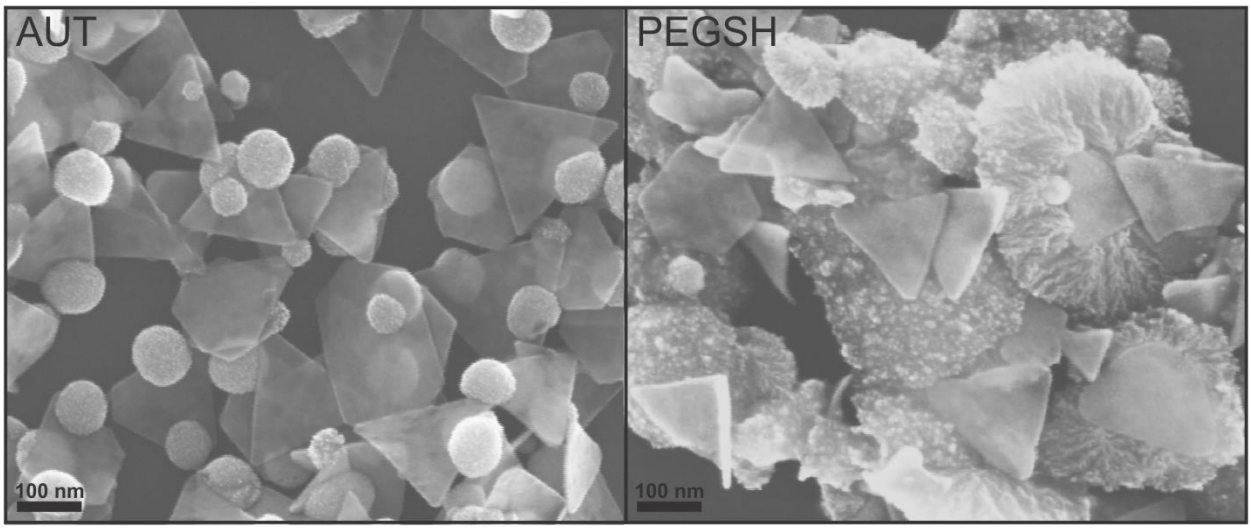

Figure 46. Morphologies observed for H_2PtCl_6 deposition on AUT- (left) and PEGSH- (right) functionalized gold nanoprism substrates. Deposition of H_2PtCl_6 on AUT-functionalized prisms led to the formation of 1-2 large Pt nanoparticles (80 ± 12 nm) appended to the prism edges or vertices. Deposition of H_2PtCl_6 on PEGSH-functionalized prisms resulted in polydisperse growth, primarily originating at nanoprism edges. Linear Pt island growth was not observed for either AUT or PEGSH functionalized prisms, suggesting that molecular adsorbates on the surface of the Au nanoprism play a large role in the resulting secondary metal deposition pathway.

3.4 CONCLUSIONS

In summary, these results highlight Pt speciation as a crucial component of Pt-containing NP synthesis and should provide guidance in the development of new Pt-containing NP systems as well as clarify observations in existing strategies. For example, these mechanistic insights facilitated the investigation of NP deposition patterns that were shown to be a function of organic ligands on the surface of the nanoprisms and may indicate a new method for controlling the pattern of secondary metal deposition onto NP substrates. Ultimately, the combination of metal precursor speciation and seed particle surface chemistry should be powerful tools for the synthesis of a wide variety of highly tailored multimetallic substrates with applications ranging from therapeutics to catalysis.

4.0 LIGAND MEDIATED DEPOSITION OF NOBLE METALS AT NANOPARTICLE PLASMONIC HOTSPOTS.

4.1 INTRODUCTION

Multimetallic nanoparticles are an emerging class of materials with the ability to synergistically enhance optoelectronic,[1-2] magnetic,[3-4] and/or catalytic[5-7] properties of the elemental constituents. Of particular interest are strongly plasmonic metals (e.g. Cu, Ag, and Au) combined with transition metals of catalytic importance (e.g. Cu, Pt, Pd), where the conversion of light into hot charge carriers can be used for subsequent application via transfer of these carriers to neighboring molecules or materials.[160-161] However, the efficacy of these processes is influenced by both the mode of metal incorporation and the compositional architecture (i.e. alloy, core@shell, or Janus-type) of the final multimetallic nanoparticle construct.

A widely adapted strategy for synthesizing multimetallic noble metal nanoparticles involves the separation of nanoparticle nucleation and growth through the use of seed-mediated techniques.[162] Typically, introduction of a "lossy" metal (e.g. Pt, Pd, Rh) onto the surface of a plasmonic nanoparticle substrate can damp the surface plasmon resonance and increase spectral breadth while decreasing spectral intensity via direct coupling of interband transitions.[163-164] With this in mind, an attractive strategy to effectively couple two metals while mitigating unfavorable changes in the LSPR would be to confine metal deposition only where it is most

effective for an application, for example selectively depositing the second metal only at plasmonic "hotspots" on the underlying nanoparticle substrate.[165,74] Indeed, anisotropic gold nanoparticles, such as nanorods,[166] nanostars,[167] and nanoprisms,[168] concentrate light to small, well-defined volumes referred to as "hotspots" of local electromagnetic field enhancement. However, targeted deposition of a secondary metal is synthetically challenging and requires specific experimental conditions for each composition of depositing metal and nanoparticle substrate.

4.2 EXPERIMENTAL

4.2.1 General Materials and Methods

4-aminothiophenol (ATP, 97%), chloroplatinic acid (H_2PtCl_6, 8 wt. % in H_2O), hexadecyltrimethylammonium bromide (CTAB, 99%), hydrogen tetrachloroaurate trihydrate ($HAuCl_4 \bullet 3H_2O$, 99.999%), L-ascorbic acid (99%), sodium borohydride ($NaBH_4$, 99.99%), sodium hydroxide (99.99%), sodium iodide (NaI, 99.999%), and trisodium citrate (99%) were obtained from Sigma Aldrich and used as received. 11-amino-1-undecanethiol hydrochloride (AUT, 99.2%) was purchased from Dojindo (Rockville, MD) and used as received. Acetonitrile (ACN, 99.8%) was obtained from Fisher Scientific (Waltham, MA). Deuterium oxide (D2O, 99.9%) was obtained from Cambridge Isotope Laboratories, Inc. (Tewksbury, MA) and used as received. NANOpure™ water (Thermo Scientific, > 18.2 MΩ•cm) was used for all washing, synthesis, and purification protocols as well as in the preparation of all solutions. 11-Mercaptoundecanoic acid (MUA, 98%) and 3-mercapto-2-methylpropanoic acid (MMPA) was

purchased from Santa Cruz and used as received. All stock solutions were aqueous and prepared fresh before each reaction, unless otherwise noted. All glassware was washed with aqua regia (3:1 ratio of concentrated HCl and HNO_3 by volume) and rinsed thoroughly with water. *Caution: Aqua regia is highly toxic and corrosive and requires personal protective equipment. Aqua regia should be handled in a fume hood only.*

4.2.2 Synthesis and Purification of Au Nanoprisms

Au nanoprisms were synthesized according to literature protocols (vide supra, 3.2.2).[151,169]

4.2.3 Pd Island Nanoprism Synthesis

1.0 mL of Au nanoprisms ($OD_{\lambda max}$ = 1.0 a.u.) was added to a 1.5 mL centrifuge tube. 30 µL of 10 mM ascorbic acid was added (for final $PdCl_2$:ascorbic acid molar ratio of 1:10), and the solution was briefly mixed by vortexing for 5 seconds. 30 µL of 2 mM $PdCl_2$ was added, and the solution was mixed by vortexing again. After allowing one hour for completion of nanoparticle growth, the reaction mixture was purified from excess reagents by centrifugation (5 minutes at 2200 rcf using a Spectrum mini-centrifuge (SC1006-R)). The supernatant was removed and the particles were resuspended in 1.0 mL of H_2O by brief sonication (~10 s).

4.2.4 Disrupting Pd Nanoisland Linearity by Decreasing [CTAB]

In order to obtain randomly aligned Pd nanoisland deposition, Au nanoprisms were purified as described above, except an additional wash was performed (5 minutes at 2200 rcf using a

Spectrum mini-centrifuge (SC1006-R), see Figure 47). The supernatant was removed, and the colloid concentration was adjusted to an O.D. of 1.0 at λ_{max}. The concentration of CTAB was qualitatively monitored throughout the washing procedure by measuring the volume of the pellet remaining after each washing step; for a pellet volume of 10 μL, each wash constitutes a 1:100 dilution from the original CTAB concentration of 50 mM. After two washes and subsequent dilution to 1.0 O.D at λ_{max}, the approximate CTAB concentration was measured to be approximately 5 μM. Immediately after purification, Pd was deposited as described above to yield Au nanoprisms decorated with randomly organized Pd nanoislands.

4.2.5 Restoring Pd Nanoisland Linearity by Increasing [CTAB]

Au nanoprisms were synthesized and purified by centrifugation two times as described above (yielding an approximate CTAB concentration < 5 μM, see Figure 47). After purification, the concentration of the Au nanoprisms was measured by UV-vis-NIR spectroscopy, and the nanoprism colloid was diluted to an O.D. of 1.0 at λ_{max} with water and 100 mM CTAB for a final CTAB concentration of 0.5 mM. Au nanoprisms were vortexed briefly for 5 seconds, and allowed to equilibrate at room temperature for one hour. After the equilibration period, Pd was deposited as described above to yield Au nanoprisms with linearly arranged Pd islands.

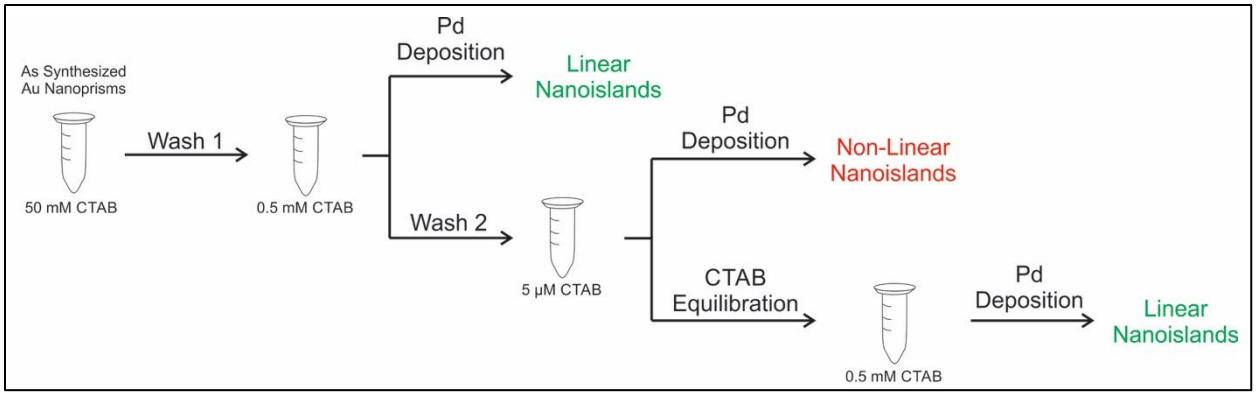

Figure 47. Scheme depicting the removal and addition of CTAB to Au nanoprisms. Following this protocol, changes in surface CTAB concentration disrupt and then restore Pd nanoisland linearity.

4.2.6 UV-vis-NIR Spectroscopy Methods

Colloids were measured by ultraviolet-visible-near infrared (UV-vis-NIR) spectroscopy using a Cary 5000 spectrophotometer (Agilent, Inc.). Spectra were baseline corrected to the spectrum of water for optical density measurements.

4.2.7 Transmission Electron Microscopy (TEM) Methods

After Pd deposition, the resulting nanoparticle products were purified by centrifugation using a Spectrum mini-centrifuge (SC1006-R). After removal of the supernatant, the pellet was resuspended in 1.0 mL of H_2O and the process was repeated. After subsequent removal of the supernatant, nanoprism products were resuspended in 30 μL of H_2O by briefly vortexing the solution (~ 5 s) followed by brief sonication (~ 5 s). A 5 μL aliquot of each concentrated nanoprism sample was dropcast onto a carbon-backed Cu TEM grid (Ted Pella, carbon on 200 mesh Cu), allowed to dry under ambient conditions and stored under vacuum prior to analysis. a JEOL JEM 2100F equipped with a Gatan Imaging Filter (GIF) Tridiem camera and Oxford Inca EDS detector at 200 kV (Nanoscale Fabrication and Characterization Facility (NFCF), Petersen Institute of Nanoscience and Engineering (PINSE), University of Pittsburgh), or a Hitachi H-9500 TEM at 200-300 kV. Images were analyzed using Digital Micrograph v2.10.1282.0 (Gatan, Inc.) and/or ImageJ v 1.47d (National Institutes of Health, USA) software. Fast Fourier transform (FFT) images were indexed according to standard face-centered cubic (FCC) diffraction patterns. Scanning transmission electron microscopy energy dispersive X-ray spectroscopy (STEM-EDS) elemental maps and linescans were collected using the JEOL JEM 2100F electron microscope (NFCF, PINSE, University of Pittsburgh). Oxford Inca software was

used for data processing and generation of elemental maps. EDS spectra were collected using a beryllium double tilt holder (JEOL #31640), a tilt angle of 14 degrees in the positive X direction toward the EDS detector and a STEM probe diameter of 1.5 nm. The EDS was acquired using 2k channels from 0 to 20 keV. Elemental maps were collected for 40-60 minutes and the site lock feature (Oxford Inca software) was used to correct for sample drift during acquisition, with a pixel dwell time of 1000 μs and a pixel resolution of 128x128.

4.2.8 Selected Area Electron Diffraction (SAED) Measurements

SAED images were obtained using the JEOL JEM-2100F or the Hitachi H-9500 TEM and were analyzed using Digital Micrograph v2.10.1282.0 (Gatan, Inc.) and/or ImageJ v 1.47d (National Institutes of Health, USA) software. Standard face-centered cubic (FCC) diffraction patterns were used to index the spots. The angles between spots and the distances from the spots to the center point were measured to determine the orientation of the crystal lattice. As all SAED patterns were in the [111] orientation, distances from the center point to the outer spots were averaged to obtain Au and Pd d-spacings and lattice parameters.

4.2.9 Ligand Exchange of Au Nanoprisms

To exchange the CTAB on the Au nanoprisms with a thiolated ligand of interest, Au nanoprisms were synthesized and purified by two rounds of purification (800 rcf for 15 minutes on an Eppendorf centrifuge (5804 with swing bucket rotor A-4-44), followed by another wash for 5 minutes at 2200 rcf using a Spectrum mini-centrifuge (SC1006-R)). After diluting to an O.D. of 1.0 at λ_{max}, 1.0 mL of the Au nanoprisms were added to a microcentrifuge tube. To this, 1-20 μL

of a 1 mM solution of the thiolated ligand (AUT, MUA, 4-ATP, or MMPA) was added (Note, solutions of MUA and 4-ATP were 10 mM in NaOH to ensure ligand solubility). Immediately after addition of the thiolated ligand, the Au nanoprism colloid was vortexed for 30 seconds, and the solutions were allowed to equilibrate at room temperature for 24 hours. After ligand exchange and purification (see above), the prisms were used as substrates for secondary metal deposition by addition of a 20 μL of a 2 μM solution of either $PdCl_2$, $HAuCl_4$,or H_2PtCl_6 at a 1:10 ratio of metal precursor to ascorbic acid (i.e. 20 μL of a 10 mM solution of ascorbic acid).

4.2.10 ^{1}H NMR Methods

All NMR measurements were performed on a Bruker 600 Ultrashield magnet with an AVANCE III 600 Console (Bruker Biospin, Billerica, MA) at 298 K. For all experiments, a minimum recycle delay of 5 s was used, which was sufficiently greater than T_1. NMR samples were prepared by concentrating ligand exchanged nanoprisms via centrifugation (5 minutes at 2200 rcf using a Spectrum mini-centrifuge (SC1006-R)), followed by digestion with 1 drop (~5 μL) of concentrated ultrapure aqua regia. These samples were allowed to digest overnight at 37 °C before dilution with D_2O to a total volume of 500 μL. An ACN reference was used for the determination of unknown ligand concentrations. To each sample, 5 μL of dilute ACN (0.24% v/v; 15 μL of ACN in 6 mL of D_2O) was added. The unknown ligand concentrations were determined by comparison to a five-point standard curve with a range of 1.00−0.01 mM ligand (1.00, 0.50, 0.10, 0.05, and 0.01 mM, prepared in D_2O). For each standard, the integral of a specific ligand peak was divided by the integral of the ACN peak and plotted against the known concentration of ligand (Figure 49-50). For all quantitative analyses, a minimum signal-to-noise ratio of 20 was used. Following an internal standard approach for the unknown concentrations of

ligand on the AuNP, the ligand peak was integrated and similarly divided by the known integrated ACN peak to yield the concentration upon comparison with the calibration curve.

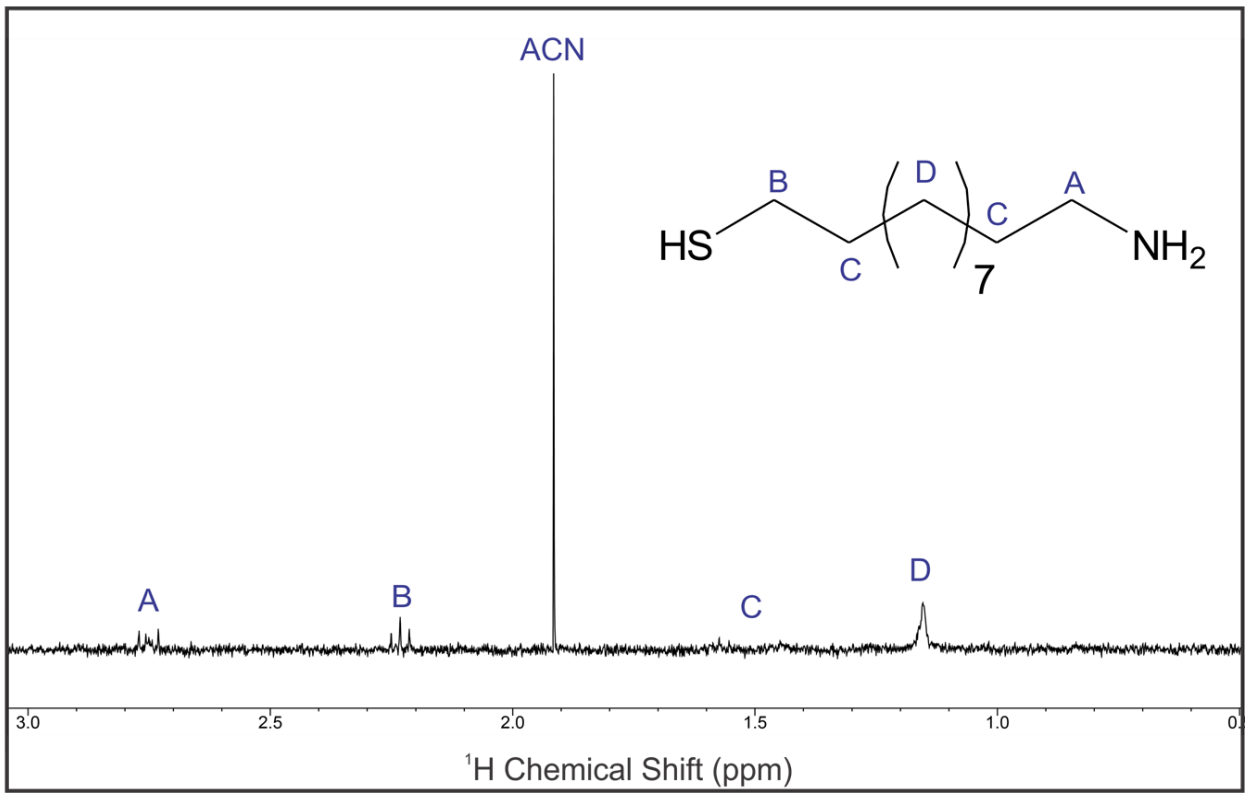

Figure 48. Representative ^{1}H NMR spectrum of AUT-exchanged Au prisms in D_2O following digestion with aqua regia, with its labeled structure corresponding to plotted ^{1}H NMR peak locations. For calculation of AUT concentration, Peak D is integrated and compared to the integrated intensity of the ACN peak.

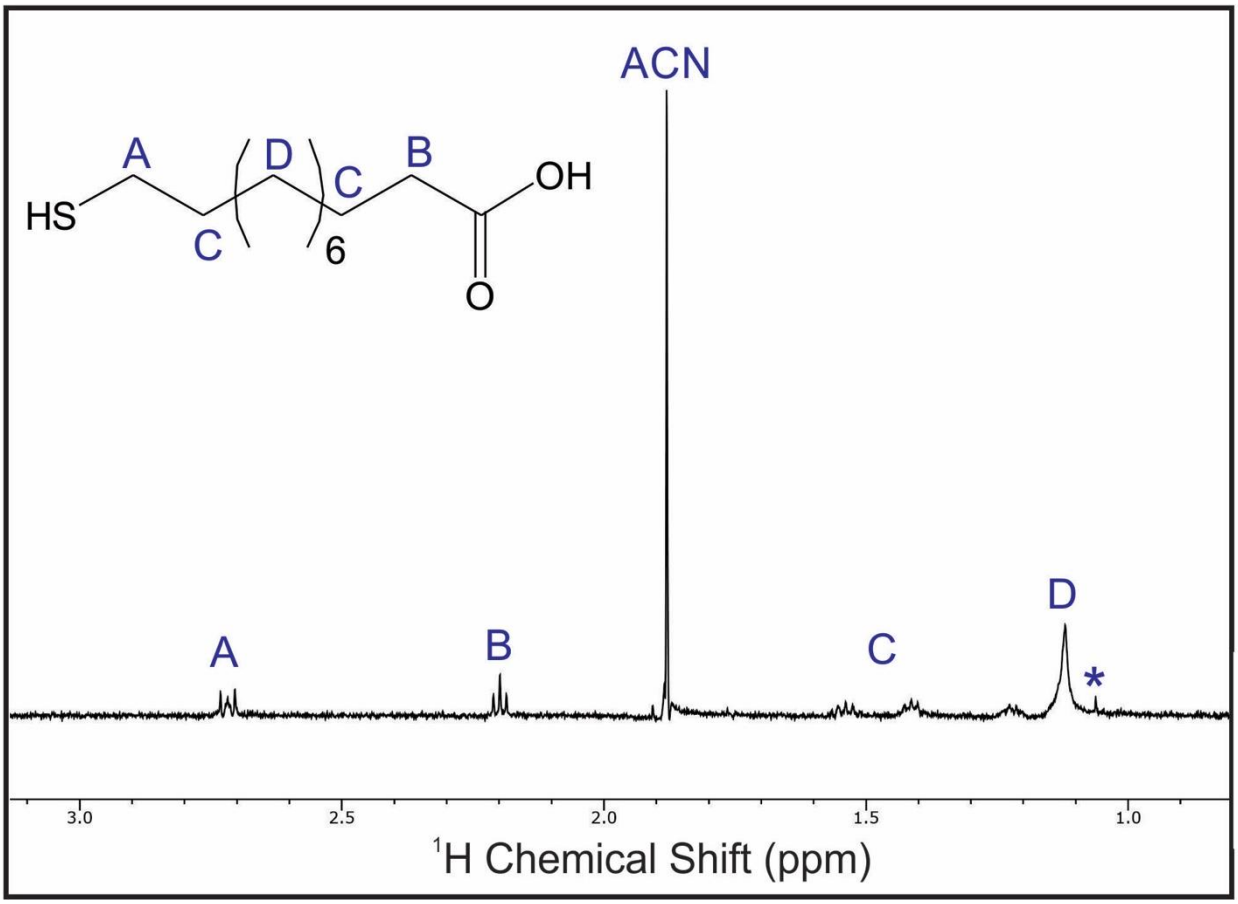

Figure 49. Representative ^{1}H NMR spectrum of MUA-exchanged Au prisms in D_2O following digestion with aqua regia, with its labeled structure corresponding to plotted ^{1}H NMR peak locations. The peak labelled with (*) indicates trace amounts of residual CTAB remaining after the ligand exchange. For calculation of MUA concentration, Peak B is integrated and compared to the integrated intensity of the ACN peak.

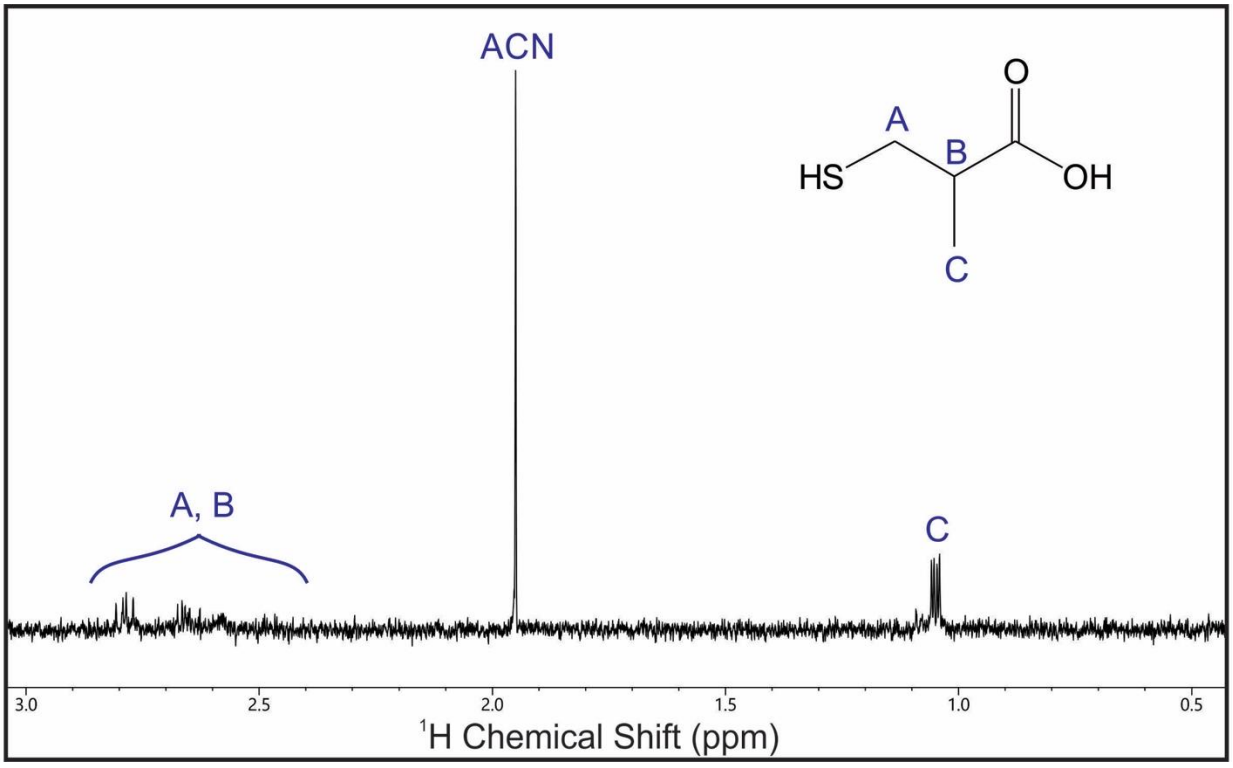

Figure 50. Representative ^{1}H NMR spectrum of MMPA-exchanged Au prisms in D_2O following digestion with aqua regia, with its labeled structure corresponding to plotted ^{1}H NMR peak locations. For calculation of MMPA concentration, Peak C is integrated and compared to the integrated intensity of the ACN peak.

4.2.11 ICP-MS Methods

Inductively coupled plasma mass spectrometry (ICP-MS) analysis was performed using an argon flow with a NexION spectrometer (PerkinElmer, Inc.). An aqua regia solution was prepared with a 3:1 ratio of hydrochloric acid (Sigma-Aldrich, > 99.999% trace metal basis): nitric acid (Sigma-Aldrich, > 99.999% trace metal basis) and diluted with water for a 5% (by volume) aqua regia matrix. Samples were taken from the NMR samples, which were prepared by digestion of the concentrated Au nanoprism pellet and resuspension in D_2O described above. Aliquots of 1 μL of the NMR sample were then diluted to a total volume of 15 mL using 5% aqua regia matrix and analyzed by ICP-MS.

Unknown Au concentrations were determined by comparison to a 5-point standard curve with a range of 1 - 30 ppb (1, 5, 10, 20, and 30 ppb prepared by volume) from a gold standard for ICP (Fluka, TraceCERT 1,001 ± 2 mg/L Au in HCl) diluted in the 5% aqua regia matrix. All standards were measured 5 times and averaged, while all unknown samples were measured in triplicate and averaged. A 5 minute flush time with 5% aqua regia matrix was used between all runs, and a blank was analyzed before each unknown sample to confirm removal of all residual metals from the instrument.

4.2.12 Quantification of Ligand Density on Au Nanoprisms

Ligand footprints were quantified using a combination of ICP-MS and ^{1}H NMR as previously reported.[170] Au nanoprism dimensions were measured from TEM images using ImageJ, where average edge lengths were determined by counting at least 100 nanoparticles.

4.2.13 X-ray Photoelectron Spectroscopy Methods

Silicon wafer substrates (University Wafer, p-doped, 200 nm thermal oxide (SiO2)) were cleaned by sonication in ethanol for 5 minutes. The substrates were then rinsed with ethanol and dried under air. Nanoparticle products were concentrated and purified as described for TEM analysis, and a 10 μL aliquot of the resulting solution was dropcast onto a 1x1 cm silicon wafer substrate and allowed to dry. The samples were placed under vacuum for 24 hours to mitigate surface contamination. XPS spectra were obtained using an ESCALAB 250XI XPS with a monochromated, micro-focused Al Kα X-ray source (spot size = 200 μm; step size = 0.1 eV, pass energy = 50 eV). Spectra were charge referenced to adventitious carbon (284.8 eV). For sputtering analysis, samples were sputtered with Ar ions (current = 500 mV) for a period of ten seconds.

4.2.14 Synthesis and Purification of Au Nanorods

Au nanorods were synthesized and purified according to previous literature protocols.[171-172] Approximately 24 hours after addition of the seeds to the growth solution, the Au nanorods were purified by centrifugation (5 minutes at 2200 rcf using a Spectrum mini-centrifuge (SC1006-R)) and the concentration of the rods was standardized by diluting to an O.D. of 1.0 a.u. at λ_{max} of the longitudinal LSPR (at approximately 675 nm) prior to Pd deposition or ligand exchange (see respective protocols for Pd deposition and ligand exchange of Au nanoprisms, where 1.0 mL of Au nanorods were used in place of the 1.0 mL of Au nanoprisms).

4.2.15 Ligand Exchange and Pd Deposition on Au Nanorods

Ligand exchange and Pd deposition on Au nanorods was identical to that of the Au nanoprisms. Briefly, after synthesis, the Au nanorods were washed one additional time via centrifugation at 8,000 rcf followed by removal of the supernatant and resuspension in H_2O to a standard O.D. at λ_{max} (approximately 700 – 800 nm depending on the nanorod aspect ratio) to 1.0 a.u. Afterwards, Pd deposition and ligand exchange was identical to the purified Au nanoprism stock solution.

4.3 RESULTS AND DISCUSSION

In this report, we use metal-ligand surface chemistry to selectively deposit secondary metals at specific locations (i.e. face, edge, or vertex) of the underlying nanoparticle substrate. Here, we examine trends in metal-ligand surface chemistry by a combination of electron microscopy and ^{1}H NMR spectroscopy to identify mechanisms guiding the selective incorporation of Pd at Au nanoparticle substrate hotspots. Importantly, we demonstrate that this method is applicable for a variety of depositing metals and nanoparticle substrate morphologies.

In a typical experiment, Au nanoprism substrates (edge length = 150 ± 25 nm, thickness = 8 ± 2 nm) were synthesized and purified using literature protocols (see supporting information (SI) for full experimental details).[151,169] Reduction of the $PdCl_2$ precursor by ascorbic acid (1:5 molar ratio of $PdCl_2$:ascorbic acid) in the presence of purified Au nanoprisms results in the deposition of a linear arrays of Pd nanoislands across the Au nanoprism surface (average thickness of Pt island row of 4.0 ± 0.7 nm**,** Figure 51). UV-vis-NIR spectroscopy indicates that as Pd island

density increases, the in-plane dipole LSPR blue-shifts by approximately 80 nm and becomes increasingly attenuated (full width at half maximum increases from 190 to 370 nm, decrease in intensity by 26%, Figure 51) Importantly, both the mode of island deposition, pattern of island arrangement, and decrease in LSPR intensity with increasing island density is consistent with our previous investigations regarding mechanisms of Pt nanoisland deposition on Au nanoprism substrates.[169]

We initially performed high resolution transmission electron microscopy (HRTEM) analysis of the AuPd nanoprisms in order to determine the crystallinity and mode of Pd deposition. Scanning transmission electron microscopy coupled with X-ray energy dispersive spectroscopy (STEM-EDS) indicates that Pd deposits in an island growth mode, and indicates no additional galvanic replacement reactions between Au and Pd constituents (Figure 52). Selected area electron diffraction (SAED) indicates that the Pd nanoislands are singly crystalline and are in epitaxial contact with the Au nanoprism surface (Au and Pd lattice mismatch of 4.6%, Figure 53). The Pd nanoislands are linearly arranged across the surface of the nanoprism in rows, with average row-to-row separation distances of approximately 3.6 ± 0.6 nm. Interestingly, a majority of the Pd nanoislands unidirectionally fuse into linear stripes (Figure 54). We hypothesize that this unidirectional fusion indicates the presence of a strongly bound ligands between rows of Pd islands which may act as a template the observed linear pattern of arrangement. Indeed, previous AFM analysis of CTAB on graphite indicate CTAB self-assembly CTAB into rows of hemimicelles with row-to-row separation distances of approximately 4.2 ± 0.4 nm, consistent with the separation distance between Pd rows.[173] Indeed, after several days of aging, we observe subsequent fusion of the Pd stripes into a uniform core@shell Au@Pd nanostructure, consistent

with Pd island fusion with gradual dissociation of CTAB ligands on the surface of the Au nanoprism (Figure 54D).

To gain insight into the driving force for Pd island linear self-assembly, we next repeated the Pd island deposition under conditions with depleted CTAB concentrations (approximately 0.5 mM, refer to Figure 47 for a schematic of the reaction protocol). Indeed, when the Au nanoprisms are purified from excess CTAB prior to Pd deposition, we observe random Pd island nucleation and a marked decrease in linear organization (depleted conditions, Figure 55B). Remarkably, the linearity can subsequently be restored by equilibrating the depleted Au nanoprisms in a 1 mM solution of CTAB for one hour prior to Pd deposition (Figure 55C, *N.B.* equilibration times of less than one hour resulted in less ordered Pd island growth). This result suggests that the time-dependent reorganization of the CTAB supramolecular architecture impacts the location of Pd island nucleation and the ability to self-assemble into linear arrays.

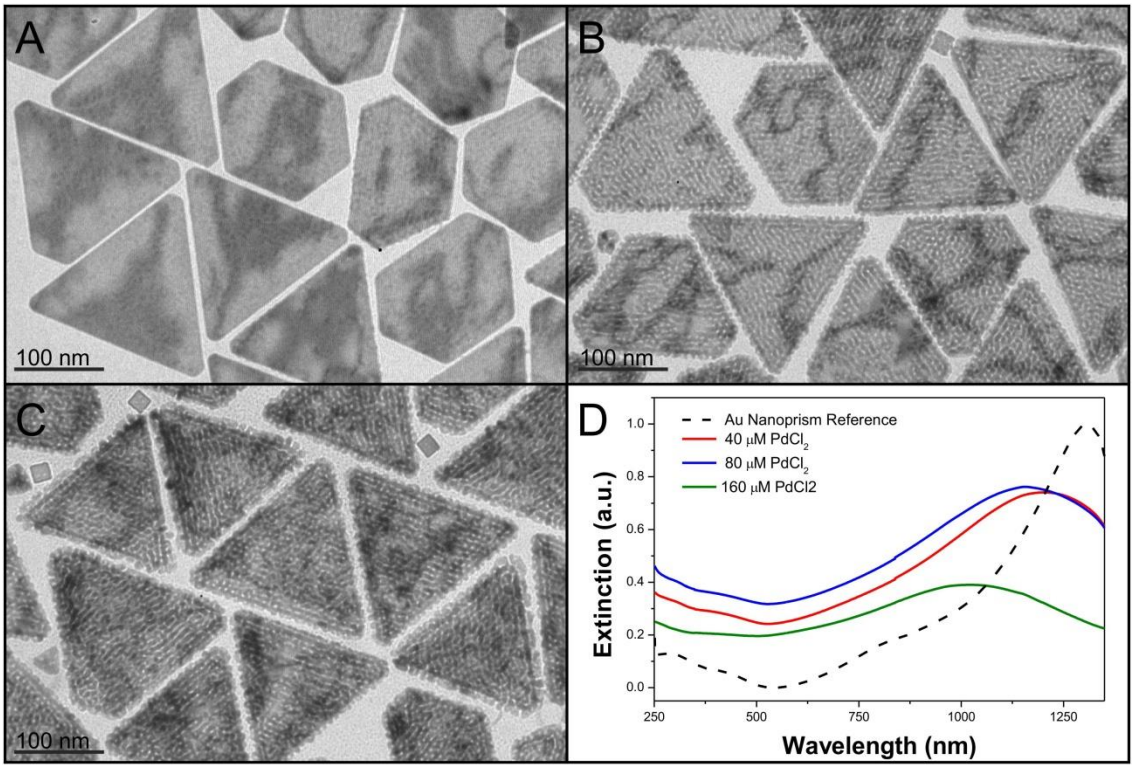

Figure 51. Changes in the extent of Pd island density by increasing the concentration of reagents (1:5 molar ratio of $PdCl_2$:ascorbic acid) relative to the concentration of gold nanoprism seeds. (A) 20 μL of 2 mM $PdCl_2$ and 10 mM ascorbic acid. (B) 40 μL of 2 mM $PdCl_2$ and 10 mM ascorbic acid. (C). 20 μL of 2 mM $PdCl_2$ and 10 mM ascorbic acid (D). Representative UV-vis-NIR spectra of the nanoparticle colloids featured in panels A-C.

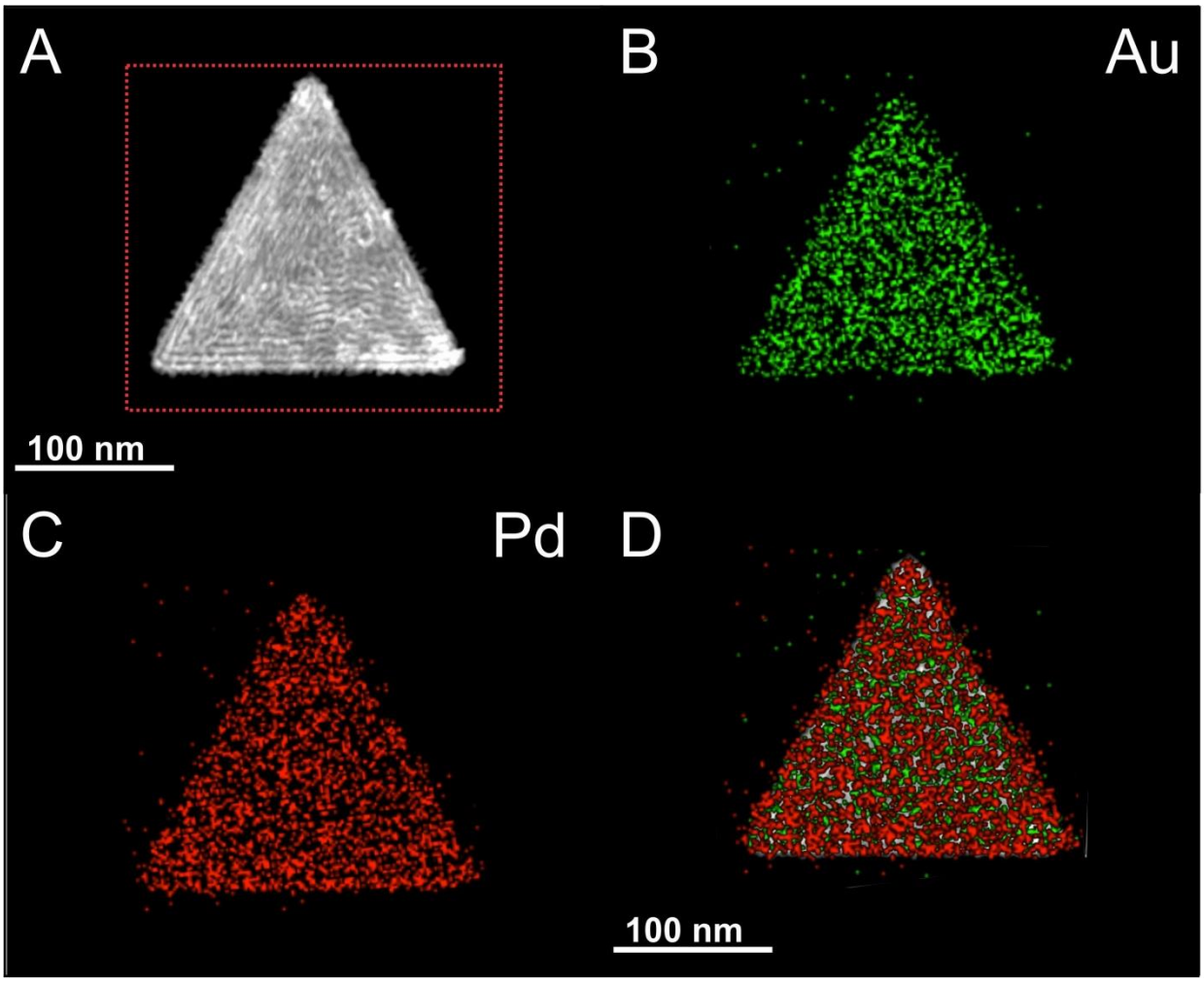

Figure 52. STEM-EDS mapping of Au nanoprisms decorated with Pd islands. (A) High angle annular dark field (HAADF) STEM image depicting the Pd nanoislands (darker contrast spots), (B) Au map, (C) Pd map, and (D) overlay of Au and Pd signals.

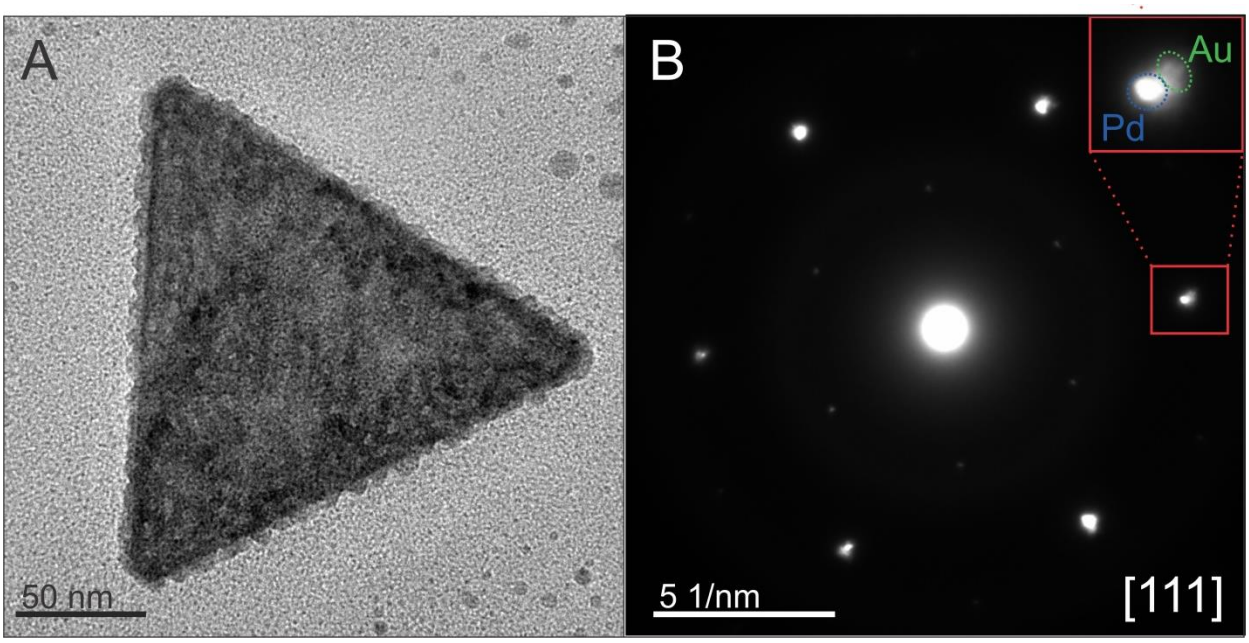

Figure 53. (A) TEM image and (B) corresponding selected area electron diffraction (SAED) pattern indicating that the Pd nanoislands are aligned in the [111] direction and are in epitaxial contact with the Au nanoprism surface. The inset in Panel B is a magnified outer diffraction spot in order to show that the Pd and Au diffraction spots are resolvable. Pd and Au d-spacings were measured to be 2.24 and 2.35 Å, respectively.

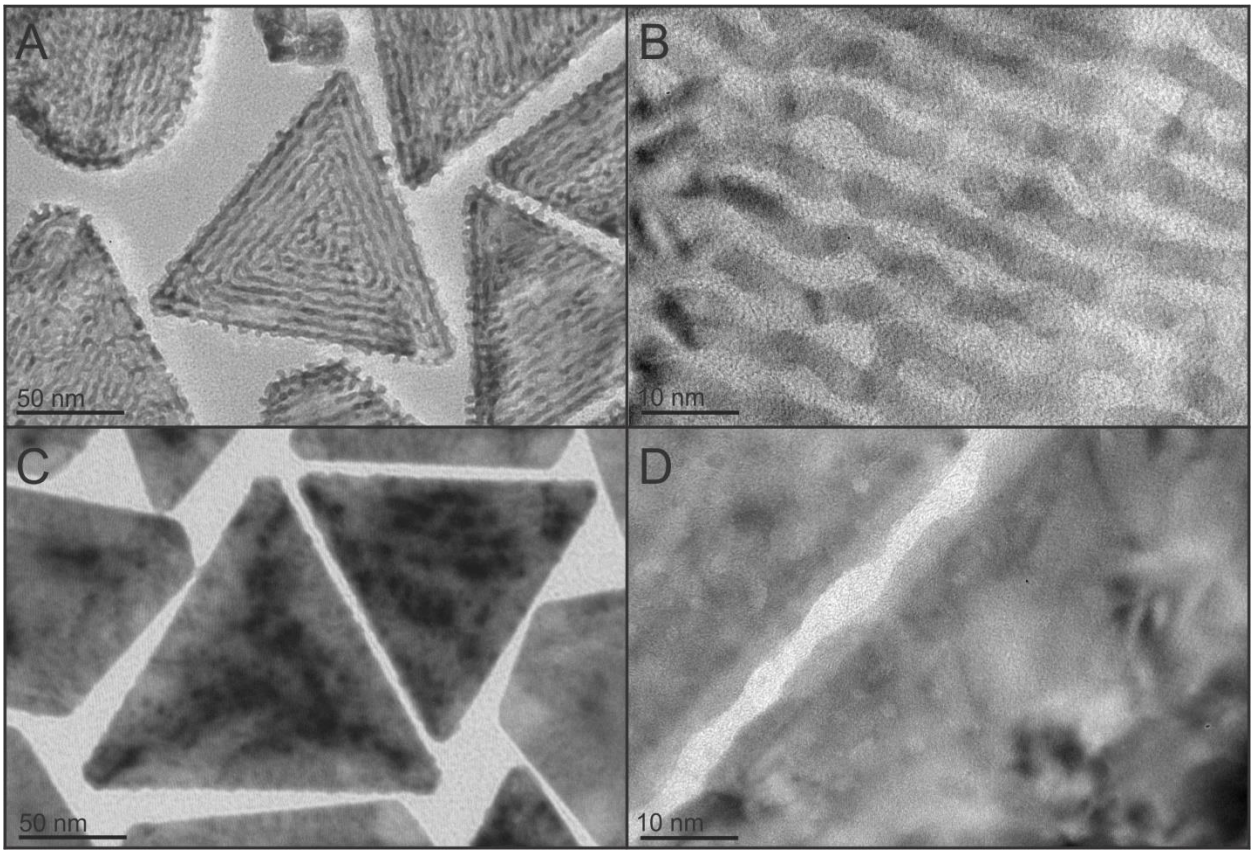

Figure 54. HRTEM depicting Pd nanoisland fusion on the surface of the Au nanoprism. (A) After purification and equilibration of the Au nanoprisms in 0.5 mM CTAB for one hour, the majority of Pd nanoislands unidirectionally fuse into lines, possibly indicating the presence of strongly adsorbed CTAB between rows of Pt islands. (B) Close up image of the prism in (A) illustrating the fusion of Pd nanoislands into linear formations. (C, D) After one week of aging, a core@shell Au@Pd morphology is observed. Here, gradual reorganization or disassociation of the CTAB over the duration of one week likely facilitates uniform fusion of Pd nanoislands and formation of the core@shell architecture.

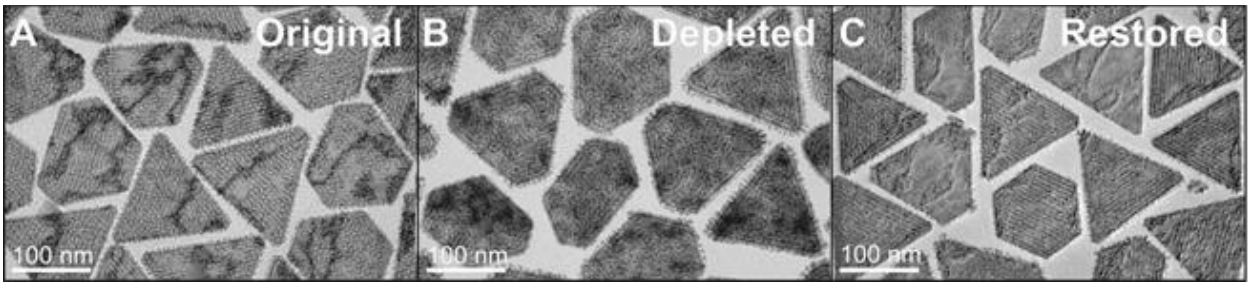

Figure 55. TEM image series illustrating the influence of CTAB concentration on the linear organization of the Pd nanoislands across the surface of Au nanoprisms. (A) Pd reduction in the presence of Au nanoprisms (see SI, approximate [CTAB] = 500 μM) results in linear deposition of Pd nanoislands. (B). If the nanoprisms are purified by an additional round of centrifugation (approximate [CTAB] = 5 μM), Pd nanoisland deposit in a disordered fashion (C) After adding in additional CTAB to the purified nanoprisms (approximate [CTAB] = 500 μM), Pd nanoislands deposit in a linear fashion.

With an understanding between the observed patterns of Pd island alignment and the surface chemistry of the Au nanoprism substrate, we next ligand exchanged the prisms with a thiolated small molecule (11-amino-1-undecanethiol, AUT) to either fully replace CTAB or selectively "fill in" voids in the surfactant layer. Here, we selected a thiol-based ligand, because thiols bind strongly to the Au(111) three-fold hollow sites.[174] The amine functionality was initially selected to facilitate ligand exchange without inducing nanoprism aggregation or oxidative tip-rounding. Ligand exchange was monitored using ^{1}H NMR spectroscopy and inductively coupled plasma mass spectroscopy (ICP-MS) according to previous protocols[170] in order to qualitatively monitor the extent of CTAB displacement by thiolated ligands. Following ligand exchange and Pd deposition, we observed a correlation between the AUT surface coverage and the observed Pd deposition morphology (Figure 56). In the presence of low AUT surface coverage (concentration at the time of ligand exchange = 5 nM, surface coverage of 1.1 ligands/nm^2 by ^{1}H NMR and ICP-MS), the island density substantially decreased and random island nucleation was observed. Upon doubling the concentration of AUT during the ligand exchange procedure from 5 to 10 nM (approximate AUT surface coverage of 1.5 ± 0.1 ligands/nm^2), Pd was observed to grow in dendritic structures. Here, increased thiol density is expected to passivate nucleation sites on the surface of the Au nanoprism substrate, resulting in an extended duration of Pd nanoisland growth and a transition to a dendritic morphology, consistent with previous results.[175] At this AUT density, multiple Pd dendrites (approximately 10-20 per nanoprism, average diameter of 18 ± 9 nm) were observed to grow from the surface of the Au nanoprism in close proximity to triangular edges (Figure 56B). As the extent of surface thiolation increased (concentration of AUT during ligand exchange of 15 nM, density of 1.8 ligands/nm^2), we observe the formation of 1-3 Pd dendrites per nanoprism (average diameters of 47 ± 10 nm), similar to our previous

investigations concerning Pt deposition on AUT functionalized nanoprisms.[169] Importantly, Pd nucleation occurs more frequently towards the edges of the prism, likely due to the high energy of the side facets and defects in the ligand shell near Au nanoprism edges or vertices. Attempts to deposit Pd with higher AUT surface coverages resulted in limited deposition and the formation of discreet Pd nanoparticle dendrites (Figure 57), possibly indicating complete passivation of the Au nanoparticle surface. Most importantly, UV-vis-NIR spectroscopy indicates no significant changes between the bare nanoprisms and the nanoprisms with pendant Pd dendrites (Figure 56D).

We next analyzed the composition and crystallinity of the Pd dendrites by HRTEM. SAED measurements indicate that the Pd nanoparticles are aligned in the [111] direction and are in epitaxial contact with the underlying Au nanoprism surface, consistent with either Pd heterogeneous nucleation or deposition by oriented attachment (Figure 58).[18] STEM-EDS indicates that Pd is selectively located towards the edges of the nanoprism, as opposed to forming a thin continuous Pd shell (Figure 59). To further probe the influence of pendant Pd dendrites on the optical features of the Au nanoprism, we next increased the concentration of metal precursor and reducing agent (constant $PdCl_2$:ascorbic acid ratio of 1:5) relative to the concentration of Au nanoprism seeds to increase the average diameter of the Pd dendrites. With this method, an increase in the average diameter of the Pd dendrites from 30±7 to 50±11 nm was observed (Figure 60). Attempts to grow smaller dendrites resulted in scattered deposition of Pd islands, likely due to insufficient Pd monomer and a shortened phase of particle growth. Attempts to grow larger dendrites resulted in a competing pathway of Pd homogeneous nucleation of free Pd dendritic particles as opposed to an increase in the average Pd dendrite diameter (Figure 57). Importantly, no reduction in the Au nanoprism in-plane dipole LSPR

intensity was observed, as compared to the 26% decrease in intensity for Au nanoprisms fully coated with Pd nanoislands.

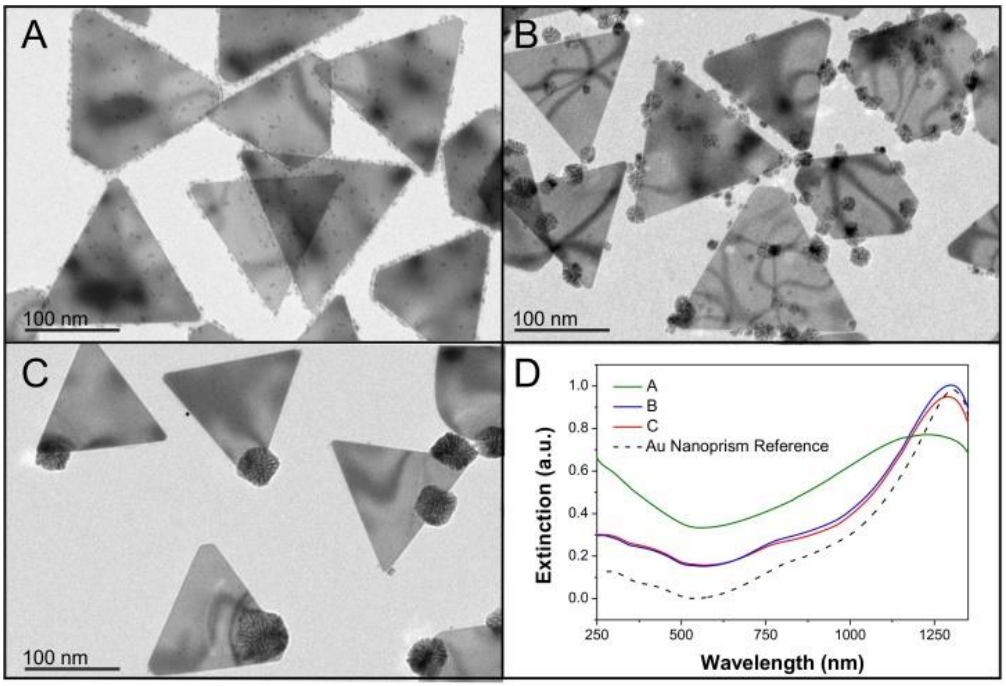

Figure 56. TEM images depicting the change in Pd deposition pathway with increasing AUT ligand density on the surface of the Au nanoprism substrates. (A) In the presence of mixed AUT/CTAB ligand shells (as determined by ^{1}H NMR spectroscopy, AUT surface coverage of 1.1 ± 0.2 ligands/nm^{2}), a mixture of island and dendrite like deposition was observed. (B) As the extent of AUT functionalization increases (1.5 ± 0.1 ligands/nm^{2}), we observe deposition locations move towards the edges of the Au nanoprisms and become more dendritic in nature. Note that scattered Pd island deposition is still observed. (C) At nearly full passivation (1.8 ± 0.1 ligands/nm^{2}) approximately 1-3 Pd dendrites (42 ± 7 nm) are observed to nucleate towards the edges and vertices of the Au nanoprism. (D). UV-vis-NIR spectra of the colloids featured in panels A-C.

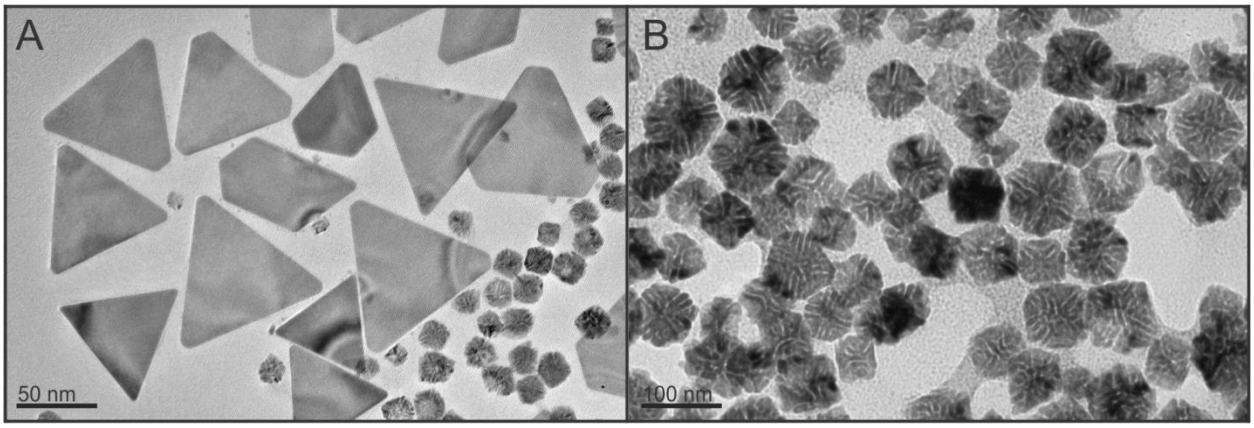

Figure 57. Addition of excess AUT (approx. greater than 20 μL of a 1.0 mM solution) prohibits deposition of Pd onto the nanoprism. Interestingly, discrete Pd NPs with radial, cubic morphologies are observed, similar to the dendrites on the edges of the nanoprisms under conditions with decreased amounts of AUT. .

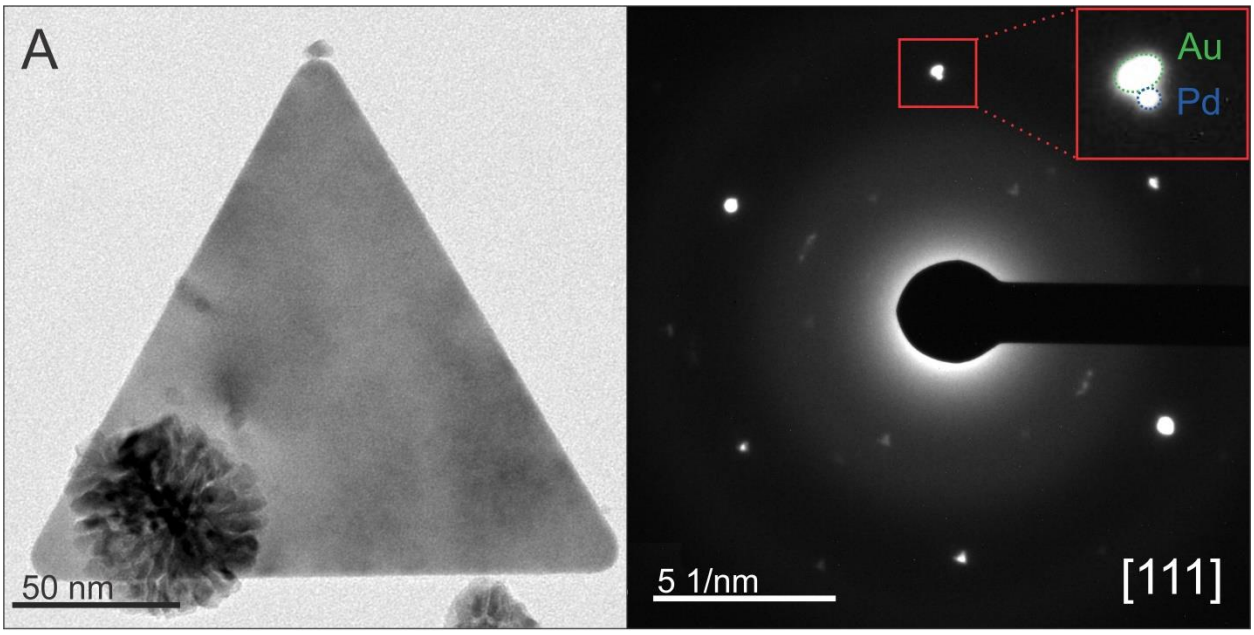

Figure 58. (A) TEM image and (B) corresponding SAED pattern of Pd dendrites attached to Au nanoprisms. The Pd dendrites were found to be single crystals, epitaxially attached from the gold surface in the [111] orientation. Pd and Au d-spacings and were measured to be 2.24 and 2.35 Å, respectively.

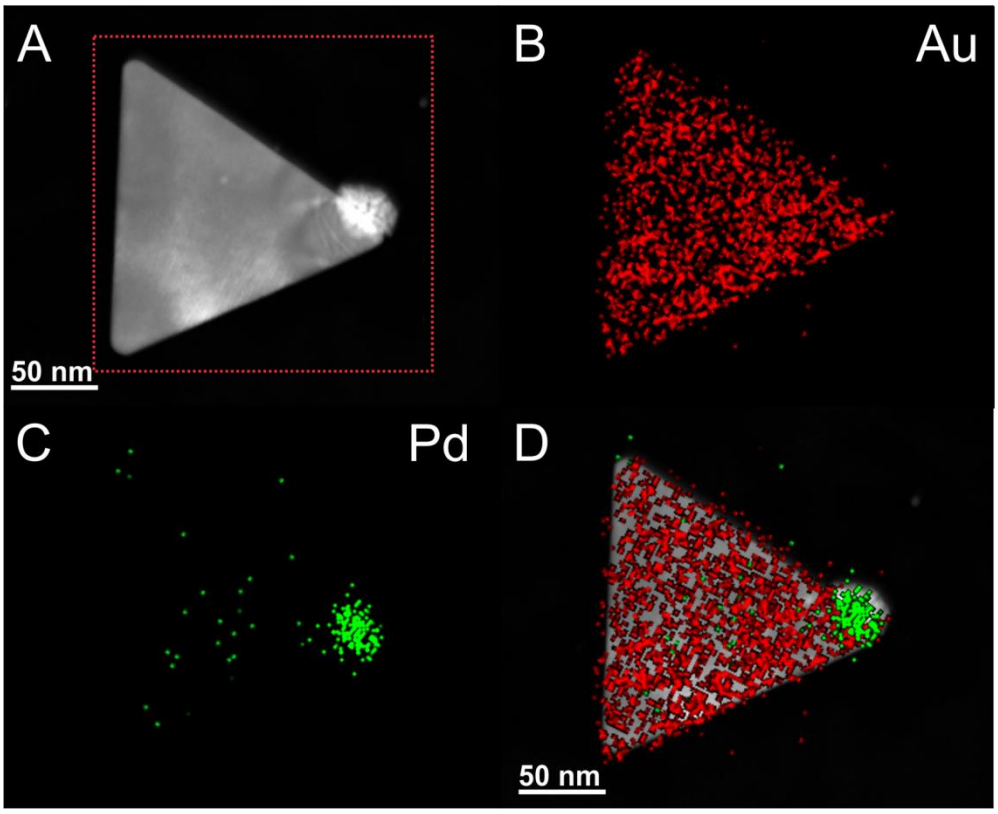

Figure 59. STEM-EDS mapping of Pd deposition on AUT-functionalized Au nanoprisms where a single Pd dendrite is attached pendant to the side of the Au nanoprism. (A) HAADF-STEM image, (B) Au map, (C) Pd map, and (D) Au and Pd signal overlayed on the HAADF-STEM image.

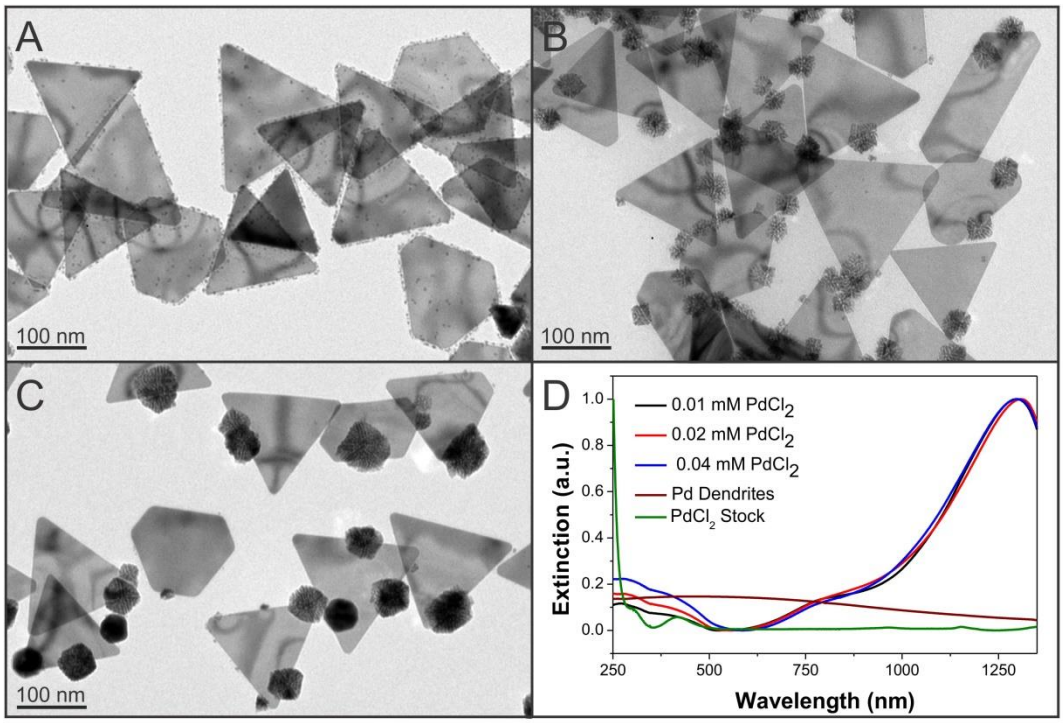

Figure 60. TEM image series and UV-vis-NIR spectra for Au nanoprisms with Pd dendrites of sizes ranging from 5.0 ± 1.0 nm to 50 ± 11 nm. (A) For the lowest growth solution concentrations of $PdCl_2$ (0.01 mM), islands were found to form along the sides of the Au nanoprism, yet dendritic growth was not observed. (B) Increasing the concentration of $PdCl_2$ to 0.02 mM yields dendritic particles at the vertices of the nanoprism (approximate diameter of 30 ± 7 nm, approximately 4.5 ± 3.0 Pd nanoparticles per prism). (C) At the highest concentration of $PdCl_2$ (where subsequent increases in [$PdCl_2$] led to the homogeneous nucleation of "free" Pd dendritic NPs similar to those in Figure 57), Pd dendrites were found to increase in size to 50 ± 11 nm, and a corresponding reduction in the number of Pd dendrites per nanoprism to 2.3 ± 1.9 was measured.

With these results in mind, we next wanted to explore the effect of thiol ligand identity and surface density on the observed Pd deposition pathway. Here, we selected two thiolated ligands with terminal thiol and carboxylic acid functionalities; 11-mercaptoundecanoic acid (MUA) and 3-mercapto-2-methylpropinoic acid (MMPA). We chose MUA as an analogue to AUT to demonstrate that similar alkanethiols (C_{11}) with polar solvent-facing functionalities promote similar Pd deposition pathways. Nanoprisms were also ligand exchanged with MMPA, which is anticipated to have higher densities on lower energy crystallographic facets due to the short chain length (C_3).[176] Ligand exchange efficacy was qualitatively monitored using a combination of ^{1}H NMR and ICP-MS (*vide supra*). In the case of MUA (ligand density of 2.8 ligands/nm^2), dendritic Pd growth at the Au nanoprism vertices was observed, analogous to AUT functionalized nanoprisms (Figure 61). Interestingly, we observed an increased MUA surface density relative to AUT (Table 8), perhaps due to association between the COO^- MUA headgroups and CTA^+ micelles on the surface of the Au nanoprism. On the other hand, for MMPA functionalized nanoprisms, we observed a decreased extent of ligand exchange (from 1.7 to 1.0 ligands/nm^2 with respect to AUT) and deposition of Pd primarily towards the high energy edge facets of the Au nanoprism substrate (Figure 61B).

Due to the statistical deviation in Au nanoprism edge lengths (approximate edge lengths of 150 ± 25 nm), we also correlated the efficacy of thiol ligand exchange by monitoring the iodide surface coverage using ICP-MS. Iodide, a necessary shape directing agent for Au nanoprism growth,[151] binds strongly to the Au(111) surface and is typically not completely removed during washing by centrifugation (Figure 62). Since iodide and thiols both bind to Au(111) three-fold hollow sites (and therefore compete for surface sites),[177] monitoring the decrease in iodide concentration after ligand corroborates ^{1}H NMR analysis of Au nanoprism surface chemistry. As

indicated in Table 8, Au nanoprisms with less iodide on the surface (and correspondingly more thiol coverage by ^{1}H NMR spectroscopy) exhibit a higher extent of Pd incorporation and analogous changes in the extent and location of Pd deposition. Here, this inverse relationship between thiol and iodide surface coverage indicates that while thiols passivate the surface from Pd deposition, adsorbed halides may act as nucleation sites to facilitate Pd growth.

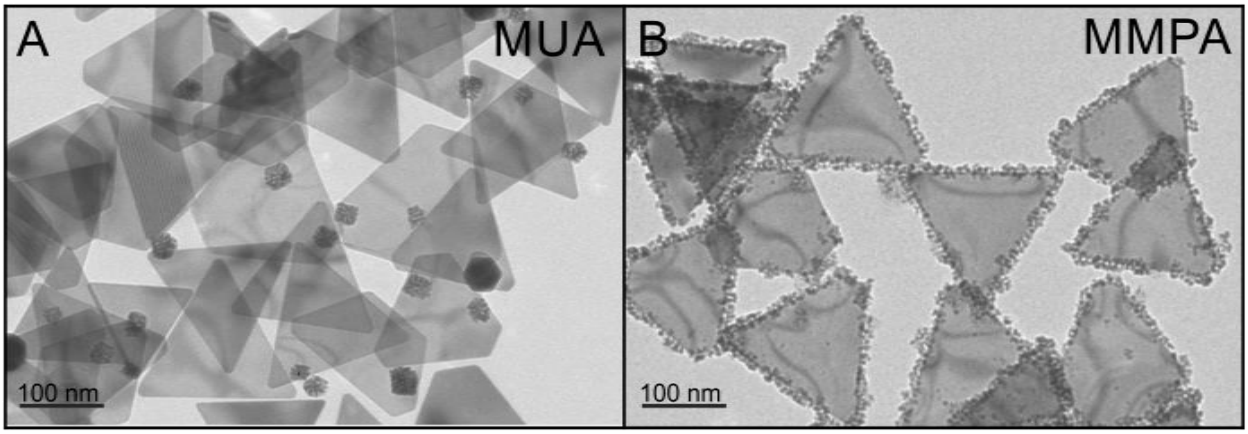

Figure 61. Influence of ligand environment on the Pd deposition pathway for (A) MUA and (B) MMPA functionalized prisms, depicting that the initial surface chemistry of the Au nanoprism substrates affects the extent, location, and morphology of Pd incorporation.

Table 8. ^{1}H NMR and ICP-MS correlating nanoprism surface ligand with the observed deposition pathway and surface chemistry.

Ligand	Deposition Mode	Thiol Density (ligands / nm^2)	Iodide / Prism	Au:Pd Ratio
CTAB	Island	--	14.58	1:0.99
AUT	Vertex	1.7	2.73	1:0.33
MUA	Vertex	2.8	2.30	1:0.36
MMPA	Edge	1.0	5.02	1:0.74

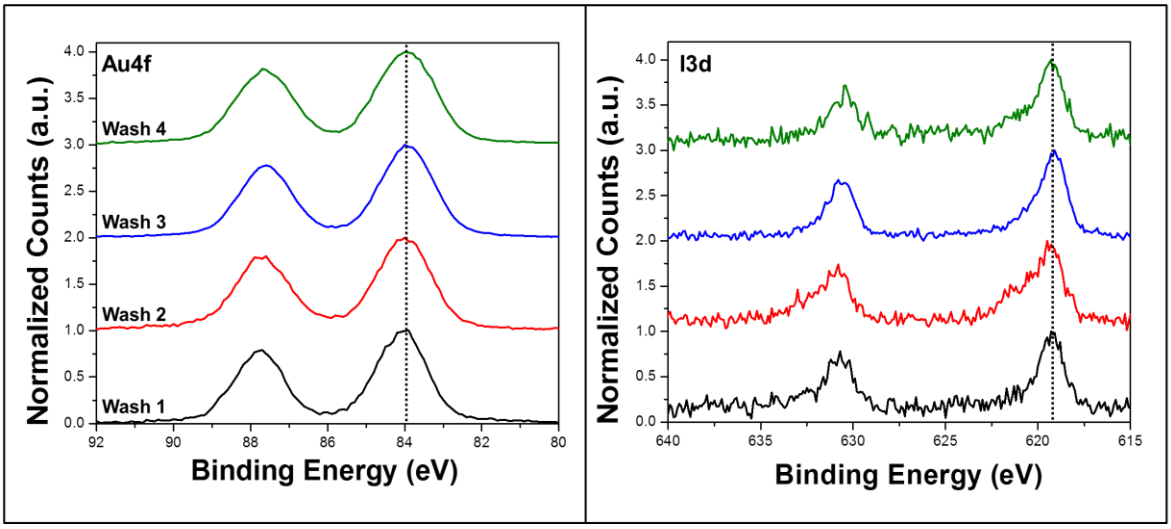

Figure 62. High resolution Au4f (left) and I3d (right) XPS spectra depicting no change in the Au:I ratio even after 4 washes (Au:I compositional ratios from Wash 1 to Wash 4 range from 90 ± 1 % Au relative to 10 ± 1 % I). No further washes were performed, because complete removal of CTAB promotes nanoprism aggregation and oxidative rounding.

Importantly, we demonstrate that trends between ligand surface chemistry and the resulting deposition pathway are relatively general for both nanoprism and nanorod substrates. In a typical experiment, Au nanorods were synthesized according to previous literature procedures[59] and were purified and ligand exchanged with AUT prior to Pd deposition (Figure 63A). The resulting Pd deposition pathway was observed using HRTEM. Importantly, similar trends between metal-ligand surface chemistry and the observed Pd deposition location were observed for both Au nanoprisms and nanorods. In the absence of AUT, reduction of Pd by ascorbic acid in the presence of the purified Au nanorods yields a core@shell Au@Pd morphology, likely due to rapid fusion of Pd islands on the highly-faceted Au nanorod (Figure 64). Images of the nanorods along their longitudinal axis (Figure 63B, inset) reveal a transition from the original Au nanorod octagonal faceting to a rectangular core@shell Au@Pd structure (Figure 63A, inset). After ligand exchange in a solution of 1 μM AUT, "patchy" core@shell Au@Pd structures were observed, likely resulting from partial passivation of the Au nanorod surface. Upon increasing the concentration of AUT during ligand exchange to 5 μM AUT, Pd deposition becomes confined to the ends of the rods at the areas of highest curvature, analogous to Pd dendrite formation on the vertices of the Au nanoprism substrates (Figure 63D). UV-vis-NIR spectra indicates slight shifts (± 20 nm) from the initial maximum absorption wavelength λ_{max} of the longitudinal LSPR after Pd deposition (Figure 65).

Finally, we demonstrate that these methods can be used to direct the incorporation of other noble metals, even Au (Figure 66). Here, we repeat the ligand exchange and secondary metal deposition protocols under identical conditions, except with either H_2PtCl_6 or $HAuCl_4$ metal precursors. In both cases, similar deposition trends were observed, where the number of secondary metal nucleation sites decreased and moved towards the edges or vertices of the

nanoparticle substrate with increasing extents of thiol density. For Pt, low extents of thiol surface density (1.1 AUT/nm^2, *vide supra*) led to a decrease in the number of Pd islands and a loss of linear arrangement. As the concentration of AUT increases (1.5 ligands/nm^2), we observed a transition from Pt island to Pt dendrite growth, consistent with our previous observations.[169] Similar results were obtained when depositing Au on the surface of Au nanoparticle substrates. In the absence of AUT, the nanoprisms oxidized from a triangular to a disc-like morphology, consistent with previous reports of spatially directed oxidation by Au-CTA complexes (Figure 68).[178] After thiol ligand exchange (1.1 AUT/nm^2), however, Au NPs (average diameters of 16 ± 5 nm) deposited in a scattered pattern across the entirety of the Au nanoprism. As the thiol density increased, the size of pendant AuNPs increased to 32 ± 8 nm, and deposition was located primarily towards the edges of the nanoprism. At the highest thiol density, the extent of deposition was reduced with AuNPs confined towards the vertices of the prism, likely due to the competing formation of small (2-3 nm) Au nanoparticles.

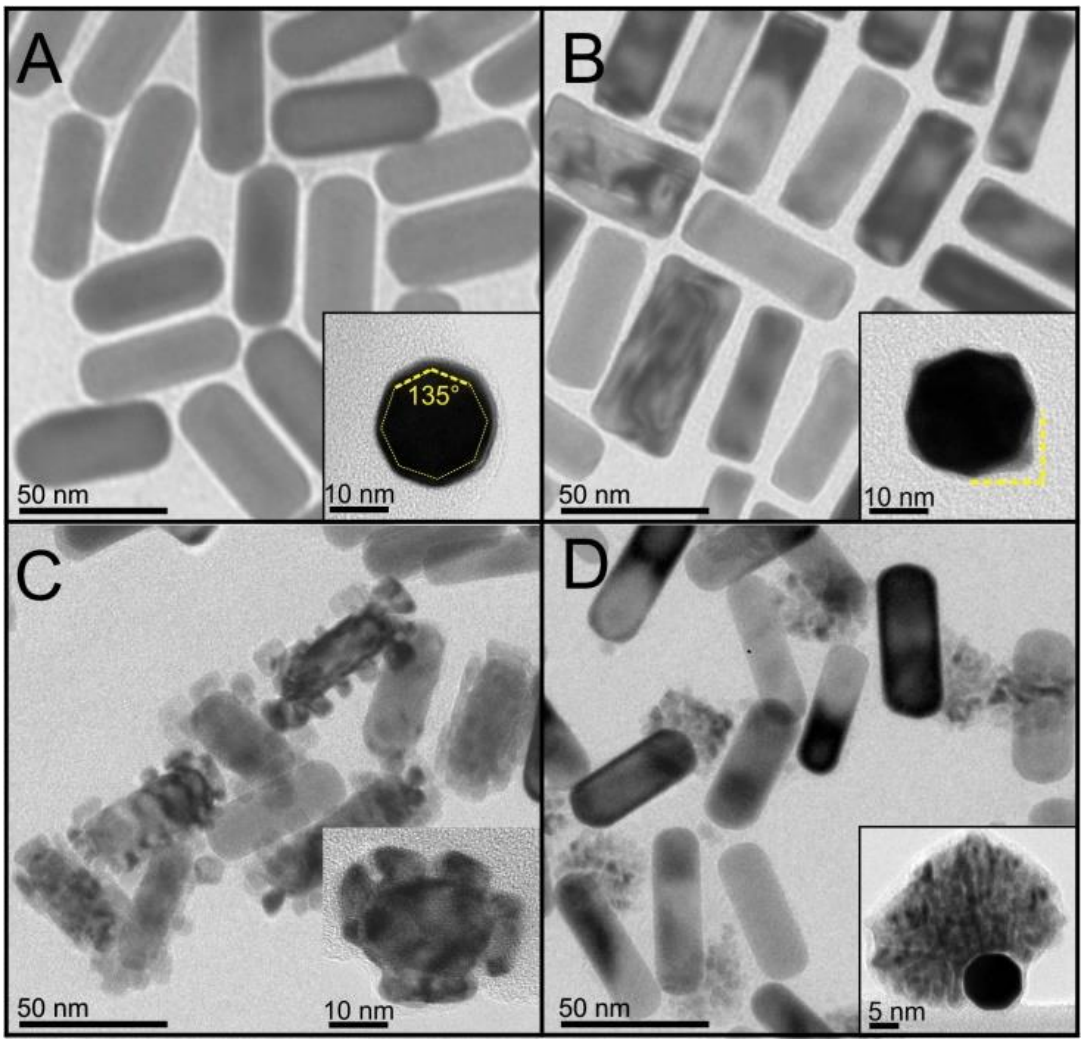

Figure 63. TEM series depicting Pd deposition pathways on Au nanorod substrates. (A) Au nanorods prior to Pd deposition. (B) Core@shell Au@Pd nanobars in the absence of AUT. (C) Partial passivation of the Au nanorod surface (after ligand exchange in a 1 nM solution of AUT) results in patchy Pd deposition. (D) "Complete" surface passivation achieved using a 5 nM solution AUT leads to similar dendritic growth with the Pd dendrite attached to the end facets of the nanorod.

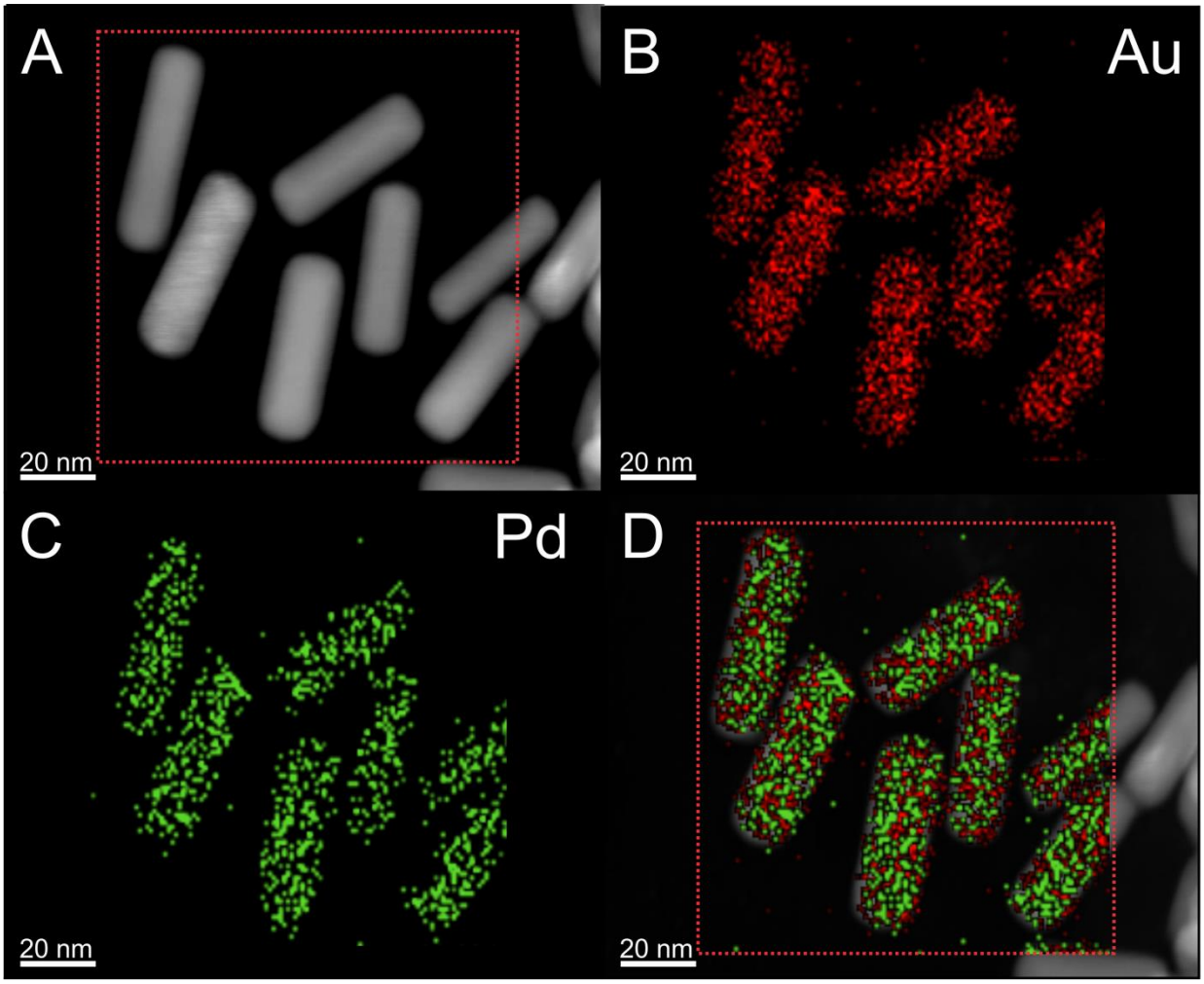

Figure 64. STEM-EDS maps of core@shell Au@Pd nanorods. (A) STEM-HAADF image of Au@Pd nanorods, (B) Au map (C) Pd map and (D) overlay indicating Pd coverage across the majority of the Au nanorod substrate. Au and Pd signals were measured at 9.7 and 2.8 keV, respectively.

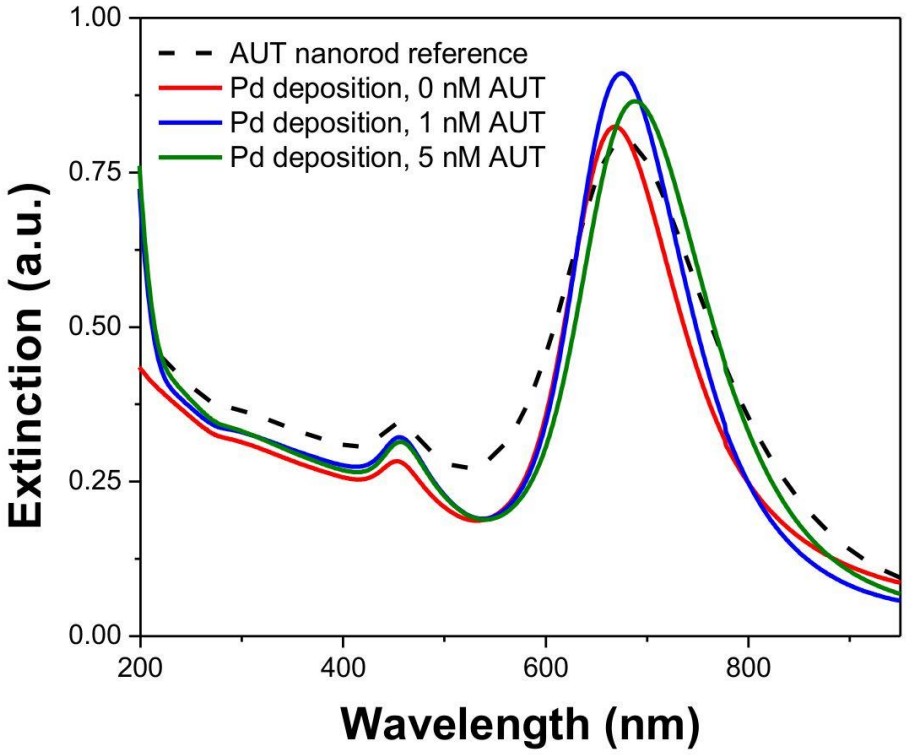

Figure 65. UV-vis-NIR spectra of AUT-functionalized Au nanorods before and after Pd deposition.

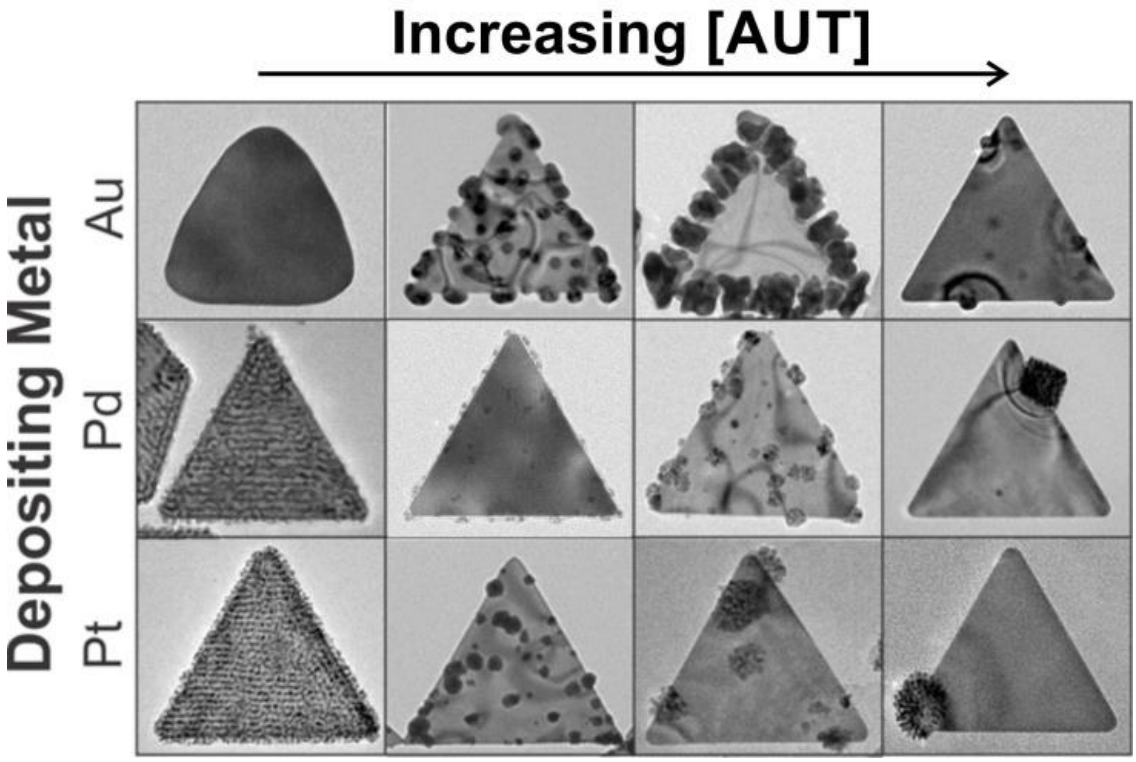

Figure 66. TEM images of Au, Pd, and Pt deposited on Au nanoprisms functionalized with increasing concentrations of AUT. Similar trends are observed for both Pd and Pt, where increasing the density of AUT coverage on the nanoprism surface at the time of Pd deposition results in a decrease in the average number of nucleation sites and a preference for deposition at the edges and/or vertices of the Au nanoprism substrate (Figure 56, *vide supra*). Similar deposition trends were even observed for Au on Au deposition as opposed to layer-by-layer epitaxial deposition. See Figures 67 and 68 for TEM images of Au deposition on Au nanoprisms with increasing AUT densities, and for STEM-EDS maps of each nanoprism product (Au, Pd, and Pt) observed for the highest density of AUT functionalization (right column).

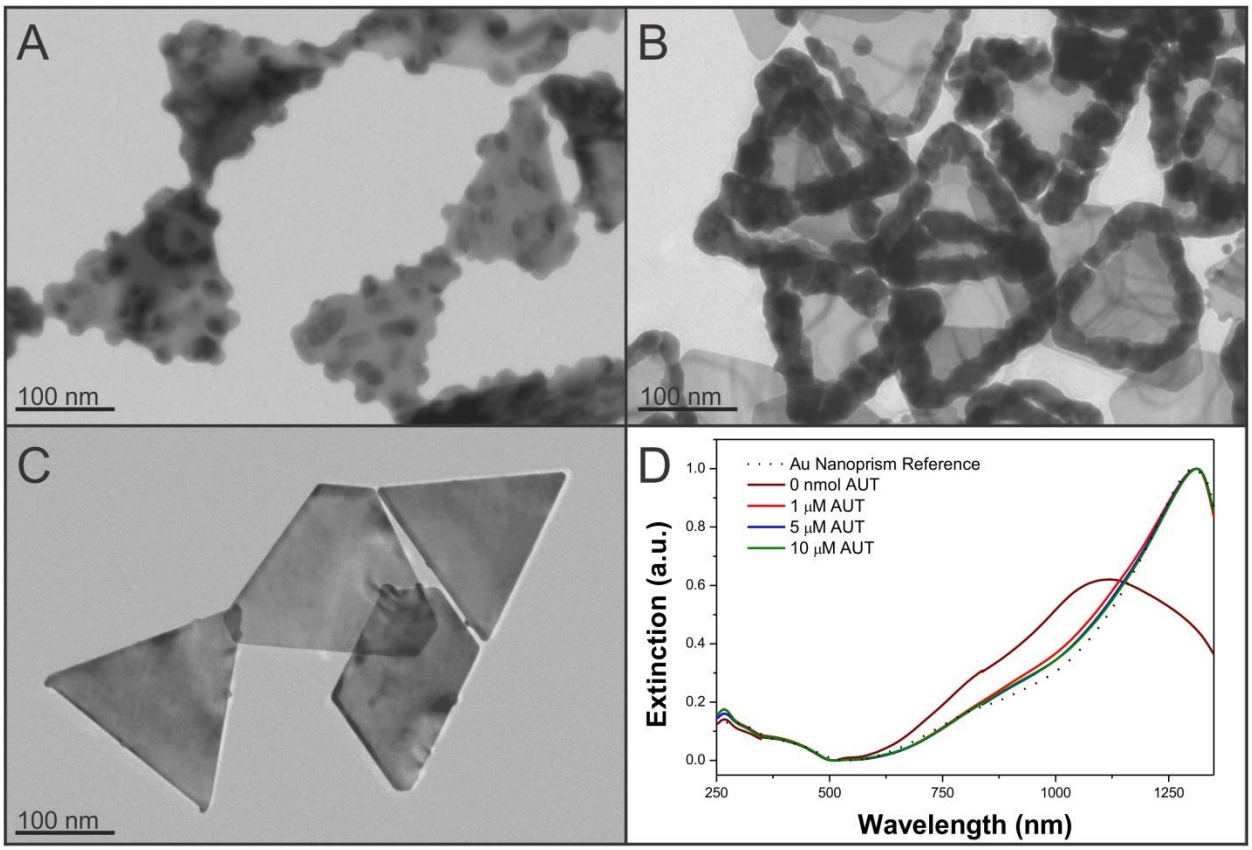

Figure 67. TEM series and UV-vis-NIR spectra of Au deposition on Au nanoprisms ligand exchanged in a 1 μM (A), 5 μM (B), and 10 μM (C) AUT and corresponding UV-vis-NIR spectra. In the absence of AUT, oxidation of the Au nanoprisms into a mixture of discs and irregular plates was observed, consistent with previous reports of Au oxidation by CTA-Au complexes (D, dark red trace).[179] (A) Partial thiolation prior to Au deposition results in the formation of Au islands scattered across the entirety of the nanoprism surface. (B) Edge selective deposition is observed in the presence of 5 μM AUT. (C) Increasing the concentration of AUT in the ligand exchange step to 10 μM results in decreased extent of Au growth located towards the tips of the Au nanoprism.

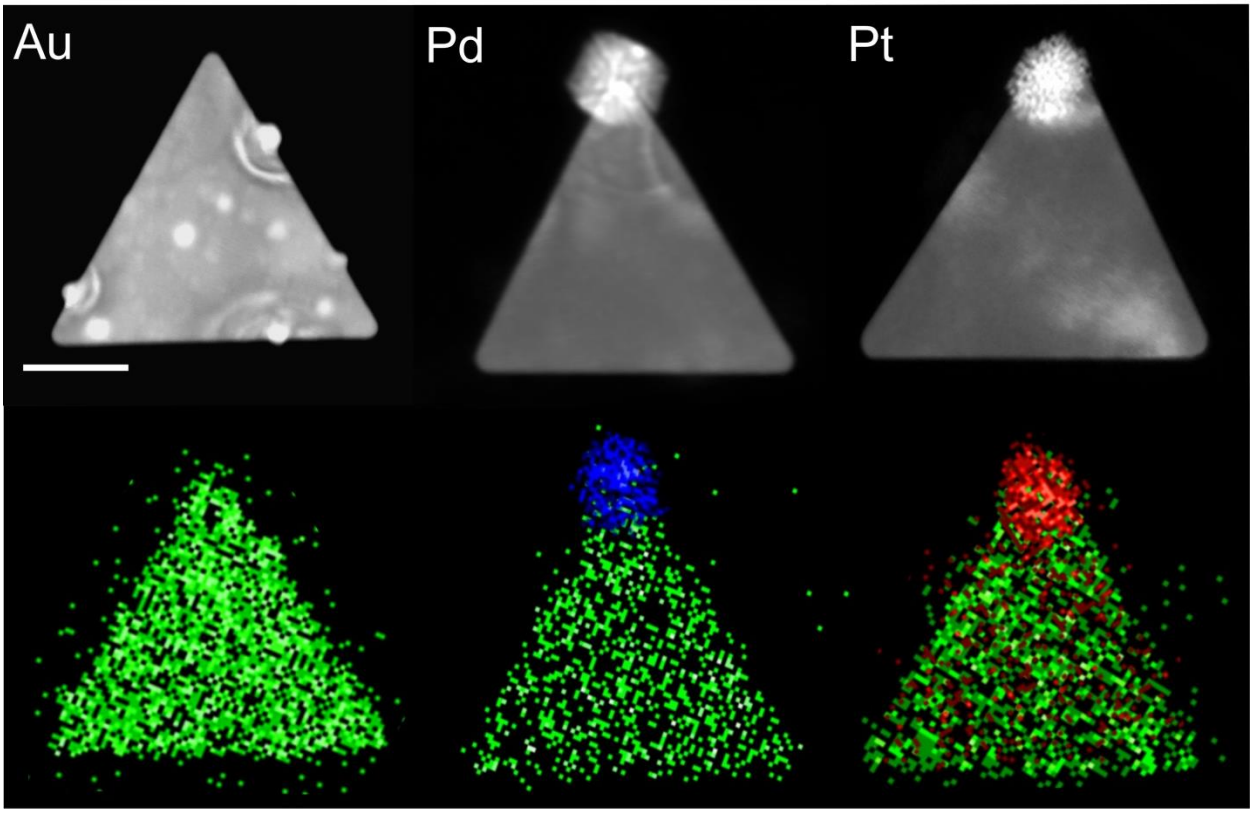

Figure 68. STEM-EDS maps of Au nanoprisms after deposition with Au, Pd, and Pt. (Top row) HAADF-STEM images of the Au nanoprisms after deposition using either Au, Pd, or Pt (from left to right). (Bottom row) STEM-EDS maps corresponding to the HAADF images in the above panels (Au, Pd, and Pt are represented by green, blue, and red, respectively). While Pd and Pt deposit as dendritic structures, Au was found to deposit in island like structures predominantly towards the edge of the prism. Scale bar for all images = 50 nm.

4.4 CONCLUSIONS

In conclusion, we demonstrate metal-ligand surface chemistry as a straightforward and robust approach to tune secondary metal deposition pathways on the surface of anisotropic Au nanoparticles. Depending on the thiolated ligand packing density and iodide surface coverage, Pd deposition could be tuned from island to dendritic morphologies and for edge or vertex selective growth. Similar trends were observed for both alternative substrate morphologies as well as alternative depositing metals, marking metal-ligand surface chemistry as a robust and practical tool for the incorporation of catalytic metals onto plasmonic hotspots.

5.0 COPPER DEPOSITION ON GOLD NANOPRISM SUBSTRATES

(Portions of this work were published previously and are reprinted with permission from Straney, P. J.; Andolina, C. M.; Millstone, J. E. *Isr. J. Chem.*, **2016**, *56*, 257-261. Copyright 2016 Wiley Online Library.

5.1 INTRODUCTION

Multimetallic nanoparticles (NPs) may synergistically combine the properties of individual metals, and have been shown to exhibit enhanced optical[13] electronic,[180] and/or catalytic[181] properties with respect to their monometallic counterparts. In particular, there is strong interest in incorporating earth-abundant metals within, on, or in place of architectures containing precious metals such as Pt, Pd, Au, and Ag. In some cases, incorporating earth-abundant metals not only can reduce the cost of such architectures, but also improve their performance in technological applications.[182-185]

However, developing synthetic methods that can combine or replace precious metals with oxophilic metals, such as those in the 3d block, can be challenging due to competing processes such as metal oxidation[186] or redox-related metal segregation.[187-188] An attractive synthetic strategy for combining these two types of elements would leverage the extensive knowledge

gained in the study of noble metal nanoparticle synthesis. For example, a common synthetic pathway for the formation of multimetallic nanostructures involves reduction of the secondary metal in the presence of a metal nanoparticle substrate or "seed".[53,71,189-190] During this process, the second metal can have several possible reactions with the existing nanoparticle substrate including diffusion into the substrate to create an alloyed region,[191] deposition onto the substrate to form core@shell or "island" architectures,[152,192-193] and/or oxidation of the underlying particle to form hollow structures.[194] For many of these syntheses, reduction rate of the metal precursors as well as their relative reduction potentials play a significant role in the final particle composition and composition architecture[169,195-196] (similar to the important influence of these parameters in controlling nanoparticle size and shape).[55,88,197-198]

In the case of the 3d transition metals, standard reduction potentials of cation precursors are typically lower than those of precious metal cation precursors. Therefore, while galvanic replacement reactions become less of a concern, stronger reducing agents are needed to reduce 3d transition metal cations. Yet, controlled reactions are required for well-defined nanocrystal growth (here, "reaction" refers to both the reduction of metal cations as well as subsequent nanoparticle nucleation and growth). Here, we use Cu as a representative late 3d transition metal, and report the synthesis of various Au-Cu nanoparticles using Au nanoprism seeds. We specifically focus on approaches that indicate bottom-up control over the final hybrid morphologies including both core@shell and island deposition products.

5.2 EXPERIMENTAL

5.2.1 General Materials and Methods

Cetyltrimethylammonium bromide (CTAB, 99%), copper (II) acetate monohydrate ($Cu(OAc)_2 \cdot H_2O$, >99.0%), hydrogen tetrachloroaurate trihydrate ($HAuCl_4 \cdot 3H_2O$, 99.99%), L-ascorbic acid (99%), sodium borohydride ($NaBH_4$, 99.99%), sodium iodide (NaI, 99.999%), tetrabutylammonium borohydride (Bu_4NBH_4, 98%), and trisodium citrate (99%) were obtained from Sigma-Aldrich, sodium hydroxide (NaOH, 99.0%) was obtained from Fisher Scientific, and all reagents were used as received. All solutions were prepared using NANOpure™ (Thermo Scientific, >18.2 MΩ·cm) H_2O and were made fresh prior to use. All H_2O used during synthesis and reaction work-up was NANOpure™. All reagents were used in air at room temperature unless otherwise noted. All solutions were prepared in H_2O unless otherwise noted. All glassware was washed with aqua regia (3:1 ratio of concentrated hydrochloric acid and nitric acid by volume) and rinsed copiously with H_2O. *Caution: aqua regia is toxic and corrosive and must be handled in a fume hood with proper personal protection equipment.*

5.2.2 Synthesis and Preparation of Au Nanoprism Substrate

First, Au nanoprisms were synthesized according to previous protocols.[63,169] Two hours after Au nanoparticle seeds were added to the nanoprism growth solution, the reaction mixture was heated in a H_2O bath to 37 °C for 1 minute to dissolve any CTAB that may have recrystallized during the growth period (this crystallized CTAB can interfere with nanoprism purification by centrifugation). To separate the nanoprisms from pseudospherical nanoparticle reaction

byproducts, 90 mL of the reaction mixture was divided into 15 mL conical tubes and centrifuged at 820 rcf for 15 minutes (Eppendorf centrifuge 5804 with swing bucket rotor A-4-44). The supernatant and pellet were both extracted and the nanoprism thin film was resuspended in 1.0 mL of H_2O by vortexing for 5 seconds. To remove additional CTAB and excess reagents, this mixture was transferred to 1.5 mL centrifuge tubes, and the prisms were then centrifuged using a Spectrum mini-centrifuge (SC1006-R) for approximately 5 minutes. After centrifugation, the supernatant was removed and the prisms were resuspended in 1.0 mL of H_2O and subsequently combined in a 15 mL conical tube. The concentration of the purified nanoprisms in the nanoprism stock solution was then adjusted to an optical density (O.D.) of 1.0 a.u. at the maximum absorption wavelength (λ_{max}, approximately 1300 nm) by ultraviolet-visible-near infrared (UV-vis-NIR) spectroscopy.

5.2.3 UV-vis-NIR Spectroscopy

Nanoprism solutions were analyzed by UV-vis-NIR spectroscopy using a Cary 5000 spectrophotometer (Agilent, Inc.). Baselines were collected using H_2O as reference solutions.

5.2.4 Transmission Electron Microscopy

After Cu deposition, the resulting nanoparticle products were purified by centrifugation using a Spectrum mini-centrifuge (SC1006-R). After removal of the supernatant, the pellet was resuspended in 1.0 mL of H_2O and the process was repeated. After subsequent removal of the supernatant, nanoprism products were resuspended in 30 μL of H_2O by briefly vortexing the solution (~ 5 s) followed by brief sonication (~ 5 s). A 5 μL aliquot of each concentrated

nanoprism sample was dropcast onto a carbon-backed molybdenum TEM grid (Pacific Grid Tech, 400 mesh Mo with thin carbon film), allowed to dry under ambient conditions and stored under vacuum prior to analysis. Samples were imaged on one of the following microscopes: a FEI Morgagni 268 at 80 kV (Microscopy and Imaging Facility, Department of Biology, University of Pittsburgh), a JEOL JEM 2100F equipped with a Gatan Imaging Filter (GIF) Tridiem camera and Oxford Inca EDS detector at 200 kV (Nanoscale Fabrication and Characterization Facility (NFCF), Petersen Institute of Nanoscience and Engineering (PINSE), University of Pittsburgh), or a FEI Tecnai G2 using a 200 kV accelerating voltage (Department of Mechanical Engineering and Materials Science characterization facility, University of Pittsburgh). Images were analyzed using Digital Micrograph v2.10.1282.0 (Gatan, Inc.) and/or ImageJ v 1.47d (National Institutes of Health, USA) software. Fast Fourier transform (FFT) images were indexed according to standard face-centered cubic (FCC) diffraction patterns. Scanning transmission electron microscopy energy dispersive X-ray spectroscopy (STEM-EDS) elemental maps and linescans were collected using the JEOL JEM 2100F electron microscope (NFCF, PINSE, University of Pittsburgh). Oxford Inca software was used for data processing and generation of elemental maps. The copper Kα and gold Lα lines were selected for elemental characterization due to their respective signal strengths. EDS spectra were collected using a beryllium double tilt holder (JEOL #31640), a tilt angle of 14 degrees in the positive X direction toward the EDS detector and a STEM probe diameter of 1.5 nm. The EDS was acquired using 2k channels from 0 to 20 keV. Elemental maps were collected for 40-60 minutes and the site lock feature was used to correct for sample drift during acquisition, with a pixel dwell time of 1000 μs and a pixel resolution of 128x128.

5.2.5 Synthesis of Cu Island and Core@Shell Nanoprisms

1.0 mL of the purified nanoprism stock solution ($O.D._{\lambda max}$ = 1.0 a.u.) and 7.5 – 30.0 μL of 10 mM tetrabutylammonium borohydride were added to a 1.5 mL centrifuge tube and vortexed (Analogue Vortex Mixer, 120 V, Fisher Scientific) for 10 seconds. To this solution, 7.5 to 30.0 μL of a 4 mM solution of $Cu(OAc)_2$ was then added over the course of 45 seconds (as measured on a standard lab timer) while gently vortexing (for a final $Cu(OAc)_2$:Bu_4NBH_4 ratio of 1:2.5). While the reagent order or rate of addition was not critical to achieving Cu deposition on the surface of the nanoprism, the described procedure did help to prevent homogeneous nucleation of discrete CuNPs. After synthesis, the reaction was allowed to rest for 30 minutes before further analysis.

5.2.6 X-ray Photoelectron Spectroscopy (XPS) and Auger Electron Spectroscopy (AES) Methods

Silicon wafer substrates (University Wafer, p-doped, 200 nm thermal oxide (SiO2)) were cleaned by sonication in ethanol for 5 minutes. The substrates were then rinsed with ethanol and dried under air. Nanoparticle products were concentrated and purified as described for TEM analysis, and a 10 μL aliquot of the resulting solution was dropcast onto a 1x1 cm silicon wafer substrate and allowed to dry. The samples were placed under vacuum for 24 hours to mitigate surface contamination. XPS spectra were obtained using an ESCALAB 250XI XPS with a monochromated, micro-focused Al Kα X-ray source (spot size = 200 μm; step size = 0.1 eV, pass energy = 50 eV). Spectra were charge referenced to adventitious carbon (284.8 eV). For

sputtering analysis, samples were sputtered with Ar ions (current = 500 mV) for a period of ten seconds.

In order to determine the oxidation state of Cu, the Au-Cu prisms were analyzed using a combination of XPS and AES. While these techniques are convenient in differentiating between types of Cu species (i.e. metallic, oxide, or hydroxide), exposure of the Cu containing nanoparticles to air during sample preparation may influence the observed Cu compositions. For this reason, two sets of samples were analyzed: one sample was dried and stored under ambient conditions and the other sample was dried and stored under vacuum. For the sample prepared and stored under ambient conditions, initial analysis of the surface indicates the presence of surface oxygen species. Here, the presence of oxygen may indicate either formation of a Cu oxide or surface-adsorbed oxygen containing species.[3] These features disappeared after either simply incubating the sample in UHV conditions for 16h (Figure 84) or by brief Ar ion sputtering (Figure 85), indicating the presence of oxide species are not indicative of a copper oxide, but rather environmental contamination.

5.3 RESULTS AND DISCUSSION

In a typical experiment, an aqueous solution of Au nanoprisms (edge length = 150 ± 25 nm, thickness = 8 ± 2 nm) was synthesized and purified using literature protocols[63,169] (see Supporting Information (SI) for full details). Cu growth was initiated by dropwise addition of copper (II) acetate (7.5-30 μL of 4 mM, $Cu(OAc)_2$) to an aqueous solution of purified Au nanoprisms and tetrabutylammonium borohydride (7.5-30 μL of 10 mM, Bu_4NBH_4) under ambient conditions. The choice of reagents reflects several requirements of incorporating metallic Cu in or on the Au nanoparticle surface. First, we found that approaches using weaker reducing agents such as ascorbic acid do not effectively reduce the Cu precursor for deposition. However, when stronger reducing agents are introduced, the increased rate of Cu cation reduction leads to both heterogeneous (on the Au nanoparticle) and homogeneous nucleation of Cu nanostructures. Therefore, we mediate the reduction of Cu in two ways: chemically and by synthetic procedure.

First, we mediate the reduction rate by raising the energy barrier to reduction via coordinating ligand effects on the Cu cation and borohydride precursors (assuming the rate of Cu reduction follows Arrhenius behavior). In the case of the Cu precursor, $Cu(OAc)_2$ exhibits complex speciation in aqueous solution, including the formation of binuclear complexes,[199] which impacts the reduction rate of Cu(II) (*N.B.* while standard reduction potential can also be impacted by speciation, the case of the Cu cation precursors considered here are not known to exhibit marked changes in this parameter, *vide infra*). Formation of elemental Cu is also observed by partial reduction of Cu(II) to Cu(I), which then undergoes disproportionation to form both Cu(0) and Cu(II) species.[200] Together, these processes may contribute to slower production of Cu(0) using $Cu(OAc)_2$ in comparison to chloride or nitrate analogues, despite

nominal change in standard reduction potentials between the three precursors. Likewise the reducing agent, BH_4^-, has been found to exhibit similar reduction potentials with a variety of coordinating cations. However, Bu_4NBH_4 reacts more slowly than analogues such as $NaBH_4$, and this difference in reaction rate has been attributed to steric hindrance imposed by the butyl groups[201] (see Figure 69 for reference comparison between Bu_4NBH_4 and $NaBH_4$ in a traditional AuNP synthesis). In short, ligands in the synthesis influence reaction barriers via steric and other coordinating effects, even for reagents that have similar standard reduction potentials.

The ratio and rate of reagent addition was also found to influence the presence and extent of Cu deposition onto the Au nanoprism substrates, likely by mediating the concentration of Cu(0) in solution during the initial growth stages of Cu nanostructures. Various ratios of metal cation to reducing agent were tested (1:0.1, 1:1, 1:2.5, 1:5, and 1:10), and a molar excess of reducing agent was needed to generate mixed-metal structures. Deposition of Cu on the Au nanoprism surface was observed at a 1:2.5 molar ratio of Cu precursor to reducing agent. While an excess of reducing agent is important to ensure complete conversion from Cu(II) to Cu(0), further increasing the Bu_4NBH_4 concentration decreased the observed selectivity for Cu deposition onto the Au nanoprism surface. It is important to note that even in the experimental conditions leading to well-defined Cu deposition on the prism substrate, there is likely a competing reaction of discrete, pure CuNP formation via homogeneous nucleation. However, at metal precursor to reducing agent ratios of 1:2.5, we find that homogeneous nucleation can be further mitigated by using a dropwise addition of the Cu precursor (total Cu precursor volume added dropwise over the course of 45 s). CuNPs were rarely observed in these syntheses during any of our analysis both by electron microscopy and absorption spectroscopy techniques (Figure 70). We also note that although the Au nanoprisms are synthesized in the presence of cetyltrimethylammonium

bromide (CTAB), excess CTAB is removed during prism purification prior to secondary metal deposition (approximate CTAB concentration is <5 μM during reaction with secondary metal). The resulting Au-Cu nanoparticle products were discrete, triangular gold nanoprisms with Cu deposition densities that could be tuned using classic colloidal synthesis strategies. Specifically, Cu density could be modified by changing the total concentration of reagents in the reaction solution (at a 1:2.5 ratio of $Cu(OAc)_2$:Bu_4NBH_4) and/or adjusting the concentration of the nanoprism seeds at the time of Cu reduction (Figure 71). Cu nanoisland growth was observed for volumes ranging from 7.5-15.0 μL of 4 mM $Cu(OAc)_2$, where increasing the total concentration of $Cu(OAc)_2$ proportionally increased the Cu coverage densit. Interestingly, further increasing the $Cu(OAc)_2$ concentration results in a transition to a core@shell structures.

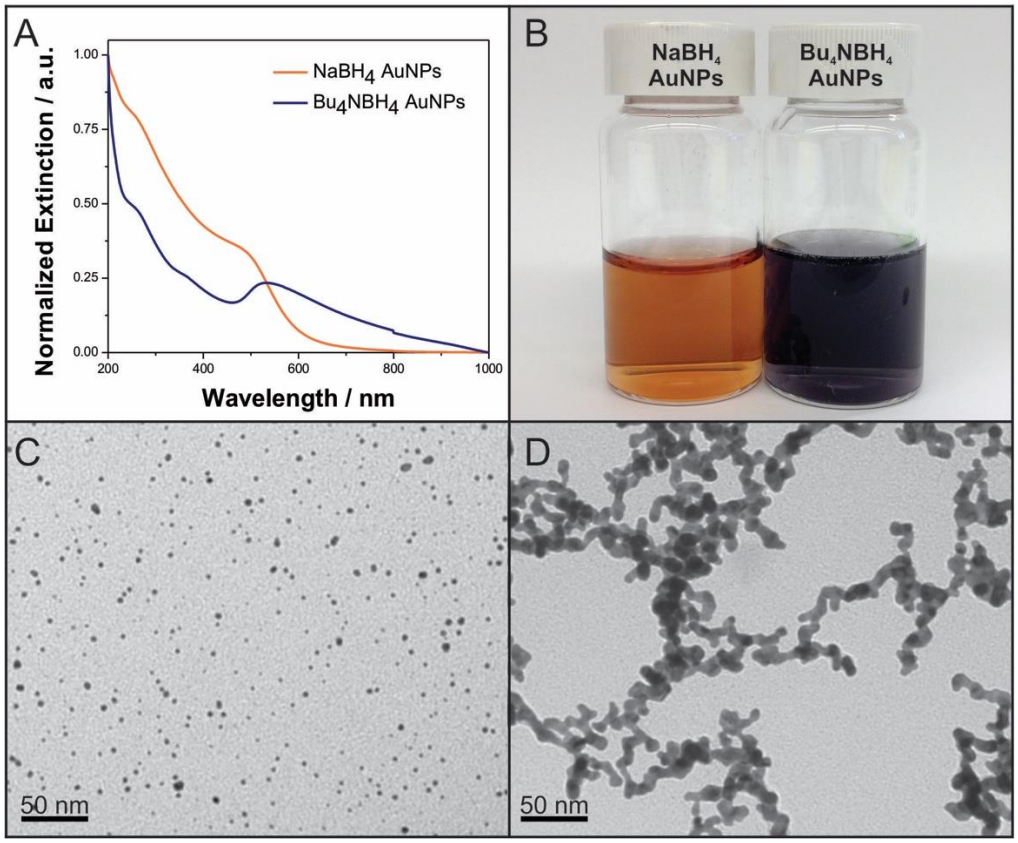

Figure 69. Comparison between AuNPs synthesized using $NaBH_4$ and Bu_4NBH_4, where 10 mL of 0.25 mM $HAuCl_4$ was reduced by rapidly injecting 0.25 mL of an aqueous solution of the BH_4^- reducing agent while vortexing. (A) UV-vis-NIR spectra of AuNPs synthesized using $NaBH_4$ (orange trace) and Bu_4NBH_4 (blue trace). (B) Photograph of as-synthesized AuNP solutions, where color change from orange to purple indicated colloid aggregation, (C) TEM of AuNPs synthesized with $NaBH_4$ (average NP diameter approximately = 3.1 ± 1.4 nm). (D) TEM of AuNPs synthesized with Bu_4NBH_4 depicting increased NP size polydispersity and aggregation of NPs into large networks.

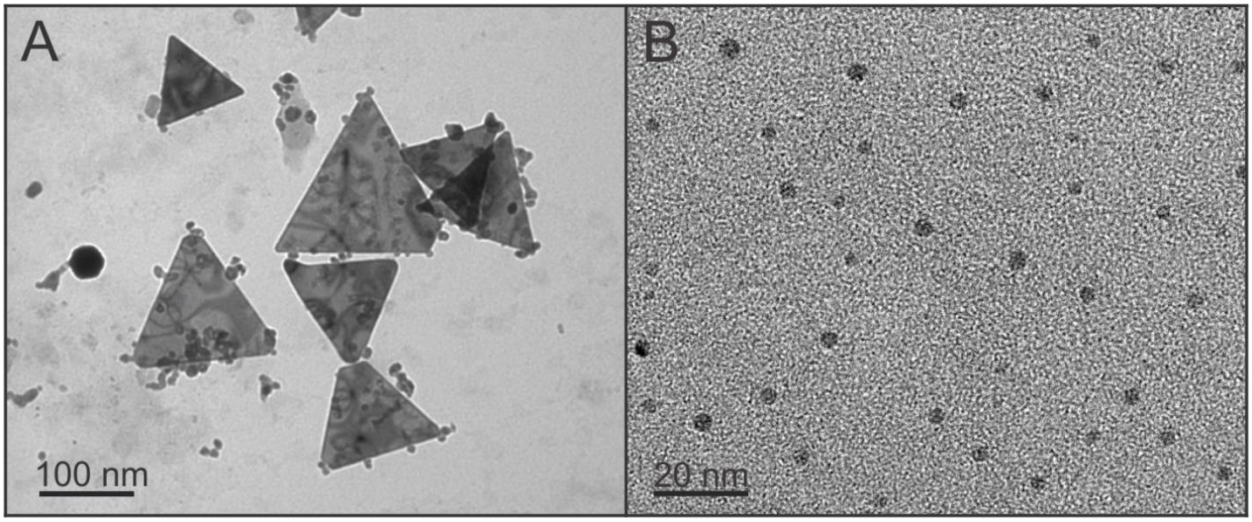

Figure 70. TEM images depicting homogeneous nucleation of CuNPs (~4.4 ± 1.0 nm in diameter) in a single addition synthesis.

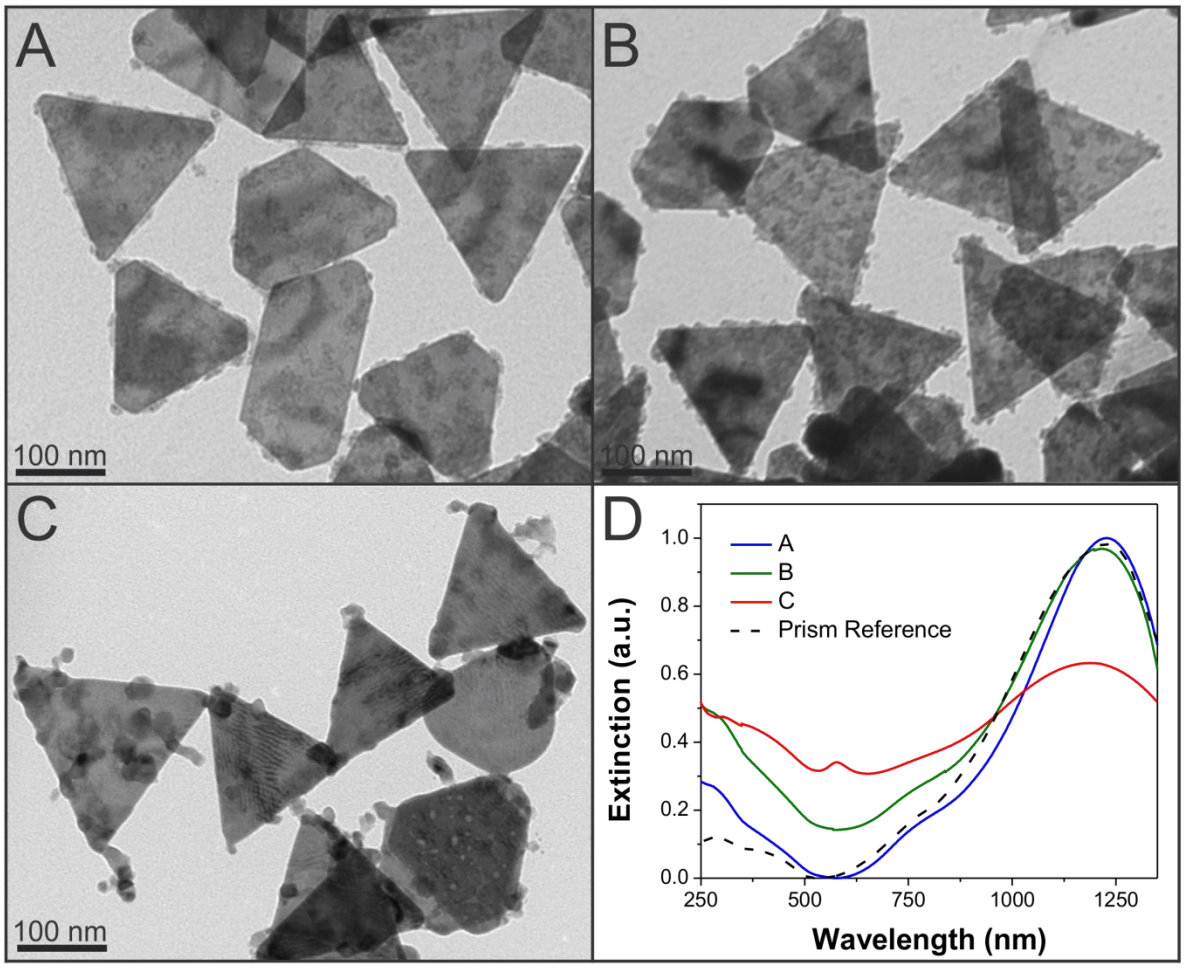

Figure 71. TEM images of Cu deposition on Au nanoprisms synthesized with 7.5 (A), 15.0 (B), and 30.0 μL (C) of 4 mM $Cu(OAc)_2$ at a $Cu(OAc)_2$:Bu_4NBH_4 ratio of 1:2.5. (D) Corresponding extinction spectra showing both increasing spectral breadth and decreasing intensity of the Au LSPR as a function of increasing Cu deposition.

Correlations between extent of Cu deposition and the resulting changes in nanoparticle optical properties were measured using absorption spectroscopy (Figure 71D). As the extent of Cu density on the nanoprism surface increased, the Au nanoprism in-plane dipole localized surface plasmon resonance (LSPR) ($\lambda_{max} \approx 1225$ nm, full width at half maximum (FWHM) ≈ 375 nm) blue-shifted and the FWHM increased ($\Delta\lambda_{max=}$ 20 nm, ΔFWHM ≈ 40 nm). For core@shell products, Cu surface coverage of the Au nanoprism further damped the LSPR, causing an approximate 40% reduction in peak intensity. At the same time, a new feature was observed in the visible region ($\lambda_{max} = 578$ nm). The peak position of this feature is consistent with the LSPR of CuNPs observed previously.[202-203] However, contributions from the underlying prism substrate may be influencing its spectral position, intensity and lineshape. Therefore, a definitive assignment is not possible without further modeling. We note that the peak does not match either the spectrum of aqueous $Cu(OAc)_2$ or free CuNPs at the size range observed in these syntheses (4.4 ± 1.0 nm, Figure 72).

For nanoparticle products with island-like Cu morphologies, high angle annular dark-field scanning transmission electron microscopy (HAADF-STEM) imaging indicates the location and extent of Cu deposition because changes in contrast correspond to changes in both elemental composition and material thickness (Figure 73). Here, the increase in material thickness allows the Cu island structures to appear in higher c**o**ntrast relative to the Au nanoprism despite lower atomic number. At low concentrations of $Cu(OAc)_2$ (final concentrations of 30 to 60 μM, corresponding to 7.5 and 15 μL of 4 mM $Cu(OAc)_2$ additions), Cu deposited in heterogeneous island-like structures growing directly from the surface of the Au nanoprism. On the interior terrace of the triangular face, the Cu structures resemble a Volmer-Weber growth mode of island formation, consistent with previous thin-film investigations of Cu deposition on Au(111)

substrates.[204-205] While there is a strong driving force for Au-Cu bond formation in the gas phase,[206] elastic strain and tensile stress between the Au and Cu layers generally prevent formation of a uniform Cu monolayer[207-208] and hence areas of the Au nanoprism remain exposed after growth. The extent of Cu deposition was found to increase towards the edges of the Au nanoprisms, as indicated by the increased contrast of the Au nanoprism triangular tips. At higher concentrations of $Cu(OAc)_2$ (final concentration of 90 μM, corresponding to 30 μL of 4 mM $Cu(OAc)_2$ addition), Cu islands were found to fuse into a heterogeneous Cu shell encapsulating the nanoprism (Figure 74 - Figure 77).

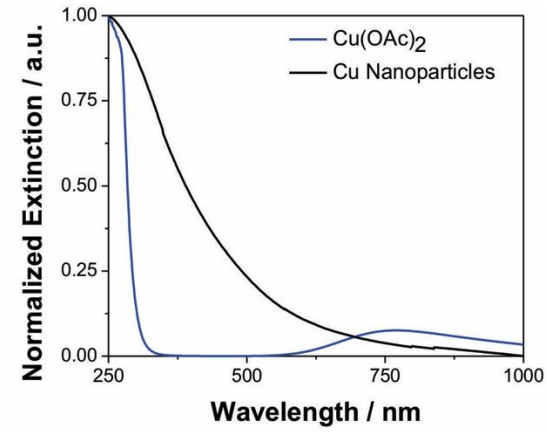

Figure 72. UV-vis-NIR spectra of $Cu(OAc)_2$ precursor solution and discrete, homogeneously nucleated CuNPs (4.4 ± 1.0 nm). Here, CuNPs were formed by Bu_4NBH_4 reduction of $Cu(OAc)_2$ in H_2O in the absence of Au nanoprism substrates.

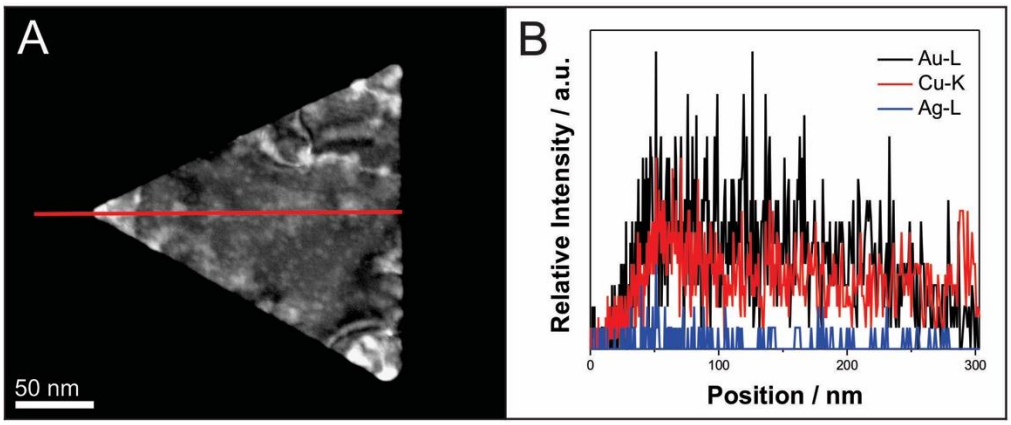

Figure 73. **(**A) High Angle Annular Dark Field (HAADF)-STEM image of a Au-Cu island nanoprism and (B) corresponding STEM-EDS linescan of the Au-L and Cu-K edge intensity as a function of position corresponding to the red line in panel A. Ag-L edge is included for reference, and samples were analyzed using a Mo support.

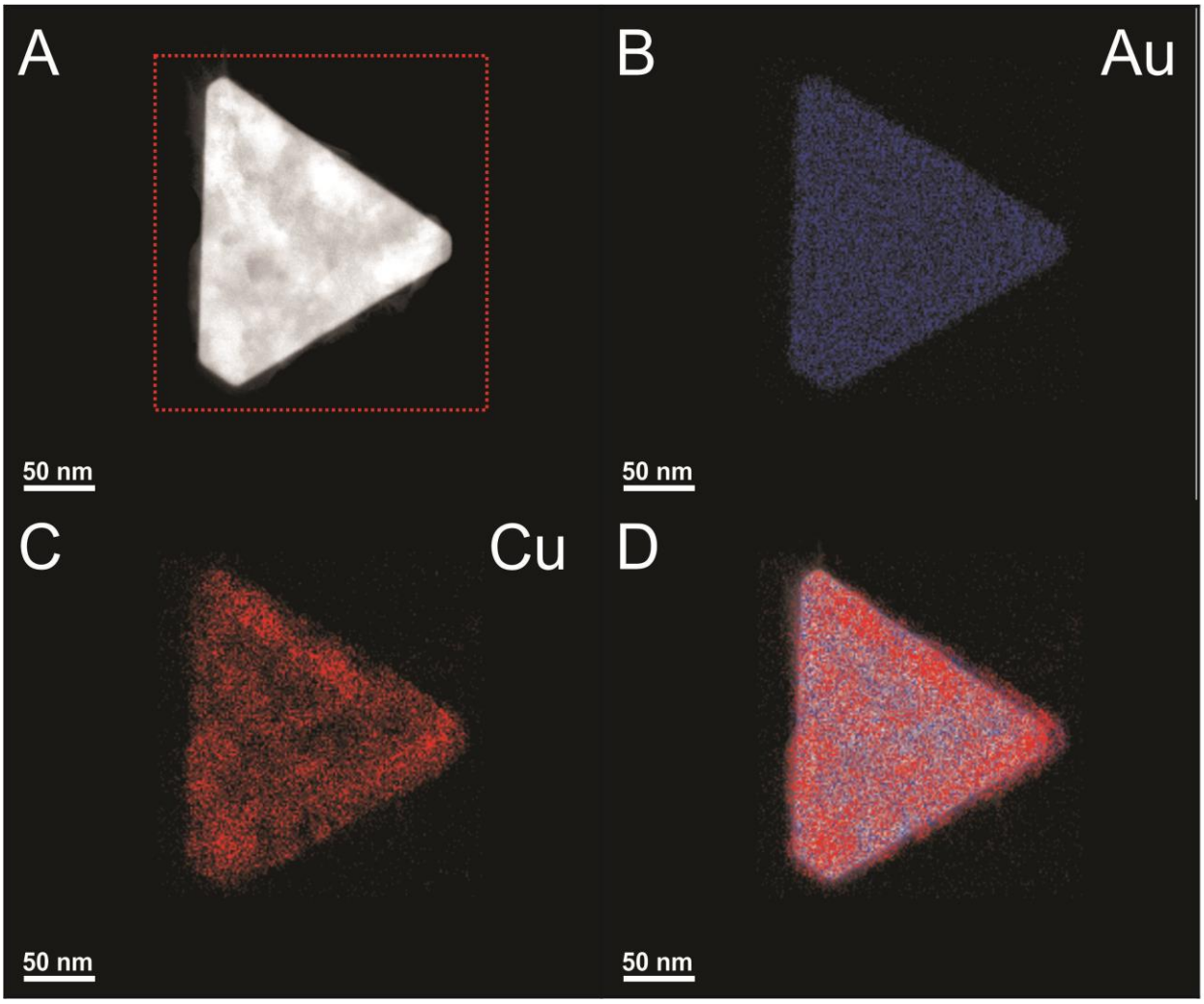

Figure 74. STEM-EDS analysis of the Au@Cu nanoprisms. (A) High angle annular dark-field (HAADF) STEM image of the Au@Cu nanoparticle products. (B) Au STEM-EDS map (Au Lα line intensity), (C) Cu STEM-EDS map (Cu Kα line intensity), and (D) overlay of (B) and (C) on HAADF-STEM image (A). Cu was found to form a heterogeneous shell across the Au nanoprism surface.

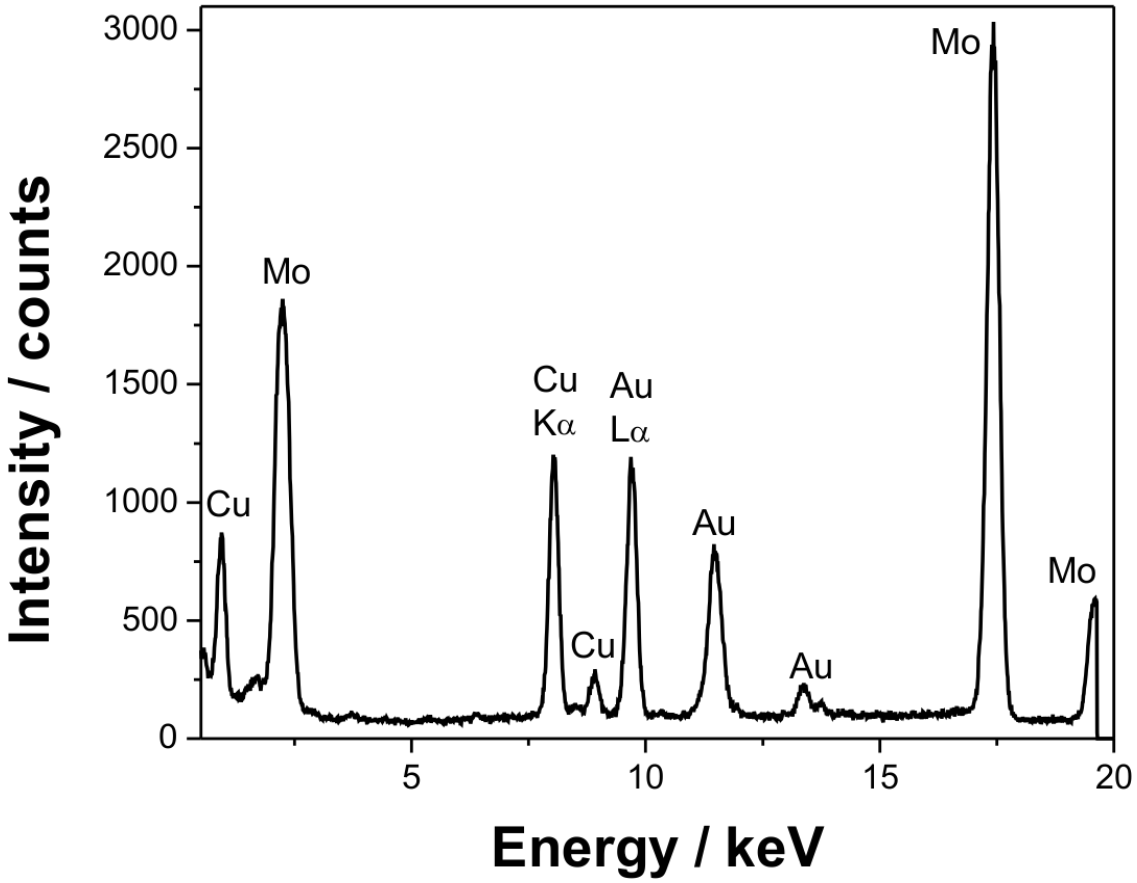

Figure 75. EDS sum spectra corresponding to the STEM-EDS maps in Figure 74. Intensity of the Cu and Au signals were measured by the Cu Kα and Au Lα lines at 8.0 and 9.7 eV, respectively.

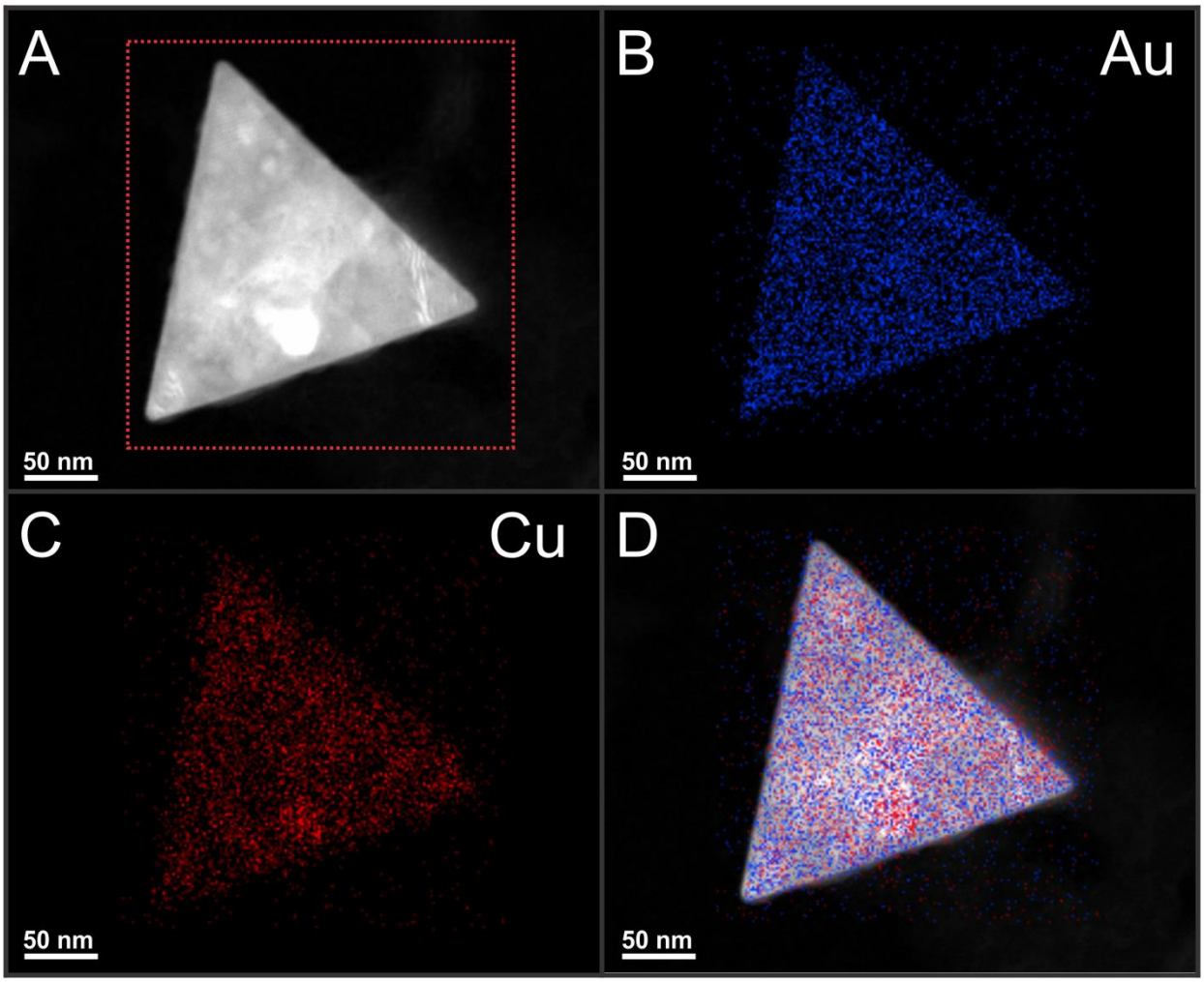

Figure 76. STEM-EDS map of the Au@Cu nanoprisms. (A) HAADF-STEM image of the Au@Cu nanoparticle products. (B) Au STEM-EDS map, where the Au signal was measured by Au Lα line intensity (Figure 77). (C) Cu STEM-EDS map, where the Cu signal was measured by Cu Kα line intensity (Figure 77). (D). Overlay of images (B) and (C) on top of panel (A), indicating that the nanoparticle products are comprised of both Au and Cu.

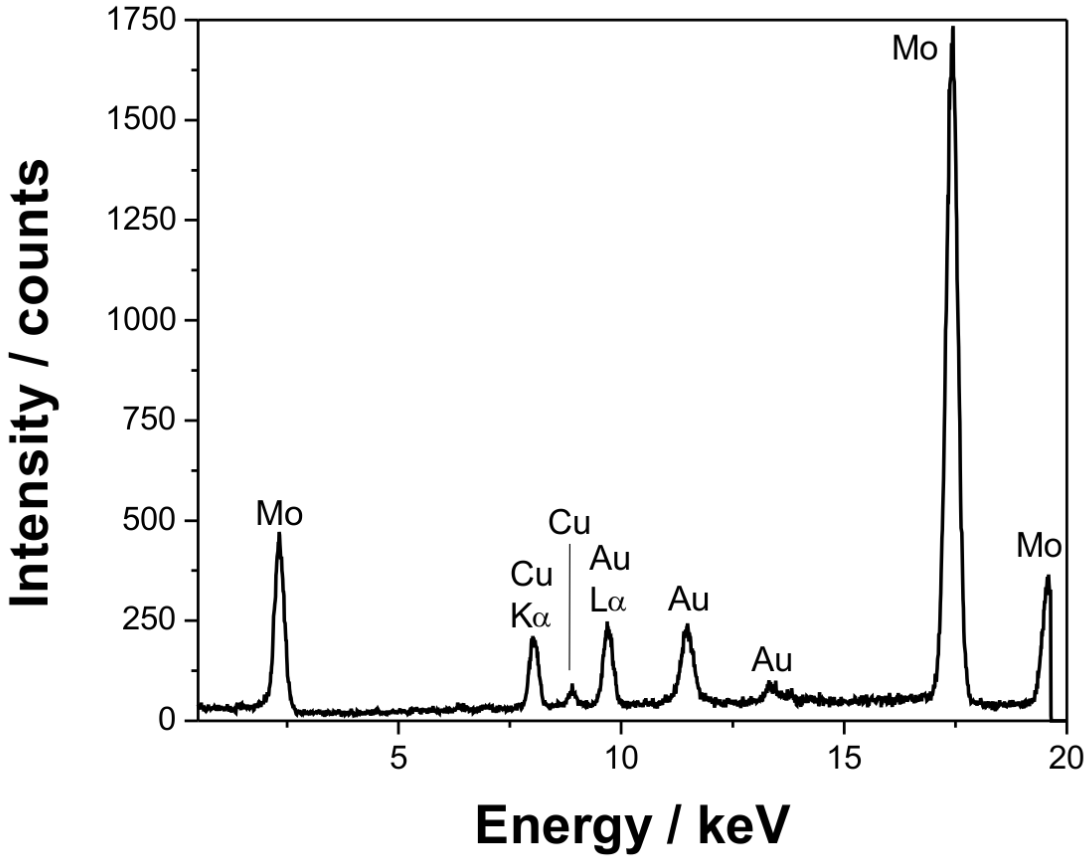

Figure 77. EDS sum spectra corresponding to the STEM-EDS maps in Figure 76. Intensity of the Cu and Au signals for elemental maps were measured by the Cu Kα and Au Lα lines at 8.0 and 9.7 eV, respectively.

High-resolution transmission electron microscopy (HRTEM) was used to analyze the crystallinity of both the island and core@shell nanoparticle products (Figure 78). Crystallinity of Cu islands could be observed from CuNPs pendant to the sides of the nanoprism. Often, individual islands were found to fuse together, forming polycrystalline extensions with multiple points of attachment to the Au lattice. For the Au nanoprisms fully coated in Cu, stripe-like features are evident across the surface of the nanoprisms, consistent with the formation of a Cu shell of varying morphology (Figure 78-Figure **80**). Fast Fourier transform (FFT) analysis of the lattices indicates that Cu is polycrystalline but is generally oriented in a [111] direction with respect to the electron beam. We hypothesize that the Cu shell originates as a collection of islands and progresses to a full Cu coating via fusion of individual Cu island structures.

An important question concerning the formation of Cu features on the nanoprism surface is their oxidation state after deposition. Competing oxide formation processes can influence CuNP formation kinetics (e.g. rate constants for Cu(II) reduction and Cu(0) oxidation may be similar) or CuNP stability (e.g. a metallic Cu nanostructure may develop a surface oxide layer). Previous studies of discrete monometallic CuNPs have shown that synthesis of metallic CuNPs is possible under ambient conditions, but that the particles form a surface oxide over time (studies report both CuO and Cu_2O species).[209-210]

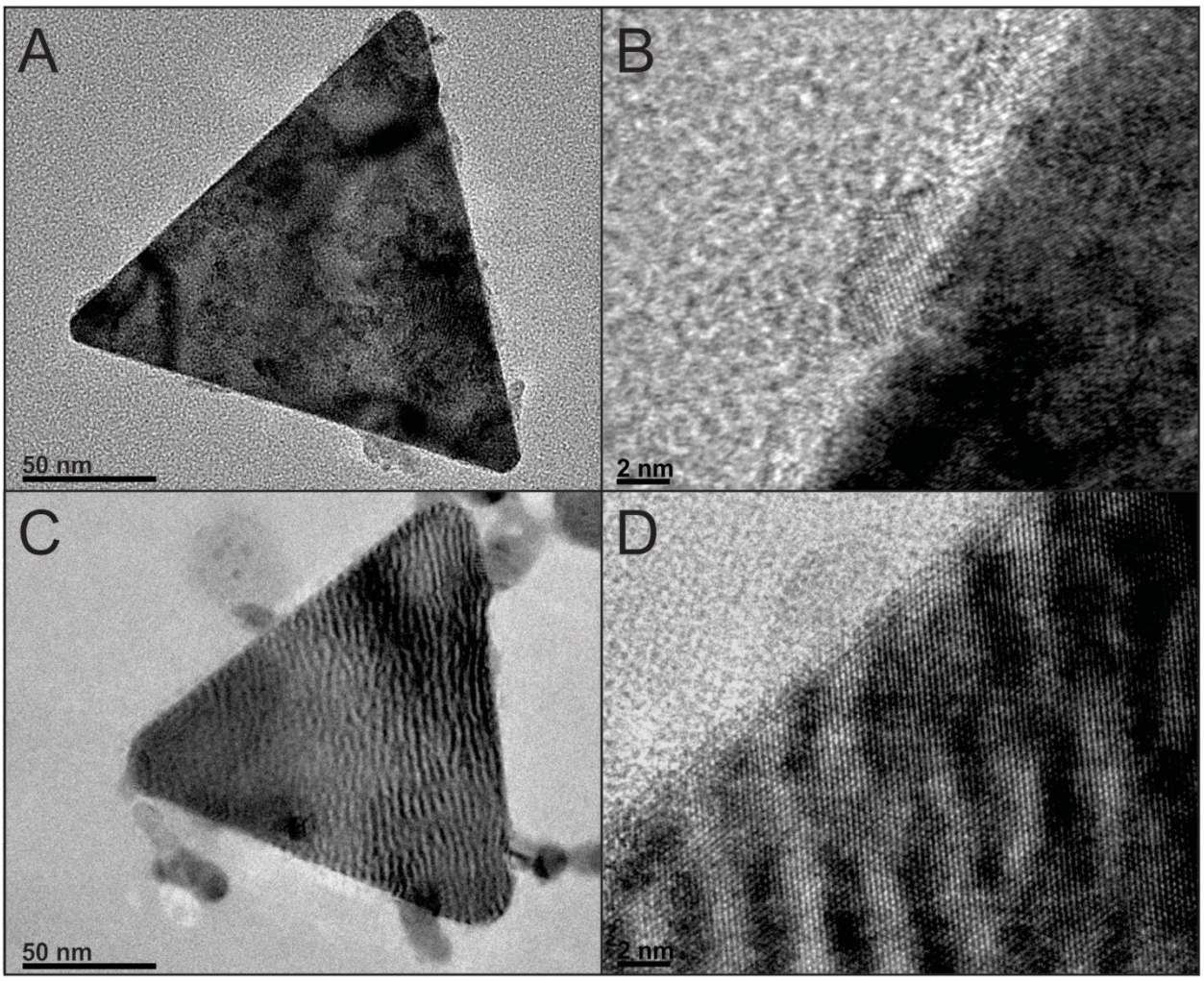

Figure 78. HRTEM images of Au-Cu nanoprisms with varying extents of Cu deposition. (A) Au nanoprisms corresponding to Figure 1A, (B) with a higher magnification image of the islands pendant on the nanoprism side. (C) Au@Cu nanoprisms corresponding to Figure 1C and exhibiting a "buckled" shell architecture (D) Higher magnification image of the Au-Cu nanoprism surface.

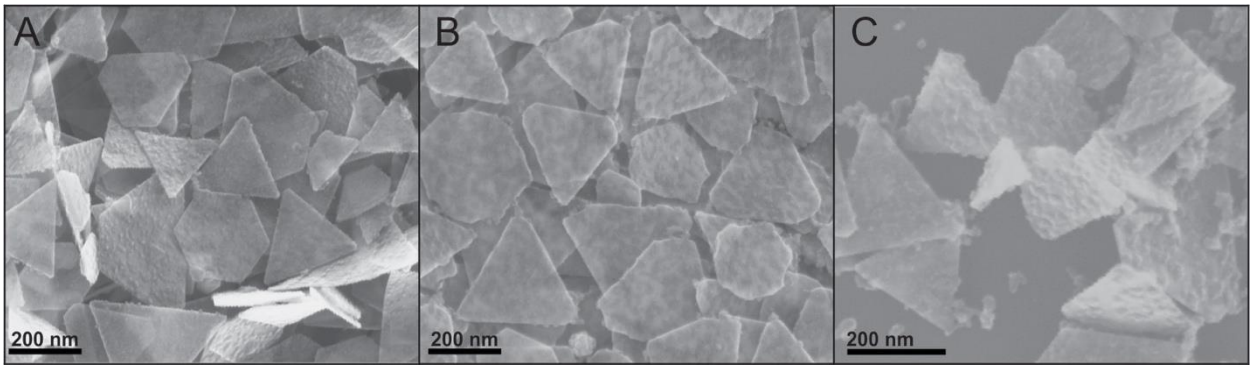

Figure 79. Representative SEM images of Au-Cu nanoprisms with increasing density of Cu coverage. (A) At the lowest densities of Cu growth observed, Cu was found to grow in an island like fashion. (B) For increased extents of Cu deposition, Cu was found to preferentially grow laterally with respect to the prism surface. (C) A heterogeneous, complete Cu layer results likely from a combination of continued Cu island growth and Cu island fusion (e.g. lower right of Panel C) (see also Figure 74-Figure 77).

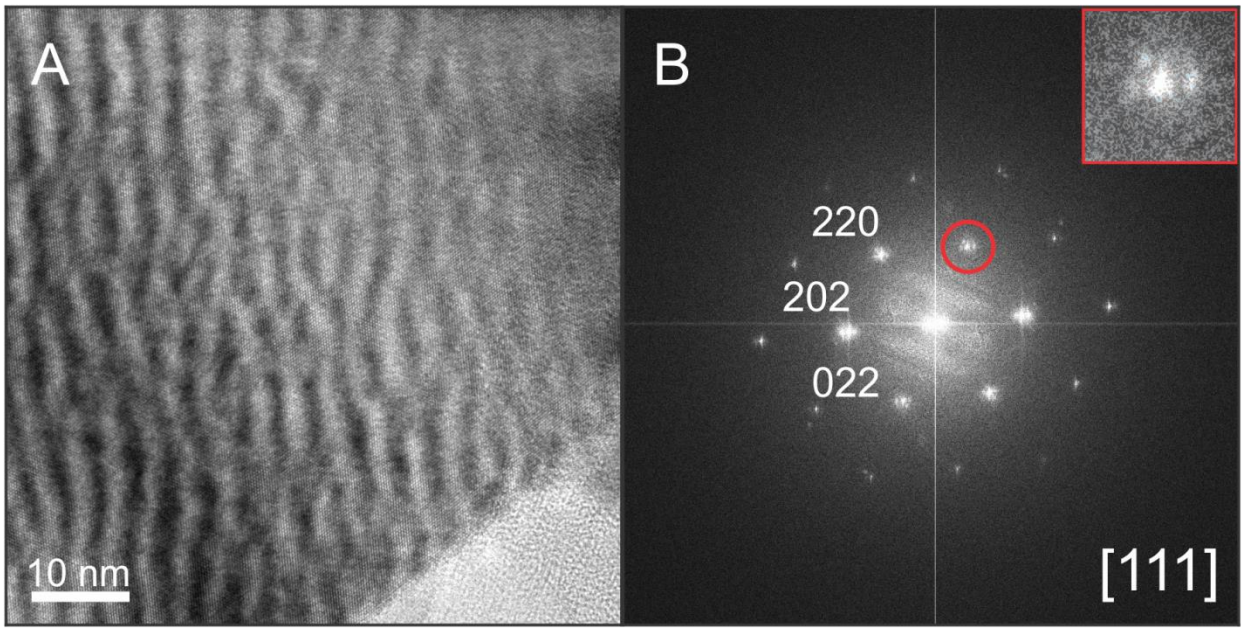

Figure 80. HRTEM and corresponding FFT of the Au@Cu nanoprisms. (A) A "buckled" surface architecture was observed after Cu shell formation. (B) Fast Fourier transform (FFT) analysis of the entire image indicates that Cu likely grows in a [111] direction and is polycrystalline, consistent with the observed double-diffraction pattern (inset).

X-ray photoelectron spectroscopy (XPS) and Auger electron spectroscopy (AES) were used to analyze the oxidation state of Cu deposits on the Au nanoprisms within 48 h of synthesis. As the amount of Cu deposited on the Au nanoprism surface increases, there is a concomitant shift of Au4f peaks to higher binding energies (Figure 81), consistent with metallic Au-Cu interactions in an alloy or at a Au-Cu interface.[211] To assess the presence of Cu metal and metal oxide species we analyzed particles stored under vacuum after synthesis (~ 30 mbar) as well as samples stored in ambient conditions. For each sample, we considered three possible scenarios for their resulting oxidation states. First, Cu features on the Au nanoprism are metallic and stay metallic over the course of both synthesis and analysis. Second, Cu features are initially metallic, but oxidize during analysis of their morphology and chemical composition. Last, Cu features on the nanoprisms form as copper oxides.

For samples stored under vacuum, the $Cu2p_{3/2}$ peak position at 932.7 eV and lack of Cu(II) satellites indicates that surface Cu atoms are metallic (Figure 82). To further distinguish between Cu(0) and Cu(I)/Cu(II) contributions to the $Cu2p_{3/2}$ XPS signal, the Cu $L_3M_{45}M_{45}$ Auger electrons were also analyzed. Here, the $L_3M_{45}M_{45}$ Auger electron peaks at 917.0 and 918.9 eV are characteristic of metallic Cu.[212] These data indicate that Cu nanostructures are deposited as metallic Cu and persist as metallic Cu for some time. Particles stored under ambient conditions showed the presence of oxygen species, however these oxide features dissipate after either exposure to ultrahigh vacuum conditions (~ 16h,) or after brief sputtering (Figure 85), consistent with surface absorbed species and not a copper oxide shell.

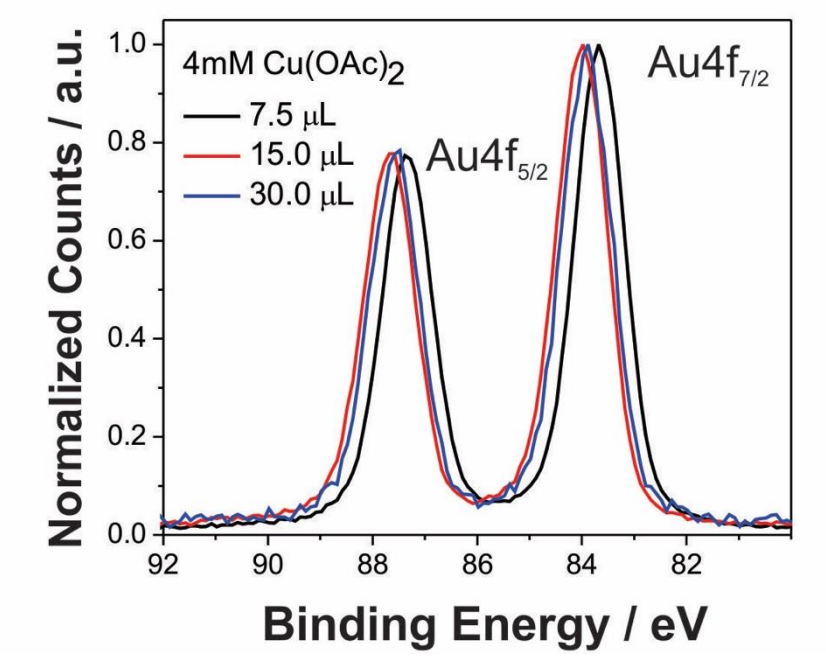

Figure 81. High-resolution Au4f XPS spectra of the Cu island and Au@Cu nanoprism products. As the extent of Cu deposition on the surface of the nanoprism increases, a shift towards higher binding energies was observed, consistent with metallic Au-Cu interactions or an alloyed Au-Cu interface.

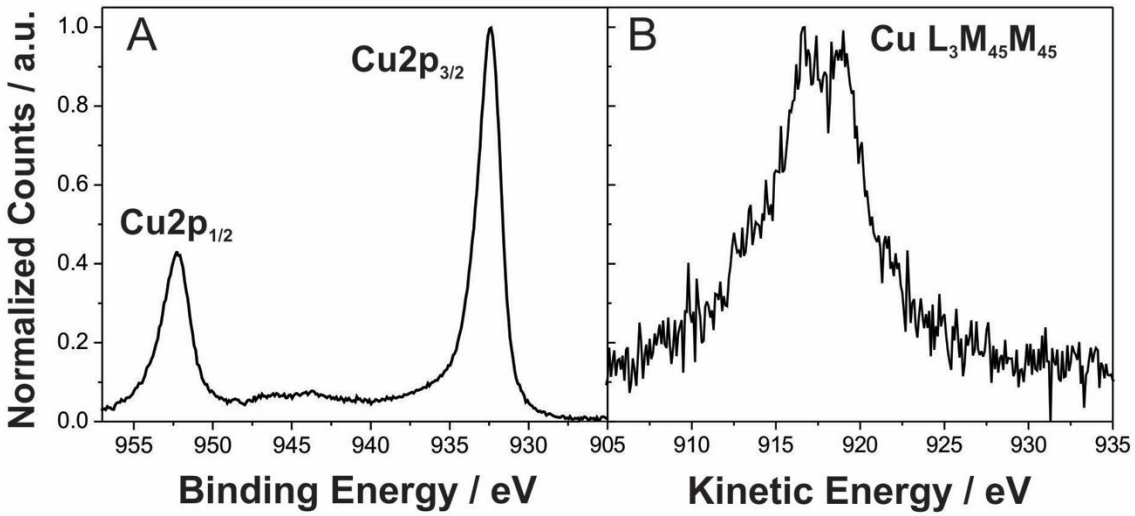

Figure 82. XPS Cu2p and AES Cu $L_3M_{45}M_{45}$ data for samples stored under vacuum after synthesis under ambient conditions. (A) High-resolution Cu2p XPS spectra where both the peak position of the $Cu2p_{3/2}$ peak at 923.7 eV and absence of satellite peaks indicate the presence of metallic Cu. (B) Corresponding AES spectra supporting the presence of metallic Cu.

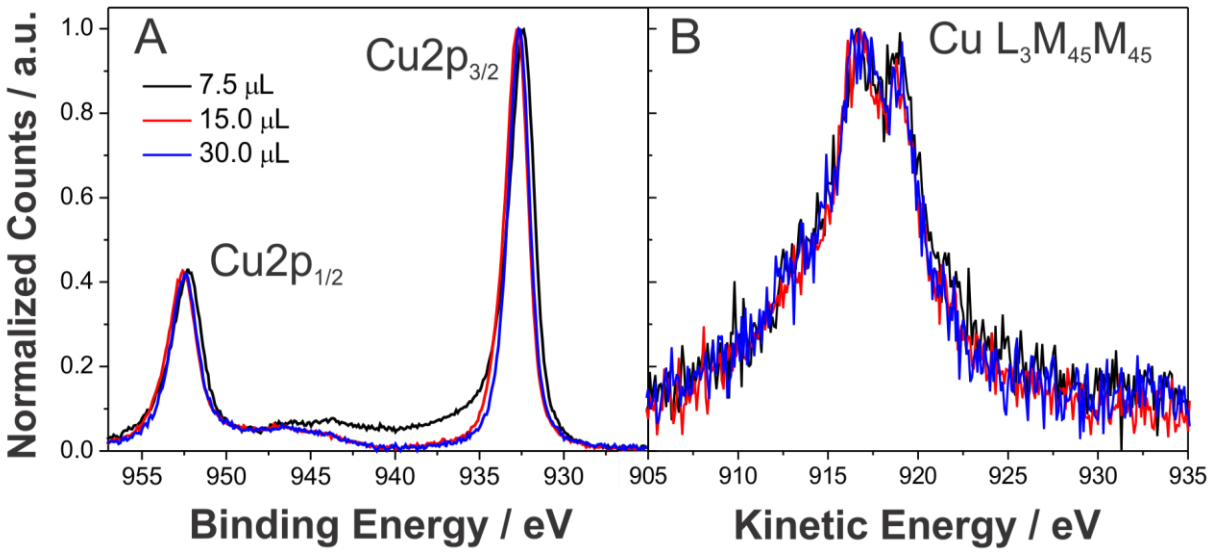

Figure 83. (A) High-resolution Cu2p XPS spectra of the Au-Cu nanoprism products, where both the binding energies and peak shapes are consistent with metallic Cu species. (B) To distinguish between Cu(0) and Cu(I)/Cu(II) contributions, nanoparticle products were also characterized by AES examining the Cu $L_3M_{45}M_{45}$ peak positions. Peaks at 918.9 and 917.0 eV are consistent with previous reports of metallic Cu. *N. B.* The main line peak for $Cu2p_{3/2}$ has a similar binding energy for both metallic and oxide species of copper and typically precludes definitive assignment by XPS alone.[212]

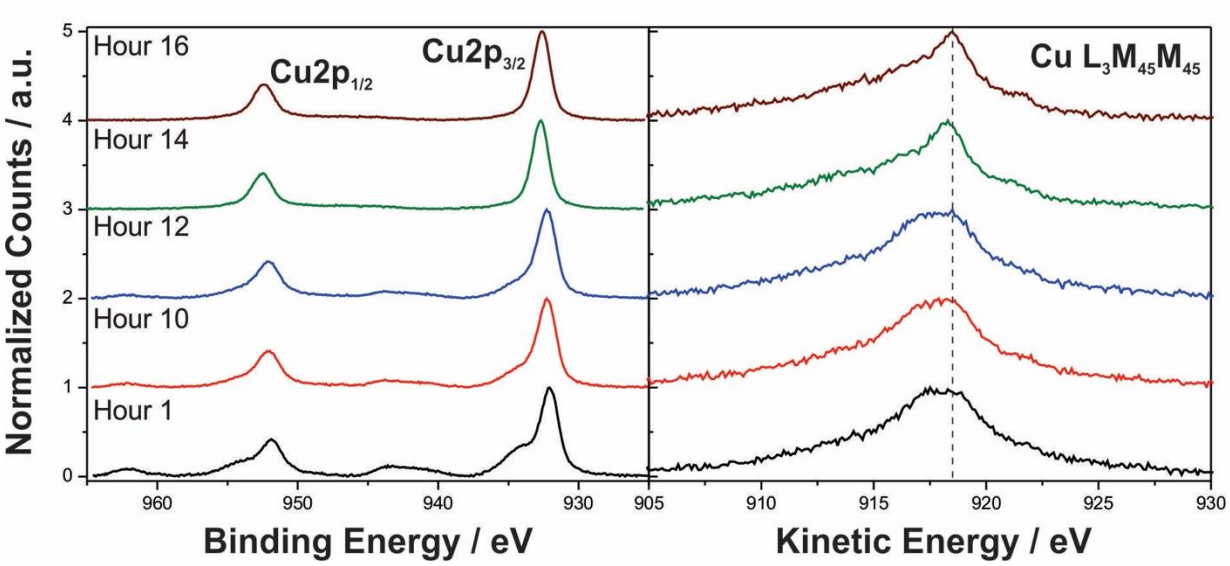

Figure 84. Representative Cu XPS (left) and AES (right) analysis of nanoprism samples dried and stored under ambient conditions, and then introduced to UHV conditions for a set time. Initial analysis showed the presence of oxygen (*hour 1, black trace)*, as indicated by the $Cu2p_{3/2}$ and $Cu2p_{1/2}$ peaks at 934.0 and 954.5 eV, respectively, as well as by the Cu(I)/Cu(II) satellites at 942.4 and 961.7 eV. However, evidence of oxygen species dissipates with time under vacuum. At the same time, AES spectra of the $L_3M_{45}M_{45}$ peak are consistent with metallic Cu throughout the experiment. These results are consistent with the deposition of metallic Cu and post-synthetic adsorption of oxygen or oxygen containing species.[212]

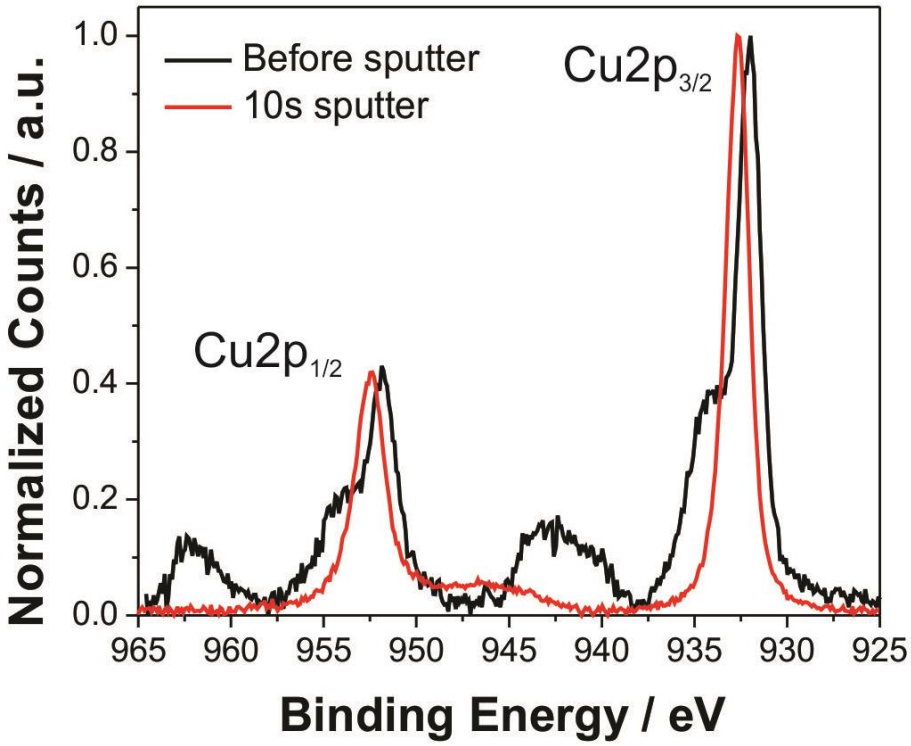

Figure 85. Representative Cu2p XPS spectra of the Cu island nanoprisms before (black) and after (red) Ar ion sputtering indicating the presence of copper oxide species prior to sputtering. The presence of CuO/Cu_2O was indicated by shoulders on the $Cu2p_{3/2}$ and $Cu2p_{1/2}$ peaks at 934.0 and 954.5 eV, respectively, as well as by the Cu(I)/Cu(II) satellites at 942.4 and 961.7 eV. After sputtering, traces of oxidized copper are removed from all samples. The slight feature at 947 eV is commonly observed in spectra of metallic copper and is assigned to a "shake-up" peak due to multiple excitations within the metal. These results are consistent with deposition of metallic Cu and post-synthetic oxidation or adsorption of oxide species on the nanoprism surface.

5.4 CONCLUSIONS

In conclusion, we report an aqueous synthesis of Cu-containing multimetallic nanoparticles under ambient conditions. Metallic Cu was observed to deposit in either an island or core@shell motif on the surface of the Au nanoprism and conditions to tune these motifs were presented. Both the selection of reagents and the rate of reagent addition were critical to achieving Cu deposition. Specifically, ligands on both the metal cation precursor and reducing agent may be used to mediate reduction kinetics even when the reduction potential of the ligand analogues are similar. These results elucidate trends for the synthesis of 3d transition metal-containing nanoparticles under conditions that allow one to leverage the vast established literature of aqueous noble metal nanoparticle syntheses.

REFERENCES

(1) Stamenkovic, V. R.; Mun, B. S.; Mayrhofer, K. J. J.; Ross, P. N.; Markovic, N. M. *J. Am. Chem. Soc.* **2006**, *128*, 8813-8819.
(2) Mayer, M.; Scarabelli, L.; March, K.; Altantzis, T.; Tebbe, M.; Kociak, M.; Bals, S.; García de Abajo, F. J.; Fery, A.; Liz-Marzán, L. M. *Nano Lett.* **2015**, *15*, 5427-5437.
(3) Jain, P. K.; Xiao, Y.; Walsworth, R.; Cohen, A. E. *Nano Lett.* **2009**, *9*, 1644-1650.
(4) Marbella, L. E.; Andolina, C. M.; Smith, A. M.; Hartmann, M. J.; Dewar, A. C.; Johnston, K. A.; Daly, O. H.; Millstone, J. E. *Adv. Funct. Mater.* **2014**, *24*, 6532-6539.
(5) Antosiewicz, T. J.; Apell, S. P. *RSC Adv.* **2015**, *5*, 6378-6384.
(6) Swearer, D. F.; Zhao, H.; Zhou, L.; Zhang, C.; Robatjazi, H.; Martirez, J. M. P.; Krauter, C. M.; Yazdi, S.; McClain, M. J.; Ringe, E.; Carter, E. A.; Nordlander, P.; Halas, N. J. *P. Natl. Acad. Sci.* **2016**.
(7) Laskar, M.; Skrabalak, S. E. *J. Mater. Chem. A* **2016**, *4*, 6911-6918.
(8) Roldan Cuenya, B. *Accounts Chem. Res.* **2012**, *46*, 1682-1691.
(9) Liu, X.; Wang, D.; Li, Y. *Nano Today* **2012**, *7*, 448-466.
(10) Hou, S.; Hu, X.; Wen, T.; Liu, W.; Wu, X. *Adv. Mater.* **2013**, *25*, 3857-3862.
(11) Toshima, N.; Yonezawa, T. *New. J. Chem.* **1998**, *22*, 1179-1201.
(12) Zhang, Q.; Liu, S.-J.; Yu, S.-H. *J. Mater. Chem.* **2009**, *19*, 191-207.
(13) Cortie, M. B.; McDonagh, A. M. *Chem. Rev.* **2011**, *111*, 3713-3735.
(14) Walther, A.; Müller, A. H. E. *Chem. Rev.* **2013**, *113*, 5194-5261.
(15) Lattuada, M.; Hatton, T. A. *Nano Today* **2011**, *6*, 286-308.
(16) Ghosh Chaudhuri, R.; Paria, S. *Chem. Rev.* **2011**, *112*, 2373-2433.
(17) Lim, B.; Jiang, M.; Camargo, P. H. C.; Cho, E. C.; Tao, J.; Lu, X.; Zhu, Y.; Xia, Y. *Science* **2009**, *324*, 1302-1305.
(18) Lim, B.; Xia, Y. *Angew. Chem. Int. Ed.* **2011**, *50*, 76-85.
(19) Zheng, Z.; Tachikawa, T.; Majima, T. *J. Am. Chem. Soc.* **2014**, *136*, 6870-6873.
(20) Linic, S.; Christopher, P.; Ingram, D. B. *Nat. Mater.* **2011**, *10*, 911-921.
(21) Read, C. G.; Gordon, T. R.; Hodges, J. M.; Schaak, R. E. *J. Am. Chem. Soc.* **2015**, *137*, 12514-12517.
(22) Baskaran, A.; Smereka, P. *J. Appl. Phys.* **2012**, *111*, 044321.
(23) Oura, K.; Lifshits, V. G.; Saranin, A.; Zotov, A. V.; Katayama, M. *Surface Science: An Introduction*; Springer Berlin Heidelberg, 2013.
(24) Lorenz, W. J.; Staikov, G. *Surf. Sci.* **1995**, *335*, 32-43.
(25) Takayanagi, K.; Kolb, D.; Kambe, K.; Lehmpfuhl, G. *Surf. Sci.* **1980**, *100*, 407-422.
(26) Fan, F.-R.; Liu, D.-Y.; Wu, Y.-F.; Duan, S.; Xie, Z.-X.; Jiang, Z.-Y.; Tian, Z.-Q. *J. Am. Chem. Soc.* **2008**, *130*, 6949-6951.
(27) Harsdorff, M. *Thin Solid Films* **1982**, *90*, 1-14.

(28) Friesen, C.; Seel, S.; Thompson, C. *J. Appl. Phys.* **2004**, *95*, 1011-1020.
(29) Seel, S. C.; Thompson, C. V. *J. Appl. Phys.* **2003**, *93*, 9038-9042.
(30) Yu, H. Z.; Thompson, C. V. *Acta Mater.* **2014**, *67*, 189-198.
(31) Michely, T.; Krug, J. *Pattern Formation in Multilayer Growth*, 2004.
(32) Pao, C.-W.; Foiles, S. M.; Webb, E. B.; Srolovitz, D. J.; Floro, J. A. *Phys. Rev. Lett.* **2007**, *99*, 036102.
(33) Venables, J.; Spiller, G.; Hanbucken, M. *Rep. Prog. Phys.* **1984**, *47*, 399.
(34) Lagally, M. G.; Zhang, Z. *Nature* **2002**, *417*, 907-910.
(35) Ratsch, C.; Zangwill, A. *Surf. Sci.* **1993**, *293*, 123-131.
(36) Mathur, A.; Erlebacher, J. *Surf. Sci.* **2008**, *602*, 2863-2875.
(37) Trushin, O. S.; Kokko, K.; Salo, P. T.; Hergert, W.; Kotrla, M. *Phys. Rev. B* **1997**, *56*, 12135-12138.
(38) Strbac, S.; Magnussen, O.; Behm, R. *Phys. Rev. Lett.* **1999**, *83*, 3246.
(39) Brune, H. *Surf. Sci. Rep.* **1998**, *31*, 125-229.
(40) Grillo, F.; Früchtl, H.; Francis, S. M.; Richardson, N. V. *New. J. Phys.* **2011**, *13*, 013044.
(41) Chen, J. G.; Menning, C. A.; Zellner, M. B. *Surf. Sci. Rep.* **2008**, *63*, 201-254.
(42) Corcoran, S. G.; Chakarova, G. S.; Sieradzki, K. *Phys. Rev. Lett.* **1993**, *71*, 1585-1588.
(43) Mo, Y.-W.; Savage, D.; Swartzentruber, B.; Lagally, M. G. *Phys. Rev. Lett.* **1990**, *65*, 1020.
(44) Gillet, E.; Gruzza, B. *Surf. Sci.* **1980**, *97*, 553-563.
(45) Weiss, W.; Ritter, M. *Phys. Rev. B* **1999**, *59*, 5201-5213.
(46) Herrero, E.; Buller, L. J.; Abruña, H. D. *Chem. Rev.* **2001**, *101*, 1897-1930.
(47) Brankovic, S.; Wang, J.; Adžić, R. *Surf. Sci.* **2001**, *474*, L173-L179.
(48) Brankovic, S.; Dimitrov, N.; Sieradzki, K. *Electrochem. Solid St.* **1999**, *2*, 443-445.
(49) Kibler, L.; Kleinert, M.; Randler, R.; Kolb, D. *Surf. Sci.* **1999**, *443*, 19-30.
(50) Härtel, T.; Strüber, U.; Küppers, J. *Thin Solid Films* **1993**, *229*, 163-170.
(51) Ball, M.; Lucas, C.; Markovic, N.; Stamenkovic, V.; Ross, P. *Surf. Sci.* **2002**, *518*, 201-209.
(52) Kibler, L. A.; Kleinert, M.; Kolb, D. M. *J. Electroanal. Chem.* **1999**, *467*, 249-257.
(53) Brown, K. R.; Natan, M. J. *Langmuir* **1998**, *14*, 726-728.
(54) Wiley, B.; Sun, Y.; Mayers, B.; Xia, Y. *Chem. Euro. J.* **2005**, *11*, 454-463.
(55) Personick, M. L.; Mirkin, C. A. *J. Am. Chem. Soc.* **2013**, *135*, 18238-18247.
(56) Wang, Y.; Xie, S.; Liu, J.; Park, J.; Huang, C. Z.; Xia, Y. *Nano Lett.* **2013**, *13*, 2276-2281.
(57) Zeng, J.; Zheng, Y.; Rycenga, M.; Tao, J.; Li, Z.-Y.; Zhang, Q.; Zhu, Y.; Xia, Y. *J. Am. Chem. Soc.* **2010**, *132*, 8552-8553.
(58) Seo, D.; Yoo, C. I.; Chung, I. S.; Park, S. M.; Ryu, S.; Song, H. *J. Phys. Chem. C* **2008**, *112*, 2469-2475.
(59) Nikoobakht, B.; El-Sayed, M. A. *Chem. Mater.* **2003**, *15*, 1957-1962.
(60) Johnson, C. J.; Dujardin, E.; Davis, S. A.; Murphy, C. J.; Mann, S. *J. Mater. Chem.* **2002**, *12*, 1765-1770.
(61) Jiu, J.; Murai, K.; Kim, D.; Kim, K.; Suganuma, K. *Mater. Chem. Phys.* **2009**, *114*, 333-338.
(62) Métraux, G. S.; Mirkin, C. A. *Adv. Mater.* **2005**, *17*, 412-415.
(63) Millstone, J. E.; Wie, W.; Jones, M. R.; Yoo, H.; Mirkin, C. A. *Nano Lett.* **2008**, *8*, 2526-2529.
(64) Xiong, Y.; Chen, J.; Wiley, B.; Xia, Y.; Aloni, S.; Yin, Y. *J. Am. Chem. Soc.* **2005**, *127*, 7332-7333.

(65) Bratlie, K. M.; Lee, H.; Komvopoulos, K.; Yang, P.; Somorjai, G. A. *Nano Lett.* **2007**, *7*, 3097-3101.
(66) An, K.; Hyeon, T. *Nano Today* **2009**, *4*, 359-373.
(67) Liu, M.; Guyot-Sionnest, P. *J. Phys. Chem. B* **2005**, *109*, 22192-22200.
(68) Smith, A. M.; Mohs, A. M.; Nie, S. *Nat. Nanotechnol.* **2008**, *4*, 56-63.
(69) *CRC Handbook of Chemistry and Physics*; 92 ed.; CRC Press: Boca Raton, 2011.
(70) Wang, H.; Sun, Z.; Yang, Y.; Su, D. *Nanoscale* **2013**, *5*, 139-142.
(71) Lim, B.; Jiang, M.; Camargo, P. H.; Cho, E. C.; Tao, J.; Lu, X.; Zhu, Y.; Xia, Y. *Science* **2009**, *324*, 1302-1305.
(72) Leary, R. K.; Kumar, A.; Straney, P. J.; Collins, S. M.; Yazdi, S.; Dunin-Borkowski, R. E.; Midgley, P. A.; Millstone, J. E.; Ringe, E. *J. Phys. Chem. C* **2016**, *120*, 20843-20851.
(73) Waibel, H. F.; Kleinert, M.; Kibler, L. A.; Kolb, D. M. *Electrochim. Acta* **2002**, *47*, 1461-1467.
(74) Griffin, S.; Montoni, N. P.; Li, G.; Straney, P. J.; Millstone, J. E.; Masiello, D. J.; Camden, J. P. *J. Phys. Chem. Lett.* **2016**, *7*, 3825-3832.
(75) Wang, F.; Liu, P.; Zhang, D. *J. Mol. Model.* **2011**, *17*, 1069-1073.
(76) Love, C. J.; Estroff, L. A.; Kriebel, J. K.; Nuzzo, R. G.; Whitesides, G. M. *Chem. Rev.* **2005**, *105*, 1103-1169.
(77) Kim, Y.; Hong, J. W.; Lee, Y. W.; Kim, M.; Kim, D.; Yun, W. S.; Han, S. W. *Angew. Chem. Int. Ed.* **2010**, *49*, 10197-10201.
(78) Feng, L.; Wu, X.; Ren, L.; Xiang, Y.; He, W.; Zhang, K.; Zhou, W.; Xie, S. *Chem. Euro. J.* **2008**, *14*, 9764-9771.
(79) Carbó-Argibay, E.; Rodríguez-González, B.; Gómez-Graña, S.; Guerrero-Martínez, A.; Pastoriza-Santos, I.; Pérez-Juste, J.; Liz-Marzán, L. M. *Angew. Chem. Int. Ed.* **2010**, *122*, 9587-9590.
(80) Min, M.; Kim, C.; Lee, H. *J. Mol. Catal. A Chem.* **2010**, *333*, 6-10.
(81) Sneed, B. T.; Kuo, C.-H.; Brodsky, C. N.; Tsung, C.-K. *J. Am. Chem. Soc.* **2012**, *134*, 18417-18426.
(82) Fennell, J.; He, D.; Tanyi, A. M.; Logsdail, A. J.; Johnston, R. L.; Li, Z.; Horswell, S. L. *J. Am. Chem. Soc.* **2013**, *135*, 6554-6561.
(83) Xie, W.; Herrmann, C.; Kömpe, K.; Haase, M.; Schlücker, S. *J. Am. Chem. Soc.* **2011**, *133*, 19302-19305.
(84) Grzelczak, M.; Perez-Juste, J.; Rodriguez-Gonzalez, B.; Liz-Marzan, L. M. *J. Mater. Chem.* **2006**, *16*, 3946-3951.
(85) Jang, H.-J.; Hong, S.; Ham, S.; Shuford, K. L.; Park, S. *Nanoscale* **2014**, *6*, 7339-7345.
(86) Jain, P. K.; Huang, X. H.; El-Sayed, I. H.; El-Sayed, M. A. *Acc. Chem. Res.* **2008**, *41*, 1578-1586.
(87) Luk'yanchuk, B.; Zheludev, N. I.; Maier, S. A.; Halas, N. J.; Nordlander, P.; Giessen, H.; Chong, C. T. *Nat. Mater.* **2010**, *9*, 707-715.
(88) Grzelczak, M.; Perez-Juste, J.; Mulvaney, P.; Liz-Marzan, L. M. *Chem. Soc. Rev.* **2008**, *37*, 1783-1791.
(89) Xia, Y.; Xiong, Y.; Lim, B.; Skrabalak, S. E. *Angew. Chem. Int. Edit.* **2009**, *48*, 60-103.
(90) Salem, A. K.; Searson, P. C.; Leong, K. W. *Nat. Mater.* **2003**, *2*, 668-671.
(91) Jones, M. R.; Millstone, J. E.; Giljohann, D. A.; Seferos, D. S.; Young, K. L.; Mirkin, C. A. *ChemPhysChem* **2009**, *10*, 1461-1465.

(92) Lyons, P. E.; De, S.; Elias, J.; Schamel, M.; Philippe, L.; Bellew, A. T.; Boland, J. J.; Coleman, J. N. *Phys. Chem. Lett.* **2011**, *2*, 3058-3062.
(93) Murphy, C. J. *J. Mater. Chem.* **2008**, *18*, 2173-2176.
(94) Dahl, J. A.; Maddux, L. S.; Hutchison, J. E. *Chem. Rev.* **2007**, *107*, 2228-2269.
(95) Anastas, P.; Warner, J. *Green Chemistry: Theory and Practice*; Oxford University Press: New York, 1998.
(96) Rodriguez-Fernandez, J.; Perez-Juste, J.; Mulvaney, P.; Liz-Marzan, L. M. *Phys. Chem. Lett. B* **2005**, *109*, 14257-14261.
(97) Nikoobakht, B.; El-Sayed, M. A. *Chem. Mater.* **2003**, *15*, 1957-1962.
(98) Lofton, C.; Sigmund, W. *Adv. Funct. Mater.* **2005**, *15*, 1197-1208.
(99) Imae, T.; Kamiya, R.; Ikeda, S. *J. Colloid Interf. Sci.* **1985**, *108*, 215-225.
(100) Goyal, P. S.; Dasannacharya, B. A.; Kelkar, V. K.; Manohar, C.; Srinivasa Rao, K.; Valaulikar, B. S. *Physica B* **1991**, *174*, 196-199.
(101) Gao, J.; Bender, C. M.; Murphy, C. J. *Langmuir* **2003**, *19*, 9065-9070.
(102) Wu, H.; Kuo, C.; Huang, M. H. *Langmuir* **2010**, *26*, 12307-12313.
(103) Sánchez-Iglesias, A.; Pastoriza-Santos, I.; Pérez-Juste, J.; Rodríguez-González, B.; García de Abajo, F. J.; Liz-Marzán, L. M. *Adv. Mater.* **2006**, *18*, 2529-2534.
(104) Langille, M. R.; Personick, M. L.; Zhang, J.; Mirkin, C. A. *J. Am. Chem. Soc.* **2012**, *134*, 14542-14554.
(105) Kim, D. Y.; Im, S. H.; O., P. O. *Cryst. Growth. Des.* **2010**, *10*, 3321-3323.
(106) Jana, N. R.; Gearheart, L.; Murphy, C. J. *J. Phys. Chem. B* **2001**, *105*, 4065-4067.
(107) Halder, A.; Ravishankar, N. *Adv. Mater.* **2007**, *19*, 1854-1858.
(108) DeSantis, C. J.; Sue, A. C.; Bower, M. M.; Skrabalak, S. E. *ACS Nano* **2012**, *6*, 2617-2628.
(109) Jana, N. R. *Small* **2005**, *1*, 875-882.
(110) Ali, M. R. K.; Snyder, B.; El-Sayed, M. A. *Langmuir* **2012**, *28*, 9807 - 9815.
(111) Uppal, M. A.; Kafizas, A.; Lim, T. H.; Parkin, I. P. *New. J. Chem.* **2010**, *34*, 1401-1407.
(112) Yoshida, K.; Bright, A.; Tanaka, N. *J. Electron. Microsc.* **2012**, *61*, 99-103.
(113) Murphy, C. J.; Thompson, L. B.; Chernak, D. J.; Yang, J. A.; Sivapalan, S. T.; Boulos, S. P.; Huang, J. Y.; Alkilany, A. M.; Sisco, P. N. *Curr. Opin. Colloid In.* **2011**, *16*, 128-134.
(114) Chatenet, M.; Micoud, F.; Roche, I.; Chainet, E. *Electrochim. Acta* **2006**, *51*, 5459-5467.
(115) Polte, J.; Ahner, T. T.; Delissen, F.; Sokolov, S.; Emmerling, F.; Thünemann, A. F.; Kraehnert, R. *J. Am. Chem. Soc.* **2010**, *132*, 1296-1301.
(116) Millstone, J. E.; Hurst, S. J.; Metraux, G. S.; Cutler, J. I.; Mirkin, C. A. *Small* **2009**, *5*, 646-664.
(117) Shuford, K. L.; Ratner, M. A.; Schatz, G. C. *J. Chem. Phys.* **2005**, *123*, 1147131-1147139.
(118) Katz-Boon, H.; Rossouw, C. J.; Weyland, M.; Funston, A. M.; Mulvaney, P.; Etheridge, J. *Nano Lett.* **2010**, *11*, 273-278.
(119) Edgar, J. A.; McDonagh, A. M.; Cortie, M. B. *ACS Nano* **2012**, *6*, 1116.
(120) Kelly, K. L.; Coronado, E.; Zhao, L. L.; Schatz, G. C. *J. Phys. Chem. B* **2003**, *107*, 668-677.
(121) Metraux, G. S.; Mirkin, C. A. *Adv. Mater.* **2005**, *17*, 412-415.
(122) Millstone, J. E.; Metraux, G. S.; Mirkin, C. A. *Adv. Funct. Mater.* **2006**, *16*, 1209-1214.
(123) Yoo, H. J.; Millstone, J. E.; Li, S. Z.; Jang, J. W.; Wei, W.; Wu, J. S.; Schatz, G. C.; Mirkin, C. A. *Nano Lett.* **2009**, *9*, 3038-3041.
(124) Alkilany, A. M.; Nagaria, P. K.; Hexel, C. R.; Shaw, T. J.; Murphy, C. J.; Wyatt, M. D. *Small* **2009**, *5*, 701-708.

(125) Nikoobakht, B.; El-Sayed, M. A. *Langmuir* **2001**, *17*, 6368-6374.
(126) Millstone, J. E.; Park, S.; Shuford, K. L.; Qin, L.; Schatz, G. C.; Mirkin, C. A. *J. Am. Chem. Soc.* **2005**, *127*, 5312-5313.
(127) Greeley, J.; Mavrikakis, M. *Nat. Mater.* **2004**, *3*, 810-815.
(128) Chen, C.; Kang, Y.; Huo, Z.; Zhu, Z.; Huang, W.; Xin, H. L.; Snyder, J. D.; Li, D.; Herron, J. A.; Mavrikakis, M.; Chi, M.; More, K. L.; Li, Y.; Markovic, N. M.; Somorjai, G. A.; Yang, P.; Stamenkovic, V. R. *Science* **2014**, *343*, 1339-1343.
(129) Ghosh Chaudhuri, R.; Paria, S. *Chem. Rev.* **2011**, *112*, 2373-2433.
(130) Chen, A.; Holt-Hindle, P. *Chem. Rev.* **2010**, *110*, 3767-3804.
(131) Greeley, J.; Nørskov, J. K.; Mavrikakis, M. *Annu. Rev. Phys. Chem.* **2002**, *53*, 319-348.
(132) Cui, C.; Gan, L.; Heggen, M.; Rudi, S.; Strasser, P. *Nat. Mater.* **2013**, *12*, 765-771.
(133) Snyder, J.; Livi, K.; Erlebacher, J. *Adv. Funct. Mater.* **2013**, *23*, 5494-5501.
(134) He, C.; Desai, S.; Brown, G.; Bollepalli, S. *Electrochem. Soc. Interface* **2005**, *14*, 41-46.
(135) Koenigsmann, C.; Wong, S. S. *Energy Environ. Sci.* **2011**, *4*, 1161-1176.
(136) DeSantis, C. J.; Weiner, R. G.; Radmilovic, A.; Bower, M. M.; Skrabalak, S. E. *J. Phys. Chem. Lett.* **2013**, *4*, 3072-3082.
(137) DeSantis, C. J.; Skrabalak, S. E. *J. Am. Chem. Soc.* **2012**, *135*, 10-13.
(138) Fan, F.; Liu, D.; Wu, Y.; Duan, S.; Xie, Z.; Jiang, Z.; Tian, Z. *J. Am. Chem. Soc.* **2008**, *130*, 6949-6951.
(139) Lee, Y. W.; Kim, D.; Hong, J. W.; Kang, S. W.; Lee, S. B.; Han, S. W. *Small* **2013**, *9*, 660-665.
(140) He, W.; Wu, X.; Liu, J.; Zhang, K.; Chu, W.; Feng, L.; Hu, X.; Zhou, W.; Xie, S. *J. Phys. Chem. C* **2009**, *113*, 10505-10510.
(141) Spieker, W. A.; Liu, J.; Miller, J. T.; Kropf, A. J.; Regalbuto, J. R. *Appl. Catal. A-Gen.* **2002**, *232*, 219-235.
(142) Mang, T.; Breitscheidel, B.; Polanek, P.; Knozinger, H. *Appl. Catal. A-Gen.* **1993**, *106*, 239-258.
(143) Shelimov, B.; Lambert, J.; Che, M.; Didillon, B. *J. Am. Chem. Soc.* **1999**, *121*, 545-556.
(144) Flynn, N. T.; Gewirth, A. A. *J. Raman. Spectrosc.* **2002**, *33*, 243-251.
(145) Zhang, H.; Jin, M.; Wang, J.; Li, W.; Camargo, P. H. C.; Kim, M. J.; Yang, D.; Xie, Z.; Xia, Y. *J. Am. Chem. Soc.* **2011**, *133*, 6078-6089.
(146) Schmid, G.; Lehnert, A.; Malm, J.; Bovin, J. *Angew. Chem. Int. Ed.* **1991**, *30*, 874-876.
(147) Yu, Y.; Zhang, Q.; Yao, Q.; Xie, J.; Lee, J. Y. *Chem. Mater.* **2013**, *25*, 4746-4756.
(148) Shelimov, B.; Lambert, J.-F.; Che, M.; Didillon, B. *J. Am. Chem. Soc.* **1999**, *121*, 545-556.
(149) Liu, M.; Mao, X.-a.; Ye, C.; Huang, H.; Nicholson, J. K.; Lindon, J. C. *J. Magn. Reson.* **1998**, *132*, 125-129.
(150) Zeng, J.; Zhu, C.; Tao, J.; Jin, M.; Zhang, H.; Li, Z.-Y.; Zhu, Y.; Xia, Y. *Angewandte Chemie International Edition* **2012**, *51*, 2354-2358.
(151) Millstone, J. E.; Wei, W.; Jones, M. R.; Yoo, H.; Mirkin, C. A. *Nano Lett.* **2008**, *8*, 2526-2529.
(152) Grzelczak, M.; Pérez-Juste, J.; García de Abajo, F. J.; Liz-Marzán, L. M. *J. Phys. Chem. C* **2007**, *111*, 6183-6188.
(153) Millstone, J. E.; Park, S.; Shuford, K. L.; Qin, L.; Schatz, G. C.; Mirkin, C. A. *J. Am. Chem. Soc.* **2005**, *127*, 5312-5313.

(154) Dahanayaka, D. H.; Wang, J. X.; Hossain, S.; Bumm, L. A. *J. Am. Chem. Soc.* **2006**, *128*, 6052-6053.
(155) Villars, P.; Prince, A.; Okamoto, H. *Handbook of Ternary Alloy Phase Diagrams*; ASM International: Materials Park, OH, 1995.
(156) Hubbard, A. T.; Anson, F. C. *Anal. Chem.* **1966**, *38*, 1887-1893.
(157) Levitt, M. H. *Spin Dynamics: Basics of Nuclear Magnetic Resonance*; 2nd ed.; John Wiley & Sons: West Sussex, UK, 2008.
(158) Carr, C.; Goggin, P. L.; Goodfellow, R. J. *Inorg. Chim. Acta.* **1984**, *81*, L25-L26.
(159) Manne, S.; Cleveland, J. P.; Gaub, H. E.; Stucky, G. D.; Hansma, P. K. *Langmuir* **1994**, *10*, 4409-4413.
(160) Brongersma, M. L.; Halas, N. J.; Nordlander, P. *Nat. Nanotechnol.* **2015**, *10*, 25-34.
(161) Narang, P.; Sundararaman, R.; Atwater, H. A. *Nanophotonics* **2016**.
(162) Xia, Y.; Gilroy, K. D.; Peng, H. C.; Xia, X. *Angew. Chem. Int. Ed.* **2016**.
(163) Pirzadeh, Z.; Pakizeh, T.; Miljkovic, V.; Langhammer, C.; Dmitriev, A. *ACS Photonics* **2014**, *1*, 158-162.
(164) Weaver, J. *Phys. Rev. B* **1975**, *11*, 1416.
(165) Ringe, E.; DeSantis, C. J.; Collins, S. M.; Duchamp, M.; Dunin-Borkowski, R. E.; Skrabalak, S. E.; Midgley, P. A. *Sci. Rep.* **2015**, *5*, 17431.
(166) Doherty, M. D.; Murphy, A.; McPhillips, J.; Pollard, R. J.; Dawson, P. *J. Phys. Chem. C* **2010**, *114*, 19913-19919.
(167) Hrelescu, C.; Sau, T. K.; Rogach, A. L.; Jäckel, F.; Laurent, G.; Douillard, L.; Charra, F. *Nano Lett.* **2011**, *11*, 402-407.
(168) Zhai, Y.; DuChene, J. S.; Wang, Y.-C.; Qiu, J.; Johnston-Peck, A. C.; You, B.; Guo, W.; DiCiaccio, B.; Qian, K.; Zhao, E. W.; Ooi, F.; Hu, D.; Su, D.; Stach, E. A.; Zhu, Z.; Wei, W. D. *Nat. Mater.* **2016**, *15*, 889-895.
(169) Straney, P. J.; Marbella, L. E.; Andolina, C. M.; Nuhfer, N. T.; Millstone, J. E. *J. Am. Chem. Soc.* **2014**, *136*, 7873-7876.
(170) Smith, A. M.; Marbella, L. E.; Johnston, K. A.; Hartmann, M. J.; Crawford, S. E.; Kozycz, L. M.; Seferos, D. S.; Millstone, J. E. *Anal. Chem.* **2015**, *87*, 2771-2778.
(171) Nikoobakht, B.; El-Sayed, M. A. *Chem. Mater.* **2003**, *15*, 1957-1962.
(172) Straney, P. J.; Andolina, C. M.; Millstone, J. E. *Langmuir* **2013**, *29*, 4396-4403.
(173) Manne, S.; Cleveland, J.; Gaub, H.; Stucky, G.; Hansma, P. *Langmuir* **1994**, *10*, 4409-4413.
(174) Grönbeck, H.; Curioni, A.; Andreoni, W. *J. Am. Chem. Soc.* **2000**, *122*, 3839-3842.
(175) Li, J.; Zheng, Y.; Zeng, J.; Xia, Y. *Chem. Euro. J.* **2012**, *18*, 8150-8156.
(176) Love, J. C.; Estroff, L. A.; Kriebel, J. K.; Nuzzo, R. G.; Whitesides, G. M. *Chem. Rev.* **2005**, *105*, 1103-1170.
(177) Yamada, T.; Batina, N.; Itaya, K. *J. Phys. Chem.* **1995**, *99*, 8817-8823.
(178) Rodríguez-Fernández, J.; Perez-Juste, J.; Mulvaney, P.; Liz-Marzan, L. M. *J. Phys. Chem. B* **2005**, *109*, 14257-14261.
(179) Rodríguez-Fernández, J.; Pérez-Juste, J.; Mulvaney, P.; Liz-Marzán, L. M. *J. Phys. Chem. B* **2005**, *109*, 14257-14261.
(180) Brongersma, M. L.; Halas, N. J.; Nordlander, P. *Nature Nano.* **2015**, *10*, 25-34.
(181) Greeley, J.; Nørskov, J. K.; Kibler, L. A.; El-Aziz, A. M.; Kolb, D. M. *ChemPhysChem* **2006**, *7*, 1032-1035.
(182) Ferrando, R.; Jellinek, J.; Johnston, R. L. *Chem. Rev.* **2008**, *108*, 845-910.

(183) Hung, W. H.; Aykol, M.; Valley, D.; Hou, W.; Cronin, S. B. *Nano Lett.* **2010**, *10*, 1314-1318.
(184) Holewinski, A.; Xin, H.; Nikolla, E.; Linic, S. *Curr. Opin. Chem. Eng.* **2013**, *2*, 312-319.
(185) Marimuthu, A.; Zhang, J.; Linic, S. *Science* **2013**, *339*, 1590-1593.
(186) Kanninen, P.; Johans, C.; Merta, J.; Kontturi, K. *J. Colloid. Interf. Sci.* **2008**, *318*, 88-95.
(187) Zhu, H.; Sigdel, A.; Zhang, S.; Su, D.; Xi, Z.; Li, Q.; Sun, S. *Angew. Chem.* **2014**, *126*, 12716-12720.
(188) Xia, X.; Xie, S.; Liu, M.; Peng, H.-C.; Lu, N.; Wang, J.; Kim, M. J.; Xia, Y. *P. Nat. A. Sci.* **2013**, *110*, 6669-6673.
(189) Grzelczak, M.; Pérez-Juste, J.; Rodríguez-González, B.; Liz-Marzán, L. M. *J. Mater. Chem.* **2006**, *16*, 3946-3951.
(190) Weiner, R. G.; DeSantis, C. J.; Cardoso, M. B.; Skrabalak, S. E. *ACS Nano* **2014**, *8*, 8625-8635.
(191) Chen, W.; Yu, R.; Li, L.; Wang, A.; Peng, Q.; Li, Y. *Angew. Chem. Int. Ed.* **2010**, *49*, 2917-2921.
(192) Han, L.; Cui, P.; He, H.; Liu, H.; Peng, Z.; Yang, J. *J. Power Sources* **2015**, *286*, 488-494.
(193) Xia, X.; Figueroa-Cosme, L.; Tao, J.; Peng, H.-C.; Niu, G.; Zhu, Y.; Xia, Y. *J. Am. Chem. Soc.* **2014**, *136*, 10878-10881.
(194) Liu, R.; Sen, A. *Chem. Mater.* **2011**, *24*, 48-54.
(195) Hodges, J.; Biacchi, A.; Schaak, R. *ACS Nano* **2014**, *8*, 1047-1055.
(196) Ortiz, N.; Weiner, R. G.; Skrabalak, S. E. *ACS Nano* **2014**, *8*, 12461-12467.
(197) Sau, T. K.; Murphy, C. J. *J. Am. Chem. Soc.* **2004**, *126*, 8648-8649.
(198) Pastoriza-Santos, I.; Sánchez-Iglesias, A.; Rodríguez-González, B.; Liz-Marzán, L. M. *Small* **2009**, *5*, 440-443.
(199) Kochi, J.; Subramanian, R. *Inorg. Chem.* **1965**, *4*, 1527-1533.
(200) Toledo, I.; Arancibia, M.; Andrade, C.; Crivelli, I. *Polyhedron* **1998**, *17*, 173-178.
(201) Eckert, J.; Sewell, T. D.; Kress, J. D.; Kober, E. M.; Wang, L. L.; Olah, G. *J. Phys. Chem. A* **2004**, *108*, 11369-11374.
(202) Lisiecki, I.; Pileni, M. *J. Phys. Chem.* **1995**, *99*, 5077-5082.
(203) Chan, G. H.; Zhao, J.; Hicks, E. M.; Schatz, G. C.; Van Duyne, R. P. *Nano Lett.* **2007**, *7*, 1947-1952.
(204) Hölzle, M.; Apsel, C.; Will, T.; Kolb, D. *J. Electrochem. Soc.* **1995**, *142*, 3741-3749.
(205) Radisic, A.; Vereecken, P.; Searson, P.; Ross, F. *Surf. Sci.* **2006**, *600*, 1817-1826.
(206) Haynes, W. M. *CRC Handbook of Chemistry and Physics, 93rd Edition*; Taylor & Francis: Boca Raton, FL, 2012.
(207) Xu, J. G.; Wang, X. W. *Surf. Sci.* **1998**, *408*, 317-325.
(208) Koch, R.; Hu, D.; Das, A. *Phys. Rev. Lett.* **2005**, *94*, 146101.
(209) Ghodselahi, T.; Vesaghi, M.; Shafiekhani, A.; Baghizadeh, A.; Lameii, M. *Appl. Surf. Sci.* **2008**, *255*, 2730-2734.
(210) Rice, K. P.; Walker Jr, E. J.; Stoykovich, M. P.; Saunders, A. E. *J. Phys. Chem. C* **2011**, *115*, 1793-1799.
(211) Tominaka, S. *J. Mater. Chem.* **2011**, *21*, 9725-9730.
(212) Schön, G. *Surf. Sci.* **1973**, *35*, 96-108.